# High Dynamic Range Analog Photonic Links

# Design and Implementation

by

David Marpaung

**Samenstelling van de promotiecommissie:**

**Voorzitter & secretaris:**

| | |
|---|---|
| prof.dr.ir. A.J. Mouthaan | University of Twente, The Netherlands |

**Promotor:**

| | |
|---|---|
| prof.dr.ir. W. van Etten | University of Twente, The Netherlands |

**Assistent-promotor:**

| | |
|---|---|
| dr.ir. C.G.H. Roeloffzen | University of Twente, The Netherlands |

**Leden:**

| | |
|---|---|
| prof.dr. J. Schmitz | University of Twente, The Netherlands |
| prof.dr. A. Driessen | University of Twente, The Netherlands |
| prof.dr.ir. F. E van Vliet | University of Twente, The Netherlands |
| prof.dr.rer.nat. D. Jäger | University of Duisburg-Essen, Germany |
| dr.ir. D.H.P. Maat | ASTRON, The Netherlands |

The work described in this thesis is is supported by the Dutch Ministry of Economic Affairs under the PACMAN project. Senter Novem project number TSIT 3049.

The research presented in this thesis was carried out at the Telecommunication Engineering group, Faculty of Electrical Engineering, Mathematics and Computer Science, University of Twente P.O. Box 217, 7500 AE Enschede, The Netherlands.



ISBN: 978-90-365-2860-3

Printed by Ipskamp Drukkers B.V., Enschede, The Netherlands

Typeset in LaTeX

# HIGH DYNAMIC RANGE ANALOG PHOTONIC LINKS: DESIGN AND IMPLEMENTATION

PROEFSCHRIFT

ter verkrijging van
de graad van doctor aan de Universiteit Twente,
op gezag van de rector magnificus,
prof.dr. H. Brinksma,
volgens besluit van het College voor Promoties
in het openbaar te verdedigen
op donderdag 27 agustus 2009 om 15.00 uur

door

David Albert Immanuel Marpaung

geboren op 19 maart 1979
te Balikpapan, Indonesië

Dit proefschrift is goedgekeurd door:

De promotor: prof.dr.ir. W. van Etten

De assistent-promotor: dr.ir. C.G.H. Roeloffzen

# Summary

Recently, there is an increasing interest in the distribution of (analog) radio frequency (RF) or microwave signals over the optical fibers. In this so-called analog photonic links (APL) an RF signal is converted into an optical signal, distributed via an optical fiber and subsequently restored to the electrical format at the recipient's end using a photodetector. Using the advantage of a low propagation loss of the optical fiber, the APL has become the heart of an emerging field of microwave photonics (MWP), in which various functionalities like generation, distribution, control and processing of RF signals have been explored. To perform these complex functionalities, it is imperative for the APL to provide a high performance. This is challenging since such an analog system is relatively susceptible to noise and nonlinearities. In this thesis, the techniques to optimize the performance of APLs are presented.

A set of parameters, commonly defined for RF components, have been used to describe the performance of an APL. The most important parameters are the link gain, the noise figure and the spurious-free dynamic range (SFDR). The link gain describes the RF-to-RF transfer of the signals from the input to the output of the APL while the noise figure describes the signal-to-noise ratio (SNR) degradation in the APL. The SFDR, on the other hand, describes the range of RF signal power that can be accommodated by the APL, taking into account the effects of noise and nonlinear distortions.

In general there are two types of APL, the directly modulated and the externally modulated ones. In the former, the injection current of a laser is directly modulated by the RF signal while in the latter the light from a continuous wave (CW) laser is modulated using an external electro-optic modulator. The most popular type of such a modulator is the Mach-Zehnder modulator (MZM). The characteristics of direct and external modulation APLs are somewhat different. For this reason, a distinction is made between the performance enhancement techniques for these modulation formats.

For an externally-modulated APL with an MZM, increasing the optical power to the modulator is very attractive for increasing the link gain, which increases in a quadratic manner with the optical power. Depending on the dominant noise source, this will also reduce the noise figure and subsequently increasing the SFDR. In combination with a high input optical power, low biasing the MZM away from the quadrature bias point effectively reduces the APL noise figure and limits the average photocurrent in the photodetector to avoid saturation. But these advantages come at the expense of a reduced linearity due to elevated even-order distor-

tion levels, which in turn restricts the APL to sub-octave (narrowband) applications. This limitation can be mitigated using a pair of low-biased MZMs and a balanced photodetector, known as the Class-AB scheme. Beside the Class-AB scheme, an architecture using a dual-output MZM combined with a balanced detection scheme is also promising to provide very high link performance.

Compared to its externally-modulated counterpart, enhancing the performance of a directly-modulated laser (DML) APL is more challenging. Unlike in the case of an MZM APL, simply increasing the emitted optical power from the laser will not improve the link gain of a DML APL. Moreover, low biasing the lasers in the DML link is not advantageous to reduce the link noise due to the relative-intensity noise (RIN) enhancement near the laser threshold. Characterization results on a novel scheme that utilized a pair of low-biased laser diodes and a balanced detector have shown that the low biasing reduces the lasers responses and the modulation bandwidths as well as enhancing the noise and the nonlinear distortions. Overall, low biasing the lasers significantly reduces the SFDR of the APL.

Despite the fact that low biasing degrades the link performance, the premise of using a pair of laser diodes and a balanced detector is still promising for a performance enhancement purpose. Instead of biasing close to the threshold, the lasers bias currents are optimized to obtain the lowest third order intermodulation (IMD3) powers. Then, these lasers are modulated in a push-pull manner and, subsequently, the RF modulation amplitude and phase of each laser were adjusted using variable optical attenuator and delay line such that the second-order intermodulation distortion (IMD2) power at the output is minimized. With this arrangement, a high multioctave SFDR can be achieved. One of the highest broadband SFDR ever shown with a directly modulated laser link has been demonstrated at the frequency of 2.5 GHz using this arrangement. The SFDR value was 120 dB.Hz$^{2/3}$ and an IMD2 power suppression of 40 dB was obtained. In a wide frequency range of 600 MHz (2.60 to 3.20 GHz), an IMD2 suppression as high as 23 dB and an improvement of 5 to 18 dB of the second-order SFDR, relative to a conventional single arm photonic link, have been demonstrated.

# Contents

# 1 Introduction

## 1.1 Microwave Photonics

Over the past thirty years, the field of optical communication has enjoyed major growth and development. This progress has been initiated by the invention of optical fibers [1]. The low loss and the ultrawide bandwidth of these optical fibers are the main advantages of signal distributions in the optical domain. Although most of the optical systems deployed nowadays are carrying baseband digital signals (for example, multi gigabit long haul links [2] or access networks [3]), some portions of the system are dedicated for analog applications. While relatively lower in volume compared to their digital counterparts, these so-called analog photonic links (APLs) have recently enjoyed a surge in both scientific interest and real-life applications.

In their early developments, the APLs were used in applications where analog-to-digital conversions are either undesirable or too difficult to perform, due to the additional requirements on power, cost and complexity [4]. The applicability of these APLs was initially limited because analog links have more stringent performance requirements relative to digital optical links [5]. But the availability of diode lasers, high speed optical modulators and detectors have driven the APLs development [6] to perform more functionalities. Nowadays, the APLs have become the main alternative to coaxial-cable links which are heavy, less flexible and have very high losses for long distance transmissions of high-frequency signals. Since the loss of optical fibers are the same for virtually any microwave frequency, using an APL offers transparencies (i.e. the same transmission medium for all frequencies) as well as lightweight and flexibility. Moreover, the links have been aimed at performing very complex functions, which were impossible to be done directly in the radio frequency (RF) or microwave domains [7]. In this sense, the APLs have increas-

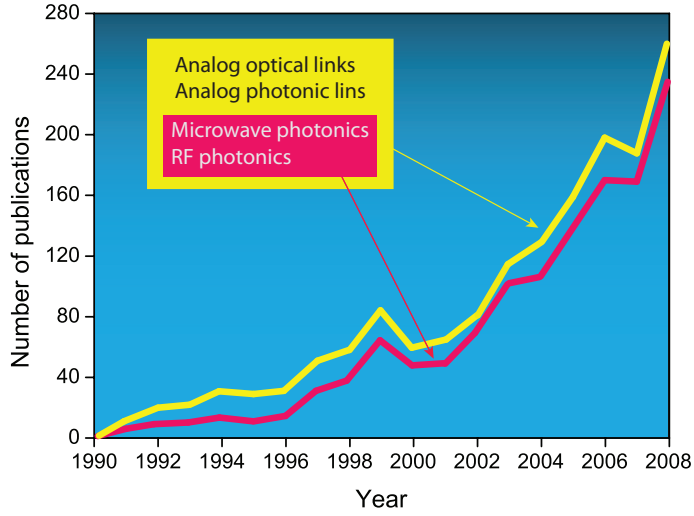


**Figure 1.1:** The number of publications related to the field of microwave photonics in the period of 1990 until 2008. The data is compiled from the ISI Web of Knowledge [10]. The search terms used to obtain the data are microwave photonics, RF photonics, analog optical links and analog photonic links.

ingly become an essential part of an emerging field known as microwave photonics (MWP).

The term microwave photonics itself was introduced as early as 1991 [8], describing the novel optoelectronic components based on interaction of traveling optical waves and microwaves. Later on, the definition was widened to describe the study of optoelectronic devices and systems processing signals at microwave rates, or the use of optoelectronic devices and systems for signal handling in microwave systems [9]. Over the past few years, the interest of the scientific community to the field of MWP has grown considerably. This is illustrated in Figure 1.1 where the number of scientific publications within the topic of MWP published per year is depicted. The data was compiled from the ISI Web of Knowledge [10] using search queries depicted in the box in the figure. It is clear that the number of publications in this field has increased rapidly, notably in the last five years. Additionally, various review papers [4, 6, 7, 9, 11–16] and books [17–19] have also been published related to the field. Note that the data depicted in Figure 1.1 was not meant to completely represent the number of publications in MWP but used to give impressions of how the field has evolved.

The results presented in Figure 1.1 do not comprise the papers published in conferences, symposiums or meetings, where the topic has also been well received. A topical meeting on MWP has been held every year regularly since 1996 [20] while the topic has also been included regularly in special sessions of major conferences, for example the IEEE MTT International Microwave Symposium [21], the European

Conference on Optical Communications (ECOC) [22] and the Optical Fiber Communication Conference (OFC) [23].

## 1.2 Analog Photonic Links (APLs)

In the heart of any MWP system is an analog photonic link (APL). In its most simple arrangement, the APL consists of a modulation device and a photodetector, connected with an optical fiber as illustrated in Figure 1.2. A high frequency RF or microwave signal is converted to an optical signal in the modulation device. After the transmission or distribution, the optical signal is converted back to the electrical format in the photodetector. The main advantage of the transmission in the optical format stems from the very low propagation losses in the optical fiber, which can be as low as 0.2 dB/km at the optical wavelength of 1550 nm [24] and is virtually the same for all RF or microwave frequencies. If the signal transmission or distribution is instead done in the native electrical format with a coaxial cable, the loss will be extremely high and it increases with the signal frequency. For example, a current low-loss coaxial cable has the attenuation of 190 dB/km at the frequency of 5.8 GHz [25, 26], while the loss of a more common 1/2 inch cable (RG-214) exceeds 500 dB/km [27].

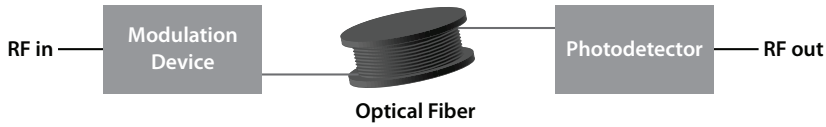


**Figure 1.2:** A generic schematic of an analog photonic link.

Although the propagation losses in APLs are low, the electrical-to-optical (E/O) conversion and vice-versa (O/E) will contribute to signal losses. In addition, these conversions lead to added noise and nonlinear distortions. The APL requires linearity and low noise, such that the analog signals can be transmitted with high fidelity [4]. Unless the system is optimized, severe performance degradation will occur leading to worse performance relative to the coax-based links [26, 28]. Thus, the APLs design and performance optimizations are paramount, to ensure the applicability of such links in various microwave photonics systems.

## 1.3 Modulation and Detection Schemes

In general, the RF or the microwave signal can be conveyed over an APL by modulating either the intensity, phase or the frequency of the optical carrier. As for the detection scheme, two ways can be implemented, direct detection, which work for intensity modulation scheme, and coherent detection which works with phase or frequency modulations. Due to its simplicity, the intensity modulation combined with direct detection (IMDD) is by far the most popular and the most widely em-

ployed scheme. For this reason, we limit the discussion in this thesis to the IMDD scheme. The reader can refer to [29, 30] for the topic of coherent detection.

Two choices to implement the IMDD scheme are to use direct modulation or external modulation schemes. In direct modulation systems, the laser injection current is directly modulated by the RF signal and the information is impressed in the output intensity of the laser. In contrast, in an externally-modulated link, the laser is operated in a continuous wave (CW) mode and the modulation is done externally with an optical modulator. The advantage of a directly modulated laser link lies on their simplicity and low cost. But for high frequency and high performance applications, the externally modulated link is more popular. This is because direct modulation is limited in frequency due to the relaxation oscillation [6] and chirp, which refers to inadvertent frequency modulation in an intensity modulated signal, which will induce pulse broadening [31]. In this thesis, the performance of directly modulated laser APLs will be discussed in Chapter 4 and Chapter 5 while the external modulation is investigated in Chapter 3 and Chapter 6.

## 1.4 Link Components

One of the important aspects of an APL design is component selections. So far there have been various different components considered to be used in an APL. They can be categorized into three major divisions, namely light sources, optical modulators and photodetectors. In addition we briefly discuss the characteristics of the optical fibers which are relevant to APLs performance.

### 1.4.1 Light Sources

For direct modulation, virtually all links use diode (semiconductor) lasers [13], as illustrated in Figure 1.3. To carry the high frequency signals with high fidelity, the desired characteristics of these lasers are high modulation bandwidth, high slope efficiency, high linearity and low intensity noise. The slope efficiency is a laser figure of merit that describes the conversion efficiency of electrical modulation to optical modulation, and has the unit of W/A [17]. The laser intensity noise is usually described in a quantity called relative intensity noise (RIN), which is the variance of the optical power fluctuations relative to the square of the average optical power [32], commonly expressed in dB/Hz. The majority of laser diodes used in the APLs are edge emitting lasers: Fabry-Perot (FP) or distributed feedback (DFB) lasers [33–35]. However, in the past few years, the vertical-cavity-surface-emitting lasers (VCSELs) have gained popularity. These lasers offer low cost and very low power consumption due to the low threshold current. More importantly, their performance is improving, where long wavelength (1310 nm), large modulation bandwidth and good linearity and dynamic range characteristics have been recently demonstrated [36–39].

As for external modulation, the desired features of the CW laser source are high output optical power and low RIN. As will be explained in Chapter 3, the performance of an external modulation link improves with the input optical power to the

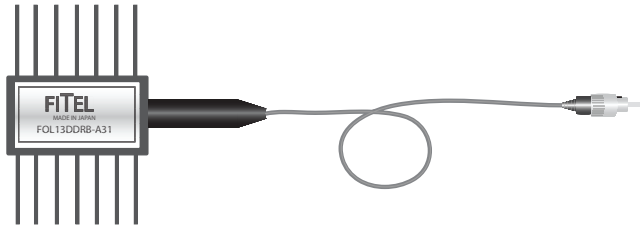


**Figure 1.3:** Semiconductor laser diode in a 14-pin butterfly package used in analog photonic links.

modulator. Optical sources with narrow linewidth such as semiconductor, solid-state and doped-fiber lasers are appropriate choices [11]. An output optical power of 150 mW has been achieved using a high-power semiconductor DFB laser [40]. High power (100 mW) at 1550 nm in a 14-pin butterfly package is already available commercially [41]. Diode-pumped solid-state lasers (DPSS) have a superior noise performance compared to the semiconductor laser and can provide higher optical power [42]. This type of laser, for example Nd:YAG or erbium-doped glass lasers, has been used in high performance links shown over the years [43–45] but the main drawbacks are their bulk size and high price. Moreover, such light sources operating at 1550 nm are not commercially available [13]. Recently, external modulation links with the best performance (in terms of gain and noise figure) have been shown with a fiber laser oscillator followed with an Erbium-doped fiber amplifier to create master-oscillator power amplifier (MOPA) [46, 47]. This MOPA, which has an output power in excess of 3 W at 1550 nm and a RIN lower than -150 dB/Hz, is already available commercially [48].

### 1.4.2 Optical Modulators

The most widespread type of optical modulator is the Mach-Zehnder modulator (MZM). The principal of operation of this type of modulator is shown in Figure 1.4. A voltage applied to the electrodes of the MZM (commonly fabricated in lithium niobate) will induce a change of refractive index in one or in both arms of the MZM. The refractive index change induces an optical phase-shift between the arms. If there is no phase-shift, the waveguides are designed such that the light in the upper and the lower arms interfere constructively, yielding a maximum output power (the upper part of Figure 1.4). When the applied voltage induces a $180^{o}$ phase shift between the arms, the light will interfere destructively yielding to a minimum output power. This voltage is known as the DC half-wave voltage, or $V_{\pi,\mathrm{DC}}$. Continuous change of voltage will yield the well-known sinusoidal transfer characteristics of the MZM. In its most common mode of operation, the MZM is biased at its quadrature point, which is the half of the half-wave voltage and the modulating RF voltage is applied on top of this bias.

The desired characteristic of an MZM in order to achieve a high performance are low RF half-wave voltage $V_{\pi,\mathrm{RF}}$, high optical power handling, low insertion loss

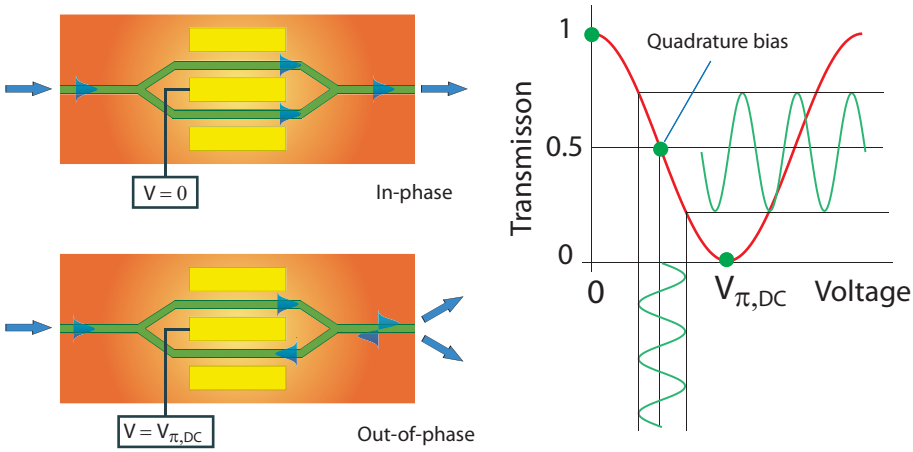


**Figure 1.4:** The principle of operation of a Mach-Zehnder modulator (MZM).

and wide bandwidth. The typical insertion loss of this type of device is 3 to 7 dB [13]. As for the RF half-wave voltage, sub-1 V value is desired. Due to design constraints, low $V_{\pi,\mathrm{RF}}$ can be achieved at the expense of the modulation bandwidth. A current state-of-the-art values are 1.15 V at 2 GHz [49] and 1.33 V at frequency of 12 GHz [47]. Beside lithium-niobate, new materials are recently considered to perform electro-optic modulation with the MZM arrangement. Electro-optic polymer materials [50, 51] and silicon [52] have been investigated, yielding very promising performances in terms of $V_{\pi,\mathrm{RF}}$, power consumption and size reduction.

Another type of modulator that is gaining popularity these days is the electroabsorption modulator (EAM). It is a semiconductor-based optical modulator which operation is based on the change of optical absorption coefficient in materials due to the presence of electric field (i.e. electroabsorption effect) [53]. There are two types of electroabsorption effect: one is the Franz-Keldysh effect in the bulk active layer, the other is the quantum-confined Stark effect in multiple-quantum-wells. The transfer function that relates the EAM transmission (i.e., the ratio of the output and the input optical powers) with the input voltage to the modulator can be mathematically written as:

$$T_{\mathrm{EAM}}(V) = t_0 e^{-\gamma\alpha(V)L_{\mathrm{m}}} \tag{1.1}$$

where $t_0$ is the modulator insertion loss at zero applied voltage, $\gamma$ is the optical confinement factor, $\alpha(V)$ is the change of optical absorption coefficient due to the applied voltage, $V$, and $L_{\mathrm{m}}$ is the modulation length. An attractive feature of electroabsorption modulators is that they can be integrated with semiconductor lasers to form compact optical sources capable of ultrafast modulation [54, 55]. Since the electroabsorption effect is accompanied by photocurrent generation [53], the EAM can simultaneously be used as a modulator and a photodetector [8, 56]. Such dual function EAM is called electroabsorption transceiver and it is used to simplify the

remote antenna unit (RAU) in a radio over fiber system. Although initially showed a limited optical power handling, recently high power handling EAMs have been reported in [57] and [58], where optical powers as high as 100 mW and 300 mW, respectively, have been handled without any damage. The EAM is also promising to achieve high spurious-free dynamic range (SFDR), as demonstrated in [59].

### 1.4.3 Photodetectors

Virtually all photodetectors used in APLs nowadays are based on a P-I-N structure. Avalanche photodetectors (APDs) have been considered to be used in APLs, where a high gain-bandwidth product has been achieved [11]. A moderate dynamic range has also been shown with an APD [60]. However, the power handling capability of the APD is currently too low for applications in low noise figure APLs, which utilize high received optical power [9]. Thus, these detectors are more suited for applications like high-bit-rate long-haul fiber optic communications, where the received optical power is typically low. In this case, the APD internal gain provides a sensitivity margin relative to P-I-N photodiodes [61].

A high performance APL requires an efficient, linear and fast photodetector. This means that high responsivity (the produced photocurrent per unit received optical power), high linearity and large bandwidth are desired. As we will see later on in Chapter 3, high performance external modulation APLs require increasingly higher optical power. Thus, in addition to the high responsivity, linearity and bandwidth, high optical power handling is becoming important. However, these desired characteristics cannot be simultaneously achieved due to the trade-offs in the photodetector design [11]. But recent advancements in the design, which include surface illuminated design, such as partially depleted absorber photodiode (PDA-PD) has shown remarkably high current handling (beyond 100 mA) and high linearity [62, 63] while very high bandwidth (beyond 150 GHz) have been achieved with good responsivity and high photocurrent using the InP-based photodetectors [64].

### 1.4.4 Optical Fibers

For APLs considered in this thesis, the optical fiber connecting the modulation device and the photodetector can be regarded ideal, from the point of view of attenuation, dispersion and nonlinearities. Unlike in the case of long haul digital links, where the transmission distance can reach tens of kilometers, most of the time an APL should only bridge a distance of typically less than 1 km. For standard single mode fibers, the loss for this transmission distance due to the fiber attenuation is less than 0.2 dB at the wavelength of 1550 nm (Figure 1.5). Thus, the effect is negligible. This is also true for the chromatic dispersion effect, i.e. the change of propagation velocity with frequencies, of the fibers. It has been shown in [65] that for a standard single mode fiber with a chromatic dispersion of 17 ps/km·nm and a length of 1 km, the SNR-penalty induced by the fiber dispersion for a signal frequency of 30 GHz is less than 1 dB. The effect is even less prominent for lower signal frequencies, which is the case considered throughout this thesis. For this reason,

we also neglect the effects of chromatic dispersions in the optical fibers.

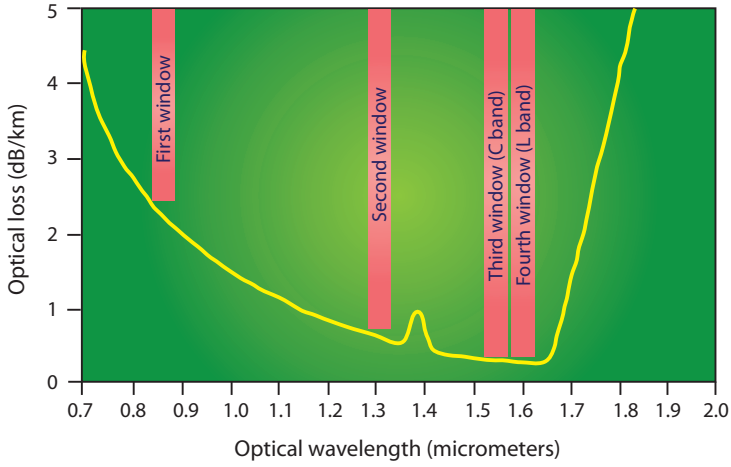


**Figure 1.5:** Optical fiber attenuation as function of the wavelength.

As mentioned earlier, the trend in enhancing the performance of external modulation APLs is to use higher and higher optical power. In this case, fiber nonlinearities might come into play. The most detrimental effect can occur from the stimulated Brillouin scattering (SBS) [47, 66, 67] which is a scattering of light backwards towards the transmitter caused by acoustic vibrations in the fiber [68]. The SBS limits the amount of optical power that can be transmitted as well as adding intensity noise to the propagating light [66]. To give an example, a 20 km effective length of fiber has an SBS threshold power of 1 mW. However, this power threshold is inversely proportional to the transmission distance. For distances less than a kilometer, which is typical for the APLs, the threshold is 100 mW or more [4]. For this reason, in this thesis, we neglect the contribution from the nonlinear characteristics of the optical fibers.

## 1.5 APL Applications

The APLs have been used in various systems involving the generation, processing, control and distribution of RF or microwave signals [16]. Here we will review some of the notable applications of APLs. We start with the distribution of cable television (CATV) signals, which initiated the interests in APLs. Moreover, we will discuss radio over fiber systems for wireless applications, antenna remoting for warfare and radio astronomy as well as processing of high frequency signals. Other ongoing and potential applications are briefly discussed in the last subsection.

### 1.5.1 CATV Distribution Network

During 1970s, the prospects of replacing copper cables by optical fibers in the CATV distribution networks were investigated [69–72]. The idea was to modulate the optical carrier with multiple CATV signals, thereby exploiting the available bandwidth of the optical fibers. This technique is also known as the subcarrier multiplexing (SCM). However, since the system uses a large number of RF carriers (in some cases up to 110 carriers), it requires high linearity and, in an addition to that, low noise. In such a system, the performance is quantified in terms of carrier-to-noise ratio (CNR) to describe the effect of noise, and composite second-order (CSO) and composite triple beat (CTB) to describe the relative level of interfering spurious signals generated by quadratic and cubic nonlinearities. The comprehensive research on the APL performance in such systems were described in [73] and [74].

### 1.5.2 Radio over Fiber for Wireless Systems

Radio over fiber (ROF) systems use APLs to distribute RF signals from a central location to remote antenna units (RAUs). This allows the RAUs to be very simple because they only need to contain E/O and O/E conversion devices and amplifiers. Functions like coding, modulation, multiplexing and upconversion can be performed at a central location [19] because the low-loss of the optical fiber permits the shift of these functions away from the antenna. The RAUs simplification is attractive for efforts to increase the capacity of wireless communication systems, which can be done by either reducing the cell size or to increase the carrier frequencies to avoid the congested ISM (industrial, scientific and medical) band frequencies [27]. Smaller cell size means that a large number of RAUs are needed and their simplification will significantly limit the cost of their deployment.

An ROF system has been demonstrated as early as 1990 [75] where four-channel second-generation cordless telephony signals were distributed over single-mode fiber by using SCM technique. From this point onwards, various ROF architectures were proposed and investigated. The dynamic range requirements of such systems were investigated in [76]. ROF systems operating in the millimeter-wave band have been investigated [77] and the feasibility of operation at the frequency band as high as 120 GHz has been demonstrated [78]. To reduce the cost further, ROF architecture using a multimode fiber was also investigated [26]. The performance of a single sideband modulation technique to combat dispersion effect were investigated in [79]. Recently, a demonstration of optically-powered RAUs has also been shown. The remote unit was powered with a laser with a wavelength of 830 nm, delivered with a multimode optical fiber. The results show that a modest optical power of 250 mW, converted to electrical power via a photovoltaic converter, can be used to power the unit containing a laser diode, a photodiode and amplifiers [80]. This technique is very attractive in cases where a provision of a conventional electrical power supply is impractical, for example in high voltage environments.

### 1.5.3 Antenna Remoting for Military Applications

Employing APLs for antenna remoting is attractive in military and warfare applications. A typical application in this field requires the APL to bridge very short distance which is less than 100 m [28]. The APL is used to replace the coaxial cables due to their low propagation loss, wide bandwidth, small size, light weight, flexibility for system reconfiguration and immunity to electromagnetic interference [81]. The large number of coaxial cables used on military platforms make the size of the cable plant a significant issue for avionic, submarine, and even surface ship applications. Especially in avionics applications, the heavy weight of these cables become an issue. From the flexibility point of view, particular copper coax and waveguides are installed based on the frequencies transmitted by the systems involved. Thus system reconfiguration involving replacing or adding new RF sensors requires modification or addition to the cable plant. Installation/routing of stiff coax and waveguide in confined spaces is also a significant issue. The APL reduces the size and weight of the cable plant. System reconfiguration can be done without modifying the cable plant, as the same optical fiber is used no matter the frequency of the RF signal being transmitted. Additionally, providing dark fiber adds only a little to the size of the cables and wavelength division multiplexing (WDM) can be considered for running multiple wideband RF signals over the same fiber [82].

However, to perform these tasks in the military platforms, the APL should show adequate performance, notably in terms of RF gain, noise figure, linearity and dynamic range. For example, the SFDR[§] requirements of a stringent application like an anti-jamming radar is around 120-130 dB.Hz$^{2/3}$ [83]. Additionally, for remoting modern radars, the APL should also meet stringent phase noise requirements [84, 85]. Various demonstrations of APLs deployment in military platforms have been reported [28, 81–89]. Promising results have been reported, notably in terms of the phase noise performance [84, 85], multioctave dynamic range [87] and signal processing capabilities [82, 83, 88, 89]. But beside these promising results, various issues still need to be addressed, such as E/O and O/E conversions efficiencies to achieve high link gain and enhancement in SFDR. These improvements are imperative to leverage the advantage of using APLs in this platform over the existing coaxial cable links, especially in short distance applications.

### 1.5.4 Radio Astronomy Applications

The use of APLs in radio astronomy is mainly directed towards antenna remoting [90–96] and local oscillator (LO) signal distribution [95, 97–100]. To increase the sensitivity, radio telescopes nowadays are designed as arrays of small antennas capable of very large collecting areas. Some of the examples of these antenna arrays are the Allen Telescope Array (ATA) [101], Atacama Millimeter Array (ALMA) [102], the Low Frequency Array (LOFAR) [103] and the Square Kilometer Array (SKA) [104]. These arrays contain of a large number of elements, covering a large area. This is illustrated in Figure 1.6 where an artist impression of the SKA antenna is depicted.

[§]The definition of SFDR is given in Chapter 2.

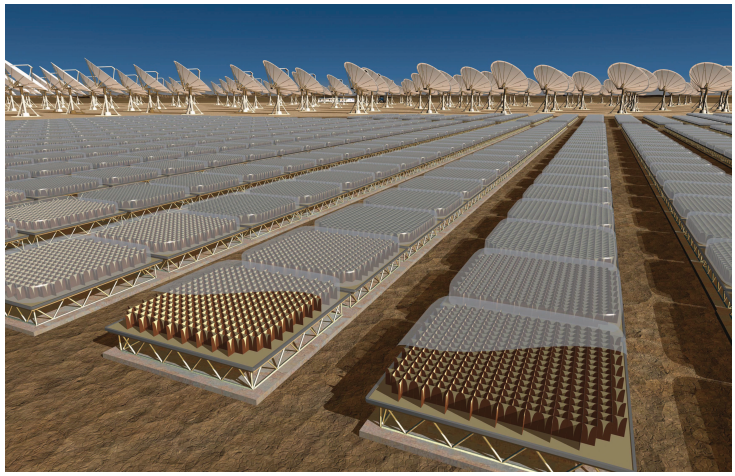

**Figure 1.6:** An artist impression of the square kilometer array (SKA) antenna.

APLs can be used in such a large scale antenna array to distribute the signals among the antenna elements (or antenna tiles) and the connections to the central processor. The APLs offer low propagation loss independent of the frequency in contrast with the coaxial cables. However, the APLs should show very high performance because the systems are very demanding in terms of multioctave SFDR and phase noise for the LO distribution. Demonstrations of these APLs in the radio astronomy systems have been investigated. The notable reported results include the study of the SFDR and phase stability for the SKA platform [90], the use of integrated DFB laser and EA modulator in the ATA platform [93], the use of external modulation link in to distribute the LO signal in the NASA Deep Space Network [100] and the use of directly modulated VCSEL in the Australian SKA Pathfinder (ASKAP) [96]. The results show promising potentials in applying APLs in these large scale antenna arrays.

### 1.5.5 Other Applications

Although in smaller volumes compared to the previously mentioned applications, APLs have also found their way in applications like EMC sensors [105–107] and MRI signal distribution [108, 109] taking advantage of their EMI immunity characteristics.

Beside signal distributions, Microwave Photonics also offers other capabilities. The most investigated functionalities are carrier generation [110] and signal processing [7, 16]. The latter functionality includes filtering [111–113] and beamforming, where photonic techniques are used to obtain true-time delays of microwave signals [114–120].

## 1.6 The Research Project

The work presented here is part of the PACMAN (Phased Array Communication antennas for Mass-market Application Needs) project funded by the Dutch Ministry of Economic Affair, SenterNovem project number TSIT3049. The goal of the project is to research and develop integrated technology for the design and manufacturing of mass-market, low cost phased-array antenna that can be applied in various domains, such as telecom, wireless internet, satellite communication, radars, large area astronomic antenna, automotive and security.

The collaborative partners in this project are Thales Netherlands, ASTRON (The Netherlands Institute of Radio Astronomy), the Electromagnetics group of the Eindhoven University of Technology (TUE) and two research groups from the University of Twente, which are the Design, Production and Management group and the Telecommunication Engineering group, where most of the work presented here was executed. The measurement results presented in Chapter 6 was part of the work executed in the R&D department of ASTRON.

The aim of the work is to investigate the feasibility of photonics technology insertions in large scale phased-array antennas. As shown in Figure 1.7, more and more functionalities are projected to be performed in the optical domain, departing from the all-electronics systems that are currently employed. These functionalities include antenna remoting and signal distribution using the APLs, photonic beamforming with true time delay [120], filtering and carrier generation for LO using photonic techniques (shown as the mixer system in Figure 1.7). The work in this thesis, thus belongs to the first functionality, which is the signal distribution, using APLs. The task was to investigate the performance of current APL architectures and to propose new schemes for their performance enhancements. A special emphasis was paid to the DML links due to their low cost potential and simplicity.

## 1.7 Outline of the Thesis

The thesis consists of seven chapters. In the first chapter, the introduction to the field Microwave Photonics and, especially, the analog photonic links (APLs) are given. The aim is to give an idea of the type of components, modulation schemes as well as current and future applications that are associated with the APLs. Reference to various publications have been made to direct the readers towards relevant sources related to microwave photonics. At the end of this chapter, the research objective of the thesis is explained.

In the second chapter, the performance of an analog photonic link is discussed in depth. Four important aspects of the APL, namely the gain, noise, nonlinearity and spurious-free dynamic range (SFDR) are introduced and their mathematical descriptions are presented. A clear distinction is made between the direct laser modulation and external modulation schemes. The explanations in this chapter are accompanied by various examples where the performance metrics of the APL are calculated using realistic link parameters.

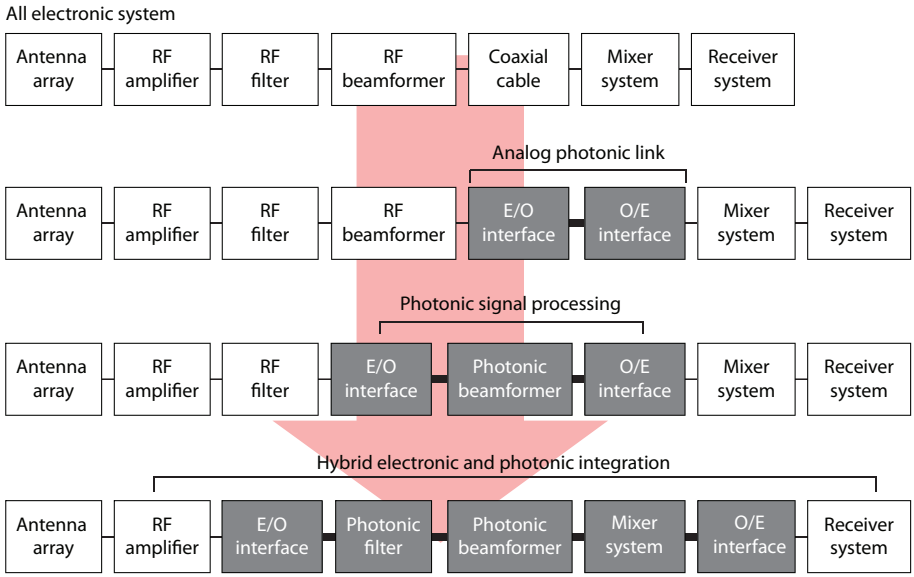


**Figure 1.7:** The evolution of photonic technology insertion in a large-scale phased-array antenna systems [94]. The part that is carried out in this thesis is the APLs technology for antenna remoting and signal distributions.

In Chapter 3, the existing efforts for performance enhancement of APLs are reviewed and discussed. A heavy emphasis was made on the efforts towards link gain enhancement and noise figure reduction in APLs using Mach-Zehnder modulators (MZMs). Linearization of this type of link is also discussed. The performance enhancement of directly-modulated laser (DML) links are also studied. Although considerably more briefly compared to the discussion of the MZM APL, this part serves as an adequate introduction to Chapter 4 and Chapter 5 that are devoted to DML links.

The concept of low biasing a DML to increase the link performance is the starting point of the investigation presented in Chapter 4. A novel architecture called the Balanced Modulation and Detection (BMD) scheme is introduced and its advantage are investigated by means of simulations. The realization and characterization of such a link are also presented. We discuss and explain the reason why the measured performance of this scheme deviates from the expected behavior predicted from the simulations.

Chapter 5 has a strong connection with the materials presented in Chapter 4. A similar but simpler architecture as the BMD link is investigated here. The link employs push-pull modulation of a pair of semiconductor laser diodes. The aim is to suppress even order nonlinearity and to maximize the multioctave SFDR. This investigation results is one of the highest broadband SFDR ever shown in a DML link.

In Chapter 6, measurement results on the performance of an MZM link are presented. Three different arrangements of optical sources are considered here. A medium power laser, a high power laser and a laser with an optical amplifier have been used to power the link. The link performance is quantified in terms of gain, noise figure, input intercept points and SFDR. Finally, the thesis ends with conclusions and recommendations in Chapter 7.

# 2

# Key Parameters of Analog Photonic Links

## 2.1 Introduction

The main requirement of an Analog Photonic Link (APL) is to transmit the analog signal from point to point with high fidelity. However, as in any analog system, APLs are relatively susceptible to various signal impairments, such as signal loss, noise and nonlinearities. This is especially true if we compare them to a digital optical link. These signal impairments are quantified into a number of parameters that at the end define the performance of the APL. These parameters, gain, noise figure and dynamic range to name a few, are very similar to the one used to characterize a two-port radio frequency (RF) component, for example an amplifier or an attenuator. This is because in general an APL can be regarded as a black box characterized by an RF input and an RF output. In this chapter, the definition and the mathematical expressions of the performance parameters are given. The concept of link gain of directly and externally modulated APLs are given in Section 2.2. In Section 2.3, the dominant noise sources and the definition of noise figure are introduced. The fourth section is devoted to the nonlinear effects in an APL, which includes the definitions of intermodulation distortions and intercept points. Finally, the spurious-free dynamic range commonly defined for APLs is discussed in Section 2.5. This chapter closes with a summary.

## 2.2 Link Gain

A general schematic of an APL is shown in Figure 2.1. The link consists of a modulation device which converts the electrical (RF) signal into an optical signal, an optical fiber and a photodetector which recovers the modulated light back to the electrical domain. These signal conversions, from electrical to optical domains (E/O) and vice-versa (O/E) are by and large inefficient and will eventually lead to signal loss as one compares the APL input and output RF powers. To describe the transfer

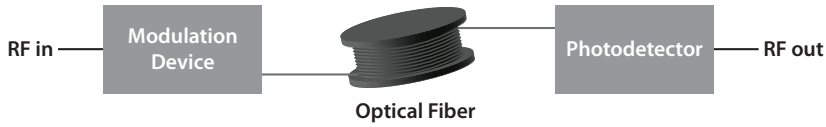


**Figure 2.1:** Schematic of an analog photonic link

characteristics of an APL, we can start with a general expression of the link transfer function

$$H(\omega) = |H(\omega)| \exp\left(\mathrm{j}\phi(\omega)\right) \tag{2.1}$$

where $|H(\omega)|$ and $\phi(\omega)$ are the APL magnitude and the phase responses, respectively. For the rest of our discussion in this chapter we will assume that the APL shows an ideal linear phase response and focus instead to the magnitude response. The square of this magnitude response, $|H(\omega)|^2$, describes the power transfer from the input to the output of the APL as a function of the signal frequency. This is illustrated in Figure 2.2, which depicts the typical measured $S_{21}$ parameter, i.e. power transmission, of an APL.

This power transmission is known as the link gain, which essentially is the ratio of the RF power observed at the output of the APL relative to the input power. We will derive this link gain expression in terms of the physical parameters of the APL. However, in doing so, we will require a the concept of available power, commonly used in network theory [121]. Consider an arrangement consisting of a voltage source $V_S$ with a source impedance $R_S$ loaded with a load impedance of $R_L$, as shown in Figure 2.3. The available power, $P_S$ is defined as the electrical power delivered to the load in the case where the load impedance is matched to the source impedance ($R_L = R_S$). Thus the available power- in Watt- can be written as

$$P_S = \frac{V_S^2}{4R_S}. \tag{2.2}$$

We will use this concept of available power in defining the APL link gain. We start by modeling the APL as a two-port RF system connected in series with a voltage signal source, with a series resistance $R_S$ and a load resistance of $R_L$ as shown in Figure 2.4. The link gain, being the ratio of the output and the input powers to the APL, is then defined as

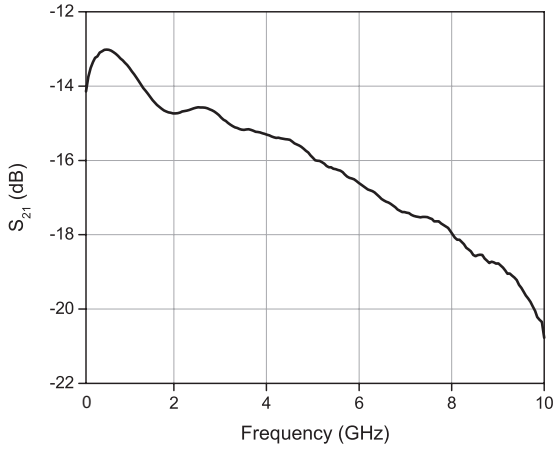


**Figure 2.2:** The typical measured power transmission in an APL

$$g = \frac{P_L}{P_S} = \frac{\langle {I_L}^2(t)\rangle R_L}{\langle {V_S}^2(t)\rangle / 4R_S} \tag{2.3}$$

where $P_S$ is the source available power, $P_L$ is the power delivered to the load, $V_S$ is the source voltage and $I_L$ is the current flowing through the load.[‡] The notation $\langle\cdot\rangle$ indicates the temporal average defined as

$$\langle A(t)\rangle \triangleq \lim_{T\to\infty} \frac{1}{2T}\int_{-\infty}^{\infty} A(t)\,\mathrm{d}t \tag{2.4}$$

where $A(t)$ is a time dependent function and $T$ is the time interval in which the function is evaluated. Later on, when we explicitly define the source voltage as a sinusoidal RF signal, the signal period will be used as the time interval, $T$.

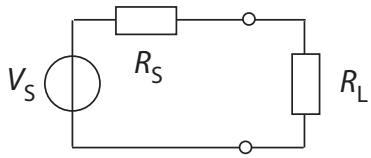


**Figure 2.3:** Series connection of a voltage source and a load resistance

The use of the available power in Equation (2.3) suggests that the source is impedance matched to the input of the APL. Although there are various impedance matching schemes that have been implemented at both the input and at the output of an APL, in this thesis we will restrict ourselves only to the scheme known as the lossy impedance matching. In this scheme, the impedances of both the modulation device and the photodetector are regarded as purely resistive, and resistors

[‡]Later on we will see that this current is proportional to the detected optical power.

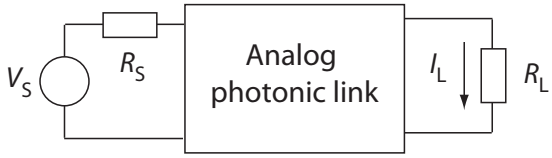


**Figure 2.4:** Series connection of a source, an APL and a load

are added in series or in parallel to match the input and output impedances to the 50 Ω source and load resistances. This choice is motivated by the fact that most of our components used in the experiments (lasers, modulators and photodetectors) are applying this matching scheme. The reader can refer to [17] for an overview of various other matching schemes.

To determine the APL link gain, we have to examine the current delivered to the load, $I_L$ in Equation (2.3). This parameter is closely related to the received optical power at the detector, $P_{det}$, which can be split into the (constant) average optical power, $P_{av}$, and the modulated optical power, $P_{mod}$, obeying the relation

$$P_{det}(t) = P_{av} + P_{mod}(t) . \tag{2.5}$$

The received optical power is then converted to the detected photocurrent, which can also be split into a DC component, $I_{av}$ and a modulated current, $I_{mod}$, via the relations

$$\begin{aligned} I_{det}(t) &= r_{PD} P_{det}(t) \\ &= r_{PD} [P_{av} + P_{mod}(t)] \\ &= I_{av} + I_{mod}(t) \end{aligned} \tag{2.6}$$

with $r_{PD}$ to be the detector responsivity, in A/W. Recall that a lossy impedance matching is imposed at the photodetector, which is modeled as a current source due to its relatively high resistance (see Figure 2.5). A matching resistor, $R_{match,PD}$, is thus added in parallel to the photodetector to match the output load resistance, $R_L$. In case of $R_{match,PD} = R_L$, the current delivered to the load, $I_L$, is simply half of the modulated photocurrent $I_{mod}$ as the matching network acts simply as a current divider. Thus, the load current can be written as:

$$I_L(t) = \frac{1}{2} r_{PD} P_{mod}(t) . \tag{2.7}$$

Adding the photodetector matching resistor will minimize the signal reflection back to the detector but, as evident from Equation (2.3), this has the consequence of a reduced link gain by as much as 6 dB compared to the case where there is no impedance matching. As we will see later on, the APL link gain is premium and numerous effort has been spent in maximizing this quantity. Clearly its reduction is highly undesirable and one can argue if it is necessary to add this matching resistor. In our analysis, however, we will proceed with the matched case merely for

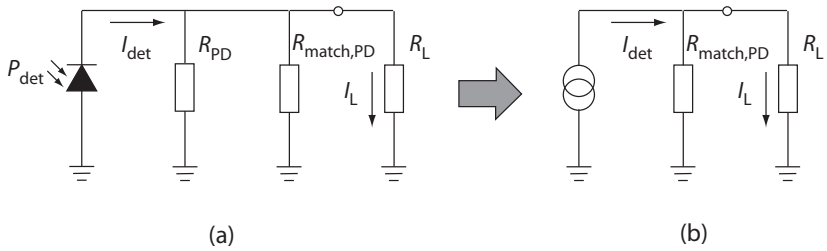


**Figure 2.5:** (a) Schematic of a photodiode with a matching impedance $R_{\text{Match,PD}}$, (b) Equivalent model of the photodiode as a current source

the sake of having a better comparison between the theoretical expressions and the measurement results.

At this point, we are ready to evaluate the expression of an APL link gain if we have the the expression for the modulated optical power, $P_{\text{mod}}$, in Equation (2.7). However, this term depends on whether a direct modulation or an external modulation scheme is used. For this reason, we separate the link gain evaluation for these two cases in the following subsections.

### 2.2.1 Direct Modulation

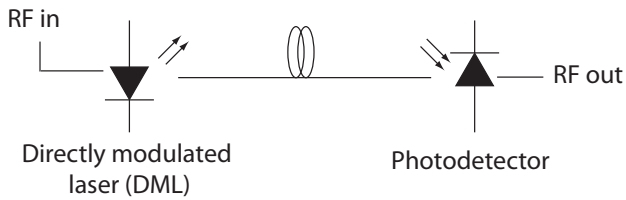


**Figure 2.6:** Schematic of a directly modulated APL

A typical direct modulation APL consists of a laser diode an optical fiber and a photodetector, as shown in Figure 2.6. The injection current to the laser is modulated with the RF signal resulting in a modulated output optical power. Hence, in the directly modulated laser (DML) APL, the laser acts both as the optical source and the modulation device. In this subsection, we will derive the link gain expression for such an APL. We start with the expression of the injection current to the laser diode (LD),

$$I_{\text{LD}}(t) = I_{\text{bias}} + I_{\text{sig}}(t) \tag{2.8}$$

where $I_{\text{bias}}$ is the DC bias current and $I_{\text{sig}}$ is the AC signal current. The DC bias is necessary to avoid signal clipping and to ensure linearity. This injection current is converted to optical power at the LD output, $P_{\text{LD}}$, via the relation

$$P_{\text{LD}}(t) = s_{\text{LD}}\left(I_{\text{LD}}(t) - I_{\text{th}}\right). \tag{2.9}$$

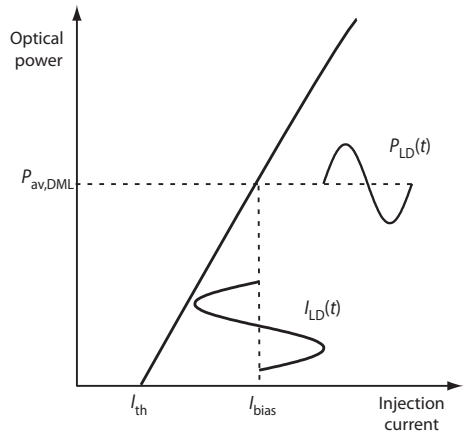


**Figure 2.7:** LI curve of a laser diode

Here, $I_{\text{th}}$ is the laser threshold current and $s_{\text{LD}}$ is the laser slope efficiency expressed in W/A. This transfer is illustrated at Figure 2.7, where the the ideal light-current (L-I) curve of a laser is depicted. Note that we have considered a strictly linear relation between the current and the optical power in Equation (2.9). In practice, however, the relation is nonlinear, but we will defer the discussion about laser nonlinearities when we discuss the nonlinear distortion in APLs in Section 2.4.

Our next step is to express the laser signal current, $I_{\text{sig}}$ in terms of the voltage of the signal source $V_{\text{S}}$. Let us consider the series connection of a voltage source and the laser diode as shown in the schematic in Figure 2.8. We have assumed that a lossy impedance matching scheme is implemented between this signal source and the laser diode. Here, the laser impedance is modeled as a resistor, $R_{\text{LD}}$, connected in series with the laser diode. The value of this laser resistance is usually low, typically around $5\,\Omega$. Thus a matching resistor, $R_{\text{match,LD}}$, is added in series to $R_{\text{LD}}$ such that their combination fulfill the relation

$$R_{\text{LD}} + R_{\text{match,LD}} = R_{\text{S}} \tag{2.10}$$

with $R_{\text{S}}$ being the source resistance. Thus, the signal current to the laser can be written as

$$I_{\text{sig}}(t) = \frac{V_{\text{S}}(t)}{R_{\text{S}} + R_{\text{match,LD}} + R_{\text{LD}}}\,. \tag{2.11}$$

Assuming that the optical loss in the APL is $L$, the detected optical power arriving at the photodetector can be written as

$$\begin{aligned} P_{\text{det,DML}}(t) &= \frac{P_{\text{LD}}(t)}{L} \\ &= P_{\text{av,DML}} + P_{\text{mod,DML}}(t) \end{aligned} \tag{2.12}$$

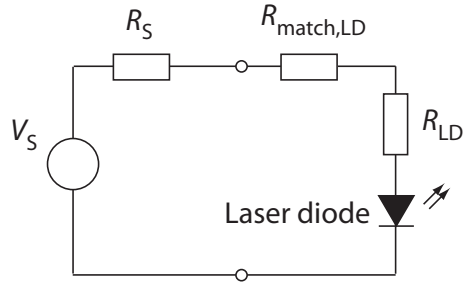


**Figure 2.8:** Laser diode impedance matching circuit

where $P_{av,DML}$ and $P_{mod,DML}$ are the average and the modulated received optical powers, respectively, defined as

$$P_{av,DML} = \frac{s_{LD}}{L}\left(I_{bias} - I_{th}\right) \tag{2.13}$$

and

$$P_{mod,DML}(t) = \frac{s_{LD}}{L} I_{sig}(t)\,. \tag{2.14}$$

The photodetector converts the received optical power in Equation (2.12) into the detected photocurrent. Recall that only the AC part of this photocurrent contributes to the link gain. The load current can be calculated by substituting the combination of Equation (2.11) and Equation (2.14) into Equation (2.7), where the result is shown below

$$I_{L,DML}(t) = \frac{r_{PD}\, s_{LD}\, V_S(t)}{2L\left(R_S + R_{match,LD} + R_{LD}\right)}\,. \tag{2.15}$$

The final step is to insert the load current expression in Equation (2.15) into the definition in Equation (2.3), yielding the expression of the link gain, $g_{DML}$, as

$$g_{DML} = \frac{R_S R_L}{\left(R_S + R_{match,LD} + R_{LD}\right)^2}\left(\frac{r_{PD}\, s_{LD}}{L}\right)^2\,. \tag{2.16}$$

If we consider the situation where the load resistance is equal to the source resistance $R_L = R_S$ and use the relation in Equation (2.10), the link gain expression is reduced to

$$g_{DML} = \frac{1}{4}\left(\frac{r_{PD}\, s_{LD}}{L}\right)^2\,. \tag{2.17}$$

Thus, the link gain of a DML in case of impedance matched source and detector depends only on three parameters, the laser slope efficiency, the photodetector responsivity and the optical loss in the APL. The fact that the link gain is proportional to $(1/L)^2$ tells us that minimizing the optical loss in an APL is premium since 1 dB of optical loss will be translated to 2 dB of RF loss. Another important conclusion that can be drawn from Equation (2.17) is that in the case of a direct laser modulation,

the link gain does not depend on the optical power. Later on we will see that this is very different from the case of external modulation, in which optical power is an important factor in link gain maximization.

Among the parameters that influence the link gain of a DML APL, the optical loss is the only system parameter whereas the laser slope efficiency and the photodetector responsivity are device parameters. This implies that while a link designer can optimize the system such that the optical loss is minimized, the slope efficiency and the responsivity are fixed once the components selection has been made. For this reason, the efforts in maximizing the link gain in a directly modulated APL is very limited, compared to the various techniques implemented in its external modulation counterpart. In order to illustrate a practical link gain value of a directly modulated link, let us consider the following example.

**Example 2.1**
Consider a distributed feedback (DFB) laser diode, with an optical wavelength, $\lambda$ = 1550 nm. A typical value of the slope efficiency of such laser is roughly between 0.1 and 0.4 W/A, while the photodetector responsivity typically has a value of 0.75 to 0.85 A/W [13]. Supposed that the optical loss in the APL amounts to 1 dB, the link gain in Equation (2.17) expressed in decibels, can assume the value between -30 dB to -17 dB, for the lowest and the highest values of $s_{\mathrm{LD}}$ and $r_{\mathrm{PD}}$, respectively. Moreover, if we consider an ideal photodiode without an internal gain, the maximum responsivity is $r_{\mathrm{PD,max}} = \lambda_0/1.25$ A/W [122], where $\lambda_0$ is the optical wavelength in $\mu$m. Setting $\lambda_0 = 1.55\,\mu$m, we obtain that $r_{\mathrm{PD,max}} = 1.25$ A/W. This corresponds to a maximum link gain of -12 dB even if there is no optical loss. This "negative link gain" means that the RF power experiences a net loss as it propagates from the input to the output of the APL.



### 2.2.2 External Modulation

In this subsection, we will derive the expression of the modulated optical power, and subsequently the link gain, of an externally-modulated APL. In an external modulation APL, the laser is operated in a continuous wave (CW) mode and the modulation is performed in an external device, which is an optical intensity modulator. Here, we will limit our discussion only to a type of optical modulator known as the Mach-Zehnder modulator (MZM). The architecture of an APL employing the MZM is shown in Figure 2.9.

The detected optical power of an APL with an MZM can be written as

$$P_{\mathrm{det,MZM}}(t) = \frac{P_{\mathrm{i}}}{2L}\left(1-\cos\left[\pi\left(\frac{V_{\mathrm{B}}}{V_{\pi,\mathrm{DC}}}+\frac{V_{\mathrm{RF}}(t)}{V_{\pi,\mathrm{RF}}}\right)\right]\right) \tag{2.18}$$

where $P_{\mathrm{i}}$ is the input optical power to the modulator, $L$ is the optical loss, $V_{\mathrm{B}}$ is the modulator bias voltage, $V_{\mathrm{RF}}$ is the modulating RF signal and $V_{\pi,\mathrm{DC}}$ and $V_{\pi,\mathrm{RF}}$ are the DC and the RF half-wave voltages, respectively. Note that $L$ in the above equation comprises two terms, the modulator insertion loss, $L_{\mathrm{mod}}$ and an excess loss, $L_{\mathrm{ex}}$,

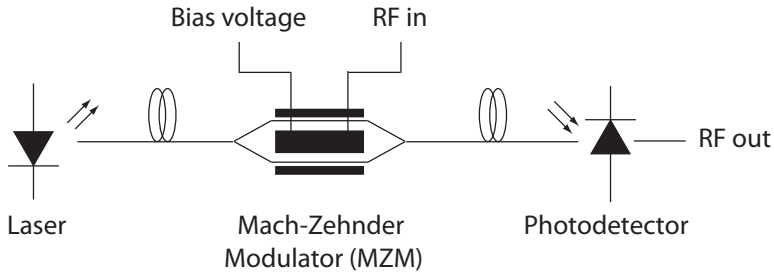


**Figure 2.9:** Schematic of an externally-modulated APL using an MZM

such that $L = L_{\text{mod}} L_{\text{ex}}$. An example of this excess loss is the connector losses in the APL.

Expanding the argument of the cosine sum and using the small signal approximation $V_{\text{RF}} \ll V_{\pi,\text{RF}}$, Equation (2.18) can be approximated as

$$P_{\text{det,MZM}}(t) \approx P_{\text{av,MZM}} + P_{\text{mod,MZM}}(t) + P_{\text{NL}_2,\text{MZM}}(t) + P_{\text{NL}_3,\text{MZM}}(t) \tag{2.19}$$

where $P_{\text{av,MZM}}$ is the average optical power, $P_{\text{mod,MZM}}$, $P_{\text{NL}_2,\text{MZM}}$ and $P_{\text{NL}_3,\text{MZM}}$ are the terms with linear, quadratic and cubic dependence on the modulating signal $V_{\text{RF}}$, respectively. These terms can be mathematically written as,

$$P_{\text{av,MZM}} = \frac{P_{\text{i}}}{2L}\left(1 - \cos\phi_{\text{B}}\right) \tag{2.20}$$

$$P_{\text{mod,MZM}}(t) = \frac{P_{\text{i}}}{2L}\frac{\pi V_{\text{RF}}(t)}{V_{\pi,\text{RF}}}\sin\phi_{\text{B}} \tag{2.21}$$

$$P_{\text{NL}_2,\text{MZM}}(t) = \frac{P_{\text{i}}}{4L}\left(\frac{\pi V_{\text{RF}}(t)}{V_{\pi,\text{RF}}}\right)^2\cos\phi_{\text{B}} \tag{2.22}$$

$$P_{\text{NL}_3,\text{MZM}}(t) = -\frac{P_{\text{i}}}{12L}\left(\frac{\pi V_{\text{RF}}(t)}{V_{\pi,\text{RF}}}\right)^3\sin\phi_{\text{B}} \tag{2.23}$$

with $\phi_{\text{B}}$ the bias angle defined as

$$\phi_{\text{B}} \triangleq \frac{\pi V_{\text{B}}}{V_{\pi,\text{DC}}}. \tag{2.24}$$

Figure 2.10 shows $P_{\text{av,MZM}}/P_{\text{i}}$ as a function of $\phi_{\text{B}}$. This relation is usually referred as the transfer function of an MZM. As we will see later, the term $P_{\text{av,MZM}}$ will contribute to the noise in the the APL, while the terms $P_{\text{NL}_2,\text{MZM}}$ and $P_{\text{NL}_3,\text{MZM}}$ are responsible for the nonlinearities. Meanwhile, for the link gain calculation, only the contribution of the linear component, $P_{\text{mod,MZM}}$, should be taken into account.

Using Equations (2.3), (2.7) and (2.21), and recognizing that $V_{\text{RF}}(t) = 1/2 V_{\text{S}}(t)$ due to the lossy impedance matching imposed at the modulator, the link gain of an

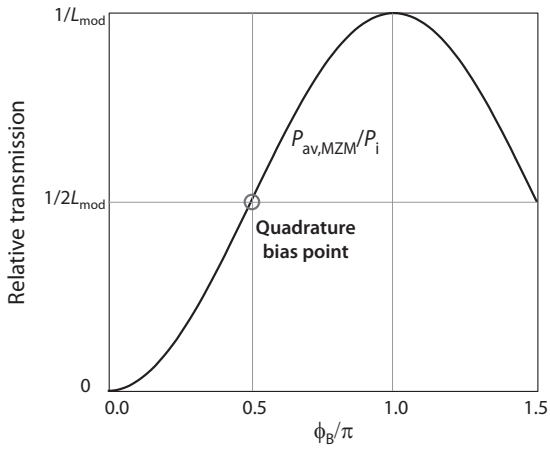


**Figure 2.10:** Transfer function of a Mach-Zehnder modulator

MZM APL can be written as

$$g_{\mathrm{MZM}} = \left( \frac{\pi \, r_{\mathrm{PD}} \, R \, P_{\mathrm{i}} \sin \phi_{\mathrm{B}}}{4 \, L \, V_{\pi,\mathrm{RF}}} \right)^2 \tag{2.25}$$

where we have set $R_{\mathrm{S}} = R_{\mathrm{L}} = R$.

Carefully inspecting Equation (2.25), we can identify several approaches to increase the link gain of an MZM APL, as listed below:

- *Increasing the optical power to the modulator.* This is an important feature of external modulation and the main difference compared to its direct modulation counterpart where the link gain is independent of the optical power. In the latter case , the link gain is virtually determined solely by the slope efficiency, which is a physical parameter of the laser and relatively more difficult to adjust. On the other hand, the input optical power to the modulator is a system parameter and, given the resources, can be increased significantly. However, increasing input optical power will demand a higher power handling of both the modulator and the detector. This is challenging especially for the photodetector, since high power handling requires a large detector area, which in turn will limit the detector bandwidth. We will return to this subject when we discuss the link gain optimization techniques in Chapter 3.

- *Reducing the modulator half-wave voltage.* The RF half-wave voltage can be regarded as the sensitivity of a modulator. The effort of reducing $V_{\pi,\mathrm{RF}}$ obviously fall in the region of component design and is beyond the scope of this thesis. We point out, however that a $V_{\pi,\mathrm{RF}}$ value as low as 1.08 V at a frequency of 6 GHz has been reported recently [47].

- *Biasing the modulator at quadrature.* The quadrature bias point is set at $\phi_B = \pi/2$ which gives $V_{\mathrm{B}} = {}^1\!/_2 V_{\pi,\mathrm{DC}}$. As evident from Equation (2.25), the link

gain reaches maximum at this bias point. Due to this reason and to the fact that all even-order distortion terms are completely suppressed at this bias point (Section 2.3), quadrature biasing is the universal mode of operation in an MZM APL. However, as we will see in Chapter 3, various techniques use non quadrature biasing in order to enhance the noise performance of an MZM APL.

- *Reducing the modulator insertion loss.* This option again falls in the domain of component design. A typical value of insertion loss is around 2 to 4 dB, depending on how well the light is coupled from the fiber to the modulator chip and back. Moreover, quadrature biasing will add 3 dB of insertion loss on top of the fiber-coupling losses. Thus, a total insertion loss of 5 to 7 dB can be expected at this bias point. Since 1 dB of optical loss will be translated to 2 dB of RF losses, this effect alone will contribute to 10 to 14 dB of RF losses, which can severely deteriorate the APL link gain.

Now let us consider a pair of examples that illustrate the importance of the MZM half-wave voltage, the input optical power to the modulator and the optical power handling capabilities of the modulator and the photodetector.

**Example 2.2**
Consider an MZM with these parameters : $V_{\pi,\mathrm{DC}} = 6.4\,\mathrm{V}$, $V_{\pi,\mathrm{RF}} = 3.8\,\mathrm{V}$, and $L_{\mathrm{mod}} = 4\,\mathrm{dB}$. Moreover we assume an excess loss ($L_{\mathrm{ex}}$) of 1 dB occurs in the APL such that the total optical loss, $L$, in Equation (2.25) amounts to 5 dB. The modulator is biased at quadrature $\left(\phi_{\mathrm{B}} = \pi/2\right)$ and the detector responsivity is taken to be 0.75 W/A, while the source and the load resistances are assumed to be 50 Ω. If the input optical power at the modulator, $P_{\mathrm{i}}$ is set at 20 mW (+13 dBm), the calculated link gain according to Equation (2.25) in decibels is −26.2 dB. Now suppose we use a different modulator with the same characteristics but with a lower RF half-wave voltage of 1.9 V, the link gain will be improved to −20.2 dB.

**Example 2.3**
Reconsider the original configuration ($V_{\pi,\mathrm{RF}} = 3.8\,\mathrm{V}$) in the previous example. If we replace the light source with a high power laser with an output optical power of +23 dBm, the theoretical link gain that can be achieved is -6.2 dB. However, the typical average optical power handling capability of a commercially available MZM is around +20 dBm. Thus, the link gain now is limited to -12.2 dB. Moreover, suppose that the maximum average optical power that can be handled by the photodetector is around +10 dBm. In this case, the usable input optical power is further limited to +18 dBm, which can be easily calculated using Equation (2.20). This will result in the achievable link gain of -16.2 dB, a ten fold reduction compared to the case where the optical power handling of the components is not an issue.

## 2.3 Noise in APLs

In the previous section we have discussed the signal transfer from the input to the output of an APL and learned that most of the time the signal experiences losses. This is one of the limitation of an APL. In this section, we will discuss another factor that limits the APL performance, which is the noise. We will start by introducing the dominant noise sources in the APL and proceed with the discussion of the total noise power in the link. Finally we will discuss the concept of noise figure, which is an important and a widely used APL parameter.

There are three dominant noise terms in APLs; thermal noise, shot noise and laser relative intensity noise (RIN). As a rule, these noise terms are modeled as current sources and they are assumed to be wide-sense stationary, ergodic and independent of each other [17, 121]. The assumption that these sources are independent implies that the total noise power in the APL is proportional to the sum of the noise power generated by the individual sources. Wide-sense-stationarity and ergodicity imply that for evaluating the noise power, the noise variance (i.e ensemble average) can be be interchanged with its mean-squared value, which is its temporal average [121]. In the following subsections, the expressions for the mean-squared current of the individual sources are derived.

### 2.3.1 Thermal Noise

Thermal noise (or Johnson noise) describes the voltage fluctuations across a dissipative circuit element, for example a resistor, which is caused by thermal motion of the charge carriers [123]. This voltage fluctuation, $v_{\text{th}}$, is modeled as a zero-mean Gaussian process, and its power spectral density (PSD) across a resistor with resistance $R$ at an absolute temperature of $T$ is [121]

$$S_{v_{\text{th}}v_{\text{th}}}(\omega) = \frac{h|\omega|R}{\pi\left[\exp\left(\frac{h|\omega|}{2\pi kT}-1\right)\right]} \tag{2.26}$$

where $\omega = 2\pi f$ is the angular frequency, $k = 1.38\times10^{-23}$ J/K is the Boltzmann constant and $h = 6.63\times10^{-34}$ Js is the Planck constant. The power spectrum shown in Equation (2.26) is flat up to frequencies around 1 THz and can be regarded as white [121]. Thus, the PSD in Equation (2.26) can be simplified into

$$S_{v_{\text{th}}v_{\text{th}}}(\omega) = 2kTR \tag{2.27}$$

Integrating the spectrum in Equation (2.27) and using the Wiener-Khinchin theorem (Appendix A), the variance of the thermal noise voltage can be written as

$$\left\langle v_{\text{th}}^2(t)\right\rangle = 4kTRB \tag{2.28}$$

where $B$ is the equivalent noise bandwidth of the receiver in Hz. Note that the additional factor of 2 in Equation (2.28) appears because both positive and negative

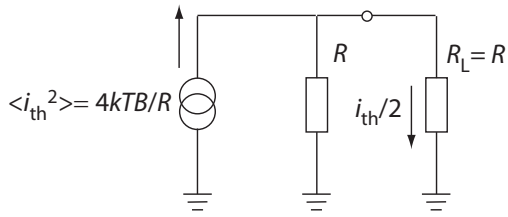


**Figure 2.11:** A noisy resistor loaded with a resistively-matched load

frequencies should be included in the integration. Finally, the variance of the thermal noise current is

$$\left\langle i_{\text{th}}^2(t)\right\rangle = \frac{4kTB}{R} \tag{2.29}$$

The electrical power in Watt delivered by this thermal noise source to a (noiseless) load resistance, $R_{\text{L}}$ is

$$p_{\text{th}} = \left\langle i_{\text{th}}^2(t)\right\rangle R_{\text{L}}\,. \tag{2.30}$$

Later on, we will numerously encounter a situation in which we have to evaluate the electrical power delivered by a thermal noise source to a load which is resistively matched to this source. This situation is illustrated in Figure 2.11. In this case, only half of the thermal noise current in Equation (2.29) is delivered to the load, yielding

$$\begin{aligned} p_{\text{th,mL}} &= \frac{1}{4}\left\langle i_{\text{th}}^2(t)\right\rangle R \\ &= kTB \end{aligned} \tag{2.31}$$

where we have used the extra subscript "mL" in the thermal noise power to indicate the matched load and set $R_{\text{L}} = R$ in the first line of Equation (2.31).

### 2.3.2 Shot Noise

Shot noise is generated at the photodetector due to the random arrival of photons which generate a random fluctuation in the detected photocurrent. Mathematically, the shot noise current, $i_{\text{shot}}$, is a random process with Poisson distribution [31]. The PSD of the shot noise current is flat and given as

$$S_{i_{\text{shot}}i_{\text{shot}}}(\omega) = q\,I_{\text{av}} \tag{2.32}$$

where $q = 1.6\times10^{-19}$ C is the electron charge and $I_{\text{av}}$ is the average received photocurrent defined in Equation (2.6). Once more using the Wiener-Khinchin theorem, the shot noise variance can be written as

$$\left\langle i_{\text{shot}}^2(t)\right\rangle = 2q\,I_{\text{av}}\,B \tag{2.33}$$

Subsequently, the electrical power (in Watts) delivered by this current to a load resistance, $R_{\mathrm{L}}$, is

$$\begin{aligned} p_{\mathrm{shot}} &= \left\langle i_{\mathrm{shot}}^2(t) \right\rangle R_{\mathrm{L}} \\ &= 2q\, I_{\mathrm{av}}\, B\, R_{\mathrm{L}} \\ &= 2q\, r_{\mathrm{PD}}\, P_{\mathrm{av}}\, B\, R_{\mathrm{L}}. \end{aligned} \tag{2.34}$$

In contrast with thermal noise, shot noise power depends linearly on the average photocurrent, and consequently, the received optical power.

### 2.3.3 Relative Intensity Noise

The relative intensity noise is generated due to the spontaneous emission added to the coherent field of the laser [31]. This results in the random fluctuation of the unmodulated optical carrier, which at the end will be observed as the fluctuation in the detected photocurrent at the receiver output.

To formulate the relative intensity noise variance, let us begin by writing the unmodulated optical power received at the detector as

$$P_{\mathrm{o}}(t) = P_{\mathrm{av}} + \Delta p(t) \tag{2.35}$$

where $P_{\mathrm{av}}$ is defined in Equation (2.5) and $\Delta p(t)$ is a random power fluctuation due to the spontaneous emission. The laser relative intensity noise, $\mathrm{rin}(\omega)$ is defined as the PSD of the relative power fluctuation $\Delta p / P_{\mathrm{av}}$ [31].

$$\left\langle \Delta p^2(t) \right\rangle = \frac{{P_{\mathrm{av}}}^2}{2\pi} \int_{-\infty}^{\infty} \mathrm{rin}(\omega)\, \mathrm{d}\omega \tag{2.36}$$

In evaluating the integral in Equation (2.36) we will make two assumptions. First, we assume that the rin is flat within the receiver noise bandwidth, $B$ such that we can completely drop its dependence on $\omega$. Secondly, instead of defining the rin as a double-sided PSD we alternatively define it as a single-sided spectra [32]. This means that the rin only exists for positive frequencies, and the measurement bandwidth will simply be $B$ instead of $2B$ like in previous cases. A factor of 2 will then be lumped to the single sided spectral density instead. We use the single sided spectra here as an exception and only for the sake of having a better agreement with the widely used definition [11, 124, 125]. Taking these assumptions into account, the variance of the optical power fluctuation then can be written as

$$\left\langle \Delta p^2(t) \right\rangle = \mathrm{rin}\, {P_{\mathrm{av}}}^2 B. \tag{2.37}$$

Finally, the variance of the relative intensity noise current, $i_{\mathrm{rin}}$, can be written as

$$\left\langle {i_{\mathrm{rin}}}^2(t) \right\rangle = \mathrm{rin}\, {I_{\mathrm{av}}}^2 B. \tag{2.38}$$

where we have used Equation (2.6) and the relation $i_{\mathrm{rin}}(t) = r_{\mathrm{PD}} \Delta p(t)$.

Keep in mind that in Equation (2.36) - (2.38), the rin PSD is expressed in a linear scale, i.e., the unit is 1/Hz. However, it is more common to express this PSD in decibels, i.e. in dB/Hz, instead. For this reason, we define RIN as

$$\mathrm{RIN} = 10 \log_{10} (\mathrm{rin}) \,. \tag{2.39}$$

Using the above equation, the expression in Equation (2.38) can be rewritten as:

$$\left\langle {i_{\mathrm{rin}}}^2 (t) \right\rangle = 10^{\frac{\mathrm{RIN}}{10}} \, {I_{\mathrm{av}}}^2 B \,. \tag{2.40}$$

Finally, we can calculate the electrical power delivered by this current to a load resistance, $R_{\mathrm{L}}$ as

$$\begin{aligned} p_{\mathrm{rin}} &= \left\langle i_{\mathrm{rin}}^2 (t) \right\rangle R_{\mathrm{L}} \\ &= 10^{\frac{\mathrm{RIN}}{10}} \, {I_{\mathrm{av}}}^2 B R_{\mathrm{L}} \,. \end{aligned} \tag{2.41}$$

### 2.3.4 Total Link Noise

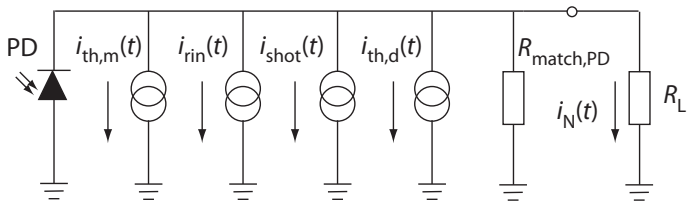


**Figure 2.12:** circuit model of dominant noise sources

In order to calculate the total noise power in an APL, consider the schematic in Figure 2.12 where the individual noise current sources are depicted. We have used two separate sources to describe the thermal noise contribution from the modulation device, $i_{\mathrm{th,m}}$ and from the detector matching resistor, $i_{\mathrm{th,d}}$. Recall that lossy impedance matching has been imposed at the source and at the detector. Thus, setting $R_{\mathrm{match,PD}} = R_{\mathrm{L}}$, the total noise current $i_{\mathrm{N}}$ flowing through the load is

$$i_{\mathrm{N}} (t) = \frac{1}{2} \left( i_{\mathrm{th,m}} (t) + i_{\mathrm{shot}} (t) + i_{\mathrm{rin}} (t) + i_{\mathrm{th,d}} (t) \right) . \tag{2.42}$$

The total noise power is simply the electrical power dissipation caused by this current in a load resistance,

$$p_{\mathrm{N}} = \left\langle i_{\mathrm{N}}^2 (t) \right\rangle R_{\mathrm{L}} \,. \tag{2.43}$$

Substituting Equation (2.29), Equation (2.33) and Equation (2.38) into Equation (2.42) and Equation (2.43) yields

$$p_{\mathrm{N}} = \left(1 + g\right) p_{\mathrm{th,mL}} + \frac{1}{4} p_{\mathrm{shot}} + \frac{1}{4} p_{\mathrm{rin}} \tag{2.44}$$

where the terms $p_{\text{th,mL}}$, $p_{\text{shot}}$ and $p_{\text{rin}}$ are defined in Equations (2.31), (2.34) and (2.41), respectively, and the factor $g$ is the link gain defined in Equation (2.3). Note that in the first term at the right hand side of equation (2.44) we have lumped together the thermal contribution from the modulation device, which amounts to $gkTB$, with the one from the photodetector matching resistor, which is simply $kTB$. The link gain factor comes into play in the thermal noise of the modulation device because the noise is initially generated at the input of the APL and later on transferred to the output, as evident from Figure 2.12. Thus, this noise power will experience an amplification (or attenuation) by the link gain.

Most of the time, it is more useful to express the noise powers in dBm/Hz (i.e. in decibels relative to 1 mW per Hertz noise bandwidth) rather than in Watt. Thus, the total noise power expressed in dBm/Hz can be written as:

$$P_{\text{N}}\,[\text{dBm/Hz}] = 10\log_{10}\left(\frac{p_{\text{N}}\,(B=1\text{Hz})}{10^{-3}}\right), \tag{2.45}$$

where we have explicitly expressed the noise power unit and the value of the equivalent noise bandwidth. To illustrate the typical value of $P_{\text{N}}$, let us consider the following example.

**Example 2.4**
Consider an external modulation APL with parameters described in Example 2.2. The average optical power at the detector can be calculated from Equation (2.20). For input optical power, $P_{\text{i}}$, of 20 mW (+13 dBm) and optical loss, $L$, of 5 dB, $P_{\text{av}}$ is equal to 5 dBm (or 3.2 mW in linear scale). The resulting average photocurrent, $I_{\text{av}}$, is 2.4 mA, using a photodetector responsivity value of 0.75 A/W. Assuming a typical laser RIN value of -155 dB/Hz, the shot noise and relative intensity noise powers (in 1 Hz bandwidth) calculated from Equations (2.34) and (2.41) are -164.2 dBm/Hz and -160.5 dBm/Hz, respectively. Keep in mind that due to the lossy impedance matching scheme, only one-fourth of these noise powers contribute to the total link noise (Equation (2.44)). Thus, the actual shot noise and RIN powers at the APL output are -170.2 dBm/Hz and -166.5 dBm/Hz, respectively. The thermal noise contributions from the modulation device and the photodetector matching resistor are independent of the optical power and amount to -200.2 dBm/Hz and -174 dBm/Hz, respectively, at room temperature ($T$ = 290 K). Thus, the noise contribution from the modulation device is negligible because the link gain is low. Finally, the total noise power according to Equation (2.45) can be calculated to be -164.4 dBm/Hz. In this case, the dominating noise term in this APL is the laser relative intensity noise.



### 2.3.5 Noise Figure

As mentioned in the beginning of this chapter, it is practical to define for an APL similar parameters as the ones initially reserved for RF and microwave components. One of these parameters is the so-called noise figure. To define the noise figure, let us start from the definition of a *noise factor*, $F$. The noise factor of a two

port device is defined as the ratio of the available output noise spectral density to the portion of that noise caused by the actual noise source connected to the input of the device, measured at the standard temperature of 290 K [17]. The noise figure, NF, is the logarithm of the noise factor, i.e., $\mathrm{NF} = 10\log_{10}(F)$. When the input noise is simply the thermal noise from a matched resistor (Subsection 2.3.1), a more useful definition of the noise figure is the ratio of the input signal-to-noise ratio (SNR) to the output SNR. Suppose that the input and output signal powers are $s_{\mathrm{in}}$ and $s_{\mathrm{out}}$ and the input and output noise powers are $n_{\mathrm{in}}$ and $n_{\mathrm{out}}$, the noise figure can be written as

$$\mathrm{NF} = 10\log_{10}\left(\frac{s_{\mathrm{in}}/n_{\mathrm{in}}}{s_{\mathrm{out}}/n_{\mathrm{out}}}\right). \tag{2.46}$$

Since the input noise power is the thermal noise from a resistive matched load, $n_{\mathrm{in}} = kTB$. Moreover, we can identify that $s_{\mathrm{out}} = g\,s_{\mathrm{in}}$, which means that the output signal is amplified (or attenuated) by the link gain. Lastly, for APLs considered here, the output noise is simply the total link noise defined in Equation (2.44), which means that $n_{\mathrm{out}} = p_{\mathrm{N}}$. Thus, the noise figure expression can be re-written as

$$\mathrm{NF} = 10\log_{10}\left(\frac{p_{\mathrm{N}}}{gkTB}\right). \tag{2.47}$$

Note that the noise figure is *independent* of the noise bandwidth since $p_{\mathrm{N}}$ in the equation above is measured in the same bandwidth, $B$, as the thermal noise in the denominator. A more common way to express the noise figure is to evaluate the logarithm in Equation (2.47) and express the total link noise in its power spectral density as shown in Equation (2.45). The result is shown in Equation (2.48), in which we have used that $10\log_{10}(kT) \approx -174$ dBm/Hz for $T$ =290 K and $G = 10\log_{10}(g)$ is the gain expressed in dB.

$$\mathrm{NF} = P_{\mathrm{N}} - G + 174\,, \tag{2.48}$$

The typical noise figure value of an APL is illustrated in the following example.

**Example 2.5**
Recall that the external modulation APL treated in previous examples has a link gain of -26.2 dB (Example 2.2) and an output noise power spectral density of -164.4 dBm/Hz (Example 2.4). Using Equation (2.48), the APL has NF = $-164.4 - (-26.2) + 174 = 35.8$ dB. Note that this noise figure is high, especially if we compare it with a conventional RF component. This value, however, can be improved by means of optimizing the APL parameters. This will be discussed in Chapter 3. ◻

## 2.4 Nonlinear Distortion

Earlier in this chapter, we have briefly mentioned that the transfer function of the modulation devices, e.g. laser diodes and MZMs, are nonlinear. For the link gain

and noise figure expressions, considering only the linear part of these transfer functions is sufficient. However, a thorough investigation of this nonlinearity is important since later on we will see that this factor will limit the APL performance.

Here, we assume that the APL nonlinearity is dominated by the modulation devices. Thus, we assume that other devices in the APL, for example the photodetector, are strictly linear. In reality, of course, these components also contribute to APL nonlinearities. However, their contributions are much smaller compared to the one of the modulation devices [17] and, hence, most of the time can be neglected. The reader can refer to [17, 126] for discussions of photodetector nonlinearities.

Moreover, the discussions presented here are limited to static weak nonlinearities [19]. This term implies that the nonlinear characteristics of the modulation device in general can be described as a set of nonlinear functions of the input signal that can be expanded into Taylor series. Furthermore, as opposed to its dynamic counterpart, a static nonlinearity dictates that no memory effect is present and the amplitudes of the generated distortion products depend only on the amplitude of the input signal and not on the frequency. Having specified this, we are now ready to discuss the nonlinearity of an APL.

We will start with a general expression of the modulation device transfer function, $y(x)$, expanded in Taylor series around the point $x_0$, yielding

$$\begin{aligned} y(x) &= \sum_{k=0}^{\infty} \frac{(x-x_0)^k}{k!} \left( \frac{\mathrm{d}^k y}{\mathrm{d}x^k} \right)_{x=x_0} \\ &= \sum_{k=0}^{\infty} a_k (x-x_0)^k \end{aligned} \tag{2.49}$$

where $a_k$ are the expansion coefficients defined as

$$a_k = \frac{1}{k!} \left( \frac{\mathrm{d}^k y}{\mathrm{d}x^k} \right)_{x=x_0}. \tag{2.50}$$

Here, $x$ is a time varying quantity representing either the input current or voltage modulation to the device while $x_0$ is related to the bias term.

The most common way to characterize the nonlinear transfer in Equation (2.49) is to perform the so-called tone modulation. In this case the modulating signal, $x(t)$, will take a form of a pure sinusoid. Generally, the tone modulation can be classified into three categories, single tone, two-tone and multitone modulations. As suggested by the names, they differ in the number of carrier frequencies included in the modulating signal. The single tone modulation uses a single frequency carrier and is used to characterize the harmonic distortion generated by the nonlinear transfer function. Two-tone modulation uses a pair of closely spaced signal frequencies and is employed to characterize the intermodulation distortion products. Finally, the multitone test uses a large number of carriers (roughly 10 - 80) to probe the so-called composite second-order (CSO) and the composite triple beat (CTB) distortion products. Our analysis presented here will be confined to single tone

and two-tone tests and we refer the readers to [17, 74] for the description of the multitone test.

### 2.4.1 Single Tone Test and Harmonic Distortion

In a single tone test, the input signal takes the form of

$$x(t) = x_0 + A\cos(\omega t) \tag{2.51}$$

where $\omega = 2\pi f$ is the angular modulating frequency, $A$ is the signal amplitude and $x_0$ is the bias current or voltage. Substituting this relation into the second form of Equation (2.49) and evaluating the result up to $k = 3$ yields

$$\begin{aligned} y(t) \approx a_0 + \frac{1}{2}a_2 A^2 + \left(a_1 A + \frac{3}{4}a_3 A^3\right)\cos(\omega t) \\ + \frac{1}{2}a_2 A^2 \cos(2\omega t) + \frac{1}{4}a_3 A^3 \cos(3\omega t) \end{aligned} \tag{2.52}$$

where we have used the trigonometric relations $\cos^2\alpha = 1/2\,(1+\cos 2\alpha)$ and $\cos^3\alpha = 3/4\cos\alpha + 1/4\cos 3\alpha$.

We can identify from Equation (2.52) that the response of the modulation device consists of a DC component which does not depend on $\omega$, the signal component with frequency $\omega$ and spurious components at frequencies of integer multiple of $\omega$ which are known as harmonic distortions (HDs). The amplitude and frequency of these components are listed in Table 2.1. The spurious components at twice and three-times the signal frequency are called second-order harmonic (HD2) and third-order harmonic (HD3) distortions, respectively.

**Table 2.1:** Harmonic distortion components

| Component | Frequency | Amplitude |
|---|---|---|
| Dc | 0 | $a_0 + \frac{1}{2}a_2 A^2$ |
| Fundamental | $\omega$ | $a_1 A + \frac{3}{4}a_3 A^3$ |
| Second-order harmonic | $2\omega$ | $\frac{1}{2}a_2 A^2$ |
| Third-order harmonic | $3\omega$ | $\frac{1}{4}a_3 A^3$ |

### 2.4.2 Two-tone Test and Intermodulation Distortion

Although the single tone test already gives sufficient insight of the device nonlinearity, a more common way to characterize this nonlinearity is to perform the so-called two-tone test. In a two-tone test, the input signal takes the form of

$$x(t) = x_0 + A\left[\cos(\omega_1 t) + \cos(\omega_2 t)\right], \tag{2.53}$$

where $\omega_1 = 2\pi f_1$, $\omega_2 = 2\pi f_2$ and $f_1$ and $f_2$ are the tone frequencies. Substituting the input signal expression into Equation (2.49) and using the trigonometric relation

$\cos\alpha\cos\beta = 1/2\left[\cos\left(\alpha-\beta\right)+\cos\left(\alpha+\beta\right)\right]$, we obtain

$$\begin{aligned} y(t) \approx & a_0 + a_2 A^2 \\ & + \left(a_1 A + \frac{9}{4} a_3 A^3\right)\left(\cos(\omega_1 t) + \cos(\omega_2 t)\right) \\ & + \frac{1}{2} a_2 A^2 \left(\cos(2\omega_1 t) + \cos(2\omega_2 t)\right) \\ & + \frac{1}{4} a_3 A^3 \left(\cos(3\omega_1 t) + \cos(3\omega_2 t)\right) \\ & + a_2 A^2 \left\{\cos\left((\omega_1-\omega_2)\, t\right) + \cos\left((\omega_1+\omega_2)\, t\right)\right\} \\ & + \frac{3}{4} a_3 A^3 \{\cos\left((2\omega_1-\omega_2)\, t\right) + \cos\left((2\omega_2-\omega_1)\, t\right) \\ & \qquad + \cos\left((2\omega_1+\omega_2)\, t\right) + \cos\left((2\omega_2+\omega_1)\, t\right)\} \end{aligned} \tag{2.54}$$

where again we have limited the infinite series in Equation (2.49) to $k = 3$. It is evident from Equation (2.54) that besides the harmonic distortions, additional spurious components appear at the output if two frequencies are present simultaneously. These terms are called intermodulation distortions (IMDs). The second-order intermodulation (IMD2) terms appear at the sum and the difference of the modulating frequencies, while the third-order intermodulation (IMD3) terms appear at the sum and the difference of twice of one frequency with the other frequency. The amplitude and the frequencies of the components present in Equation (2.54) are listed in Table 2.2.

**Table 2.2:** Intermodulation distortion components

| Component | Frequency | Amplitude |
|---|---|---|
| Dc | 0 | $a_0 + a_2 A^2$ |
| Fundamental | $\omega_1, \omega_2$ | $a_1 A + \frac{9}{4} a_3 A^3$ |
| Second-order harmonic | $2\omega_1, 2\omega_2$ | $\frac{1}{2} a_2 A^2$ |
| Third-order harmonic | $3\omega_1, 3\omega_2$ | $\frac{1}{4} a_3 A^3$ |
| Second-order intermodulation | $\omega_2 - \omega_1, \omega_1 + \omega_2$ | $a_2 A^2$ |
| Third-order intermodulation | $2\omega_1 - \omega_2, 2\omega_2 - \omega_1$ | $\frac{3}{4} a_3 A^3$ |
| | $2\omega_1 + \omega_2, 2\omega_2 + \omega_1$ | |

It is important to note that the IMD amplitudes differ from the HD amplitudes even though they are basically generated by the same mechanism. The IMD2 amplitude is twice of the HD2 amplitude while the IMD3 amplitude is three-times the HD3 amplitude. In practice, however, we measure the powers of these components rather than the amplitudes. If we regard the amplitude to be either a current or a voltage, then the power considered here is an electrical or an RF power. Thus we can easily identify that the powers of the distortion terms are proportional to the square of their amplitudes. Thus, we can deduce that the power of the IMD2 terms expressed in decibels are approximately 6 dB (or a factor of 4) higher compared to the HD2 powers, and the IMD3 powers are approximately 9.5 dB (or a factor of 9)

higher relative to the HD3 powers. This is an important conclusion and later on we will use this property when discussing about measurements of the spurious-free dynamic range.

### 2.4.3 Sub-octave and Multioctave Bandwidths

In Figure 2.13 a two-tone test output spectrum of a nonlinear device is illustrated. The input tone frequencies are assumed to be 0.95 and 1.05 GHz and their powers are set to 0 dBm. Note that the exact powers of the distortion components depend on the expansion coefficients in Equation (2.50). For illustration purposes, we have selected the values of these coefficients such that the distortion terms can easily be observed.

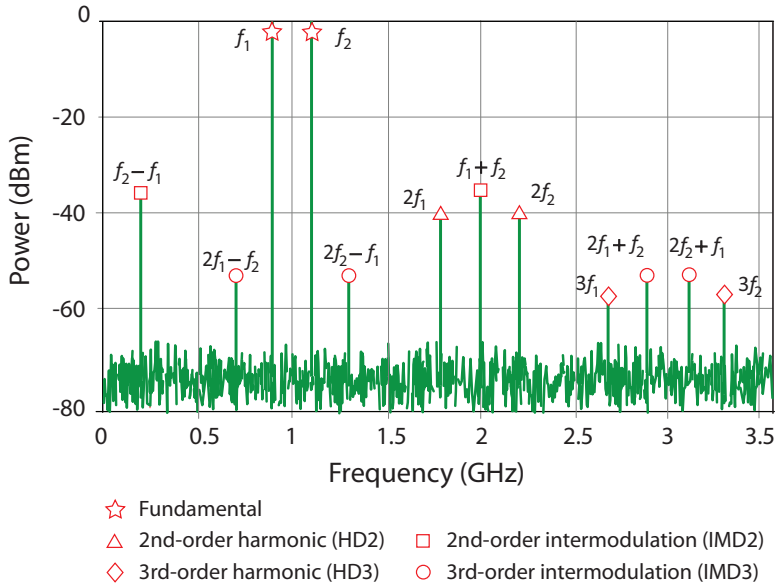


**Figure 2.13:** Two tone test output spectrum

The spectrum in Figure 2.13 reveals that the distortion component that fall closest to the fundamental signals are the IMD3 terms at $2f_1 - f_2$ and $2f_2 - f_1$, which most of the time cannot be filtered out. Thus there is hardly any usable signal bandwidth that is free from these spurious signals. For this reason the IMD3 is regarded as the main limiting distortion factor in APL. As for the even order distortions, the HD2 and IMD2 fall relatively far from the fundamental signals. But as the signal bandwidth increases, the separation between the signals and these distortion terms reduces. For a wideband system with a multioctave signal bandwidth, i.e. the case where the highest frequency component of the signal, $f_{\text{high}}$ is more that twice of the lowest frequency component, $f_{\text{low}}$, IMD2 will interfere with the signal. This is in contrast with a narrowband system with sub-octave bandwidth $\left(f_{\text{high}} < 2f_{\text{low}}\right)$,

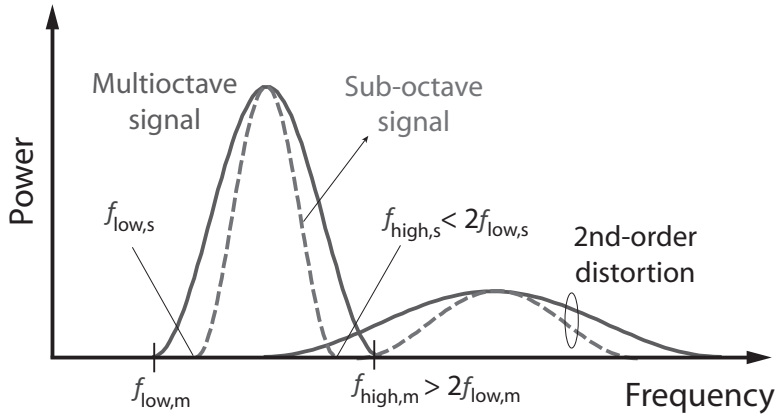


**Figure 2.14:** Sub-octave and multioctave bandwidth signal spectra. The subscripts s and m of the lower and higher frequency bounds indicate sub-octave and multioctave signals, respectively. For a multioctave signal, the second-order distortion interferes with the fundamental signal.

where IMD2 can be filtered out easily. These two situations are illustrated in Figure 2.14. We will discuss further the implications of the signal bandwidth when we get to the dynamic range of the APL.

### 2.4.4 Intercept Points and the 1-dB Compression Point

As we have seen previously, inspecting the output spectrum (Figure 2.13) gives valuable insights of the nonlinearity in the APL. In addition to that, it is often useful to investigate how the power of each component in the output spectrum varies with the input signal power. Such plot is shown in Figure 2.15. Here we have plotted the fundamental signal and an $2^{nd}$-order intermodulation distortion term (IMD2) powers in decibels. The fundamental signal, being linearly dependent on the input signal, is plotted as line with the slope of one. However, if the input signal gets higher, the fundamental term undergoes a compression, mainly due to the interference with higher order distortion terms that fall at the signal frequency. This can be understood if one examines the fundamental term amplitude listed in Tables 2.1 and 2.2 in which the terms proportional to the third-order distortion fall at the fundamental frequencies. Since a compression of the fundamental is observed (the solid line of Figure 2.15), this dictates that the value of $a_3$ in the Taylor expansion of the modulation device transfer function should be smaller than zero. If the small signal approximation is used instead, the contribution of the higher order terms on the fundamental signal is neglected. Hence, the signal power will maintain the linear relation with the input power, as shown by the dashed curve in the figure. Thus, the 1-dB compression point is defined as the output signal power that is 1 dB lower compared to the small signal approximation.

The compression is also observed at IMD2 power. Again, with small signal ap-

proximation, the IMD2 power maintains the linear behavior, with slope of 2, with respect to the input signal power. At some point, the extrapolated fundamental power and the IMD2 power will intersect. This intersection is known as the $2^{\text{nd}}$-order intercept point, as shown in Figure 2.15. Although we show this intercept point particularly for the second-order nonlinearity, it can be applied to any order of nonlinearity. The intercept point of the fundamental signal and the $n^{\text{th}}$ order IMD is thus known as the $n^{\text{th}}$ order intercept point. This point can be referred as an $n^{\text{th}}$-order input intercept (IIP$n$) or as an output intercept (OIP$n$) which are defined as

$$\text{IIP}n = P_{\text{input}}\left(P_{\text{fund}} = P_{\text{IMD}n}\right) \tag{2.55}$$

$$\text{OIP}n = P_{\text{output}}\left(P_{\text{fund}} = P_{\text{IMD}n}\right). \tag{2.56}$$

where $P_{\text{input}}$ is the input signal power per tone while $P_{\text{Fund}}$ is the fundamental (at either $\omega_1$ or $\omega_2$) and $P_{\text{IMDn}}$ is the power of one of the $n^{\text{th}}$-order IMD terms, obtained from the small signal approximation. These intercept points are related to each other by the link gain, $G$, via the relation

$$\text{OIP}n = \text{IIP}n + G. \tag{2.57}$$

Thus, it is clear from Figure 2.15 that the intercept point cannot be directly measured due to the compressions [127]. However, we will see in the following section that these intercept points have been frequently used as a common measure of the distortion [128] and, moreover, used in the definition of the the spurious free dynamic range.

### 2.4.5 DML Nonlinearity

In this part we will derive the expression of a weak-static nonlinearity in a directly modulated laser (DML). Since the laser is a dynamic system that shows memory effect and relaxation, the weak static expression is rarely applied. However, this expression is insightful in describing laser nonlinearity, although its applicability is limited. The ideal way to express laser nonlinearity is to start from the laser rate equations. However, this is beyond the scope of this thesis and we refer the reader to [17, 129, 130] for this approach.

Let us start with a general expression of the laser input current as shown in Equation (2.8). The signal current $I_{\text{sig}}$ with a two tone modulation can be written as

$$I_{\text{sig}}(t) = I_{\text{m}}\left[\cos(\omega_1 t) + \cos(\omega_2 t)\right]. \tag{2.58}$$

We will limit our discussion here to small signal modulations, such that there is no signal clipping. Thus, the maximum amplitude of the signal current should fulfill the condition

$$I_{\text{m}} = \frac{m}{2}\left(I_{\text{bias}} - I_{\text{th}}\right), \quad 0 \le m \le 1 \tag{2.59}$$

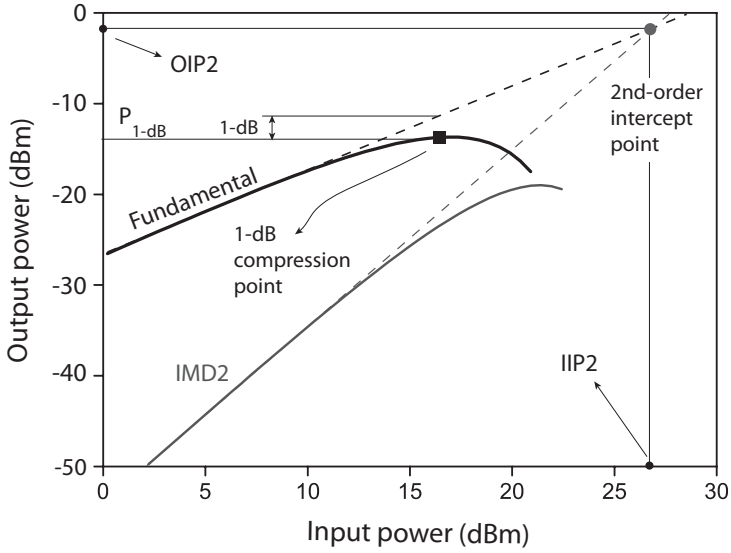


**Figure 2.15:** The 1-dB compression point and the 2nd-order intercept point

where $I_{\text{bias}}$ and $I_{\text{th}}$ are the laser bias and threshold currents and $m$ is the optical modulation index (OMI). The current amplitude is thus related to the input *RF* power per tone, $p_{\text{in}}$ as

$$I_{\text{m}} = \sqrt{\frac{2\,p_{\text{in}}}{R_{\text{S}}}} \tag{2.60}$$

where $R_{\text{S}}$ is the source resistance. The modulating current in Equation (2.58) is the input to the nonlinear transfer function of the laser, resulting in the modulated optical power

$$P_{\text{det,DML}}(t) = P_{\text{av,DML}} + P_{\text{mod,DML}}(t) + P_{\text{NL2,DML}}(t) + P_{\text{NL3,DML}}(t) \tag{2.61}$$

where

$$P_{\text{av,DML}}(t) \triangleq \frac{s_{\text{LD}}}{L}\,(I_{\text{bias}} - I_{\text{th}})\,, \tag{2.62}$$

$$P_{\text{mod,DML}}(t) \triangleq \frac{s_{\text{LD}}}{L}\,I_{\text{sig}}(t)\,, \tag{2.63}$$

$$P_{\text{NL2,DML}}(t) \triangleq \frac{c_2}{L}\,I^2_{\text{sig}}(t)\,, \tag{2.64}$$

$$P_{\text{NL3,DML}}(t) \triangleq \frac{c_3}{L}\,I^3_{\text{sig}}(t)\,. \tag{2.65}$$

Note that the expression in Equation (2.61) is similar to the one defined in Equation (2.12) only that we have added two terms, $P_{\text{NL2,DML}}$ and $P_{\text{NL3,DML}}$ to describe

the second-order and the third-order nonlinearities in the laser. The constants $s_{\mathrm{LD}}$, $c_2$ and $c_3$ are essentially the Taylor expansion coefficients of the laser nonlinear L-I curve around the selected bias point, $I_{\mathrm{bias}}$. Note that we have named the first coefficient as $s_{\mathrm{LD}}$ instead of $c_1$ because this coefficient is the laser slope efficiency.

The modulated optical power in Equation (2.61) is detected in the photodetector generating the photocurrent. The portion from this photocurrent that will contribute to the fundamental RF signal, at the output, at one of the modulating frequencies (for example $\omega_1$) is

$$I_{\mathrm{fund,DML}}(t) = \frac{1}{2}\left(\frac{r_{\mathrm{PD}}\, s_{\mathrm{LD}}}{L}\right) I_{\mathrm{m}} \cos(\omega_1 t) \tag{2.66}$$

where we have taken into account the lossy impedance matching at the detector from where the factor 1/2 comes from. The components that contribute to the IMD2 and IMD3 components at frequencies $\omega_1+\omega_1$ and $2\omega_1-\omega_2$, respectively, are

$$I_{\mathrm{IMD2,DML}}(t) = \frac{1}{2}\left(\frac{r_{\mathrm{PD}}\, c_2}{L}\right) I_{\mathrm{m}}^2 \cos((\omega_1+\omega_2)\, t) \tag{2.67}$$

and

$$I_{\mathrm{IMD3,DML}}(t) = \frac{1}{2}\left(\frac{3 r_{\mathrm{PD}}\, c_3}{4L}\right) I_{\mathrm{m}}^3 \cos((2\omega_1-\omega_2)\, t)\,, \tag{2.68}$$

respectively. Note that the factor 3/4 in Equation (2.68) is in accordance with the amplitudes listed in Table 2.2.

These current components are delivered to a load resistance of $R_{\mathrm{L}}$ generating the fundamental, IMD2 and IMD3 components of the output RF signal. The RF power of the fundamental component is thus

$$\begin{aligned} p_{\mathrm{fund,DML}} &= \left\langle I_{\mathrm{fund,DML}}^2(t)\right\rangle R_{\mathrm{L}} \\ &= \frac{1}{4}\left(\frac{r_{\mathrm{PD}}\, s_{\mathrm{LD}}}{L}\right)^2 \frac{R_{\mathrm{L}}}{R_{\mathrm{S}}}\, p_{\mathrm{in}} \end{aligned} \tag{2.69}$$

where we have used the property $\left\langle \cos^2(\omega t)\right\rangle = 1/2$ and substitute $I_{\mathrm{m}}$ with the relation in Equation (2.60) to obtain the expression in the second line of the equation above. Similarly, we can calculate the expressions for the RF power of the IMD2 component as

$$\begin{aligned} p_{\mathrm{IMD2,DML}} &= \left\langle I_{\mathrm{IMD2,DML}}^2(t)\right\rangle R_{\mathrm{L}} \\ &= \frac{1}{2}\left(\frac{r_{\mathrm{PD}}\, c_2}{L}\right)^2 \frac{R_{\mathrm{L}}}{R_{\mathrm{S}}^2}\, p_{\mathrm{in}}^2\,, \end{aligned} \tag{2.70}$$

and the RF power of the IMD3 component as

$$\begin{aligned} p_{\mathrm{IMD3,DML}} &= \left\langle I_{\mathrm{IMD3,DML}}^2(t)\right\rangle R_{\mathrm{L}} \\ &= \frac{9}{16}\left(\frac{r_{\mathrm{PD}}\, c_3}{L}\right)^2 \frac{R_{\mathrm{L}}}{R_{\mathrm{S}}^3}\, p_{\mathrm{in}}^3\,. \end{aligned} \tag{2.71}$$

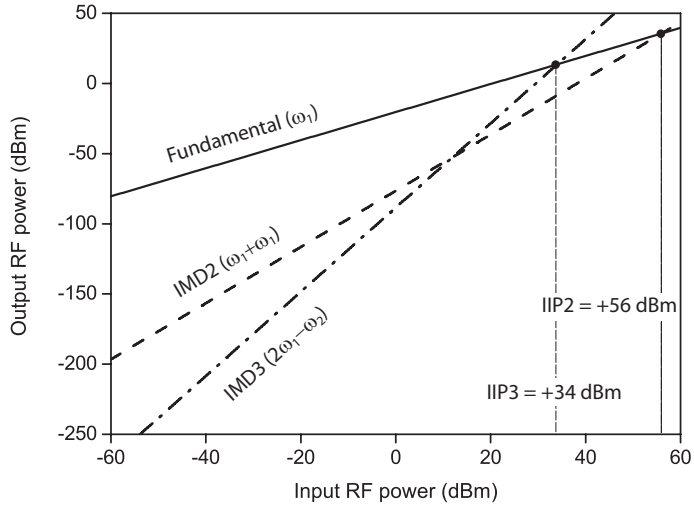


**Figure 2.16:** Output RF signal components as functions of the input signal power of a DML link described in Example 2.6

From Equations (2.69) to (2.71) we can see that the power of the fundamental signal at the output is proportional to the input signal power while the IMD2 and IMD3 powers are proportional to the square and the cubic of this RF power, respectively.

Furthermore, we derive the expression for the input intercept points of the DML. According to Equation (2.55), these intercept points can be found by inspecting the input power where the fundamental power in Equation (2.69) is equal to the IMD powers in Equations (2.70) and (2.71). The results are shown below :

$$\text{IIP2}_{\text{DML}} = \frac{1}{2}\left(\frac{s_{\text{LD}}}{c_2}\right)^2 R \tag{2.72}$$

$$\text{IIP3}_{\text{DML}} = \frac{2}{3}\frac{s_{\text{LD}}}{|c_3|} R \tag{2.73}$$

where we have set $R_{\text{S}} = R_{\text{L}} = R$. Note that because $c_3 < 0$ due the compression observed in the fundamental power (see the previous subsection) we have used the absolute value of this constant to determine the IIP3.

Equations (2.72) and (2.73) can be used to predict the nonlinearity in the LI curve. By measuring the intercept points, or using the information provided by laser manufacturers, one can calculate the expansion coefficients, $c_2$ and $c_3$ and develop a nonlinear transfer of the laser diode at a certain bias point, as described in Equation (2.61). To illustrate this, let us consider the following example.

**Example 2.6**
Consider a DML link using a DFB laser diode with $I_{\text{th}} = 10$ mA. At the operating bias point of $I_{\text{bias}} = 60$ mA, the manufacturer data give $s_{\text{LD}} = 0.32$ W/A. Moreover, at this

bias point, the laser IIP2 and IIP3, which are obtained from a two-tone test at frequencies of 1.0 and 1.01 GHz, are listed to be +34 dBm and +56 dBm, respectively. These are the typical data that are provided by the manufacturers in the datasheets or test results of analog lasers. However, usually only the IIP3 value is listed and not the IIP2. Alternatively, the manufacturers might list the data of the ratio of the fundamental to the IMD2 powers at a specified bias current, modulation frequencies and input RF power per tone.

With the available data, we can calculate back the nonlinear coefficients of the laser, $c_2$ and $c_3$, using the relation in Equations (2.72) and (2.73), respectively. The other parameters that are required for the calculations are set as follows: $r_{\mathrm{PD}} = 0.75$ A/W, $10\log_{10} L = 1$ dB, and $R = 50\,\Omega$. We obtain that $c_2 = 0.0802$ and $c_3 = -4.246$. We use these values to calculate the fundamental, IMD2 and IMD3 powers in Equations (2.69), (2.70) and (2.71), respectively, and plot them as functions of the input RF power per tone. The results are depicted in Figure 2.16.

### 2.4.6 MZM Intercept Points

In this part, we will derive the expressions for the second-order and the third order intermodulation powers and intercept points in an MZM APL. We will start with the two tone input voltage signal to the MZM,

$$V_{\mathrm{RF}}(t) = V_{\mathrm{m}} \left[\cos(\omega_1 t) + \cos(\omega_2 t)\right], \tag{2.74}$$

where $V_{\mathrm{m}}$ is the voltage signal amplitude related to the input power per tone , $p_{\mathrm{in}}$, and the source resistance, $R_{\mathrm{S}}$, as

$$V_{\mathrm{m}} = \sqrt{2 p_{\mathrm{in}} R_{\mathrm{S}}}. \tag{2.75}$$

The expression of the nonlinear transfer function of the MZM is described by Equations (2.19) to (2.23). As similarly done with the DML link in the previous subsection, we can derive the expressions of the fundamental, IMD2 and IMD3 powers of an MZM link. We start by inserting Equation (2.74) to each of Equations (2.21)-(2.23). Detection of these optical powers will result in the detected photocurrent. Half of this photocurrent (due to resistive matching) will be delivered to the load, generating various signal components such as the DC, fundamental, harmonic and intermodulation distortions. We can write the fundamental power at one of the input frequencies, as

$$p_{\mathrm{Fund,MZM}} = \frac{1}{32}\left(\frac{\pi V_{\mathrm{m}}}{V_{\pi,\mathrm{RF}}}\right)^2 \left(\frac{r_{\mathrm{PD}} P_{\mathrm{i}}}{L} \sin\phi_{\mathrm{B}}\right)^2 R_{\mathrm{L}}, \tag{2.76}$$

the power of an IMD2 term at either $\omega_2 - \omega_1$ or $\omega_1 + \omega_2$ as

$$p_{\mathrm{IMD_2,MZM}} = \frac{1}{128}\left(\frac{\pi V_{\mathrm{m}}}{V_{\pi,\mathrm{RF}}}\right)^4 \left(\frac{r_{\mathrm{PD}} P_{\mathrm{i}}}{L} \cos\phi_{\mathrm{B}}\right)^2 R_{\mathrm{L}}, \tag{2.77}$$

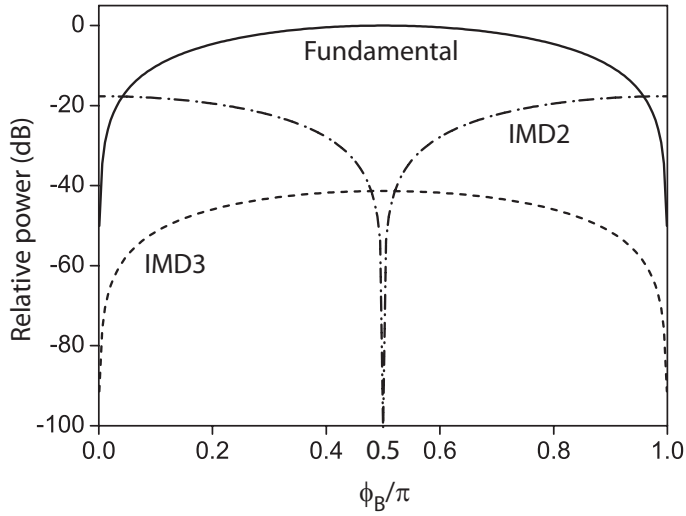


**Figure 2.17:** Distortion components vs. MZM bias angle. Here the MZM RF half-wave voltage is 3.8 V

and finally the power of an IMD3 term as

$$p_{\mathrm{IMD_3,MZM}}(t) = \frac{1}{2048}\left(\frac{\pi V_{\mathrm{m}}}{V_{\pi,\mathrm{RF}}}\right)^6 \left(\frac{r_{\mathrm{PD}} P_{\mathrm{i}}}{L}\sin\phi_{\mathrm{B}}\right)^2 R_{\mathrm{L}}. \tag{2.78}$$

The dependence of these powers are illustrated in Figure 2.17, where we have used the MZM RF half-wave voltage value of 3.8 V. In this figure, the powers are normalized relative to the peak fundamental power that occurs at the quadrature bias $(\phi_{\mathrm{B}} = \pi/2)$. At this quadrature point, the IMD2 vanishes, as well as all even order distortion, as mentioned earlier.

Using the definition in Equation (2.55), the input intercept points can be calculated by equating Equation (2.76) with Equation (2.77) for the second order intercept point ($\mathrm{IIP2_{MZM}}$), and (2.76) with Equation (2.78) for the third order intercept ($\mathrm{IIP3_{MZM}}$),yielding

$$\mathrm{IIP2_{MZM}} = \frac{2}{R}\left(\frac{V_{\pi,\mathrm{RF}}}{\pi}\tan\phi_{\mathrm{B}}\right)^2 \tag{2.79}$$

$$\mathrm{IIP3_{MZM}} = \frac{4\left(V_{\pi,\mathrm{RF}}\right)^2}{\pi^2 R} \tag{2.80}$$

where we have used the definition in Equation (2.75) and set $R_{\mathrm{L}} = R_{\mathrm{S}} = R$. The dependence of these input intercept points to the bias angle are shown in Figure 2.18. The IIP2 is very sensitive to the bias angle and ideally goes to infinity at quadrature because the even order distortion vanishes at this bias point. The IIP3 is, however,

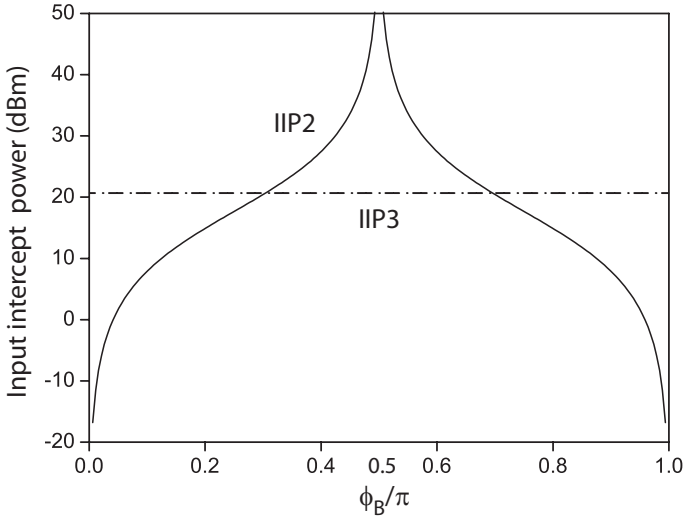


**Figure 2.18:** IIP2 and IIP3 vs. MZM bias angle. IIP3 is bias independent

independent of the bias angle. This is an important observation, as we will see later on when optimizing an MZM link for higher performance.

The output intercept points can be calculated from Equations (2.79) and (2.80) using Equation (2.56) with (2.25) as the link gain expression. The OIP3 can be written as

$$\mathrm{OIP3}_{\mathrm{MZM}} = \left(\frac{r_{\mathrm{PD}} P_{\mathrm{i}}}{2L} \sin\phi_{\mathrm{B}}\right)^2 R. \tag{2.81}$$

At quadrature bias, Equation (2.81) reduces to a very simple expression :

$$\mathrm{OIP3}_{\mathrm{MZM,quad}} = I_{\mathrm{av}}^2 R \tag{2.82}$$

where is the average (DC) photocurrent in the quadrature bias case defined as

$$I_{\mathrm{av}} = \frac{r_{\mathrm{PD}} P_{\mathrm{i}}}{2L}. \tag{2.83}$$

## 2.5 Dynamic Range

Having defined the noise and distortion aspects, we are now ready to determine the dynamic range of an APL. The dynamic range can be regarded as the range of power that can be accommodated by the APL. In this sense, it can be viewed as a ratio (a difference in decibels) between two output or input power levels subject to some constraints. These constraints are strongly related to the noise and distortion in the link. The noise will limit the minimum signal level that can be conveyed by the link while the level of distortion sets the upper limit of the signal power.

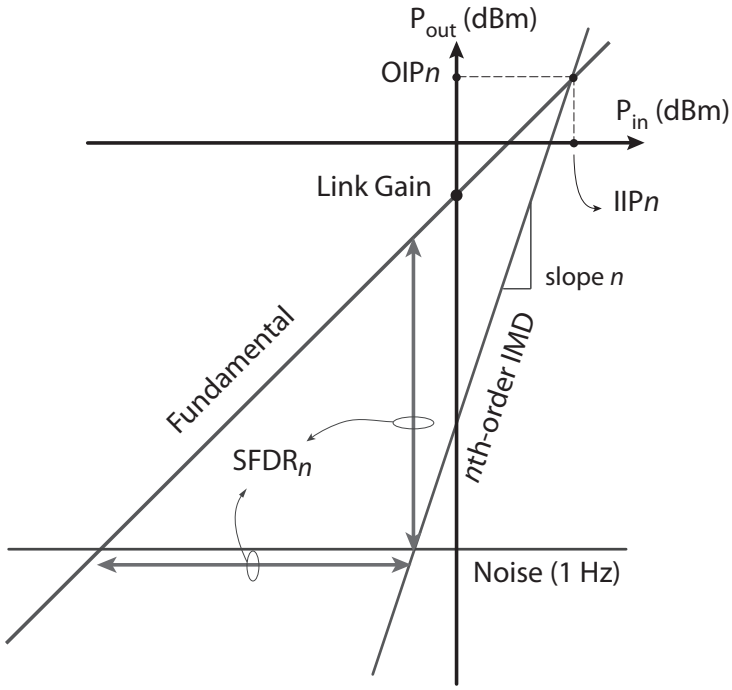


**Figure 2.19:** SFDR definition

Depending on how these upper and lower bounds of power are formulated, there are different definitions of dynamic range. In the following subsection we will focus our discussion on the definition known as the spurious-free dynamic range (SFDR), which is the most widely used for APLs. Other definitions of dynamic range are discussed in Subsection 2.5.2

### 2.5.1 Spurious-Free Dynamic Range (SFDR)

The SFDR is defined as the ratio of input powers where, on one hand, the fundamental signal power is equal to the noise power and, on the other hand, the $n^{\text{th}}$-order intermodulation distortion (IMD$n$) power is equal to the noise power. In terms of output powers, this can be interpreted as the maximum output SNR that can be achieved while keeping the IMD$n$ power below the noise floor. These definitions are illustrated in Figure 2.19 where we have plotted the components of the output signal, namely the fundamental term, the noise power spectral density (PSD) and the intermodulation distortion terms against the input RF power, all expressed in decibels. Here we also have specifically used the term $\text{SFDR}_n$ to emphasize that the limiting distortion component is IMD$n$.

For link designers, it is desirable to expressed $\text{SFDR}_n$ in terms of link parameters such as the link gain, noise figure and the intercept points. Such expressions can

be deduced from Figure 2.19 (see Appendix B for the full derivations). The $\mathrm{SFDR}_n$ in terms of $\mathrm{IIP}n$ can be written as :

$$\mathrm{SFDR}_n = \frac{n-1}{n}\left(\mathrm{IIP}n - \mathrm{NF} + 174\right). \tag{2.84}$$

Alternatively we can express the SFDR in terms of $\mathrm{OIP}n$, yielding

$$\mathrm{SFDR}_n = \frac{n-1}{n}\left(\mathrm{OIP}n - \mathrm{NF} - G + 174\right). \tag{2.85}$$

In general $\mathrm{SFDR}_n$ is expressed in dB while specifying the bandwidth in which the noise component is measured. For example a system can be specified having an $\mathrm{SFDR}_3$ of 60 dB in 1 MHz bandwidth. However, more often the SFDR is expressed in 1 Hz bandwidth. In this case, $\mathrm{SFDR}_n$ is usually expressed in $\mathrm{dB\,Hz}^{\left(\frac{n-1}{n}\right)}$. This is essentially the same as saying that the SFDR is measured in dB in 1 Hz bandwidth. The factor $\mathrm{Hz}^{\left(\frac{n-1}{n}\right)}$ is included to indicate the order of the SFDR and because SFDR follows the scaling factor as shown below:

$$\mathrm{SFDR}_n\left(B\,\mathrm{Hz}\right) = \mathrm{SFDR}_n\left(1\,\mathrm{Hz}\right) - \left(\frac{n-1}{n}\right)10\log_{10}\left(B\right). \tag{2.86}$$

This bandwidth scaling is illustrated in the following example.

**Example 2.7**
Consider a system with an $\mathrm{SFDR}_3$ of 110 $\mathrm{dB.Hz}^{2/3}$. To calculate the $\mathrm{SFDR}_3$ in 1 MHz bandwidth, first we calculate the factor $10\log_{10}(B)$ which is 60 dB for $B = 10^6$ Hz. Thus, the dynamic range in 1 MHz is simply $110 - \frac{2}{3}(60) = 70\,\mathrm{dB}$.

Following the discussion regarding the intermodulation products in Subsection 2.4.3, we can identify that $\mathrm{SFDR}_2$ and $\mathrm{SFDR}_3$, limited by IMD2 and IMD3, respectively, are the most important in the case of APLs. Their values determine if the APL can be applied in wideband systems or is merely limited to narrowband applications. Since wideband systems are limited by IMD2, the general rule is that if $\mathrm{SFDR}_2$ is comparable or larger that $\mathrm{SFDR}_3$, then the APL is suitable for wideband applications. If the opposite is true, ($\mathrm{SFDR}_2 \ll \mathrm{SFDR}_3$), then the APL is limited to narrowband applications. We will discuss more about this topic when we proceed with the techniques to increase the APL SFDR, in the following chapters.

In order to have an idea about a typical SFDR value in an APL, let us consider the following example.

**Example 2.8**
Reconsider the MZM APL described in Examples 2.2 to 2.5. The APL noise figure is 35.8 dB and according to Equation (2.80), the half-wave voltage value of 3.8 V will result in IIP3 value of 20.7 dBm. Thus, using Equation (2.84), we can calculate the $\mathrm{SFDR}_3$ of the APL to be $^{2}/_{3}(20.7 - 35.8 + 174) = 105.9$ $\mathrm{dBm.Hz}^{2/3}$. Since the MZM is biased at the quadrature, the $\mathrm{SFDR}_2 \gg \mathrm{SFDR}_3$ and the link can be applied in a broadband systems.

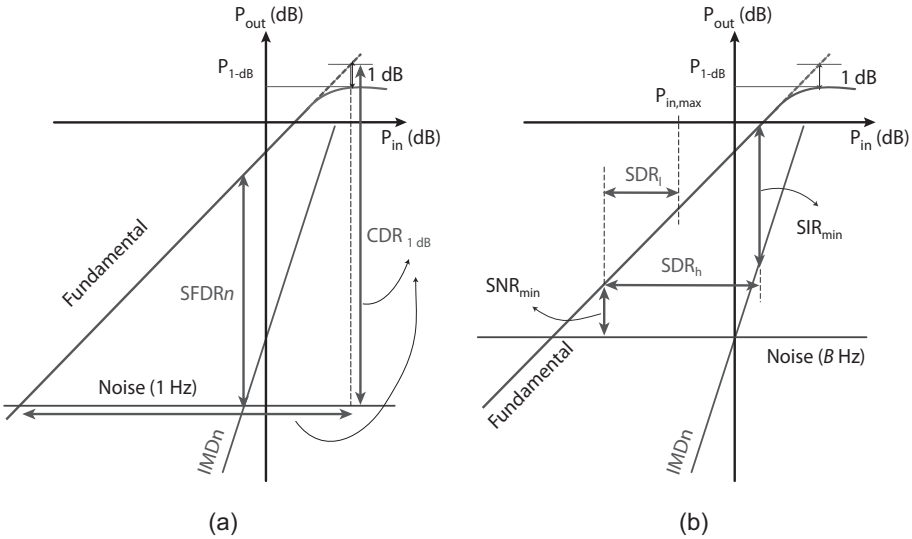


**Figure 2.20:** Various dynamic range definition in APLs. (a) SFDR and 1-dB compression dynamic range, (b) System dynamic range (SDR) used in more practical conditions.

### 2.5.2 Other Definitions

Besides the SFDR, other definitions of dynamic range have been used. One definition is the so-called 1-dB compression dynamic range ($\mathrm{CDR}_{1\,\mathrm{dB}}$) [44, 127]. The lower bound of this dynamic range is set by the input power that gives 0 dB output SNR in 1 Hz bandwidth (just like in the definition of SFDR) but the upper bound is set by the input power that corresponds to the 1-dB compression point at the fundamental output (see Subsection 2.4.4). Thus, in terms of the output powers, this dynamic range can be written as

$$\mathrm{CDR}_{1\,\mathrm{dB}}\ [\mathrm{dB}] = P_{1\,\mathrm{dB}}\ [\mathrm{dBm}] - P_{\mathrm{N}}\ [\mathrm{dBm/Hz}] + 1\,\mathrm{dB}\,. \tag{2.87}$$

where $P_{1\,\mathrm{dB}}$ is the output 1 dB compression point and $P_{\mathrm{N}}$ is the noise power spectral density defined in Equation (2.45). Note that the $\mathrm{CDR}_{1\,\mathrm{dB}}$ in the equation above is expressed in decibels. Sometimes this dynamic range is cited as the maximum usable dynamic range [127] because this dynamic range describes the maximum signal range that can be conveyed by the system regardless of the *nonlinear* distortion level, unlike the SFDR. This $\mathrm{CDR}_{1\,\mathrm{dB}}$ is illustrated in Figure 2.20 (a), where it is depicted together with the $n^{\mathrm{th}}$-order SFDR.

Another definition of dynamic range is known as the system dynamic range (SDR) [26, 92, 131]. The specific definition of the SDR is more related to the application of the system. Moreover, the SDR is often defined because the other dynamic range definitions cannot sufficiently represent the system performance. For example for APLs applied in high-frequency wireless transmission systems [26] or

in a satellite television communication link [131], the upper bound of the dynamic range is often imposed by the maximum power that can be received by the system. This power might be low enough such that it does not generate significant amount of distortion. Thus, describing the dynamic range using the SFDR, let alone the $CDR_{1\,dB}$, will be of no practical use. In general, the SDR is defined as a ratio of a maximum to a minimum powers that satisfies a certain condition, depending on the APL application. For the previously mentioned applications, the lower bound of the SDR (i.e. the minimum power) is related to the minimum SNR required by the system ($SNR_{min}$) in a certain noise bandwidth (for example $B$ Hz) while the upper bound is set by the maximum power that is received by the system. This SDR is illustrated in Figure 2.20 (b) and marked as $SDR_l$, where the subscript l denotes that this definition is often used in systems with low input RF power.

A different definition of SDR is used in radio astronomy application [92]. Here, the lower bound of the SDR is set by the minimum SNR ($SNR_{min}$) required by the system (just like in the previous case) but the upper bound is set by the minimum signal to intermodulation distortion ratio ($SIR_{min}$). Thus, this definition is more suitable for systems with either sufficiently high input RF power or systems that are very sensitive to interference like radio astronomy systems. In such a case, the $SNR_{min}$ = 20 dB and $SIR_{min}$ = 40 dB has been used [92]. This definition of SDR is also illustrated in Figure 2.20 (b), marked as $SDR_h$.

## 2.6 Summary

In this chapter the important parameters in an analog photonic link have been presented. The discussions comprise a direct modulation scheme and an external modulation scheme using a Mach-Zehnder modulator. The link gain expressions for both schemes were derived using the concept of available power. A lossy impedance matching scheme has been implemented both at the modulation device and the photodetector resulting in a 6 dB gain reduction compared to the unmatched case. Various ways to increase the link gain of an MZM APL have been explained. In general, increasing the optical power to the MZM is desirable to enhance the link gain. The dominant noise sources in APL were discussed. These are the thermal noise, shot noise and the laser relative intensity noise. The important concept of noise figure was also introduced. The nonlinearity in the APL was investigated. The static weak nonlinearities assumption was used, permitting the Taylor expansion to be implemented in describing the nonlinear transfer function of the modulation devices. The single tone and two tone tests were described and the concept of harmonic and intermodulation distortions were introduced. Important parameters such as the compression point and the intercept points were defined for both the direct modulation and the MZM links. Finally the various definitions of dynamic range have been discussed where a special attention has been paid to the so-called spurious-free dynamic range (SFDR). The APL SFDR in relation to sub-octave and multioctave bandwidths, corresponding to narrowband and wideband applications were explained.

# 3

# Performance Enhancement of Analog Photonic Links

## 3.1 Introduction

In the previous chapter we have defined the key parameters that describe the performance of an analog photonic link (APL). These parameters, namely the link gain, the noise figure, and the spurious-free dynamic range (SFDR), can be seen as the indicators of how much deleterious effects like losses, noise and nonlinearities disturb the system. In this chapter, we will focus on the existing techniques that have been employed to mitigate these effects and to enhance the APL performance. Since performance enhancement of an APL is a well explored field, numerous enhancement techniques have been proposed up to now. The description presented here makes no attempt to be complete. Instead, our discussion here is limited to a selection of enhancement techniques that employ either one of or a combination of these schemes: low biasing the modulation device(s), dual laser/modulator and balanced detection schemes, with the aim of improving the noise performance and/or the linearity of the link. We focus on these techniques because they provide valuable insights for optimizing the link performance while sharing the same basic idea with our results presented in the next chapters.

The rest of this chapter is organized as follows: in Section 3.2 enhancement techniques for external modulation APL with a Mach-Zehnder modulator (MZM) are presented. The discussion comprises link gain enhancement by increasing the optical power, low biasing and balanced detection schemes and optical linearization techniques. In Section 3.3, enhancement schemes for direct modulation are presented. The chapter closes with a summary.

## 3.2 External Modulation with MZM

### 3.2.1 Link Gain Enhancement

External modulation links with MZMs have been studied extensively during these years. The link offers high performance, notably in terms of modulation bandwidth and chirpless operation. However, in its early development, the link suffers from low link gain due to a relatively high modulator insertion loss (> 5.5 dB [132]) and a large operating voltage (i.e. high $V_{\pi,\mathrm{RF}}$, > 7 V [127]). The simplest way to mitigate this problem is to increase the input optical power to the modulator, as is evident from Equation (3.1) which has been discussed in length in Chapter 2 Section 2.2 and repeated here for convenience

$$g_{\mathrm{MZM}} = \left( \frac{\pi \, r_{\mathrm{PD}} \, R \, P_{\mathrm{i}} \sin\phi_{\mathrm{B}}}{4 \, L \, V_{\pi,\mathrm{RF}}} \right)^2 . \tag{3.1}$$

Keep in mind that using an RF amplifier can also increase the link gain. Although it is common in practice and perhaps even inevitable in some situations, using this amplifier will introduce additional noise and nonlinearity in the link, which might obscure the intrinsic characteristics of the APLs. Since our motivation is to investigate the characteristics of the APLs, we will exclude the use of any amplifier in our discussions here. Their effects, used either for pre or post-amplification, can thus be incorporated later on when the equivalent two port parameters of the APL (i.e. gain, noise figure, intercept points) has been defined. This is demonstrated, for example, in [133].

To illustrate the effect of increasing this input optical power, let us consider a quadrature-biased ($\phi_{\mathrm{B}} = \pi/2$) MZM link with parameters as the following: $V_{\pi,\mathrm{RF}} = 3.8\,\mathrm{V}$, $r_{\mathrm{PD}} = 0.75\,\mathrm{A/W}$, $\mathrm{R} = 50\,\Omega$ and $10\log_{10} L = 5\,\mathrm{dB}$. The input optical power to the modulator is increased such that the average photocurrent, $I_{\mathrm{av,MZM}}$, increases from 0.1 mA to 100 mA. This average photocurrent can be calculated from the input optical power using the relation:

$$I_{\mathrm{av,MZM}} = \frac{r_{\mathrm{PD}} P_{\mathrm{i}}}{2L} \left(1 - \cos\phi_{\mathrm{B}}\right) . \tag{3.2}$$

The relation of the gain of such link with the average photocurrent, $P_{\mathrm{i}}$ is depicted in Figure 3.1. We can see that for example, a link gain of 0 dB can be achieved with a photocurrent of around 48 mA. Using the Equation (3.2), the corresponding input optical power related to this photocurrent is approximately 400 mW (26 dBm). Although relatively high, this amount of optical power is readily available nowadays, for example from a master oscillator power amplifier (MOPA) [46, 47], which can achieve an optical power up to 10 W and with a RIN lower than -150 dB/Hz [48].

Using this high optical power in combination with low $V_{\pi,\mathrm{RF}}$ modulators have resulted in APLs with a nett gain (i.e. positive link gain in dB) instead of a loss (i.e. negative link gain in dB). A link gain as high as 24 dB at the frequency of 6 GHz has recently been shown [47]. This has been obtained using a quadrature-biased (dual output, see Subsection 3.2.7) MZM with $V_{\pi,\mathrm{RF}} = 1.1$ V and an average photocurrent of 80 mA per-photodiode (in a balanced detection scheme, see Subsection 3.2.5).

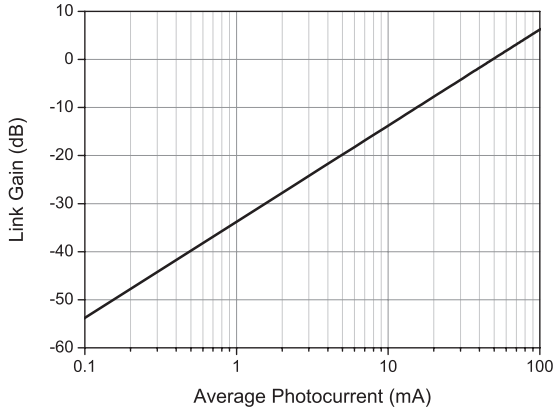


**Figure 3.1:** Link gain of an externally modulated APL with a quadrature-biased MZM as a function of the detected photocurrent.

Note that this photocurrent is exceptionally high and currently cannot be obtained using commercially available photodetectors but was shown with a specially designed rear-illuminated photodetector [47]. We will return to this photodetector power handling issue when we discuss the low biasing technique in the next subsection.

It is important to mention that besides advantageous from the link gain point of view, increasing the input optical power is also attractive for achieving a low noise figure if the link is operating in the shot noise regime [134, 135]. The link noise figure improves because the signal power increases with the optical power quadratically whereas the the shot noise increases only linearly. This improvement in the noise figure will also translate to an improvement of the spurious-free dynamic range (SFDR). However, the benefit of increasing this optical power is lost if RIN is the dominant source. In this case, low biasing will be beneficial to restore the shot noise limited performance [42]. This will be explained further in Subsection 3.2.3

### 3.2.2 Low Biasing and Carrier Filtering

Using a high optical power with a quadrature biased MZM increases not only the link gain but also the average photocurrent. Once the saturation of the photodetector is reached, additional optical power available at the modulator input cannot be used to further increase the link performance. Obviously, using a higher power handling photodetector will mitigate this limitation, as demonstrated in [47, 67] in which photodetectors with an average photocurrent as high as 80 mA and responsivities of 1.0 A/W and 0.5 A/W, respectively, have been used. However, these photodetectors are not yet available commercially. For such commercially available photodetectors, the saturation current is much lower, which is in the range of 14 mA to 28 mA, corresponding to a maximum optical power of +13 dBm to +16 dBm for a 0.7 A/W responsivity at optical wavelength of 1550 nm [136]. This is especially

true for a wide bandwidth photodetector, in which the photodetector area should be kept small to limit parasitic capacitances, that in turn will limit the power handling capability [17]. The discussion regarding high-power handling detectors is beyond the scope of this thesis and an interested reader can refer to [62, 137, 138] for progress in this area. Instead, in this part we will focus our attention to the efforts for utilizing this excess optical power by means of limiting the average photocurrent without significantly reducing the link gain. Two techniques that will be considered here are low biasing the modulator and optical carrier filtering. A different technique that employs a dual-output MZM in conjunction with a balanced detector will be discussed in Subsection 3.2.7.

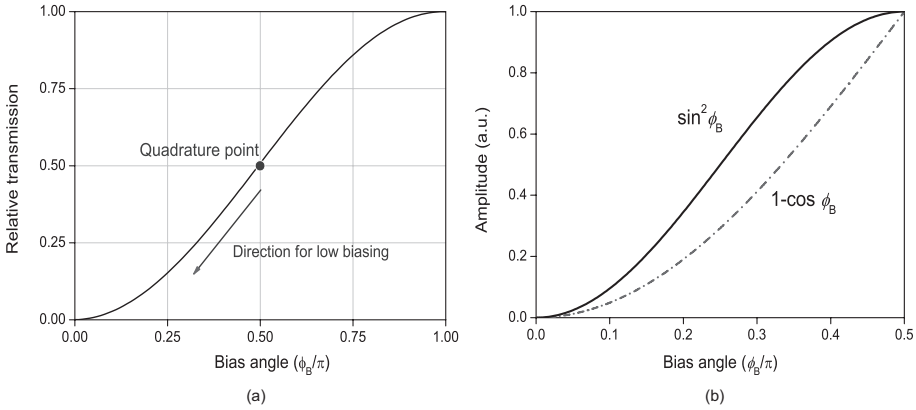


**Figure 3.2:** (a) Low biasing the MZM away from the quadrature point (b) The terms $\sin^2\phi_B$ which is proportional to the link gain and $1-\cos\phi_B$ which is proportional to the DC photocurrent.

In the previous subsection we have seen that to achieve the 0 dB link gain, an average photocurrent of 48 mA is required if the MZM is biased at quadrature. We will see that by moving the bias angle away from the quadrature towards the lowest transmission point, i.e., null bias (see Figure 3.2 (a).), the photocurrent can be reduced more significantly relative to the link gain reduction. This is known as the *low bias* technique [42, 46, 127, 139–147]. We will see later on that the technique is useful not only to avoid the detector saturation, but also to improve the link noise performance (Subsection 3.2.3). However, these improvements are not "free", but obtained at the expense of a reduced linearity, as will be explained in Subsection 3.2.4.

A careful observation of Equations (3.1) and (3.2) will reveal that by moving the bias point from the quadrature bias ($\phi_B = \pi/2$) to towards the null bias ($\phi_B = 0$), the average photocurrent will reduce in a $1-\cos(\phi_B)$ manner, while the link gain will be reduced with $\sin^2\phi_B$ dependence. These factors are plotted against the bias angle in Figure 3.2. Note that for a small angle deviation from the quadrature point, the average photocurrent falls faster compared to the signal component (link gain). To illustrate the advantage of this low biasing technique, let us consider a situation where a photonic link is limited by the photodetector power handling capability.

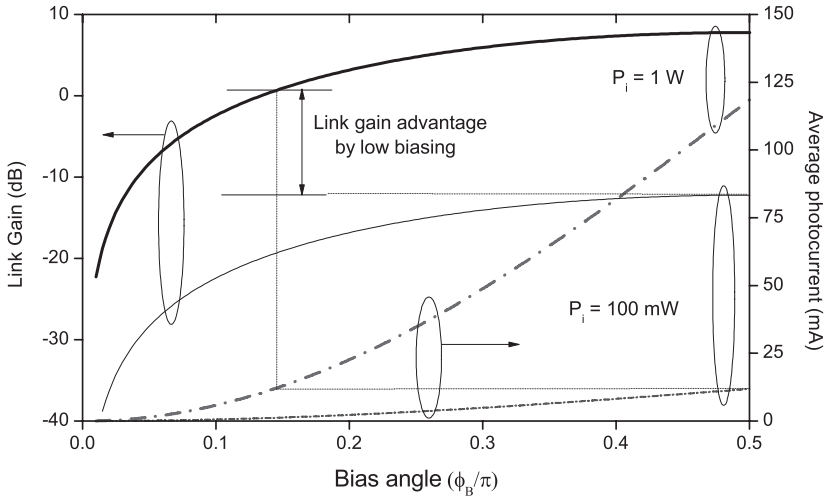


**Figure 3.3:** Link gain and the average photocurrent as functions of the bias angle, for two different input optical powers, 100 mW (thin line) and 1 W (thick line). The link gain advantage by low biasing is obtained with 1 W input power but with the same photocurrent of 12 mA.

**Example 3.1**

Consider a system with an optical source with maximum output optical power of +30 dBm (1 Watt). This source is used in an externally modulated APL with an MZM with parameters described in the previous examples ($V_{\pi,\mathrm{RF}} = 3.8$V, $r_{\mathrm{PD}} = 0.75$A/W, R = 50Ω and $10\log_{10} L = 5$dB). The modulator is biased at quadrature and we have assumed its power handling capability is not an issue. Now, suppose that the optical detector used in the system can only handle an average optical power up to +12 dBm, corresponding to an average photocurrent of 12 mA. Using Equation (3.1), the maximum link gain that can be achieved without exceeding the prescribed maximum optical power is -12 dB. In this case, we can only use a maximum optical power of +20 dBm (100 mW) supplied to the modulator. Now suppose that the whole optical power is delivered to the modulator and the bias angle of the modulator is adjusted such that the photocurrent is maintained at 12 mA, the link gain is now increased to 0.65 dB where the bias angle is $0.145\,\pi$ or 26.1 degrees. This situation is illustrated in Figure 3.3 where the link gain and the average photocurrent of the APL are plotted against the bias angle. A more general description is given in Figure 3.4, where the contour plot of the link gain as a function of the bias angle and the input optical power is depicted. In the figure it is also indicated the contour of a constant photocurrent of 12 mA. Given a modulator and a detector characteristics (i.e., $V_{\pi,\mathrm{RF}}$, $L$ and $r_{\mathrm{PD}}$), such a plot gives an insight for a link designer to optimize the link gain, in terms of input optical power and the bias angle, while keeping the average photocurrent below the specified maximum value.

As shown in the example above, high link gain can be obtained with relatively low average photocurrent by means of low biasing. For this reason, some consider the low biasing technique as a *gain enhancement* technique [146]. This is sometimes misleading, since for a *given (fixed)* optical power, quadrature biasing gives the *maximum* link gain (since the maximum of $\sin^2 \phi_B$ is at $\phi_B = \pi/2$ ) and low biasing the modulator *will only reduce* the link gain. This can also be observed from Figure 3.4 if one draws a vertical line from top to bottom of the figure for any fixed optical power. The link gain advantage is only obtained if one compares the gains of a low bias link and quadrature biased link in terms of a constant average photocurrent, i.e., if one follows the constant current contour superimposed on Figure 3.4.

Beside low biasing, a way to reduce the average photocurrent is to reduce or completely remove the optical carrier component using an optical filter. This technique was published by M. LaGasse in 1994 [134] and R.D Esman et al. [135] in 1995. Since then various publications have pursued this technique [125, 148]. However this technique does not give any advantage compared to the low biasing and even more complicated due to the need of an external optical filter [42]. This technique also increases the even-order distortions, just like the low biasing technique. We will see later on when we discuss the nonlinear distortion in a low biased APL.

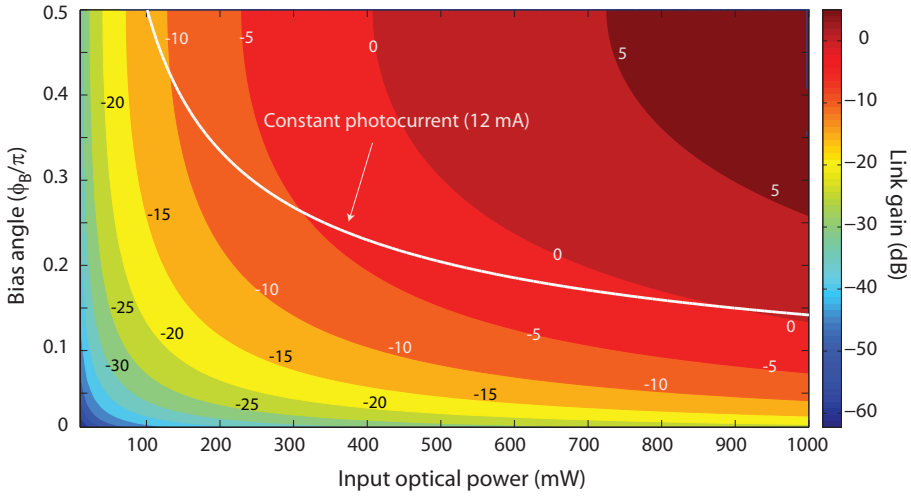


**Figure 3.4:** Contour of link gain as a function of the input optical power and the bias angle. The line indicates the contour of constant photocurrent of 12 mA. It is evident that by means of low biasing the photocurrent can be kept low while the link gain is increased by increasing input optical power.

### 3.2.3 Impact of Low Biasing on the Link Noise

Beside saturating the photodetector, the average optical power at the detector (and hence the average photocurrent) directly contributes to the noise power in the APL. Recall that the shot noise and the relative intensity noise are proportional linearly and quadratically, respectively, with respect to the DC photocurrent (Chapter 2 Section 2.3).

$$p_{\text{shot}} = 2q\,B\,R_{\text{L}}\,I_{\text{av,MZM}} \tag{3.3}$$

$$p_{\text{rin}} = 10^{\frac{\text{RIN}}{10}}\,BR_{\text{L}}\left(I_{\text{av,MZM}}\right)^2 \tag{3.4}$$

The dependence of these noise terms on the average photocurrent is shown in Figure 3.5 together with the thermal noise power which is independent of the photocurrent. Note that the noise power is expressed as the power spectral densities, PSD, where we have set $B = 1$ Hz (see Chapter 2 Section 2.3). From this figure, we can see that except for a very low average photocurrent ($I_{\text{av,MZM}} < 0.2$ mA), the shot noise and RIN dominates the total link noise. Thus, reducing this photocurrent by means of low biasing is very attractive to improve the link noise performance.

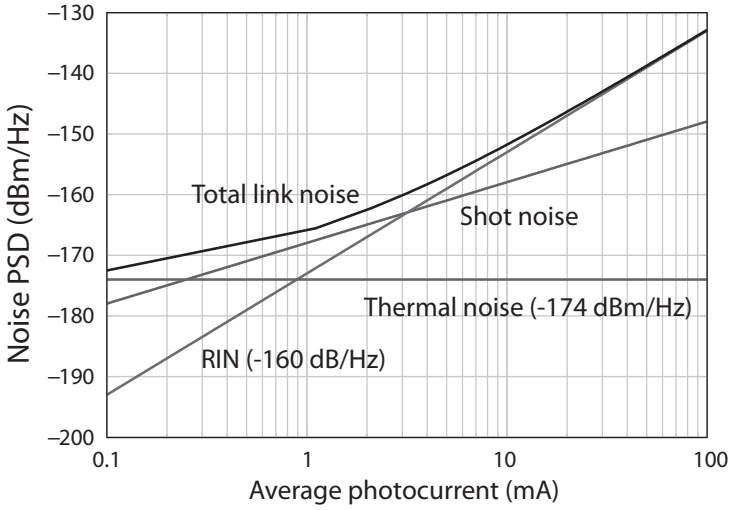


**Figure 3.5:** Noise power spectral densities of various dominant sources as functions of the detected photocurrent.

The effect of low biasing the modulator to the total link noise power is illustrated in Figure 3.6, where the noise PSD of an MZM APL with various RIN values are plotted as functions of the modulator bias angle. In this case the input optical power to the modulator is set at 100 mW while other link parameters are the same as described in the previous example. There are several interesting features that can be observed from the plot. First, for a fixed RIN value, low biasing the modulator

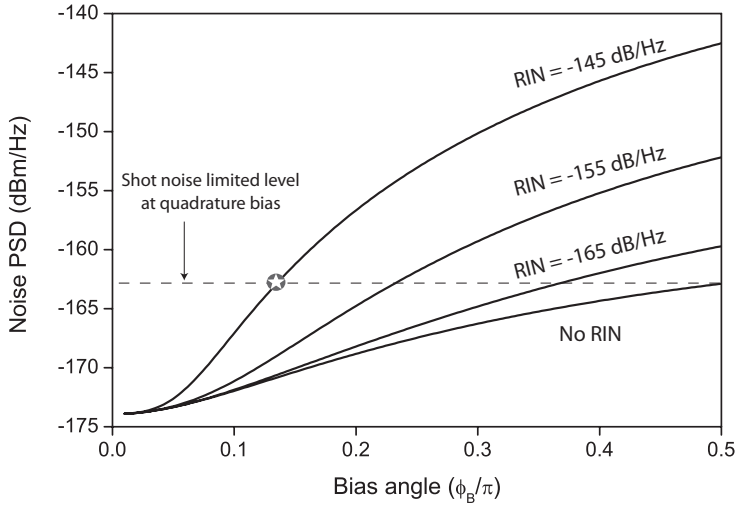


**Figure 3.6:** Noise power spectral density for various RIN values as functions of the bias angle. Low biasing the APL reduces the noise power and allows shot noise limited operation.

will reduce the noise PSD. This reduction, relative to the noise PSD at quadrature bias, is larger for higher RIN values. Thus, low biasing is more attractive for RIN dominated links. This can be understood since for RIN dominated links, the total noise power virtually has the dependence of $\left[1-\cos(\phi_B)\right]^2$ on the bias angle (see Equations (3.2) and (3.6)).

Another way to look at the plot in Figure 3.6 is to compare the noise PSDs for different RIN values. The benchmark for this comparison is a quadrature biased APL with no RIN and hence, in this case, is shot noise limited. The noise level for this shot noise limited performance is -162.8 dBm/Hz, which is shown as the dashed curve in Figure 3.6. We can see that this noise PSD value can be obtained with a RIN limited APL, in this case with a RIN of -145 dB/Hz, by reducing the MZM bias angle to $0.133\pi$ or $24^o$. This is indicated by a star symbol on the figure. This demonstrates how this technique restores the shot noise limited performance, initially obtained with a RIN-free laser source and a quadrature biased modulator, with a noisy (i.e. high RIN) laser but with reduced bias.

It is more useful however, to inspect the impact of low biasing to the link noise figure. This is because most of the time the important parameter is not the absolute value of the noise power but rather its relative value with respect to the signal power, i.e., the SNR. The variation of this SNR from the input to the output of the APL is described by the noise figure [17]. We have seen that for a fixed input optical power, low biasing will also reduce the link gain. This means that for a fixed optical power, low biasing the modulator will reduce both the signal and the noise power at the APL output. The impact of this low biasing to the overall noise figure for various RIN values are shown in Figure 3.7.

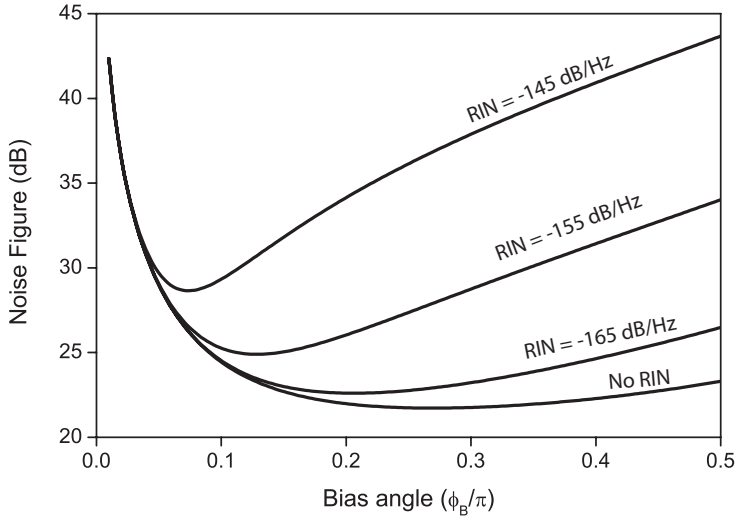


**Figure 3.7:** Link noise figure for various RIN values as functions of the modulator bias angle. The bias angle that minimizes the noise figure depends strongly on the RIN level.

Similar to the noise power trend, low biasing effectively reduces the noise figure of a RIN limited APL compared to the shot noise limited one (i.e. no RIN case). For example, for RIN =-145 dB/Hz, the noise figure is reduced from 43.68 dB at the quadrature to the minimum value of 28.65 dB at $0.07\pi$ or $13.1^{o}$. Hence the NF reduction factor is 15.03 dB. In contrast, in the absence of RIN, the NF reduction is limited to 1.58 dB if the bias is reduced from quadrature (NF = 23.3 dB) to $0.267\pi$ or $48.1^{o}$ (NF = 21.72 dB). Again this can be explained by examining the dependence of the dominant noise terms and the link gain with respect to the bias angle. The link gain is proportional to the factor $\sin^2\phi_B$ (Equation (3.1)) whereas the shot noise and RIN powers are proportional to the factor $1-\cos\phi_B$ and $\left(1-\cos\phi_B\right)^2$, respectively as shown in Equations (3.5) and (3.6). These equations are essentially Equations (3.3) and (3.4) re-written to clearly show the dependence of these noise terms on the bias angle.

$$p_{\text{shot}} = 2qBR_L\frac{r_{PD}P_i}{2L}\left(1-\cos\phi_B\right) \tag{3.5}$$

$$p_{\text{rin}} = 10^{\frac{RIN}{10}}BR_L\left(\frac{r_{PD}P_i}{2L}\left(1-\cos\phi_B\right)\right)^2 \tag{3.6}$$

The noise factor of the APL (Chapter 2, Subsection 2.3.5) can be written as

$$F_{MZM} = \frac{p_N}{g_{MZM}kTB} \tag{3.7}$$

where $p_N$ is the total noise power in Watt. This noise factor is related to the noise figure via the relation NF = $10\log_{10}(F)$. Now let us examine the case where, the link noise is dominated by the shot noise, i.e., $p_N = p_{shot}$. According to Equations (3.1), (3.5) and (3.7), the noise factor is proportional to the factor $\sin^2\phi_B/\left(1-\cos\phi_B\right)$ whereas in the case of RIN dominated link ($p_N = p_{rin}$), $F_{MZM}$ is proportional to the factor $\left[\sin\phi_B/\left(1-\cos\phi_B\right)\right]^2$. These factors, expressed in dB, are plotted in Figure 3.8. It is thus clear that the impact of low biasing is more for RIN dominated links than for shot noise limited links. Note that for shot noise limited links, a maximum noise figure improvement that can be expected is 3 dB. This was also noted by Helkey in [141].

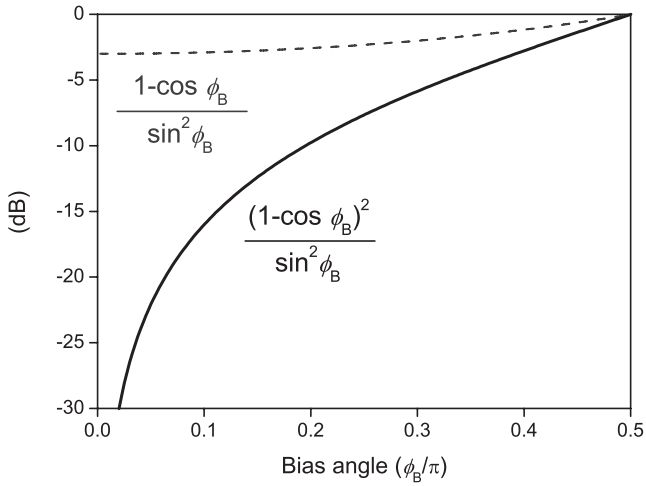


**Figure 3.8:** The factors that determine the amount of noise figure reduction for a low biased APL relative to the quadrature biased case. Solid line: RIN dominated link, dashed: shot noise dominated.

A careful observation of Figure 3.7 shows that the bias angle that gives the minimum noise figure value depends strongly on the RIN values. This optimum bias angle as a matter of fact depends on various link parameters, for example the input optical power or the loss. In general the expression of this optimum bias angle can be derived from the noise figure expression [139, 141, 143], as the following, where we take the approach presented in [143].

We start with the expression of the noise factor in Equation (3.7). Assuming that the dominant noise terms are the thermal noise, shot noise and RIN and taking into account the passive impedance matching imposed at the detector (see Chapter 2, Section 2.3), $F_{MZM}$ can be written as

$$F_{MZM} = 1 + \left(\frac{V_{\pi,RF}}{\pi}\right)^2 \frac{A + B\left(1-\cos\phi_B\right) + C\left(1-\cos\phi_B\right)^2}{\sin^2\phi_B} \tag{3.8}$$

with

$$A = \left(\frac{4L}{r_{\mathrm{PD}} P_{\mathrm{i}} R}\right)^2 \tag{3.9}$$

$$B = \frac{4qL}{r_{\mathrm{PD}} P_{\mathrm{i}} R k T} \tag{3.10}$$

and

$$C = 10^{\frac{\mathrm{RIN}}{10}} \frac{1}{kTR}. \tag{3.11}$$

The bias angle that gives minimum noise figure, $\phi_{\mathrm{B,min\,NF}}$, can be found by setting the derivative of $F_{\mathrm{MZM}}$ with respect to $\phi_{\mathrm{B}}$ equal to zero and solving for $\phi_{\mathrm{B}}$. The result is

$$\phi_{\mathrm{B,min\,NF}} = \arccos\left[1 + \frac{A}{B+2C} - \sqrt{\left(\frac{A}{B+2C}\right)\left(2 + \frac{A}{B+2C}\right)}\right]. \tag{3.12}$$

We can see that this optimized bias angle is independent of $V_{\pi,\mathrm{RF}}$, but depends on various parameters like RIN and the input optical power. It is useful for example, to consider how to optimize the system (i.e., minimize the noise figure) by means of low biasing given the input optical power ($P_{\mathrm{i}}$) and the RIN levels. For this purpose, we plot $\phi_{\mathrm{B,min\,NF}}$ as a function of RIN and $P_{\mathrm{i}}$, where the rest of the parameters are kept the same as used in the previous example. The result is depicted in Figure 3.9 (a). Using such plot, a link designer can select the bias angle that minimizes NF, given the specification of the light source. For example, using a high power and a high RIN source, the modulator should be biased very low in order to achieve the optimum NF, while for lower power and lower RIN source the optimum bias is closer to the quadrature point.

Having determined the optimum bias angle, we can inspect how the resulting minimum noise figure ($\mathrm{NF_{min}}$) compares to the NF of the same link only biased at the quadrature ($\mathrm{NF_Q}$). We call this quantity, $\mathrm{NF_{min}} - \mathrm{NF_Q}$, the noise figure reduction factor and it is plotted as a function of RIN and $P_{\mathrm{i}}$ in Figure 3.9 (b). The highest noise figure reduction is obtained in the case of a link using a noisy laser with high output power while for relatively low RIN laser the noise figure improvement is fairly limited.

### 3.2.4 Impact of Low Biasing on Nonlinearity and SFDR

In the previous subsection, we have seen that low biasing the modulator will improve the APL noise performance. Here we will evaluate the impact of low biasing to the link linearity and dynamic range. Recall that biasing the MZM at the quadrature will yield a maximum link gain and a minimum even-order distortion. This is the main reason that the quadrature biasing is the most widely used operating point. Moreover, at this bias point the APL SFDR is not limited by the second-order intermodulation (IMD2) but only by the third-order intermodulation distortion (IMD3). As a result, the APL can be used in wideband or multioctave applications, where the

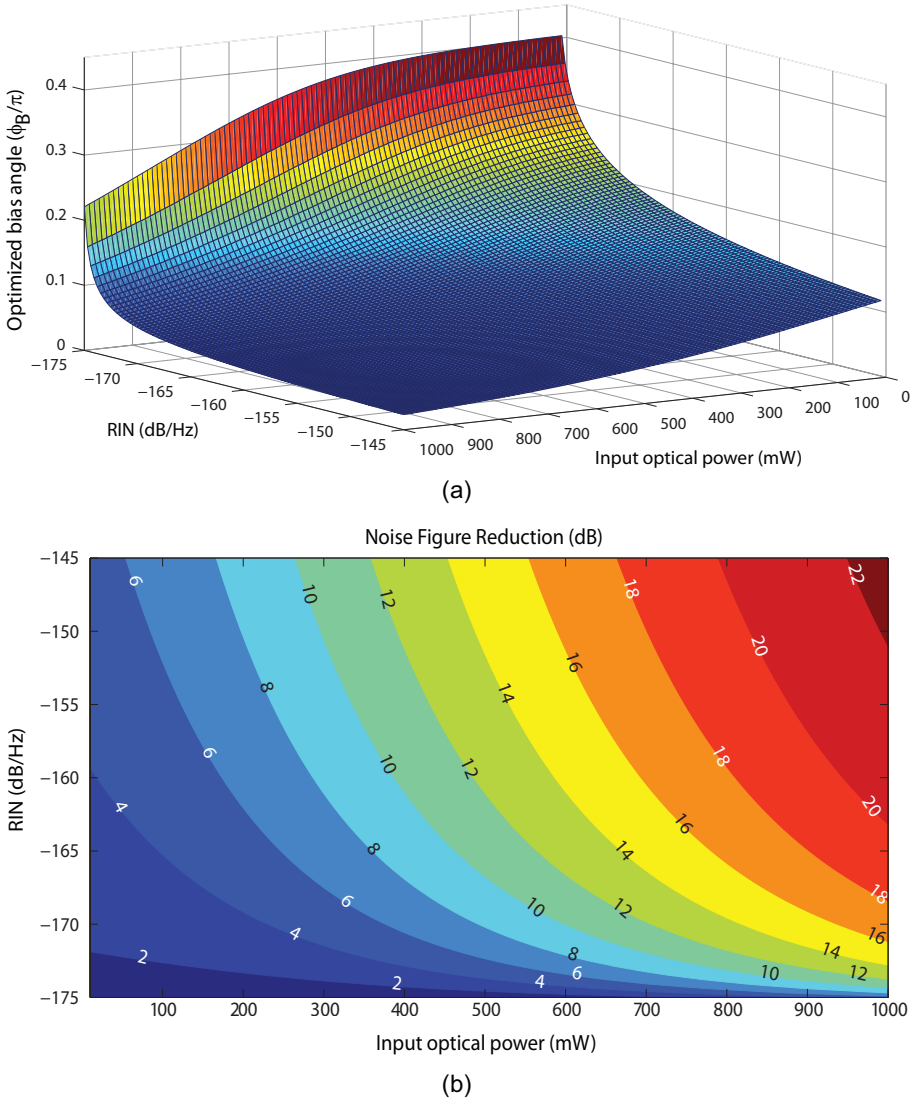


**Figure 3.9:** (a) The optimized modulator bias angle in Equation (3.12) that gives minimum noise figure and (b) The contour of the noise figure reduction factor $\left(\mathrm{NF}_{\mathrm{min}} - \mathrm{NF}_{\mathrm{Q}}\right)$ obtained by inserting Equation (3.12) into (3.8)) and divide the result with the noise factor of the same link biased at the quadrature.

relative signal bandwidth is more than one octave (see Subsection 2.43 of Chapter 2). As the bias angle reduces, the even order distortion power increases [127]. This can be observed by the increase of the second-order intercept point (IIP2),

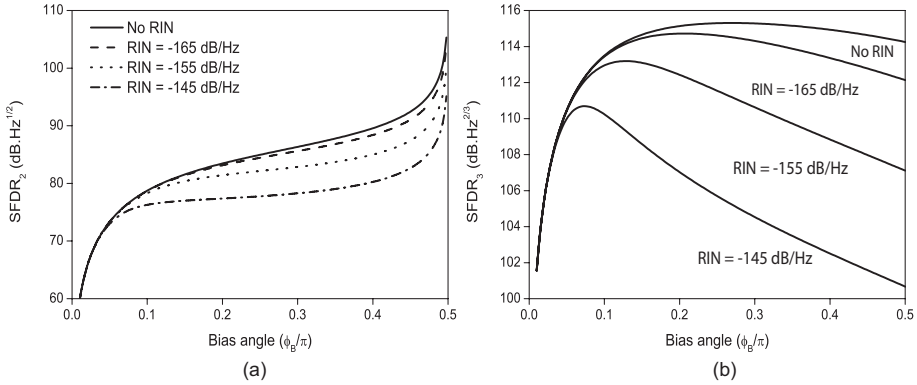


**Figure 3.10:** (a) Second-order and (b) Third-order SFDR for various RIN levels as functions of the bias angle. The $SFDR_2$ is severely limited by moving the modulator bias angle away from the quadrature

which is proportional to the factor $\tan^2\phi_B$ (Equation (2.79). and Figure 2.16 of Chapter 2). Thus, there is a trade-off between the noise power and the IMD2 power in low biasing the modulator in a sense that low biasing will induce larger even order distortion. As a result the second-order spurious-free dynamic range ($SFDR_2$) is severely limited, as shown in Figure 3.10 (a). A solution to this limitation is to use a pair of low biased modulators instead of one modulator and use a balanced detection scheme. This scheme, proposed by Burns et al. [149] in 1996 and will be discussed further in Subsection 3.2.6.

However, for applications where the bandwidth is less than one octave, low biasing can still be advantageous from the SFDR point of view. In this type of application, even order distortion can be filtered out, thus the limiting factor is the IMD3 terms. Since the third order input intercept point (IIP3) does not depend on the bias angle (Equation (2.80) of Chapter 2), the $SFDR_3$ will increase if the noise figure reduces. This is illustrated in Figure 3.10 (b).

### 3.2.5 Balanced Detection

Low biasing the modulator imposed a trade-off between the noise figure and the IMD2 power and $SFDR_2$, limiting the applicability of the APL in wideband systems. As we will see in the following subsections, a way to mitigate this limitation is to use a balanced detection scheme. A balanced photodetector (BPD) consists of a pair of photodiodes as shown in Figure 3.11. Supposing that each of the photodiodes has the responsivity of $r_{PD_1}$ and $r_{PD_2}$, and the optical powers impinging on them are $P_{o_1}$ and $P_{o_2}$, respectively, the output current of the BPD, $I_{BPD}$ is simply the difference of the currents generated by each photodiode ($I_{PD_1}$ and $I_{PD_2}$), yielding

$$\begin{aligned} I_{\mathrm{BPD}} &= I_{\mathrm{PD1}} - I_{\mathrm{PD2}} \\ &= r_{\mathrm{PD1}} P_{\mathrm{o1}} - r_{\mathrm{PD2}} P_{\mathrm{o2}} \,. \end{aligned} \tag{3.13}$$

Ideally, the photodiodes have the same responsivities, $r_{\mathrm{PD}_1} = r_{\mathrm{PD}_2}$. In this case, provided that the phase and the amplitude of the optical signal impinging on the detectors are matched, the output photocurrents of the photodiodes are the same. Subtraction of these currents will lead to a cancellation of the common mode signals of the photocurrents $I_{\mathrm{PD}_1}$ and $I_{\mathrm{PD}_2}$ . Thus, an important parameter of a BPD is the common-mode-rejection-ratio (CMRR), defined as the ratio of the differential mode signal to the common mode signal at the output of the BPD [150].

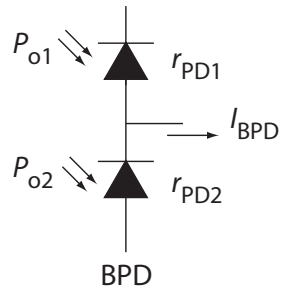


**Figure 3.11:** Balanced detection scheme. The output current of the balanced detector ($I_{\mathrm{BPD}}$) is the difference of the photocurrents generated at each photodiode (Equation (3.13)).

The scheme was initially proposed to cancel the local oscillator (LO) noise in a coherent detection scheme [31, 151]. However, in 1992, Madjar et al. [152, 153] proposed the architecture using a balanced detection to reduce the noise and to increase the dynamic range of an analog photonic link. In 1993, Ackerman et al. [154] proposed a similar setup only using a dual output MZM (Subsection 3.2.7). Since then this technique has been pursued by many to show high performance analog photonic links. [43, 44, 46, 47, 49, 87, 155–159]. Various BPD configurations have been used in such links, such as commercially available BPD modules [136, 160] or discrete photodiodes combined with a hybrid coupler [43, 49, 125].

### 3.2.6 Low Biased Parallel Modulators: Class-AB APL

The balanced detection scheme has been used to overcome the major disadvantage of low biasing which is high even-order distortion. The scheme, shown in Figure 3.12, was proposed by Burns et al. [149] in 1996. With this scheme, the deleterious effect of IMD2 can be mitigated while at the same time preserving the advantage of low biased modulators. The proposed APL consists of a pair of MZMs symmetrically biased around the lowest transmission point (null bias) as shown on the lower left of Figure 3.12. These modulators are fed with a common RF signal

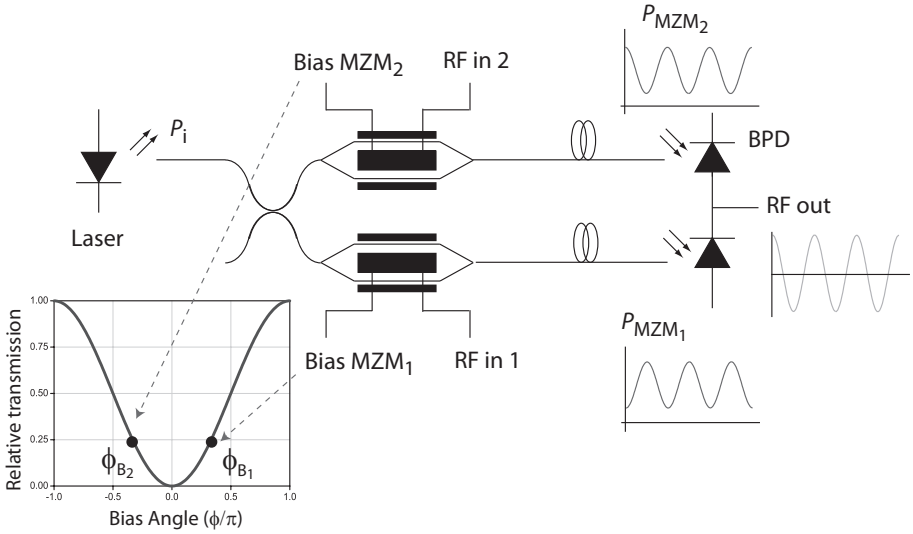


**Figure 3.12:** Schematic of the Class-AB operation.

(voltage). In this arrangement, for one MZM an increase of instantaneous voltage will result in an increase of output optical power while for the other MZM it will result in a decrease of output optical power. This means that the MZMs modulate the light in a push-pull manner and the optical signals at their outputs will be complementary, i.e., they have the same amplitude (assuming that the MZMs are identical) but opposite in modulation phase. This situation is also illustrated in Figure 3.12. These complementary optical signals are routed to a BPD at the receiving site using a pair of optical fibers. If these transmission fibers are perfectly matched in length, the optical signals will arrive at the photodiodes maintaining their amplitude and RF-modulation phase relations. The BPD will subtract these signals and, according to Equation (3.13), the fundamental signal will add-up instead due to their antiphase relation. Note that this also applies to any odd-order distortion component in the modulated optical signals. All even order distortion components and the laser intensity noise, however, are common at the two arms of the APL and hence will be cancelled at the BPD output. This is the main advantage of the scheme.

Since initially proposed in 1996, this type of APL has been investigated and optimized by Darcie et al. [161–163] who dubbed the link as a Class-AB (CAB) photonic link, due to its similarities with a class-AB electronic amplifier in which a small prebias is needed to maintain linear operation [164].

To fully understand the advantage of the CAB link over a conventional MZM link, let us consider a general case where a pair of MZMs is employed where the first MZM ($MZM_1$) has an insertion loss of $L_1$, an RF half-wave voltage of $V_{\pi,\mathrm{RF}_1}$ and biased at an angle $\phi_{\mathrm{B}_1}$, while the parameters of the second MZM ($MZM_2$) are $L_2$, $V_{\pi,\mathrm{RF}_2}$ and $\phi_{\mathrm{B}_2}$. Suppose that the optical power from the laser is $P_{\mathrm{i}}$, the input

optical power to the each modulator is $P_{\mathrm{i}}/2$. The output optical power from these modulators can be written as

$$P_{\mathrm{MZM}_1}(t) = \frac{P_{\mathrm{i}}}{4L_1}\left(1-\cos\left[\theta_1(t)+\phi_{\mathrm{B}_1}\right]\right) \tag{3.14}$$

$$P_{\mathrm{MZM}_2}(t) = \frac{P_{\mathrm{i}}}{4L_2}\left(1-\cos\left[\theta_2(t)+\phi_{\mathrm{B}_2}\right]\right) \tag{3.15}$$

where $\theta_{1,2}(t)$ is the modulating signal to $\mathrm{MZM}_{1,2}$ defined as

$$\theta_{1,2}(t) = \frac{\pi V_{\mathrm{RF}}(t)}{V_{\pi\mathrm{RF}_{1,2}}}. \tag{3.16}$$

Now let us consider an ideal case where the modulators are identical ($L_1 = L_2$ and $V_{\pi,\mathrm{RF}_1} = V_{\pi,\mathrm{RF}_2}$) and they are biased symmetrically from the null bias point such that $\phi_{\mathrm{B}_1} = -\phi_{\mathrm{B}_2} = \phi_{\mathrm{CAB}}$. The output optical powers in Equations (3.14) and (3.15) can be re-written as

$$P_{\mathrm{MZM}_1}(t) = \frac{P_{\mathrm{i}}}{4L}\left(1-\cos\left[\theta(t)+\phi_{\mathrm{CAB}}\right]\right) \tag{3.17}$$

$$P_{\mathrm{MZM}_2}(t) = \frac{P_{\mathrm{i}}}{4L}\left(1-\cos\left[\theta(t)-\phi_{\mathrm{CAB}}\right]\right). \tag{3.18}$$

The resulting optical signals are detected with an ideal BPD with responsivity of $r_{\mathrm{PD}}$. The output current of the BPD can thus be written as

$$\begin{aligned} I_{\mathrm{D,CAB}}(t) &= r_{\mathrm{PD}}\left(P_{\mathrm{MZM}_1}(t) - P_{\mathrm{MZM}_2}(t)\right) \\ &= \frac{r_{\mathrm{PD}}P_{\mathrm{i}}}{2L}\sin\theta(t)\sin\phi_{\mathrm{CAB}} \\ &\approx \frac{r_{\mathrm{PD}}P_{\mathrm{i}}}{2L}\left[\theta(t)\sin\phi_{\mathrm{CAB}} - \frac{\theta^3(t)}{6}\sin\phi_{\mathrm{CAB}} + \ldots\right]. \end{aligned} \tag{3.19}$$

From Equation (3.19), we can see that ideally, the output current will only consist of the desired signal plus odd-order distortions while the DC component and all even-order distortions are perfectly canceled.

Since the DC component is cancelled, the laser RIN ideally is also cancelled. But the shot noise contributions from the two photodiodes will add up because they are generated independently. Thus, the shot noise power in the CAB link can be written as:

$$\begin{aligned} p_{\mathrm{shot,CAB}} &= 2qBR_{\mathrm{L}}r_{\mathrm{PD}}\left(\left\langle P_{\mathrm{MZM}_1}(t)\right\rangle + \left\langle P_{\mathrm{MZM}_2}(t)\right\rangle\right) \\ &= q\,r_{\mathrm{PD}}\,B\,R_{\mathrm{L}}\frac{P_{\mathrm{i}}}{L}\left(1-\cos\phi_{\mathrm{CAB}}\right). \end{aligned} \tag{3.20}$$

The performance of the CAB link depends on how the bias angles for the modulators are selected and matched. The bias angle selection will determine the shot noise power as well as the signal power. In [149], the modulators are biased at

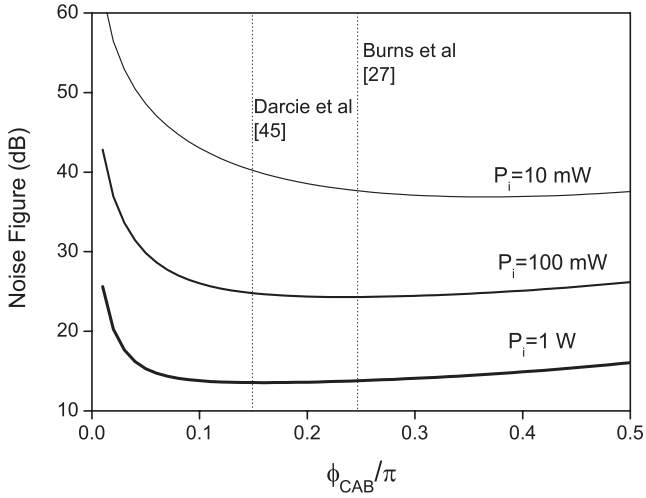


**Figure 3.13:** The class-AB APL noise figure as a function of the bias angle, $\phi_{\mathrm{CAB}}$, for various input optical power levels.

$\phi_{\mathrm{B}} = \pi/4$, yielding an $\mathrm{SFDR}_2$ of 108 dB.Hz$^{1/2}$ and $\mathrm{SFDR}_3$ of 109 dB.Hz$^{2/3}$ at the frequency of 110 MHz for 1 mA detected current per-photodiode. The IMD2 reduction obtained by balanced detection was 28 dB. Darcie et al. [161] selected a lower bias angle ($\phi_{\mathrm{B}} = \pi/6$) in order to have a larger shot noise reduction. With this arrangement, an SFDR of 110 dB.Hz$^{2/3}$ has been be achieved. To illustrate how the bias points can be selected in such a link, let us consider the following example.

**Example 3.2**
Consider a CAB link consisting of a pair of MZMs with parameters $V_{\pi,\mathrm{RF}} = 3.8$V and $10\log_{10} L = 5$ dB. Assume that the modulators are identical. The BPD is assumed to have a responsivity of $r_{\mathrm{PD}} = 0.75$A/W and a CMRR of 30 dB. A passive impedance matching scheme has been used at the BPD to match the impedance to a 50 Ω load. The optical power of the laser is $P_{\mathrm{i}}$. The APL noise figure as a function of the bias angle, $\phi_{\mathrm{CAB}}$, for various input optical power levels are shown in Figure 3.13. In this figure, the bias angles selected in [149] and in [161] are also indicated. For low input optical power, the optimum bias angle is close to the quadrature point while for high optical power low biasing is advantageous. However, the NF improvement of low biasing relative to the quadrature biasing in this case is negligible. This is because the APL is shot noise limited (since RIN is assumed to be perfectly cancelled by balanced detection) and according to Figure 3.8, the maximum NF reduction for shot noise limited link relative to quadrature is limited to 3 dB. However, low biasing is still advantageous to avoid photodiode saturation. Supposed that for $P_{\mathrm{i}} = 1$ W, choosing the bias angle of $\pi/10$ will give link parameters $G = -2$ dB, NF = 13 dB , $\mathrm{SFDR}_3$ = 120.5 dB.Hz$^{2/3}$ and noise PSD of -162.6 dBm/Hz. This is all achieved with an average photocurrent per photodiode of only 6.3 mA. Moreover, since second-

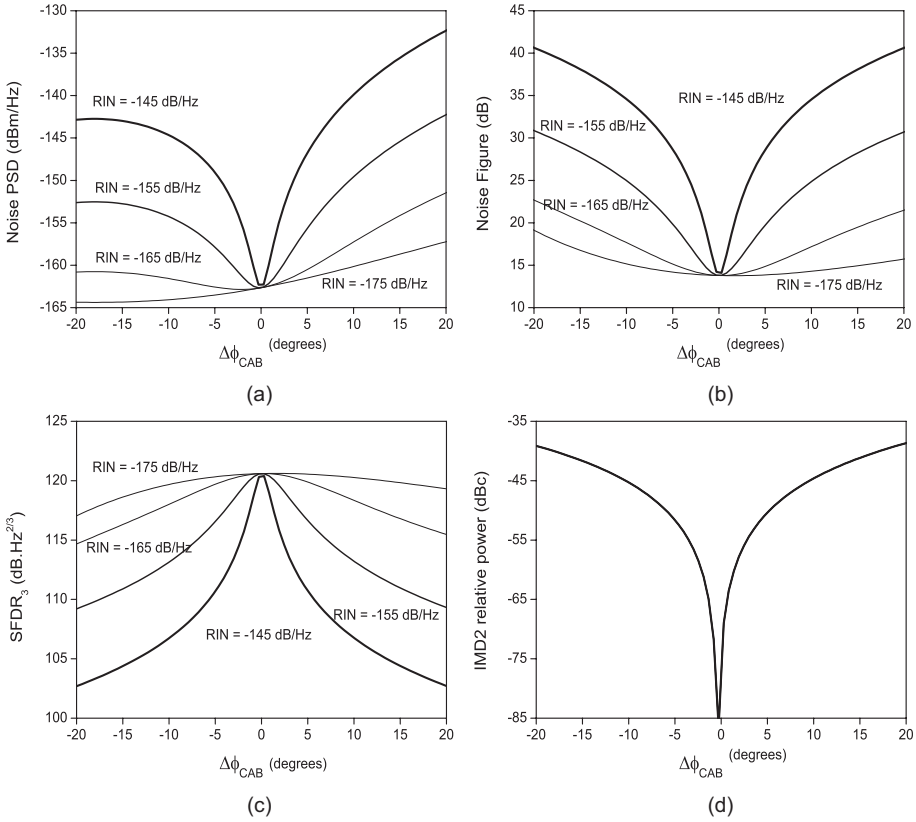


**Figure 3.14:** Class-AB link parameters as functions of the bias angle imbalance. (a) Noise PSD, (b) Noise Figure, (c) $SFDR_3$ and (d) IMD2 power relative to the carrier power.

order distortion terms are suppressed, the APL can be applied for broadband (multioctave) systems.

In general it is challenging to maintain the bias angle of the modulators to be exactly the same [161] since the modulators suffer from bias drifting which moves the bias point away from the intended bias point due to temperature dependence [165] or a memory effect [33]. To give an idea of how sensitive the APL to bias angle imbalances, let us consider the following example.

**Example 3.3**
In the previous example we have set $\phi_{CAB} = \pi/10$ and obtained that the APL gives a relatively high performance (NF = 13 dB , $SFDR_3$ = 120.5 dB.Hz$^{2/3}$) with a medium photocurrent per-photodiode (6.3 mA). Now let us assume that the bias angle of one of the modulators slightly deviates from the intended value. In the ideal case,

we have $\phi_{B_1} = -\phi_{B_2} = \phi_{CAB}$. Here we consider that $\phi_{B_2} = -\left(\phi_{CAB} + \Delta\phi_{CAB}\right)$, where $\Delta\phi_{CAB}$ is the deviation from the intended bias angle. The link performance parameters as functions of $\Delta\phi_{CAB}$ (expressed in degrees) are shown in Figure 3.14, where we have set $\phi_{B_1} = \phi_{CAB} = \pi/10$. From Figure 3.14 (a)-(c) we can see that the sensitivity of the link performance to the bias imbalance depends strongly on the laser RIN. For low RIN (for example RIN = -175 dB/Hz), bias angle deviation of -20$^o$ will increase the noise figure by 6 dB (from 13 dB to 19 dB) and reduce the $SFDR_3$ by 3.5 dB (from 120.5 to 117 dB.Hz$^{2/3}$). While in the case of high RIN (-145 dB/Hz) the effect of a same deviation is much severe, where the noise figure is increased by 27 dB and the $SFDR_3$ is reduced by 18 dB.

It is also important to note that the effect of the bias deviation is not symmetrical about the intended bias point (Figure 3.14 (a)-(c)). This is because for positive values of $\Delta\phi_{CAB}$, the bias point is deviated towards the quadrature point that increases the link gain as well as the noise power, whereas negative values of $\Delta\phi_{CAB}$ indicate a deviation towards the null bias, where both the signal and the noise vanish.

The bias deviation also affects the IMD2 suppression in the link. This is illustrated in Figure 3.14 (d) where the IMD2 power relative to the fundamental signal power as a function of the bias deviation is depicted. Here, the total RF input power of 0 dBm delivered to both modulators has been assumed. A 20$^o$ bias deviation will result in approximately 46 dB increase in the IMD2 power. This will limit the $SFDR_2$ of the link and subsequently limit the APL to sub-octave applications.

Besides maintaining the bias angles, another challenge in the CAB link is to maintain a perfect amplitude and RF-modulation phase matching for the RIN and IMD2 cancellations. For this reason, the RF phase and amplitude equalizations should be done, using attenuators (RF or optical) for the amplitudes and using phase shifters or variable optical delay lines (VODLs) for the phase. The requirements for the phase and amplitude matching to achieve a certain RIN suppression level has been well documented and can be found in references [151, 153], for example.

### 3.2.7 Dual Output MZM

To date, the highest performance APLs have been shown with a scheme using a dual-output (or X-coupled) MZM and a balanced detection scheme. The architecture of of such APL is shown in Figure 3.15. When biased at the quadrature, the X-coupled MZM outputs exhibits two complementary optical signals, as illustrated in Figure 3.15. In the ideal case, the DC component and the even-order distortion terms are common in these signals and, hence, will be cancelled upon balanced detection. The desired fundamental signal and odd-order distortion terms of these two outputs, however, will add up at the BPD output. The cancellation of the DC component will lead to RIN suppression. This is also the case for second-order harmonic and intermodulation distortion (HD2 and IMD2). For this reason, the APL is suitable for multioctave bandwidth operation. Moreover, since the complementary

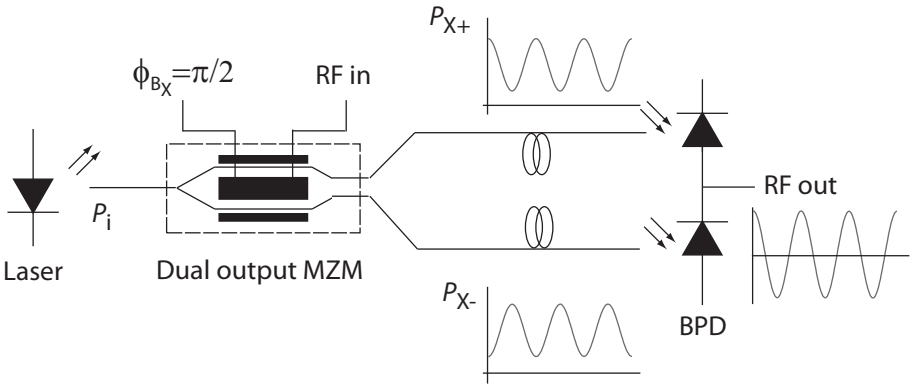


**Figure 3.15:** A schematic of the dual-output MZM link.

signals add up at the BPD output, signal power enhancement of 6 dB relative to the case where only one modulator output is used can be expected [47, 155].

Since introduced in by Ackerman et al. in 1993 [154], the scheme with dual output modulator and a balanced detector has been pursued numerously [43, 44, 47, 49, 150, 155–157, 166]. Notable results were obtained by Nichols et al. [157] that reported theoretical study of how to optimize the link performance, Williams et al. [44] that showed a high SFDR of 119.1 dB.Hz$^{2/3}$, and Islam et al. [150] that reported a 24 dB of RIN suppression and an SNR advantage of 23 dB relative to the case of single fiber link. Recently, McKinney et al. [49] reported a sub-10 dB link noise figure using x-coupled MZM with a low half-wave voltage (< 2 V at 2-12 GHz). Ackerman et al. [47] reported a link architecture which is suitable for multioctave bandwidth operation and demonstrated a noise figure of < 6.9 dB and a gain of > 17.0 dB across 6-12 GHz using this configuration.

To fully understand how these results can be obtained with the dual-output MZM link, let us consider the principle of operation of this APL. We start with the complementary outputs of the MZM,

$$P_{X\pm}(t) = \frac{P_i}{2L}\left(1 \mp \cos\left(\phi_B + \frac{\pi V_{RF}(t)}{V_{\pi,RF}}\right)\right) \tag{3.21}$$

Biasing the modulator at its quadrature point $(\phi_B = \pi/2)$ will result into equal modulated signals at each output but opposite in RF-modulation phase

$$P_{X\pm}(t) = \frac{P_i}{2L}(1 \pm \sin\theta(t)) \tag{3.22}$$

where we have defined $\theta(t) = \pi V_{RF}(t)/V_{\pi,RF}$ as we did in the case of Class-AB APL. Detection of these optical signals with a ideal (perfectly balanced) BPD with a re-

sponsivity of $r_{\mathrm{PD}}$, will yield a photocurrent of

$$\begin{aligned} I_{\mathrm{D,X}}(t) &= r_{\mathrm{PD}}\left[P_{\mathrm{X+}}(t) - P_{\mathrm{X-}}(t)\right] \\ &= \frac{r_{\mathrm{PD}}P_{\mathrm{i}}}{L}\sin\theta(t) \\ &= 2I_{\mathrm{av,PD}}\sin\theta(t) \end{aligned} \tag{3.23}$$

with $I_{\mathrm{av,PD}}$ is the average photocurrent per photodiode defined as

$$I_{\mathrm{av,PD}} = \frac{r_{\mathrm{PD}}P_{\mathrm{i}}}{2L}. \tag{3.24}$$

The ideal output current from the BPD thus contains no DC component and the RIN component associated with the DC current is completely cancelled [154, 155, 157]. However, this cancellation is limited by the power of the modulating signal [153, 166] and the intensity noise power at the output can be written as

$$p_{\mathrm{rin,X}} = \mathrm{RIN}\,BR_{\mathrm{L}}I_{\mathrm{av}}^2\left(S + 2\sin\theta(t)\right)^2 \tag{3.25}$$

where the quantity $S$ is related to the common-mode suppression factor (CMRR) of the BPD and accounts for imperfect amplitude and phase matching. Ideally $S = 0$ but typically the value will be between 0.1 and 0.01 [166]. While the RIN is cancelled at the output of the BPD, this is not the case for the shot noise. Similar as in the case of a Class-AB APL, the shot noise from the two photodiodes of the balanced detector adds up at the output yielding,

$$p_{\mathrm{shot,X}} = 4qI_{\mathrm{av}}BR_{\mathrm{L}} \tag{3.26}$$

Having defined the parameters of the dual-output MZM link, let us investigate the performance of such a link compared to the previously discussed APL types. For this purpose, we simulate the link gain, noise figure and $\mathrm{SFDR}_3$ of a single quadrature biased MZM APL, a Class-AB APL biased at $\pi/10$ and a dual-output MZM link. All links used modulators with the same half-wave voltage and insertion loss values. The BPD CMRR is taken to be 30 dB and the responsivity is 0.75 A/W. We plot the link gain, noise figure and $\mathrm{SFDR}_3$ as functions of the average photocurrent (per photodiode in case of balanced detection scheme) in Figure 3.16 (a), (b) and (c), respectively. We observed that the link gain of the X-coupled MZM link is 6 dB higher compared to the single MZM, which is expected. The noise figure of this link is better compared to the single link due to RIN cancellation. The noise figure improves with the increase of the photocurrent, indicating a shot noise limited performance. This is in contrast with the single MZM link that is RIN limited for high RIN, for example at RIN= $-155$ dB/Hz. The dual-output MZM also shows better $\mathrm{SFDR}_3$ for a given photocurrent, relative to the single MZM link (Figure 3.16 (c)). The best performance for a given photocurrent, however, is obtained with a class-AB APL. But keep in mind that since this is a low biased link, the same photocurrent as in the other two links will require a much higher input optical power in the case of the class-AB link. For example, a photocurrent of 6.3 mA requires an input optical power of 1 Watt. It is also important to note that in their ideal operations, these links can be used in multioctave bandwidth operation.

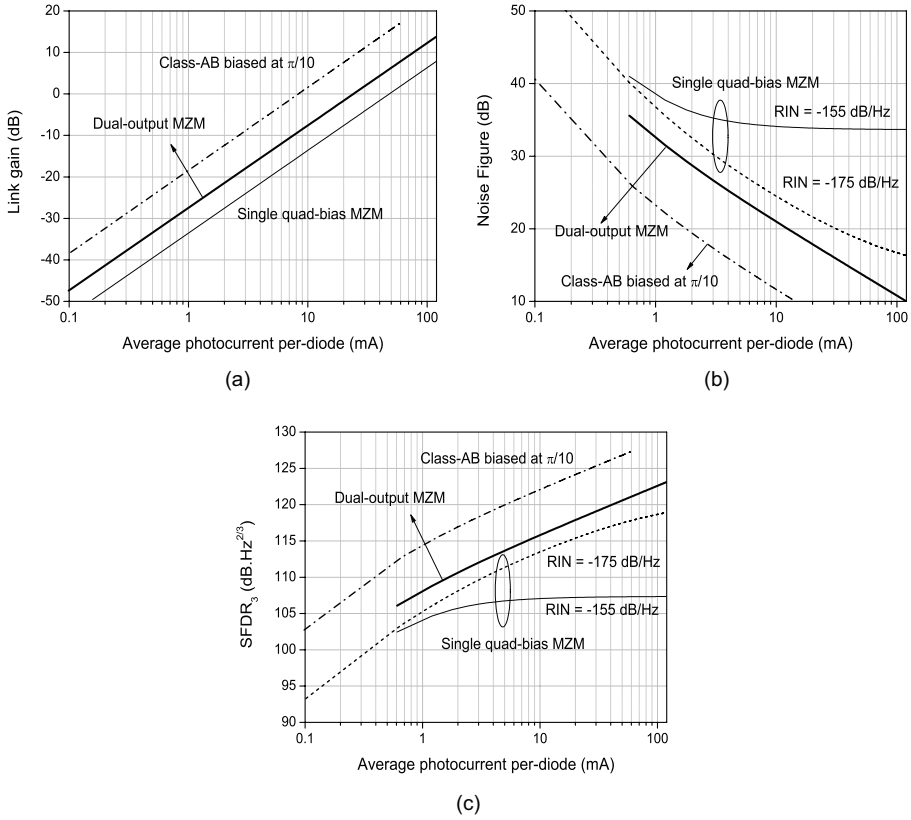


**Figure 3.16:** (a) Link gain, (b) noise figure and (c) SFDR comparisons for three different link architectures (single MZM, class-AB and dual-output MZM) as functions of the average photocurrent per-photodiode.

### 3.2.8 Linearization Schemes

So far we have seen the techniques to increase the performance of an APL. Primarily these techniques rely on either increasing the signal power (i.e. reducing the link loss) and/or reducing the noise power. Thus, the aim of these techniques is actually reducing the noise figure of the link. We have seen that for the link SFDR, there are two bounds that limit its value. The lower bound is imposed by the noise and the upper bound is imposed by link nonlinearity. This is evident if we examine Equation (3.27) where the intercept points and the noise figure clearly define the dynamic range. Thus the aim of the previous techniques discussed here is to reduce the noise figure such that the lower bound of the dynamic range is relaxed. However, a trade-off might occur such that these efforts to reduce the noise figure come with the expense of increased nonlinearities and reduced bandwidth, like in the case of low biasing which reduces the noise figure but limits the usable multi-

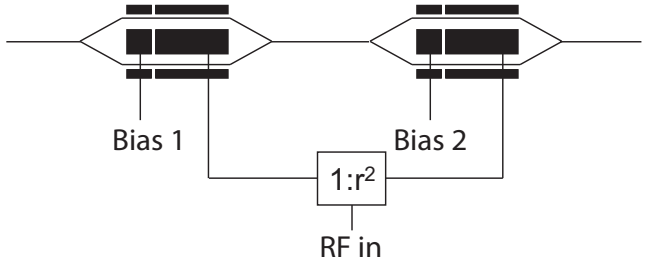


**Figure 3.17:** A linearization technique proposed by Betts [168]. The link has a high sub-octave SFDR due to minimization of third-order distortion.

octave dynamic range because it reduces the IIP2.

$$\mathrm{SFDR}_n = \frac{n-1}{n}\left(\mathrm{IIP}n - \mathrm{NF} + 174\right). \tag{3.27}$$

Clearly from Equation (3.27), the SFDR can also be increased by pushing the upper boundary by means of increasing the input intercept point (IIP$n$). This can be done by suppressing distortion terms such that larger RF signals can be transported by the link without any measurable distortion. As a matter of fact, we have discussed a type of linearization in the previous sections, when we discussed about the balanced detection scheme. Recall that in the ideal balanced detection scheme, even-order distortions are completely suppressed. This scheme has been extended even further for even-order distortion cancellation generated in the photodetectors [167]. In this part we will briefly review various linearization techniques that have been implemented in an MZM APL and discuss their impact on the link SFDR.

According to [17], linearization techniques can be divided into two categories, namely the primarily electronic and primarily optical techniques. An example of the primarily electronic schemes is the so-called pre-distortion technique. The idea of a pre-distortion is that if the nonlinear transfer function of the modulation device is well-known, a circuit with the inverse of this nonlinearity can be inserted prior to the modulation device such that the cascade of the circuit and the modulation device has a more linear transfer function. This technique has been applied in various modulation devices, notably in a directly modulated laser [169], a Mach-Zehnder modulator [170] and in an electroabsorption modulator (EAM) [171], where improvements on the link linearity have been reported. However, details on this pre-distortion technique is beyond the scope of this thesis.

The second linearization category is the primarily optical method. The idea is to use a combination of modulation devices, either in serial or parallel, and to select their parameters such that the transfer function of this combination is more linear compared to an individual device. This technique is almost exclusively applied in an externally modulated link. Here, we will discuss a linearization method that has been applied in an MZM APL. Note that the purpose of our discussion here is not to go into detail of the technique but rather to give an impression of the idea that has driven it and how it was applied. The method was proposed by Betts [168] in

1994. It consists of serially cascaded MZMs, as shown in Figure 3.17 . With this arrangement, a very high sub-octave SFDR of 132 dB.Hz$^{4/5}$ has been demonstrated. This remains one of the highest SFDR values ever shown with an MZM link. In a regular MZM, the second-order distortion is nulled at the quadrature bias point (90$^o$ bias angle). The null for the third order distortion, however, coincides with the null of the desired signal. For narrowband (sub-octave) applications, second-order distortion is not important and a scheme that minimizes the third-order distortion is desirable. This scheme uses the serial combination of MZMs to attain this minimization. There are three degrees of freedom in such link; the two biases of the MZMs and the power coupling ratio of the RF signal supplied to the modulators, denoted as $r$ in Figure 3.17 (b). For simplicity, the bias angles of the modulators are tied together, and $r$ is set to 1 [17]. With this arrangement, a minimized third-order distortion at bias angle of 104.8$^o$ was achieved. This is very advantageous since the bias point that minimized this distortion term is moved away from the null of the signal. With this approach, an SFDR improvement of 23 dB relative to the single modulator case has been shown. Detailed descriptions of the work can be found in [17, 168, 172].

Linearization of MZM APLs is a well-studied topic and various techniques have been proposed over the years. Some of the techniques that receive a lot of attention is the dual-parallel MZMs technique that uses the third-order distortion of one of the modulators to cancel the distortion of a so-called "primary" modulator. This technique was proposed by Korotky et al. [173] in 1990 and optimized by Brooks et al. [174] in 1993. Another technique uses a serial cascade of three MZMs to suppress both third and fifth-order distortions [175]. The predicted SFDR values of various linearized links were investigated in [176] while the bandwidths, taking into account the degrading effects of finite transit time and optical and electrical velocity dispersion were studied in [177]. In [133], Schaffner et al. investigate the performance of such linearized APLs when cascaded with pre and post amplifiers.

## 3.3 Direct Modulation

In the previous section, we have reviewed various techniques to increase the performance of an externally modulated link with an MZM. Here we will discuss the techniques applied in a directly modulated laser (DML) APL. Compared to the MZM links, efforts to enhance the DML link are very limited. This is because MZM link performance can be "easily" increased by varying system parameters which are directly accessible to a link engineer, such as modulator bias voltage or the input optical power. As we will see later, this is not the case for the DML link, in which fewer system parameters can be tuned to optimize the system. Most efforts to optimize such links are thus directed towards device level optimizations. For example, using an injection-locked laser to increase its modulation bandwidth [178], to reduce the RIN and enhance the SFDR [179] or to reduce nonlinearities [180]. This kind of technique is beyond the scope of this thesis. This is one reason why this section will considerably be shorter than the section on MZM links. Another reason is that the techniques that involve optimizations of system level parameters to enhance

the DML link performance will be discussed in detail in Chapter 4 and Chapter 5 of this thesis. Thus, this section mainly will serve as an introduction to such efforts.

### 3.3.1 Link Gain Enhancement

Recall that in general the link performance can be improved by means of increasing the input optical power to the modulator. The APL link gain and, depending on the dominant noise term, the noise figure and the SFDR increase with this optical power. However, this premise does not apply in the case of directly modulated laser (DML) link. Increasing the optical power from the laser by means of increasing the injection current will not increase the modulated signal power, but only increases the average DC optical power. As discussed in the previous chapter, the link gain of a DML link depends only on the laser slope efficiency and the photodetector responsivity. These parameters, unlike the optical power in an MZM link, are native to the components used in the link. This means that they are fixed once the component selection has been done.

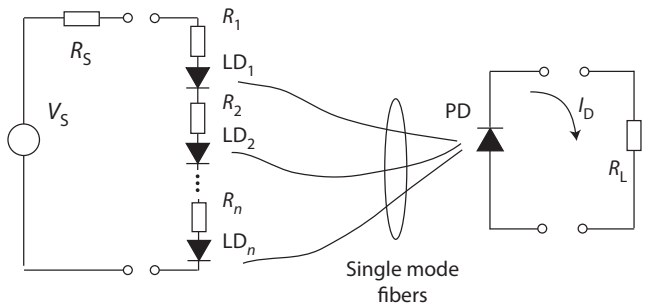


**Figure 3.18:** Directly-modulated analog link with series-connected lasers [181].

Only limited progress have been reported in the efforts of increasing the gain of a DML link. A promising way is to use the so-called cascaded lasers [181, 182]. The idea is that using a series connection of lasers (Figure 3.18), the slope efficiency of the connection is equal to the sum of the individual slopes and hence, will increase the link gain. The first demonstration using discrete butterfly-packaged components were shown in [181], in which a link gain of 3.8 dB was obtained with a cascade of six lasers. In the demonstrator, the fiber outputs of all six lasers were arranged to fall on a common, large area photodiode, i.e. no fiber coupler was used. The reported combined slope efficiency of these lasers is 1.89 W/A. Moreover, the measured noise figure for this link is 17.8 dB, a 6 dB reduction relative to the case of a single laser. This is because the RINs from the individual lasers in the cascade add up incoherently. However, the demonstration was severely limited in bandwidth (60 MHz relative to individual components bandwidth of 3 GHz) due to parasitics effect of the laser connection. This in fact, dictates monolithic integration of the laser cascade. The notable effort for such integration was reported in [182]. Analog modulation characterization of a three-stage laser shows promising results,

yielding a link gain of approximately 0 dB and an $SFDR_3$ of 119.6 $dB.Hz^{2/3}$ at the two-tone frequencies of $500 \pm 1$ MHz. These results are promising especially if the modulation bandwidth of these lasers can be increased into the multi-gigahertz region.

### 3.3.2 Low Biasing

As observed with an MZM link, low biasing of the modulation device can reduce the DC optical power to the photodetector. This gives two advantages, which are avoiding the photodetector saturation and reducing the link noise power. In DML link, low biasing is rarely pursued. In such a link, the typical detected photocurrent is relatively low and unlikely to saturate the photodetector. Moreover, unlike in the MZM link, low biased DMLs suffer from enhanced RIN, which power spectral density is inversely proportional to the cubic of the ratio between the bias and the threshold currents [183]. This effect, in turn, will impose a massive limitation on schemes relying on low biasing the DML for noise reduction [184, 185]. The significant RIN enhancement (as high as 40 dB) overshadows the advantage of having a lower detected photocurrent that gives lower shot noise [186]. This will be discussed further in Chapter 5.

Although turned out to be not promising for noise reduction, low biasing the DMLs have been used for the purpose of low-cost upconversion of digital radio signals [187, 188]. In this technique, the laser is biased close to the threshold current. The motivation behind this technique is the fact that DML is limited in modulation bandwidth that restrict the frequency of the modulating signal. By recognizing that the region close to the laser threshold is highly nonlinear [186], the low-biased DML can be used as a mixer and an upconveter. In this case the DML is modulated with either a baseband digital signal or a modulated intermediate frequency (IF) carrier and an RF local oscillator (LO) frequency. The result is a modulated carrier at the frequency of the sum of the IF and LO frequencies. This technique has been used to up convert a 10-Msymb/s QPSK signal to 3.1 GHz, using both a DFB laser [187] and a vertical-cavity surface emitting laser (VCSEL) [188].

### 3.3.3 Dual Laser and Balanced Detection Scheme

The balanced detection scheme in DML link was intially proposed in 1992 by Ogawa et al. [189]. In this paper the authors proposed a scheme using a pair of laser diodes and a pair of photodetectors, as shown in Figure 3.19. Microwave components like an in-phase combiner and an out-of phase divider are used to specify the phase relation of the upper and the lower arms of the link such that certain components of the signal are retained and others are suppressed. Ogawa et al. used this principle to cancel the fundamental signal and odd-order distortions and to retain the even-order distortion components. Thus, this link is mainly directed as an upconverter, generating the second-harmonic of the modulating RF signals. The objective is to increase the DML modulation bandwidth beyond the relaxation frequency.

In 2000, Pappert et al. [87] use the similar scheme to show an improvement of

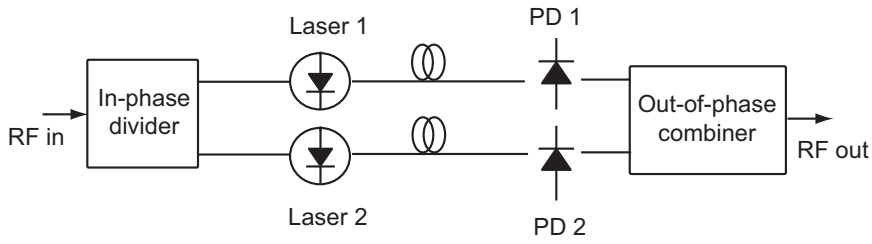


**Figure 3.19:** A dual laser and detector scheme proposed in [189] to increase the laser modulation bandwidth by means of generating second-order distortion. A similar arrangement is later used in [87] and in [159] for SFDR enhancement.

dynamic range for multioctave purpose at the frequency up to 1 GHz. In contrast with the work in [189], the configuration was used here to suppress the even order distortions to increase the operation bandwidth of the link, which was initially limited to sub-octave applications. Recently we revisited the scheme and showed one of the highest multioctave SFDR ever shown with DML at the frequency of 2.5 GHz [159]. The principal and the measurement results of this scheme will be discussed in detail in Chapter 5.

## 3.4 Summary

In this chapter the techniques to increase the performance of analog photonic links have been presented. For external modulation with MZM, generally increasing the input optical power to the modulator will increase the link performance, notably in terms of the link gain. However, high optical power at the modulator input will result in a high average photocurrent that might saturate the detector. Besides, this average current will directly contributes to APL noise. A low biasing scheme can be a solution to this limitation. In general for a given modulator characteristic, an optimum bias operation which minimizes the link noise figure can be determined, taking into account the input optical power and the laser RIN level. Although attractive from the noise figure point of view, low biasing increases second-order distortion, preventing the link to be applied in multioctave systems. A class-AB architecture using dual MZMs and balanced detection scheme can be used to mitigate this problem. Besides this scheme, dual-output MZM with balanced detection scheme is also promising to provide very high link performance. The comparisons of these techniques is summarized in Table 3.1. Besides optimization by means of noise figure reduction, linearization techniques have been well explored for MZM links. A very high SFDR can be achieved with such technique, although limited to sub-octave bandwidth. In contrast to external modulation, techniques to increase the performance of a directly modulated link are rather limited with most of them directed towards device-level improvements. Notable schemes such as cascaded lasers to increase the link gain and dual-laser plus a balanced detection schemes to

**Table 3.1:** Comparison of different schemes in MZM APL

| Schemes | Bandwidth | Advantage | Limitation |
|---|---|---|---|
| Single MZM<br>Quadrature biased | Multioctave | – Simple | – Large noise<br>– Large photocurrent |
| Single MZM<br>Low biased | Sub-octave | – Low noise<br>– Low photocurrent | – Sub-octave<br>– Needs high power |
| Dual MZM + BPD<br>(Class-AB) | Multioctave | – Reduced shot noise<br>– Cancelled RIN<br>– Low photocurrent | – Needs high power<br>– Precise matching<br>– Bias control |
| Dual-output MZM<br>+ BPD | Multioctave | – Cancelled RIN | – Precise matching |

increase the SFDR have been discussed. Unlike in an MZM link, low biasing in DML link is not promising to reduce the link noise due to RIN enhancement near threshold. It is, on the other hand, attractive for mixing and upconversion of baseband and IF signals.

# 4

# Balanced Modulation and Detection Scheme

## 4.1 Introduction

In this chapter a scheme to increase the performance of a directly-modulated laser APL is proposed. The scheme is called the balanced modulation and detection (BMD) APL and it consists of a pair of low-biased directly modulated laser diodes in combination with a balanced photodetector (BPD). The characteristics of such an APL are investigated thoroughly, both theoretically and experimentally and the results are presented in this chapter. The rest of the chapter is organized as follows: In the second section the limitation in a conventional directly modulated laser link is presented. This serves as the motivation to pursue the so-called balanced modulation and detection scheme, which is introduced and discussed in the third section. The realization and characterizations of the BMD link are presented in the fourth section. Measurements of key parameters, such as the link gain, noise, intermodulation distortions and spurious-free dynamic range are presented and discussed. Finally the chapter closes with a summary.

## 4.2 Limitation of a Conventional DML Link

In a conventional directly modulated laser (DML) link, the diode laser is biased at its most linear point, i.e. midway of its L-I curve. This is done in order to accommodate both small and large modulating signals, as indicated in Figure 4.1 (a). If, for example, the bias point is lowered towards the threshold current ($I_{\mathrm{th}}$), large mod-

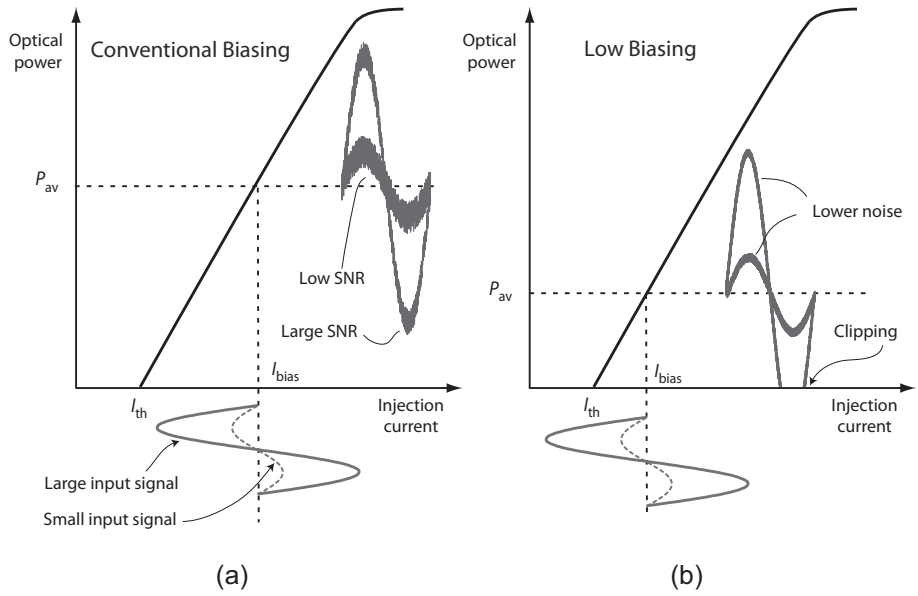


**Figure 4.1:** Biasing schemes for a laser diode. Conventional biasing (a) will prevent signal clipping but yields larger average optical power. Low biasing (b) clips large signals but promising to reduce the noise in the link.

ulating signal will be clipped, as illustrated in Figure 4.1 (b). In this case, a part of the modulating signal falls in the region below the threshold current that, from the emitted optical power point of view, corresponds to the region of spontaneous emission rather that the desired stimulated emission [31, 122]. This clipping will induce rather severe distortions of the resulting optical signal. But apart from the clipping, low biasing will result in a lower average optical power, as evident from Figure 4.1 (b). Recall from the discussion of APL noise (Chapter 2 Section 2.3) that shot noise and RIN are respectively linearly and quadratically proportional to this average optical power. Thus, low biasing is attractive to reduce this average power and, subsequently, reducing these dominant noise powers. This is especially attractive in the case where the modulating signal is small. In the conventional biasing, both small and large input RF signals will suffer from the same noise power, which is relatively large for large average optical power. Hence, the signal-to-noise ratio (SNR) for large input RF signal is high but low for small input RF signal (Figure 4.1 (a)). If the link is low biased instead, the same input signals will have improved SNR due to the lower noise from the reduced average optical power (Figure 4.1 (b)). In order to illustrate this, let us consider this following example.

**Example 4.1**
Consider a DML link with a diode laser with $s_{LD} = 0.32$ W/A and $I_{th} = 10$ mA. This laser is biased at $I_{bias} = 60$ mA, which is midway of the L-I curve and a current sig-

nal with the amplitude of 6.3 mA is applied on top of this bias current. Assuming a (single frequency) sinusoidal modulating signal, this current will deliver an RF power of 0 dBm to a 50 ohm load. The resulting optical signal from the laser is detected by a photodetector with a responsivity of 0.75 A/W. If the optical loss in the system amounts to 1 dB and the detector is resistively matched, the resulting signal power in this case is -20.4 dBm. The average optical power detected by the detector is 12.7 mW, resulting in an average current of 9.53 mA. If the laser RIN at the given bias point is -162 dB/Hz, the total noise power at the output, comprising the thermal noise, shot noise and the laser relative intensity noise, according to Equation (2.44) is -159.4 dBm/Hz. The SNR per-hertz bandwidth is thus 139 dB (1 Hz).

If the bias current is lowered to $I_{\text{bias}}$ = 20 mA instead, an RF signal with the same power can be transmitted over the link without any clipping. However, the average optical power now reduces to 2.54 mW. Since the signal power in a DML link is independent of the emitted optical power, the received RF signal power in this case remains unchanged, which is -20.4 dBm. The noise power, however, is reduced because the shot noise and the laser relative intensity noise are, in a respective way, linearly and quadratically proportional to the received average optical power. In this case, *assuming that in this bias point the RIN value remains the same* (-162 dB/Hz), the noise PSD reduces to -168.3 dBm/Hz. This will improve the link SNR to 147.9 dB (1 Hz). Note that in this link, the largest input power that can be accommodated by the link without any clipping is roughly 4 dBm.

From the example above, we can see that low biasing is highly attractive to improve the link SNR, especially in the region where the modulating signal is small. In the next section, we propose a scheme that is based on this premise and aimed at increasing the performance of a DML link.

## 4.3 The BMD Scheme

In Figure 4.2, the schematic of the so-called Balanced Modulation and Detection (BMD) APL is presented. The link consists of a pair of laser diodes (LDs) with a common input. These lasers are biased at their threshold currents and a sinusoidal RF signal is applied at the input. When the signal is positive, the lower LD is conducting and a positive half cycle of the sine wave is launched at the lower arm of the APL while no light is launched at the upper arm. When the signal is negative, the upper LD will conduct and the negative half cycle is launched at the upper arm. The optical signal in each arm comprises a half-wave-rectified version of the modulating signal. At the balanced receiver, the signal is restored by means of a differential detection scheme.

Hence, with this scheme the modulating RF signal is deliberately clipped (i.e. half-wave rectified) in a controlled manner such that it can be restored upon balanced detection. The half-wave rectification has two main effects. Firstly, each photodetector in the BPD receives no light if there is no modulation. Secondly, the average optical power in each detector is proportional to the RF power of the

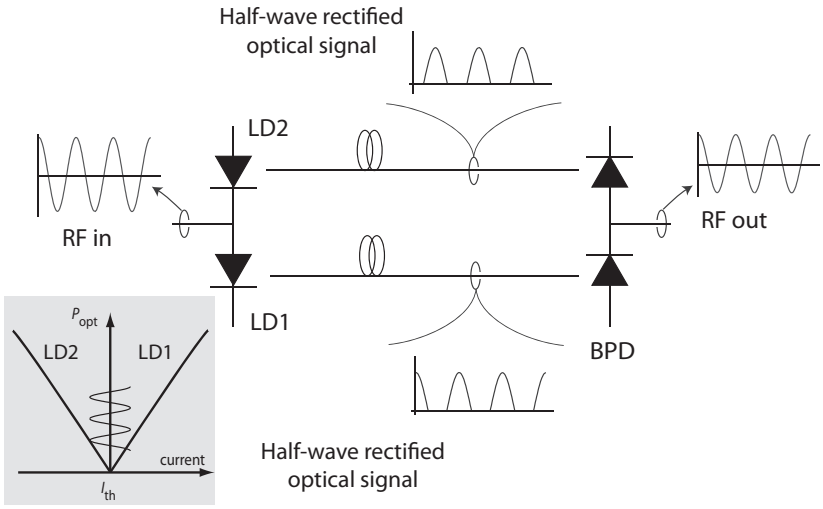


**Figure 4.2:** A schematic of the BMD scheme. The laser diodes (LDs) are biased at their threshold and connected in a way such that a modulating RF signal will yield a pair of complementary half-wave rectified optical signals which will be restored in the balanced photodetector (BPD).

modulating signal. These characteristics of the BMD scheme are in contrast with the conventional DML scheme where the existence of a bias current will result in a (DC) average optical power at the detector regardless of the modulating signal.

Let us examine the expression of the modulated optical power in this scheme. We assume a single tone modulation where the signal current to the laser can be written as

$$I_{\text{sig}}(t) = I_{\text{m}} \cos(\omega_1 t) . \tag{4.1}$$

where the current amplitude $I_{\text{m}}$ is related to the RF power of the modulating signal, $p_{\text{in}}$, and the source impedance, $R_{\text{S}}$, via the relation

$$I_{\text{m}} = \sqrt{\frac{2\, p_{\text{in}}}{R_{\text{S}}}} . \tag{4.2}$$

This signal is driving the two laser diodes (LD1 and LD2) which are biased at their threshold points. The L-I characteristics of these lasers are assumed to be ideal, i.e., we assume that they are perfectly linear and the emitted optical power is zero if the lasers are driven below their threshold. Additionally, we assume that the lasers have the same threshold current. Thus, in general, the output optical power, $P_{\text{LD}}(t)$ under any modulation $I(t)$ can be written as

$$P_{\text{LD}}(t) = \begin{cases} s_{\text{LD}} I(t), & \text{if } I(t) \geq I_{\text{th}} \\ 0, & \text{if } I(t) < I_{\text{th}} \end{cases} \tag{4.3}$$

where $s_{\mathrm{LD}}$ is the laser slope efficiency and $I_{\mathrm{th}}$ is the threshold current.

Thus, the resulting optical powers from LD1 and LD2 under the current modulation in Equation (4.1) can be written as

$$P_{\mathrm{LD1}}(t) = \begin{cases} \left| s_{\mathrm{LD1}} I_{\mathrm{sig}}(t) \right|, & \text{if } nT \le t \le (n+\frac{1}{2})T \\ 0, & \text{if } (n+\frac{1}{2})T \le t \le (n+1)T \end{cases} \tag{4.4}$$

$$P_{\mathrm{LD2}}(t) = \begin{cases} 0, & \text{if } nT \le t \le (n+\frac{1}{2})T \\ \left| s_{\mathrm{LD2}} I_{\mathrm{sig}}(t) \right|, & \text{if } (n+\frac{1}{2})T \le t \le (n+1)T \end{cases} \tag{4.5}$$

where $T = 2\pi/\omega$ is the period of the modulating signal and $n = 0, 1, 2...$ is an integer. Here we have assumed a general situation where the lasers have two different slope efficiencies, $s_{\mathrm{LD1}}$ and $s_{\mathrm{LD2}}$. The optical signals in Equations (4.4) and (4.5) are detected in the balanced detector, where the photodiodes responsivities are $r_{\mathrm{PD1}}$ and $r_{\mathrm{PD2}}$. Assuming that there is no optical loss in the APL, the average photocurrent from each photodiode can be written as

$$\begin{aligned} I_{\mathrm{av}\,k} &= \langle r_{\mathrm{PD}k} P_{\mathrm{LD}k}(t) \rangle \\ &= \frac{1}{2\pi} r_{\mathrm{PD}k} s_{\mathrm{LD}k} I_{\mathrm{m}}; \quad k = 1, 2 \end{aligned} \tag{4.6}$$

where the factor $1/2\pi$ appears from averaging of the half-wave rectified signal, i.e.,

$$\frac{1}{T} \int_0^{T/2} \cos(\omega t)\, \mathrm{d}t = \frac{1}{2\pi}. \tag{4.7}$$

The average photocurrent per photodiode will later on determine the noise power in the link. The output signal power, however, depends on the photocurrent at the BPD output, which is simply the difference of the photocurrents from the two photodiodes,

$$I_{\mathrm{BMD}}(t) = r_{\mathrm{PD1}} P_{\mathrm{LD1}}(t) - r_{\mathrm{PD2}} P_{\mathrm{LD2}}(t). \tag{4.8}$$

Now, if we consider an ideal case where $r_{\mathrm{PD1}} = r_{\mathrm{PD2}} = r_{\mathrm{PD}}$, $s_{\mathrm{LD1}} = s_{\mathrm{LD2}} = s_{\mathrm{LD}}$ and the length of the two optical fibers going to the BPD are perfectly matched, we can re-write the output photocurrent of the BPD as

$$I_{\mathrm{BMD}}(t) = r_{\mathrm{PD}} s_{\mathrm{LD}} I_{\mathrm{m}} \cos \omega t \tag{4.9}$$

and the average current per photodiode as

$$I_{\mathrm{av}} = \frac{1}{2\pi} r_{\mathrm{PD}} s_{\mathrm{LD}} I_{\mathrm{m}}. \tag{4.10}$$

Half of the current in Equation (4.9) will be delivered to a load resistance if a resistive matching scheme is imposed at the BPD. The resulting RF signal power can be calculated following the steps in Subsection 2.4.5 of Chapter 2, which will yield

$$\begin{aligned} p_{\mathrm{fund,BMD}} &= \frac{1}{4} \left\langle I_{\mathrm{BMD}}^2(t) \right\rangle R_{\mathrm{L}} \\ &= \frac{1}{4} r_{\mathrm{PD}}^2 s_{\mathrm{LD}}^2 \frac{R_{\mathrm{L}}}{R_{\mathrm{S}}} p_{\mathrm{in}} \end{aligned} \tag{4.11}$$

which is similar to the one obtained from the previous result obtained from a conventional DML link in Chapter 2.

As mentioned earlier, the noise power depends on the average current per photodiode. Both the shot noise and the RIN contributions from the two photodiodes adds up at the BPD output. These additions stem from two different reasons. The shot noises of the photodiodes are statistically independent of each other because they are generated by two different photon streams. The RIN contributions of the individual lasers, averaged over the full signal period of $T$, also add up because they come from two different lasers, in which the intensity fluctuations of one laser is independent of the other. The total shot noise power (see Equation (2.34) of Chapter 2) in noise bandwidth of $B$ Hz thus can be written as

$$\begin{aligned} p_{\text{shot,BMD}} &= \frac{1}{4} 2q \left(I_{\text{av1}} + I_{\text{av2}}\right) R_{\text{L}} B \\ &= \frac{1}{4\pi} r_{\text{PD}} s_{\text{LD}} I_{\text{m}} R_{\text{L}} B \end{aligned} \tag{4.12}$$

where we have used $I_{\text{av1}} = I_{\text{av2}} = I_{\text{av}}$ and used the expression in Equation (4.10) to arrive to the second expression of Equation (4.12).

If the RIN (in dB/Hz) of LD1 and LD2 are $\text{RIN}_1$ and $\text{RIN}_2$, respectively, the total RIN power (see Equation (2.41) of Chapter 2) can be calculated as

$$\begin{aligned} p_{\text{RIN,BMD}} &= \frac{1}{4}\left(10^{\frac{\text{RIN}_1}{10}} I_{\text{av1}}^2 + 10^{\frac{\text{RIN}_2}{10}} I_{\text{av2}}^2\right) R_{\text{L}} B \\ &= \left(\frac{1}{2\pi}\right)^2 \left(10^{\frac{\text{RIN}_1}{10}} + 10^{\frac{\text{RIN}_2}{10}}\right) r_{\text{PD}}^2 s_{\text{LD}}^2 I_{\text{m}}^2 R_{\text{L}} B \end{aligned} \tag{4.13}$$

where again we have used the expression in Equation (4.10) for the average current per-photodiode

Note that the shot noise and RIN powers in Equations (4.12) and (4.13) depend on the amplitude of the modulating current, $I_{\text{m}}$ and subsequently on the input RF power, $p_{\text{in}}$, according to Equation (4.2). This is in contrast to the case of the conventional biasing. Supposed that the bias current of the laser is $I_{\text{bias}}$, the average photocurrent is

$$I_{\text{av,DML}} = r_{\text{PD}} s_{\text{LD}} \left(I_{\text{bias}} - I_{\text{th}}\right). \tag{4.14}$$

The signal power, the shot noise and RIN powers in the case of conventional biasing can thus be written as:

$$p_{\text{fund,DML}} = \frac{1}{4} r_{\text{PD}}^2 s_{\text{LD}}^2 \frac{R_{\text{L}}}{R_{\text{S}}} p_{\text{in}}, \tag{4.15}$$

$$p_{\text{shot,DML}} = \frac{1}{2} q\, r_{\text{PD}} s_{\text{LD}} \left(I_{\text{bias}} - I_{\text{th}}\right) R_{\text{L}} B, \tag{4.16}$$

$$p_{\text{RIN,DML}} = \frac{1}{4} 10^{\frac{\text{RIN}}{10}} r_{\text{PD}}^2 s_{\text{LD}}^2 \left(I_{\text{bias}} - I_{\text{th}}\right)^2 R_{\text{L}} B. \tag{4.17}$$

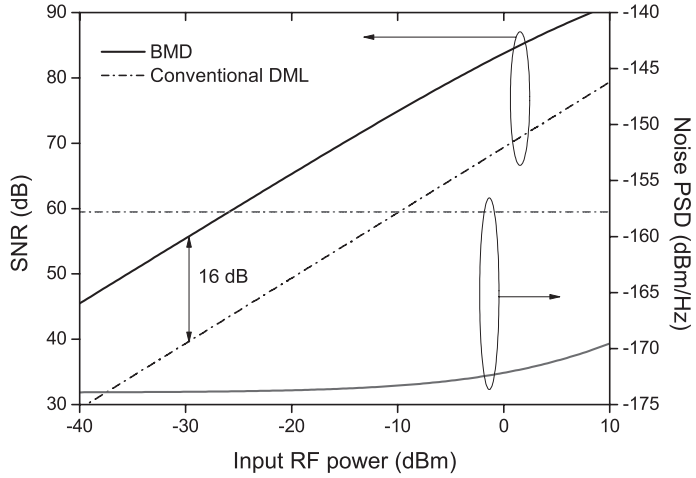


**Figure 4.3:** Simulated SNR enhancement obtained with the BMD link relative to the conventional DML link (left y-axis) and the corresponding noise PSD (right y-axis). The SNR is measured in 10 MHz noise bandwidth. The simulation parameters are listed in Examples 4.1 and 4.2.

Thus, for the conventional DML link, the shot noise and RIN powers are determined by the bias current instead of the modulation current. To fully understand the difference of the conventional DML link with the BMD APL, let us consider the following example.

**Example 4.2**
Supposed that a BMD link is constructed using a pair of identical laser diodes with parameters as follows: $I_{\text{th}} = 10$ mA, $s_{\text{LD}} = 0.32$ W/A, $\text{RIN}_1 = \text{RIN}_2 = -162$ dB/Hz. These lasers are biased at their threshold. The responsivities of the photodiodes in the BPD are assumed to be the same at the value is 0.75 A/W. The performance of such a link is then compared with a conventional DML link with parameters as used in Example 4.1, where the laser is biased at 60 mA. These links are compared in terms of their SNR, which is measured in a 10 MHz bandwidth and the result is depicted in Figure 4.3. An SNR improvement of 16 dB can be obtained with the BMD scheme.

This SNR improvement of the BMD link relative to the conventional link depends on the input RF power as well as the lasers RIN. This is illustrated in Figure 4.4, where the SNR for both the conventional link and the BMD link for three different input RF power levels are depicted as functions of the laser RIN. Two observations can be made from these results. Firstly, *given a RIN value*, the BMD scheme can achieve the same SNR as the conventional link with a lower input RF power. For example, with RIN of -156.3 dB/Hz, the SNR of 74.8 dB (1 MHz) can be achieved with an input power of 10 dBm in a conventional link while it takes only -10 dBm in the BMD link. Secondly, *given an input power level*, the performance in

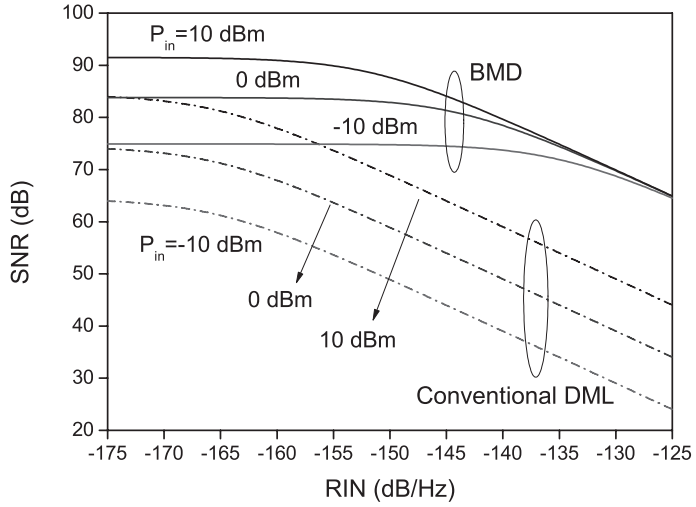


**Figure 4.4:** Simulated SNR for the BMD and the conventional DML links versus the laser RIN. The BMD link can achieve the same SNR as the conventional link with higher laser RIN.

terms of SNR for the conventional link can be realized by the BMD link using lasers with higher RIN. For example, the SNR of 74 dB (1 MHz) in the conventional link is obtained with a RIN of -175 dB/Hz while the BMD link can realize the same performance with RIN of -134.6 dB/Hz.

## 4.4 Realization of the BMD Link

### 4.4.1 Measurement Setup

From the previous section we have seen that the simulated performance of the BMD link is very promising. For this reason we proceed with the realization and the characterization of this link. The schematic of the realized BMD link is shown in Figure 4.5. The transmitter consists of a pair of DFB laser diodes (Fitel FOL13DDRB-A31-F03 and F04) with an emission wavelength of 1310 nm, a maximum output optical power of 16 mW and a modulation bandwidth of 4 GHz. These lasers (LD1, for the unit with "F03" as the last digits of the serial number, and LD2, for the "F04" unit) are mounted on a pair of laser diode mounts from ILX Lightwave (LDM-4984RF) with a modulation bandwidth of at least 2.5 GHz. The RF signals (two tones) are supplied to these lasers using a 2:1 RF combiner in conjunction with a 1:2 RF splitter. A pair of RF attenuators is placed in the RF paths going to the lasers to accommodate the difference in the lasers slope efficiencies and ensuring that the optical signals from the lasers have the same amplitude. An RF phase shifter

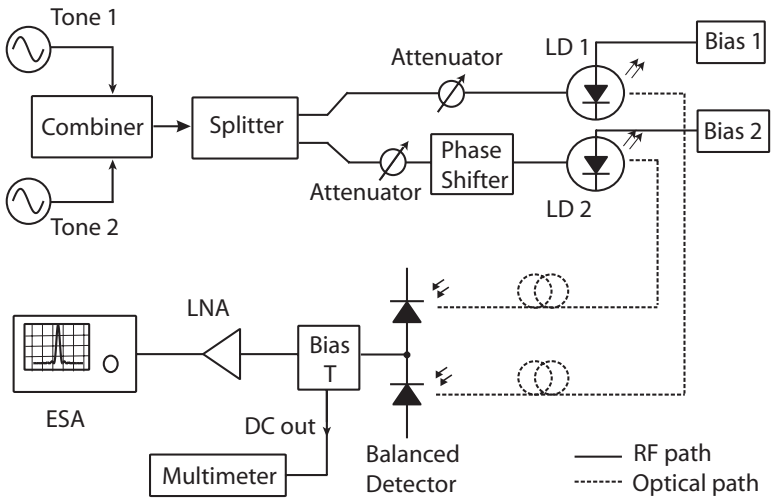


**Figure 4.5:** Experimental setup for the BMD link characterization.

(1 to 5 GHz) is used in one of the arms of the link to adjust the RF phase difference of the modulated optical signals. The complete arrangement of this transmitter is depicted in Figure 4.6.

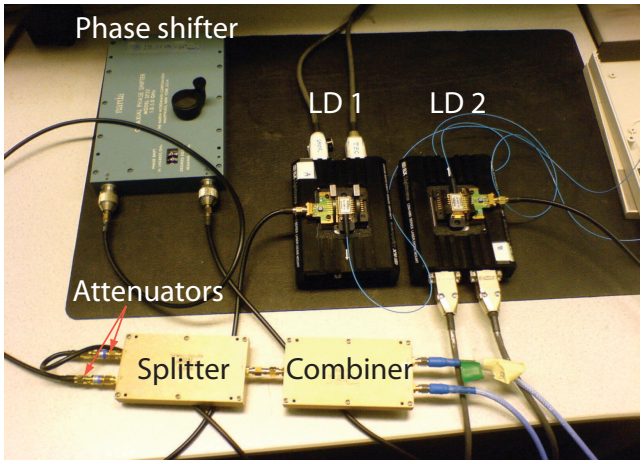


**Figure 4.6:** The transmitter in the BMD link. It consists of a pair of DMLs, an RF phase shifter and RF attenuators.

The optical signals from LD1 and LD2 are then detected at the BPD (Discovery Semiconductor DSC710) which has a 30 dB of common-mode rejection ratio (CMRR), a 10 GHz modulation bandwidth and a responsivity of 0.75 A/W at the

optical wavelength of 1310 nm. The output of the BPD is connected to a bias T (100 kHz to 14 GHz from Ortel), and the DC part of the photocurrent is detected with a multimeter while the RF part is detected with an electrical spectrum analyzer (ESA, HP 8593E). A low noise RF amplifier (Mini-Circuits ZRL-2400LN+) with a gain of 23 dB and a noise figure of 1.2 dB at 1 GHz is used during the noise measurement to reduce the ESA displayed analyzer noise level (DANL), which is simply the noise generated within the ESA itself [190]. For intermodulation distortion measurements, the amplifier is replaced by RF attenuators to minimize the internal distortion generated at the input mixer of the ESA.

### 4.4.2 Slope Efficiencies and Link Gain Measurements

Before actually operating the link in the BMD arrangement, each laser was characterized to get the information of their threshold currents and slope efficiencies. The injection currents of LD1 and LD2 were varied from 5 mA to 45 mA with a 1 mA step and the output optical power was measured with an optical power meter. The results are depicted in Figure 4.7. From these measurements, the threshold currents for LD 1 and LD 2 are determined to be 9.5 mA. The lasers however, have different slope efficiencies, which are calculated to be 0.32 W/A for LD1 and 0.37 W/A for LD2.

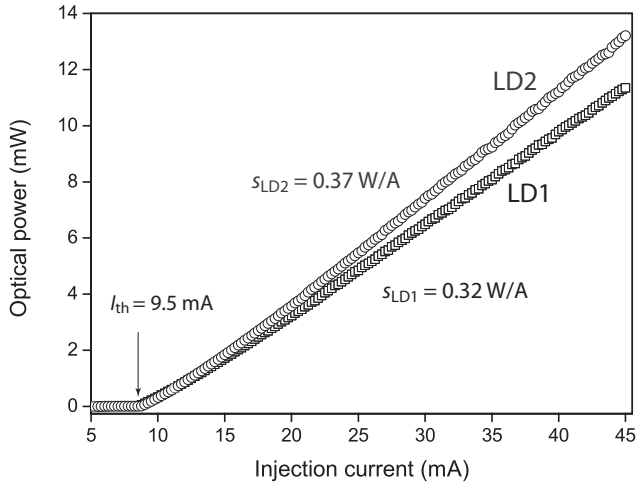


**Figure 4.7:** The measured L-I curve for the DMLs used in the BMD link.

For the link gain measurements, the measurement setup is slightly adjusted by removing both the 2:1 combiner and the 1:2 splitter, as well as the RF attenuators in order to eliminate additional loss from these components. The RF signal frequency was swept from 10 MHz to 5 GHz using a vector network analyzer (Agilent PNA 5230), with the signal power maintained at 0 dBm. The $S_{21}$ parameter (see Chapter 2 Section 2.2) is measured for each "individual" link, which can be obtained by

disconnecting the fiber connection of one of the APL arms from the balanced detector input. The measurements were repeated for various laser bias currents, namely 9.5 mA, 11 mA and 50 mA. The first two bias values correspond to low biasing while the third one represent the optimal operating point. The results are depicted in Figure 4.8. From these measurements, we can observe several phenomena. First of all, the modulation bandwidth of the laser depends on the bias current. The lasers biased at 9.5 mA yield much smaller modulation bandwidth, relative to the lasers biased at 50 mA. If we define here the 3-dB bandwidth as the frequency at which the response of the laser is half of its low-frequency response, the 3-dB bandwidths at bias currents of 9.5 mA for LD1 and LD2 are 970 MHz and 820 MHz, respectively. In contrast, the 3-dB bandwidths at 50 mA are approximately 3.75 GHz for both lasers. Note that these values are slightly lower than the modulation bandwidth of the laser (4 GHz) described in the datasheets. This can be attributed to the bandwidth limitation of the laser mounts.

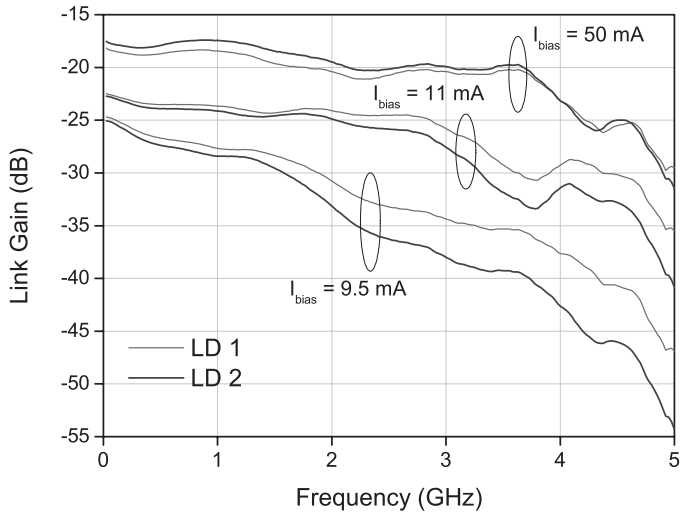


**Figure 4.8:** $S_{21}$ parameter of the individual links for various bias currents.

Beside the reduced bandwidth, low biasing exhibits a reduction in the measured $S_{21}$ response (i.e. the link gain). We believe that this can be attributed to the effects of slope efficiency reduction at the low bias region as well as the fact that low biasing causes some parts of the modulating signal current fall below the threshold and hence, inducing signal clipping.

Finally, a quick calculation reveals that the link gain obtained from these measurements matched the calculated link gain obtained from the (static) measurements of the laser L-I curve. According to Equation (2.17) of Chapter 2, the link gain for such DML link can be written as

$$g_{\mathrm{DML}} = \frac{1}{4}\left(\frac{r_{\mathrm{PD}}\, s_{\mathrm{LD}}}{L}\right)^2, \tag{4.18}$$

where $s_{LD}$, $r_{PD}$ and $L$ are the laser slope efficiencies, photodetector responsivity and the link optical loss, respectively. Using the the values of $s_{LD1}$ = 0.32 W/A, $s_{LD2}$ = 0.37 W/A, $r_{PD}$ = 0.75 A/W and assuming that the optical losses in the individual links are negligible, the calculated link gain for the LD1 and LD2 expressed in dB are -18.4 dB and -17.1 dB, respectively. These values agree very well with the values of -18.4 dB and -17.4 dB for the LD1 and LD2, obtained from the $S_{21}$ measurements at 1 GHz.

### 4.4.3 Noise Measurements

The link noise was characterized for the different LDs. The injection current of the lasers was varied from 8 mA to 50 mA with a step of 1 mA and for each step the total noise power spectral density (PSD) was measured with the ESA using the noise marker. The marker was positioned at the frequency of 1 GHz and the noise was measured in a 10 kHz noise bandwidth. The marker gave the measured noise power normalized in 1 Hz bandwidth, i.e., in dBm/Hz. The whole measurements were controlled and automated in LabVIEW.

As mentioned earlier, a low-noise RF amplifier (LNA) was used in the noise measurement due to the high DANL of the ESA. Without the LNA, the noise from the ESA will dominate over the APL noise that will be measured. The LNA amplified the APL noise above the DANL while at the same time contributed to an additional noise. Consequently, the measured noise power consists of the DANL, the link noise which is amplified by the LNA gain, and additional noise from the LNA itself. Suppose that $p_{SA}$ is the DANL in W/Hz, $p_{N,meas}$ is the measured noise PSD in W/Hz and $g_{LNA}$ is the LNA gain on linear scale, we can then express the total noise contribution from the photonic link itself as

$$p_N = \frac{p_{N,meas} - \left(p_{SA} + p_{LNA}\right)}{g_{LNA}}. \tag{4.19}$$

where $p_{LNA}$ is the LNA noise, related to the LNA noise factor, $F_{LNA}$ via the relation

$$p_{LNA} = g_{LNA}\, k\, T\, (F_{LNA} - 1)\,. \tag{4.20}$$

In the equation above, $k$ is the Boltzmann constant and $T$ = 290 K. The noise factor is related to the noise figure via the relation $NF_{LNA} = 10\log_{10} F_{LNA}$.

The link noise in Equation (4.19) consists of the shot noise, the thermal noise and the laser RIN. Suppose that the average photocurrent in the noise measurement is $I_d$ and the load resistance is $R_L$, we can write the noise PSD in W/Hz, just as described in Equation (2.44) of Chapter 2, as

$$\begin{aligned} p_N &= p_{th} + p_{shot} + p_{RIN} \\ &= \left(1 + g_{link}\right) kT + \frac{1}{4}\left(2qI_d + 10^{\frac{RIN}{10}} I_d^2\right) R_L. \end{aligned} \tag{4.21}$$

where $p_{th}$, $p_{shot}$ and $p_{RIN}$ are the thermal noise, shot noise and RIN PSDs in W/Hz and $g_{link}$ is the link gain, obtained from the measurements of the $S_{21}$ parameter, described in the previous section.

As mentioned earlier, the detected photocurrent was measured with a multimeter from the DC output of the bias T. Thus, substituting $p_N$ in Equation (4.21) with the expression in Equation (4.19), we can determine the RIN values of the lasers. This is illustrated in the following example.

**Example 4.3**
The LNA used in the measurements has the following characteristics: $G_{LNA}$ = 23 dB and $NF_{LNA}$ = 1.2 dB. Note that $G_{LNA}$ is simply the LNA gain $(g_{LNA})$ expressed in decibels. Thus, the total noise contribution from the LNA is −155.9 dBm/Hz, which can be calculated from Equation (4.20). The spectrum analyzer DANL is measured to be $P_{SA}$ = −146.5 dBm/Hz. The noise measurement was performed on the individual link with LD1, biased at $I_{bias}$ = 30 mA. The measured (amplified) noise PSD at this bias current at the frequency of 1 GHz was $P_{N,meas}$ = −135.7 dBm/Hz. Subtracting the DANL, the LNA gain, and the noise contribution of the LNA from this measured noise PSD as described in Equation (4.19), the link noise ($P_N$) is found to be −159.2 dBm/Hz. The measured photocurrent ($I_d$) for this bias point is 4.73 mA, yielding a shot noise power of −167.2 dBm/Hz while the thermal noise power is −173.9 dBm/Hz. The sum of the powers of these two noise sources amounts to −166.4 dBm/Hz. Subtracting this value from the total link noise will give the noise power contribution from the laser RIN ($p_{RIN}$ in Equation (4.21)), which amounts to −160.1 dBm/Hz. The resulting RIN, calculated from the third term of Equation 4.21 amounts to −154.6 dB/Hz. ■

The measured link noise PSD for LD1 and LD2 as functions of the injection current are depicted in Figure 4.9. The noise PSDs increase significantly around the threshold current and then reduce to almost a constant at a higher injection current. The LD2 shows a slightly higher noise relative to the the LD1. In the same figure, the calculated thermal noise PSD (dash-dotted line), the shot noise PSD (solid line) as well as the sum of of the thermal noise and the shot noise PSDs (dashed-line) for both lasers are also plotted. The shot noise PSD was calculated from the information of the measured detected photocurrent using the relation in Equation (2.34) of Chapter 2. It is evident that just above the threshold and beyond, the link noise PSD is not dominated by either the thermal noise nor the shot noise. Thus, we conclude that the dominating factor of the link noise is the laser RIN.

We proceed with determining the RIN for LD1 and LD2 for each bias current using the information of the measured noise PSD and the photocurrent, as demonstrated in Example 4.3. The results are shown in Figure 4.10. An extreme RIN enhancement at the threshold current was observed. The RIN at this region is roughly 55 dB higher relative to the RIN at high bias current (around 50 mA). This behavior can be explained by different models, notably the RIN expression which is developed from the rate equations [31, 32, 191]. However, this model requires information about the laser physical parameters, like the spontaneous emission factor or

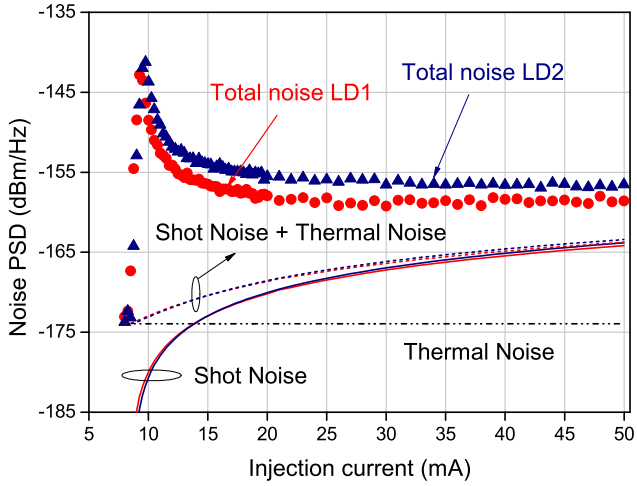


**Figure 4.9:** The measured total noise PSD for the individual links containing LD1 and LD2. Below the threshold the total noise is dominated by the thermal noise. Above the threshold, the laser RIN dominates.

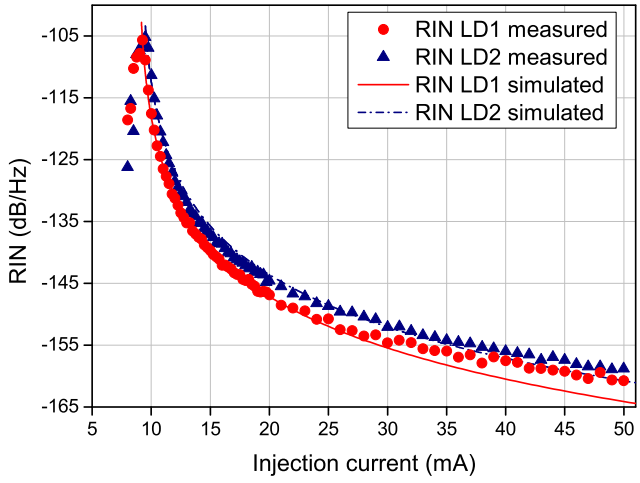


**Figure 4.10:** The RIN values for LD1 and LD2. The measured values were extracted from the total noise PSD measurements shown in Figure 4.9. The simulated values were obtained from the model in in Equation (4.22).

the laser dimensions, which most of the times are not available. Thus, the model is beyond the scope of this thesis. Instead, a simpler relation [183, 192] has been used here to model the RIN. It was initially published by Sato [192] to predict the relation

of rin* with the ratio of $I_{\text{bias}}/I_{\text{th}}$, for bias currents above the threshold. This relation can be written as:

$$\text{rin (1/Hz)} \propto \left(\frac{I_{\text{bias}}}{I_{\text{th}}} - 1\right)^{-3} \tag{4.22}$$

In order to verify this relation, we plotted the measured RIN in dB/Hz against the quantity $K = 10\log_{10}(I_{\text{bias}}/I_{\text{th}} - 1)$ and performed a linear curve fitting to the measured data. The results are shown in Figure 4.11. In the ideal case, where the relation in Equation (4.22) is fulfilled, the RIN in dB/Hz should exhibit a linear relation with $K$ with the slope of -3. Moreover, the relation in Equation (4.22) suggests that the RIN is proportional to $I_{\text{bias}}/I_{\text{th}}$. We call this proportionality factor $\alpha$ such that

$$\text{rin (1/Hz)} = \alpha\left(\frac{I_{\text{bias}}}{I_{\text{th}}} - 1\right)^{-3} \tag{4.23}$$

and consequently,

$$\text{RIN (dB/Hz)} = -3K + 10\log_{10}\alpha\,. \tag{4.24}$$

As evident from Figure 4.11, the slopes of the curves obtained from the linear fitting for LD1 (solid line) and LD2 (dash-dotted line) are -2.7 and -2.85, respectively. The proportionality factors, $10\log_{10}\alpha$ for these curve fits are no other than the curve intercepts which occur at $K = 0$. The values for LD1 and LD2 are -144 dB/Hz and -141 dB/Hz, respectively. We then insert these proportionality factors into Equation (4.24) to yield the simulated values of the RIN, which are shown in Figure 4.10 as the solid line for LD1 and the dash-dotted line for LD2. It can be seen that the measured RIN can indeed be approximated by the relation in Equation (4.22).

It is important to note here that the RIN enhancement around the threshold will impair the BMD link performance, which relies on the premise that by limiting the average optical power by means of low-biasing, the noise in the link can be significantly suppressed. We will return to this subject when we discuss the SNR and the SFDR of the BMD link.

### 4.4.4 Intermodulation Distortion Measurements

A two-tone test was used to characterize the nonlinearity in the APL. RF signals with two-tone frequencies $f_1$ = 1.0 GHz and $f_2$ = 1.01 GHz were supplied from a vector signal generator (Agilent E4438C) and a vector network analyzer (Agilent PNA N5230A). The fundamental signal, IMD2 and IMD3 powers are measured at the BPD output using an ESA at frequencies 1.0 GHz, 2.01 GHz and 1.02 GHz, respectively, corresponding to the frequencies $f_1$, $f_1 + f_2$ and $2f_2 - f_1$. In the measurements, the input attenuation of the ESA was adjusted such that there is no internal distortion generated at the ESA.

*the relative intensity noise expressed in 1/Hz, such that RIN = $10\log_{10}$ (rin)

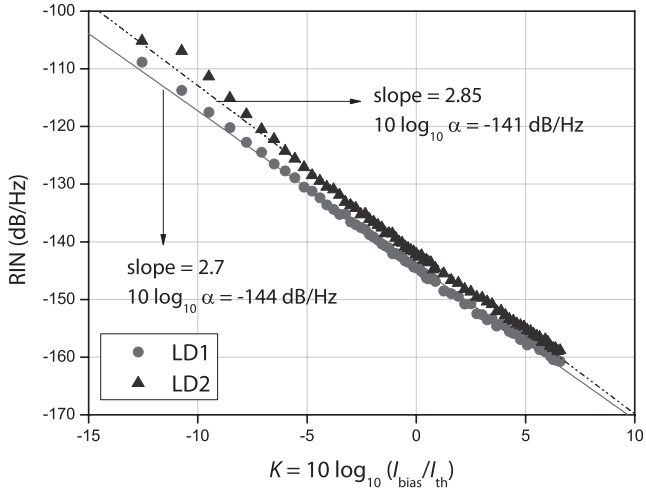


**Figure 4.11:** Curve fitting that shows the RIN dependence on the bias current as predicted in Equation (4.23).

The distortion characterizations started with the IMD measurements on the individual links, in order to determine their second-order and third-order input intercept points, IIP2 and IIP3, respectively. The RF power per tone was varied from -6 dBm to 10 dBm with a step 1 dBm and they were supplied to the 2:1 combiner and 1:2 splitter combination. The measured loss of this combination at 1 GHz amounts to approximately 8.5 dB. Thus, the RF power per tone delivered to the laser diode was actually varied from -14.5 dBm to 1.5 dBm. Note that the individual links, i.e., LD1 and LD2, were characterized independently. This means that in these measurements only one output of the 1:2 splitter was used, while the other output port was terminated with a 50 Ω load. The whole measurements process, i.e., adjusting the RF power and subsequently measuring the fundamental, IMD2 and IMD3 powers at their respective frequencies, were automated in LabVIEW.

The IMD measurement results for the individual links with LD1 and LD2 are shown in Figure 4.12 (a) and (b), respectively. In these figures, the output RF powers of the fundamental signal, the IMD2 and the IMD3 terms are plotted as functions of the input RF power per tone, all expressed in dBm. In these measurements, the LDs are biased at 50 mA, which is roughly midway of the range between their threshold current (9.5 mA) and the maximum bias current prescribed in their datasheets (100 mA). We have chosen this point in order to avoid any signal clipping that would have added significant distortion. Beside the measured values (indicated by circle, triangle and square markers for the fundamental signal, IMD2 and IMD3, respectively), we have plotted the extrapolations of these measurement results, showed as the solid, dashed and dash-dotted lines for the fundamental signal, the IMD2, and the IMD3, respectively.

The input RF power where the IMD power is equal to the fundamental signal

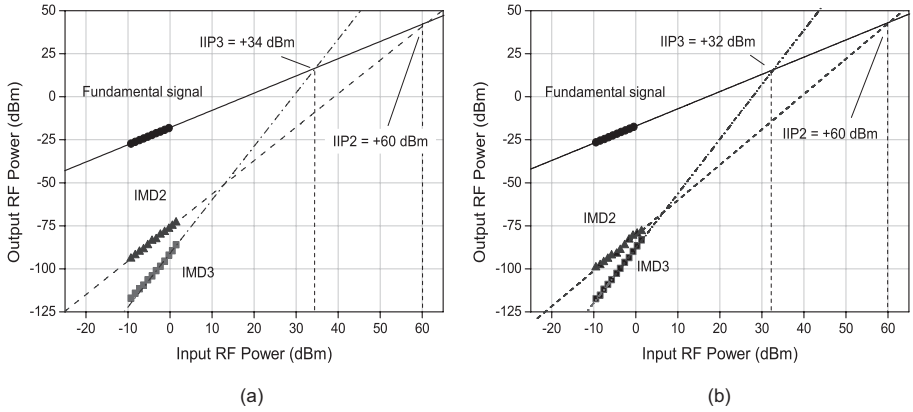


**Figure 4.12:** The measured fundamental signals and IMD terms and the extrapolated IIP2 and IIP3 values for (a) LD1 and (b) LD2.

power is defined as the input intercept point (IIP, see Chapter 2 Subsection 2.4.4). The IIP2 and IIP3 for LD1 are calculated to be +34 dBm and +60 dBm, respectively, while for LD2, the values are +32 dBm and +60 dBm, respectively. Thus, LD1 and LD2 have similar nonlinearity profiles, notably in second-order nonlinearity and a slight difference in third-order nonlinearity. Additionally, the calculated link gain for the individual links with LD1 and LD2 are -17.9 dB and -17 dB, respectively. These values agree very well with the directly measured values ($S_{21}$ parameter), presented in Subsection 4.4.2, which are -18.4 dB and -17.4 dB for LD1 and LD2, respectively.

After characterizing the individual links, we proceed with the characterization of the BMD link. Now both of the 1:2 splitter outputs are connected, each to the RF modulation inputs of the laser mounts that host LD1 and LD2. A pair of RF attenuators were used to equalize the link gain of the individual links, which is a result of the difference in their slope efficiencies. The RF phase shifter was inserted in the RF path of LD2 to adjust the RF phase of the two signals in the two arms of the APL, such that they arrive in a correct phase relation. The indicator for this phase adjustment can either be the maximum fundamental power at the BPD output or the minimum power of the IMD2. This is true because at the BPD output, the fundamental power contributions from each arm, being an odd function adds up while the IMD2, which are in phase, cancels. We have chosen to use the latter criterion since it is easier to observe in the measurement relative to the earlier.

The IMD characterizations were performed for several bias currents from 10 mA to 15 mA with a 1 mA step. In addition, the characterizations were also performed at two other points, namely bias currents of 9.5 mA and 20 mA. These points serve as the extremes of the measurements because at 9.5 mA, the link is virtually operating at the threshold. On the other hand, at 20 mA bias, it is expected that there is hardly any signal clipping because this bias is already high enough to accommodate the strongest signal supplied in the measurements. At $I_{\text{bias}}$ = 12 mA, the

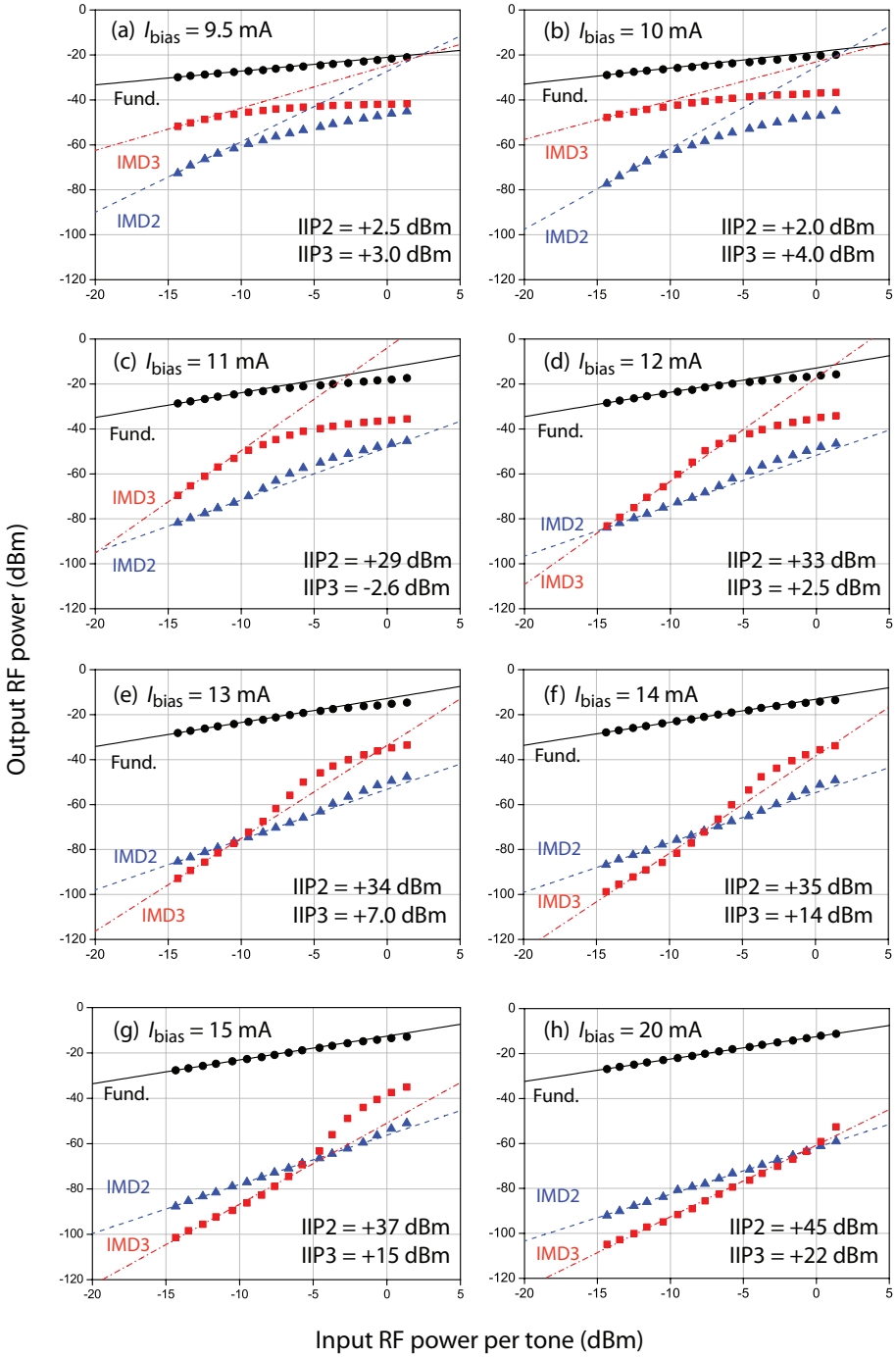


**Figure 4.13:** The measured fundamental signal and the IMD terms of the BMD link for various bias currents.

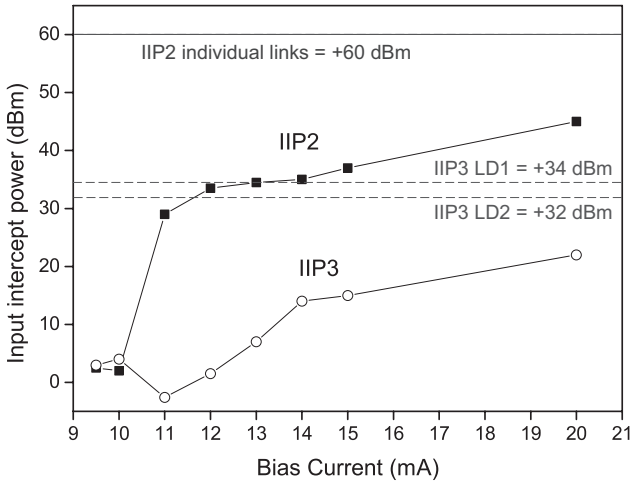


**Figure 4.14:** IIP2 and IIP3 of the BMD link as functions of the bias current. For comparison, the intercept points of the individual links biased at 50 mA are also indicated.

measurements were performed for the BMD link as well as the individual links. This was done to verify the phase adjustments criterion that was mentioned earlier. It is expected that indeed the BMD fundamental power will resemble the sum of the fundamental powers of the individual links while the IMD2 powers cancel. The IMD measurement results for the BMD link for these selected bias currents are shown in Figure 4.13 (a) to (h). Here, the output RF powers of the fundamental signal, IMD2 and IMD3 components are plotted against the input RF power per-tone. These measured values were then extrapolated to determine their IIP2 and IIP3 values, which are also indicated in these figures.

It is important to note that these extrapolations were done only to the portions of the curves that still maintain the linear input-output relations. This can be seen for example, in Figure 4.13 (c), where the measured data for the fundamental signal that were used for the extrapolation were limited to input powers of less than +5 dBm. Similarly, the extrapolations for the IMD2 and the IMD3 powers were using the measured data up to the input power of -10 dBm. In this way, we have deliberately neglected the contribution of signal clipping, which occurs at a high input RF power. This signal clipping is responsible for the saturation and the significant increase of IMD powers observed in the measurements [193]. An example of this clipping effect is the IMD3 enhancement in the input power region of -10 dBm to 1.5 dBm observed at bias currents starting from 9.5 mA up to 13 mA. Neglecting this contribution allows us to still define the intercept points using the same definition introduced in Chapter 2, which is used throughout this thesis. It is obvious that the intercept points and the SFDR values taking into account the clipping effects will be considerably different from the ones defined here. The reader can refer to [193] for the definition of the SFDR including the clipping effects.

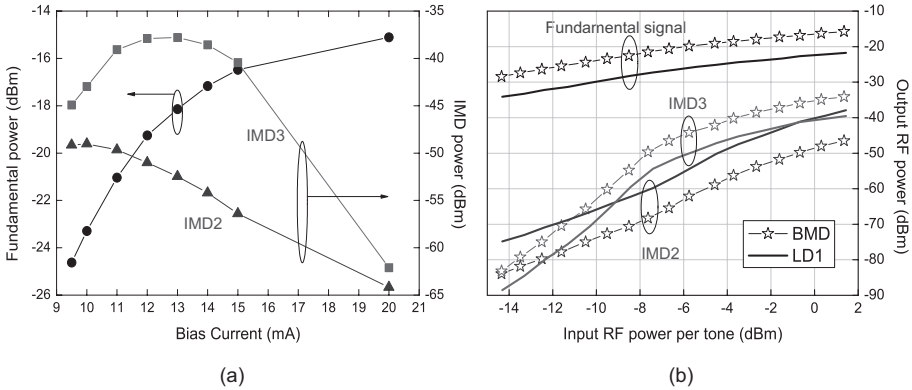


**Figure 4.15:** (a) The measured fundamental, IMD2 and IMD3 powers as functions of the bias current for an input RF power of 0 dBm. (b) The measured fundamental signal and the IMD terms at $I_{\text{bias}} = 12$ mA, of the individual and the BMD links.

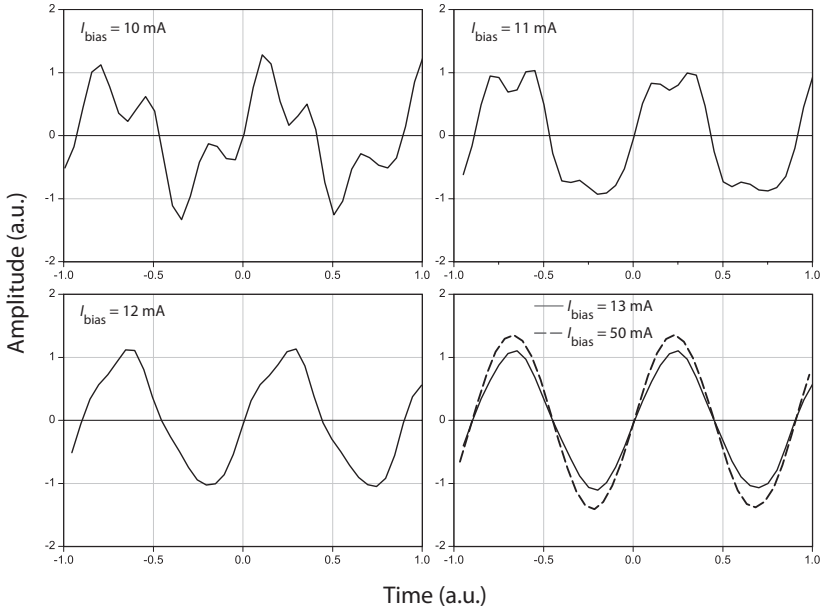


**Figure 4.16:** Output waveforms of the BMD link for various bias currents. (a) $I_{\text{bias}} = 10$ mA, (b) $I_{\text{bias}} = 11$ mA, (c) $I_{\text{bias}} = 12$ mA, and (d) $I_{\text{bias}} = 13$ mA and $I_{\text{bias}} = 50$ mA.

As evident from Figure 4.13, the realized BMD link suffered from very high intermodulation distortion powers, notably in the low bias region. Relative to the individual links biased at 50 mA, the BMD link for all bias currents up to 20 mA yields lower IIP2 and IIP3. This is illustrated in Figure 4.14 where the IIP values are plotted against the bias current, together with the IIP2 and IIP3 values of the individual link biased at 50 mA. Similar to the noise enhancement effects in the threshold region, this high distortion will eventually limit the BMD link SFDR, as will be discussed in the next subsection.

From the measurement results, presented in Figure 4.13, two further observations can be made. First is the distortion components behavior with respect to the bias current for a given input power. The IMD powers gradually decrease as the bias current increases. This is illustrated in Figure 4.15 (a), where the Fundamental signal, IMD2 and IMD3 powers are depicted against the bias currents, for a 0 dBm input RF tone power. The second is the distortion comparison of the BMD link, relative to the individual links, for a given bias point. This is needed to verify the phase shifter adjustments, which is indicated by the minimum IMD2 power. The fundamental signal and IMD powers for the BMD link and the individual links at the bias currents of 12 mA are compared, as shown in Figure 4.15 (b). The fundamental signals in the individual links add up in the BMD link such that the BMD link yields 6 dB higher fundamental power relative to the individual links. This is also observed in the IMD3 powers, which is, like the fundamental signals, are in phase in both the individual links. The IMD2, in contrast, are cancelled. A cancellation up to 8 dB has been obtained. Ideally, perfect cancellation should be obtained. However, this cancellation is very sensitive to the matching of the amplitude and RF phase of the IMD2 components of the individual links.

The high distortion can also be observed in the time-domain measurements using an oscilloscope (Agilent 54854A), as presented in Figure 4.16 (a)-(d), where the waveforms at the APL output for the bias currents of 10 mA, 11 mA, 12 mA and 13 mA, respectively, are depicted. For comparison, the waveform at the bias of 50 mA was also shown (dashed-line in Figure 4.16 (d)). The waveforms at 10 mA bias is severely distorted and the distortion reduces significantly at bias current of 13 mA. Relative to the case of a conventional DML, i.e., where the LD is biased at 50 mA, the signal at this bias current is smaller.

### 4.4.5 SNR and SFDR

The SFDR of the individual links were characterized prior to the BMD link. The measured fundamental signal, IMD terms and the noise PSD were extrapolated and the second-order and the third-order SFDRs ($SFDR_2$ and $SFDR_3$) are defined as the SNR in 1 Hz bandwidth where the extrapolated noise PSD curve intersected the IMD2 and IMD3 extrapolated curves, respectively. These SFDRs are shown in Figure 4.17 (a) and (b) for the individual links with LD1 and LD2, respectively. The measured $SFDR_2$ for LD1 and LD2 are 99 $dB.Hz^{1/2}$ and 102 $dB.Hz^{1/2}$ while the $SFDR_3$ for these links are 119 $dB.Hz^{2/3}$ and 118 $dB.Hz^{2/3}$, respectively. From these values, we can conclude two things. First of all, the individual links are capable

of providing relatively high $SFDR_3$ value, close to 120 $dB.Hz^{2/3}$, which is typically cited as one of the highest achieved values with DML link in this frequency region [14]. However, this high SFDR of the individual links are suitable only for narrowband applications because $SFDR_2$ is smaller than $SFDR_3$ (see Chapter 2, Subsection 2.5.1). Note that these observations will be the starting point of the discussion of a novel APL architecture with the potential of providing high broadband SFDR, proposed in Chapter 5.

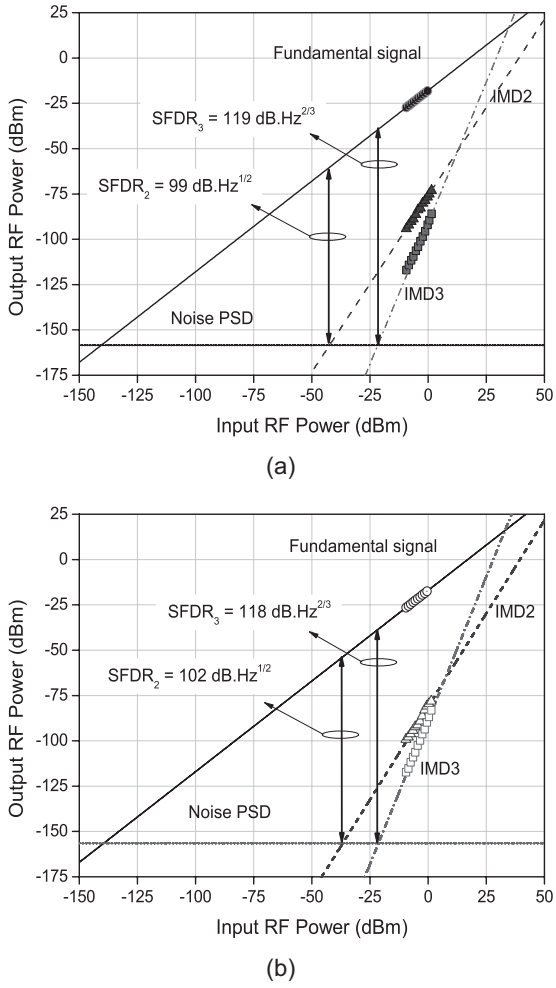


**Figure 4.17:** The measured SFDR for the individual links. (a) LD1, (b) LD2.

Subsequently, we characterized the SFDRs of the BMD link, as functions of the bias current. The results are plotted in Figure 4.18 where the SFDR values of the individual links are also indicated for comparison. The BMD link exhibits much lower SFDR relative to the individual links, with differences as much as 39 dB and 33 dB

for $SFDR_2$ and $SFDR_3$, respectively, have been observed. The reasons for these low SFDRs are the enhanced noise and distortion around the threshold, which were not predicted in the initial model of the BMD link. In the low bias region, the link gain and the modulation response of the LDs are low while the noise and distortions are too high for practical applications. Thus, unlike in the case of external modulation with MZM where low biasing is attractive in reducing the noise, we conclude that the low biasing of a directly modulated laser is not an attractive technique for enhancing the APL performance. Although this has been hinted in some publications [194, 195], to our knowledge, this has not been thoroughly investigated up to now. As mentioned in the previous chapter, the low biased LDs have found their applications not as the scheme for performance enhancement but as a cost-effective technique for signal upconversions [187, 188]. In the following chapter, we will discuss an APL with a similar architecture as the BMD link that offers a high broadband SFDR.

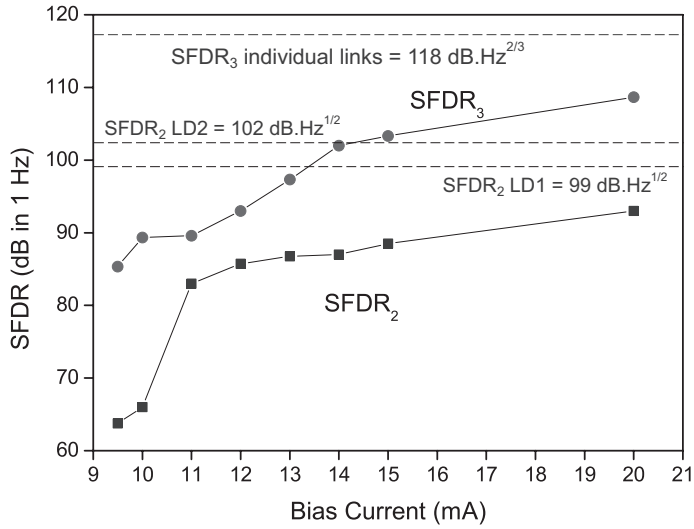


**Figure 4.18:** SFDR of the BMD link as functions of the bias current. The SFDR of the individual links at bias current of 50 mA are also indicated.

## 4.5 Summary

In this chapter theoretical and experimental investigations of the balanced modulation and detection (BMD) photonic link have been presented. The idea is to create half-wave rectified optical signals using a pair of laser diodes and restore the original signal by means of a balanced detection. Ideally, the link will yield significant performance enhancement relative to the conventional directly modulated laser (DML) link, in terms of noise and SNR. In the BMD link, the noise scales

with the modulating signals, allowing small signals to experience lower noise compared to strong signals, thereby lowering the minimum detectable signal and subsequently increasing the dynamic range. The link is also less susceptible to laser RIN relative to the conventional DML, achieving the same SNR with as the latter, only with higher RIN.

These promising features have motivated the realization and characterization of such an APL. The realized link employed a pair of DMLs mounted on a laser mount with RF capabilities. Various measurements, such as link gain, noise and intermodulation distortion measurements have been performed while varying the bias currents of the DMLs. For bias currents close to the threshold, the link gain is low and the modulation bandwidth is severely limited. Moreover, the noise and the IMD powers in the APL are significantly enhanced. Thus, in contrast with the theoretical predictions, low biasing tends to limit the dynamic range of the link. Measurement results have shown that the BMD link has a relatively lower SFDR compared to the conventional DML. An architecture that is promising to obtain large broadband dynamic range will be discussed in the next chapter.

# 5

# Push-Pull Modulation for SFDR Enhancement

## 5.1 Introduction

These past few years, there have been numerous research efforts concentrated on the spurious-free dynamic range (SFDR) enhancement of analog photonic links (APLs). In Chapter 3, we have reviewed the notable techniques used to increase the APL SFDR. Note that most of the high SFDR APLs that have been reported so far are dominated by externally-modulated links rather than directly modulated ones [17]. This stems from two reasons; firstly, the performance of an externally-modulated APL is more reliable relative to the directly modulated ones, especially in high frequency region, where the latter suffers from the frequency chirping [31] and smaller modulation bandwidth [6]. The second reason is, as discussed in Chapter 2 and Chapter 3, the performance of an externally-modulated APL can be optimized by tuning or adjusting the system parameters (as an example, the link gain can be increased by increasing the input optical power), while the degree of freedom in an directly-modulated laser link is considerably less [17]. These reasons have sprung the advancement in the externally modulated much more relative to the directly-modulated counterpart. However, for applications in which a large number of APLs are required, for example in a large-scale phased array antenna for radio astronomy, employing external modulators might become too costly. Hence, using directly modulated laser diodes (LDs) is preferred due to their low cost and simplicity. Fortunately, in such an application the APL should only bridge a relatively short length such that the chirp most of the time is not the limiting factor. Nevertheless, the application is very demanding in terms of the SFDR, which is essentially the

range of power that can be accommodated by the APL. Hence, APLs with directly-modulated lasers that can provide sufficiently large SFDR are of importance.

One of the main limitations of APLs with directly-modulated lasers is the high second-order intermodulation distortion (IMD2) [13]. This prevents the APLs to be implemented in broadband systems in which the signal has a bandwidth of more than one octave (see Chapter 2 Subsection 2.4.3). In externally-modulated links with Mach Zehnder modulator (MZM), this limitation is mitigated by means of biasing the MZM in quadrature, which minimizes IMD2 but in turn maximizes the third-order intermodulation (IMD3) [196]. Another way is to use a dual-output MZM [44, 47, 49, 154] in conjunction with a balanced photodetector (BPD) (Chapter 3 Subsection 3.2.7). In this chapter, we continue with a similar architecture proposed in [189] and [87] which employs a pair of LDs modulated in a push-pull manner and a BPD to restore the signal. The aim is to suppress the IMD2 such that the link is limited only by the third-order intermodulation distortion (IMD3). Note that this architecture is the same as the balanced modulation and detection (BMD) scheme discussed in the previous chapter, differing only in the bias operation of the LDs. Recall that from Chapter 4 we learned that the low-biasing of the LDs will result in elevated noise and IMD levels as well as a reduction in the APL frequency response, which as a whole, reduce the APL SFDR. Thus, in our push-pull APL, as we call the link here, we will omit the low biasing and instead choose the bias points of the LDs based on a different criterion. The rest of the chapter is organized as follows: the principle of operation of the APL is introduced in the second section while the measurement setup and results are presented in the third and fourth sections, respectively. Finally, the chapter ends with a summary.

## 5.2 APL Architecture

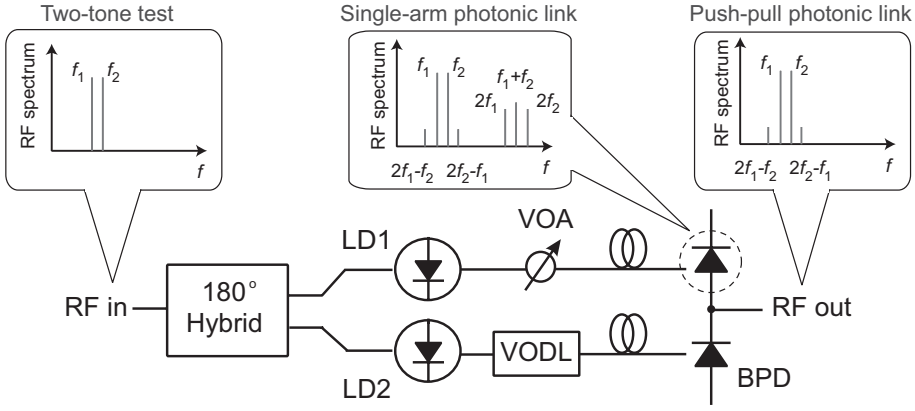


**Figure 5.1:** The proposed APL for broadband SFDR enhancement. LD: laser diode, VOA: variable optical attenuator, VODL: variable optical delay line, BPD: balanced photodetector

The APL architecture is shown in Figure 5.1. It consists of a 180$^o$ hybrid coupler that supplies antiphase RF signals to a pair of LDs. In this way, the LDs are modulated in a push-pull manner. The variable optical attenuator (VOA) and the variable optical delay line (VODL) are used to control the intensity and the (RF modulation) phase of the modulated optical signals such that upon arriving at the BPD, they have the same amplitude and maintain the 180$^o$ phase difference. The BPD simply subtracts the signals of the upper and the lower arms of the APL. In the ideal case of perfect amplitude and phase matchings, the output RF signal will be 6 dB higher compared to the case of a single arm APL (which can be obtained by means of disconnecting one of the optical fibers to the BPD while keeping the hybrid coupled connected) and the IMD2 at the output will be completely suppressed since the IMD2 components in the upper and the lower arms are in-phase. The 6-dB signal enhancement stems from the fact that the photocurrents from the photodiodes add up resulting in a detected current twice as high as the current, and subsequently four times the RF power, of the single arm link. The key component of the APL is the IMD2 suppression that allows the APL to have the same SFDR for both single-octave (narrowband) and multioctave (broadband) signals. At a glance, the principle of operation of this push-pull modulated APL is very similar to the characteristic of the dual-output MZM link discussed in Chapter 3 Subsection 3.2.7. The difference lies in the noise PSD at the link. Recall that in the case of the dual-output MZM link the relative intensity noise (RIN) of the laser source is partly suppressed in the BPD. In our case, there is no noise suppression because the noise from the LDs are uncorrelated (since they come from two independent sources), and hence will add up incoherently at the output. However, as will be shown later, we have chosen the bias current of our LDs such that the RIN is already low and the shot noise is dominant.

## 5.3 Measurement Setup

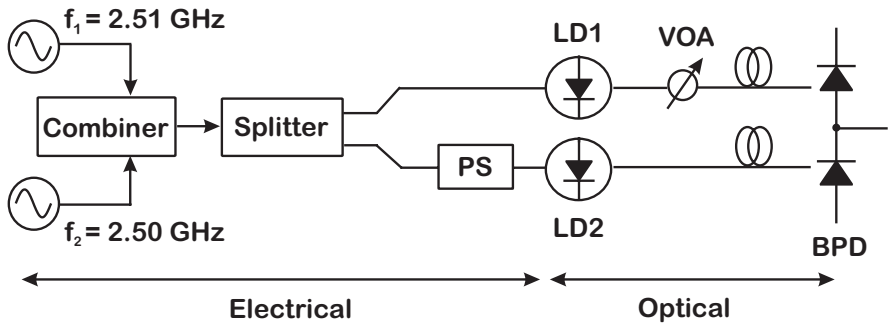


**Figure 5.2:** The measurement setup. The 180$^o$ hybrid and the variable optical delay line are replaced by a splitter and an RF tunable phase shifter (PS).

A two-tone measurement was carried out to characterize the distortion (and subsequently the SFDR) of the APL. However, due to the unavailability of the 180$^o$ hybrid and the VODL during the measurements, the measurement setup of the APL was adjusted to the one shown in Figure 5.2. An RF splitter and a tunable phase shifter (1-5 GHz frequency range) are used in place of the hybrid and the VODL to perform the push pull modulation and to correct any phase imbalance in the APL. In contrast to the VODL, the phase shifter is strongly frequency dependent and that prevents us to extend our two-tone measurements to a larger frequency range (for example to cover the complete UHF band) without making extensive adjustments in the measurement setting. For this reason, we decided to perform the two-tone test around the modulating frequency of 2.50 GHz which is limited by the laser diode mounts (ILX Lightwave LDM-4980RF, 2.5 GHz modulation bandwidth) used in the measurements.

We use a network analyzer (Agilent N5230A) and a vector signal generator (Agilent E4438C) to supply the two tones of 2.50 GHz and 2.51 GHz to the LDs via a 2:1 combiner and a 1:2 splitter. The RF insertion loss of the combiner, splitter and the phase shifter amounts to approximately 8 dB. The LDs are 1310 nm DFB lasers from Fitel which characteristics have been described in the previous chapter. In order to avoid clipping of large modulating signals, the LDs should be biased around 50 mA, which is roughly half of the difference between the maximum injection current prescribed in the datasheets (100 mA) and the threshold current. Because in the laser characterization (see Chapter 4) the LD1 has shown higher IMD2 compared to the LD2, the VOA is placed in the upper arm APL to attenuate the optical power and subsequently to match the IMD2 amplitude in both of the arms. It is also possible to equalize these amplitudes with an RF step attenuator instead of the VOA. However, in the measurement setup, finer adjustments can be obtained with the VOA (0.01 dB optical attenuation step) compared to our RF attenuator (1 dB RF attenuation step).

The fundamental, IMD2 and IMD3 powers are measured at the output of the BPD (Discovery Semiconductor DSC-710) with an electrical spectrum analyzer (HP 8593E) at frequencies of 2.50 GHz, 5.01 GHz (2.50 GHz+2.51 GHz) and 2.52 GHz (2×2.51 GHz−2.50 GHz), respectively. For the noise measurements, a low noise amplifier (LNA, Mini Circuits ZRL-2400+) with a gain of 23.2 dB and noise figure of 1.4 dB at the frequency of 2.5 GHz was used to reduce the displayed analyzer noise level (DANL) of the spectrum analyzer. The measurement results are presented in the following section.

## 5.4 Measurement Results

### 5.4.1 Characterizations of Individual Laser

We start with the characterization of the individual (i.e. single-arm) APL. The input RF power per tone was 1.5 dBm after subtracting 10.5 dBm from the input power as the RF loss of the combination of the 2:1 combiner and the hybrid coupler. From the previous IMD characterizations presented in Chapter 4, we have seen that the

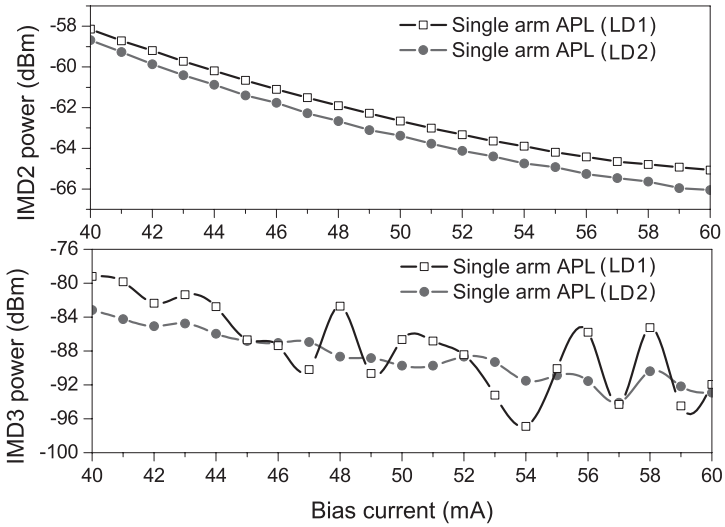


**Figure 5.3:** IMD2 and IMD3 characterizations of the single arm APLs. The input RF power to each laser is 1.5 dBm per tone.

IMD powers are high at low bias currents. For this reason, we limit our IMD characterizations in the region of 40 mA to 60 mA. The measured IMD2 and IMD3 powers as functions of the bias currents are shown in the upper and the lower part of Figure 5.3.

As expected, both LDs yield higher IMD2 power relative to the IMD3 power. In the upper part of Figure 5.3, it can be observed that the difference of the IMD2 powers of LD1 and LD2 is approximately 2 dB. Thus, the VOA placed in the arm containing LD1 was adjusted such that the IMD2 powers in the two arms are equal. Note that by introducing an attenuation in one of the arms, we actually are reducing the fundamental power of one of the individual links. This will later on be observed as the reduction of the link gain of the push-pull APL, relative to the expected 6 dB value. Obviously this is undesirable, but the main aim of the APL is to obtain the amplitude matching of the IMD2 powers at both arms such that a maximum reduction of the IMD2 power is obtained. Later on we will see that besides this amplitude matching, the RF phase matching is also crucial to obtain optimum link performance.

In the lower part of Figure 5.3, the IMD3 powers as functions of the bias current are shown. Generally, the LDs show lower third order nonlinearity compared to the second order one, as expected. However, the LD1 shows considerably larger variations of IMD3 power compared to the LD2. This is due to the amplitude instability (with respect to time) observed in the measured IMD3 of the LD1, which is not observed in the LD2. In order to reduce the variation, averaging was done in every IMD3 measurements involving LD1. These instabilities might rise from the optical reflections in the link and in the next section we will address this matter

more thoroughly.

Beside the signal and IMD powers, characterizations of the APL noise was also performed. From the results presented in Chapter 4 Subsection 4.4.3, we learn that the LDs show the best noise performance if they are biased well beyond their threshold currents. As shown in Figure 4.10 of Chapter 4, the RIN value of the LDs used in our measurements around 50 mA is better than -155 dB/Hz.

Having characterized the individual links, we selected the operating bias currents of the push-pull (dual-arm) APL. These bias currents are chosen to be 51 mA and 52 mA for LD1 and LD2, respectively. These bias currents are not optimized, but chosen based on two reasons. Firstly, at these operating points the noise PSDs are sufficiently low, which are -166.8 dBm/Hz and -164.5 dBm/Hz respectively, for LD1 and LD2. For the push-pull APL the noise contribution of the upper and the lower arm APLs add up incoherently and the PSD amounts to -163 dBm/Hz. Secondly, from the distortion point of view, these bias currents are midway of the L-I curve such that additional distortion induced by signal clipping will be avoided. In the next section, we will discuss an optimized selection of these bias currents for an application of the APL beyond the frequency discussed here (2.5 GHz).

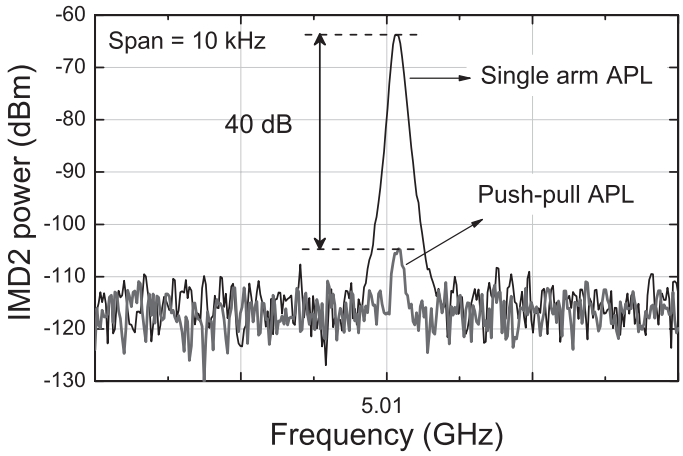


**Figure 5.4:** IMD2 power suppression at 5.01 GHz. The frequency span is 10 kHz and the input RF power per tone to each laser is 1.5 dBm.

### 5.4.2 Push-Pull APL Performance

The push-pull APL was carefully tuned to obtain the maximum IMD2 suppression at the frequency of 5.01 GHz. By fine adjustments of the VOA attenuation and the RF phase shifter, an IMD2 suppression of 40 dB relative to the IMD2 powers of the single-arm links can be achieved, as shown in Figure 5.4 . As for the fundamental tone, the powers in the individual APLs add up coherently as expected (Figure 5.5). Remember that theoretically, the photocurrents at the BPD output will double and

the fundamental RF power of the push-pull link relative to the individual link is four times higher. But since we have a gain imbalance in our individual links due to the VOA attenuation, the fundamental power in the single arm APL with LD1 is lower by 2.5 dB compared to the the one with LD2, making the signal enhancement of the push-pull APL compared to the single arm APL with LD2 amounts to approximately 4.5 dB instead of the theoretical value of 6 dB [155].

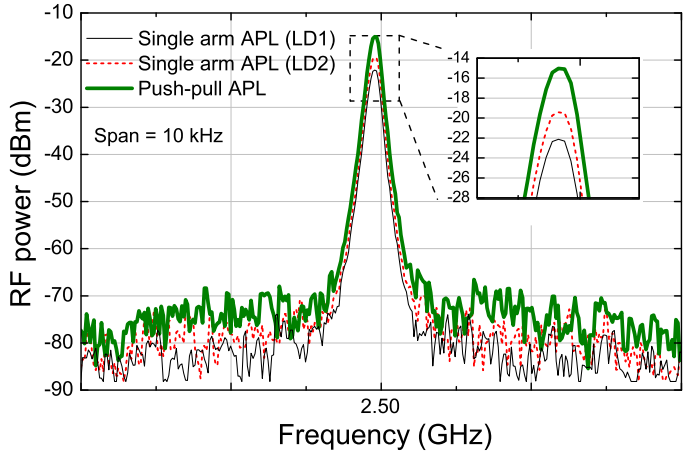


**Figure 5.5:** Coherent addition of the signal power at 2.5 GHz. The frequency span is 10 kHz and the input RF power per tone to each laser is 1.5 dBm.

The suppression shown in Figure 5.4 is highly sensitive to bias current variations. We optimized the system for maximum IMD2 suppression for bias currents of 51 mA and 52 mA, respectively for LD1 and LD2 and then varied the bias currents from 40 mA up to 60 mA with a step of 1 mA. The measurements were automated and synchronized using LabVIEW. The result is shown in Figure 5.6, where the contour plot of the IMD2 power in the push-pull link for an input RF power of -3.5 dBm is plotted. An IMD2 power variation as much as 35 dB has been observed. This is attributed to the amplitude variations of the IMD2 with respect to the bias currents, which cannot be corrected with a fixed attenuation.

### 5.4.3 SFDR Enhancement

Furthermore, we characterized the system in terms of the SFDR, defined as the output signal-to-noise ratio (SNR) at the input power where the IMD2 or IMD3 power equals to the noise power (see Chapter 2 Subsection 2.5.1). We start by characterizing the single-arm links. The RF power to the links were varied from -2.5 dBm and 1.5 dBm with a step of 1 dB. For each input RF power the fundamental signal, IMD2 and IMD3 powers were measured. The results are shown in Figures 5.7 and 5.8 for LD1 and LD2, respectively. The measured values were then extrapolated and the $SFDR_2$ and $SFDR_3$ are derived from these extrapolations. The

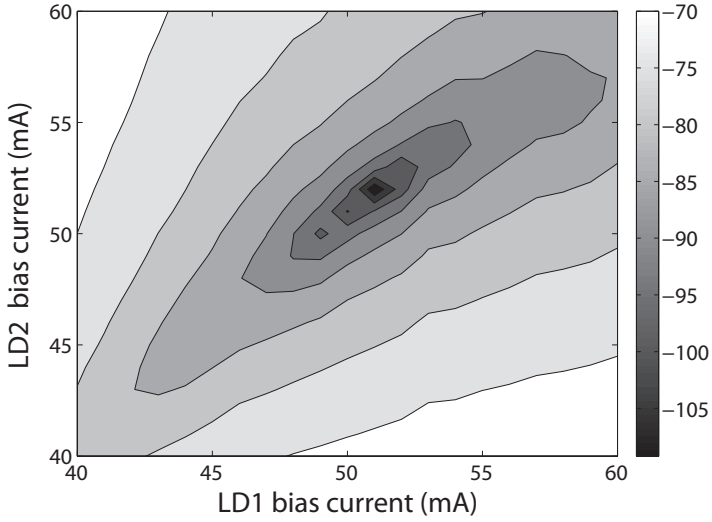


**Figure 5.6:** IMD2 power in dBm as a function of the LDs bias currents. The input RF power per tone to each laser is -3.5 dBm.

measured $SFDR_2$ and $SFDR_3$ values are 95 dB.Hz$^{1/2}$ and 120 dB.Hz$^{2/3}$, respectively for LD2, as shown in Figure 5.7. As for LD1, the measured $SFDR_2$ and $SFDR_3$ are 93 dB.Hz$^{1/2}$ and 118 dB.Hz$^{2/3}$, respectively. These values can be compared with the measured values at the frequency of 1 GHz listed in the previous chapter, which were $SFDR_3$ = 118 dB.Hz$^{2/3}$ for both LDs and $SFDR_2$ = 95 dB.Hz$^{1/2}$ for LD1 and $SFDR_2$ = 102 dB.Hz$^{1/2}$ for LD2.

As for the push-pull APL, the IMD2 is largely suppressed and the limiting distortion is IMD3. During the measurements, we measured the residual IMD2 level which was just slightly above the measurement noise floor. We suspect that this comes from the photodetector nonlinearity, which becomes dominant once the second-order nonlinearity of the LDs was suppressed. Although the instability of the IMD3 in the LD1 adds some uncertainties in the SFDR measurement, a broadband SFDR value of 120 dB.Hz$^{2/3}$ can be obtained, as shown in Figure 5.8 [159]. To our knowledge, this value is among the highest ever reported for multioctave SFDR in directly-modulated links [13]. As a comparison, the same SFDR value has been cited as the highest broadband SFDR in LDs [14], which was shown in an APL with a similar architecture as our setup but at a lower frequency of 1 GHz [87].

From these measurements we can conclude that the the push-pull APL can provide a high SFDR which is the same for both single-octave and multioctave signals. This is not the case for the single-arm link which yield a slightly higher $SFDR_3$ but suffers from low $SFDR_2$.

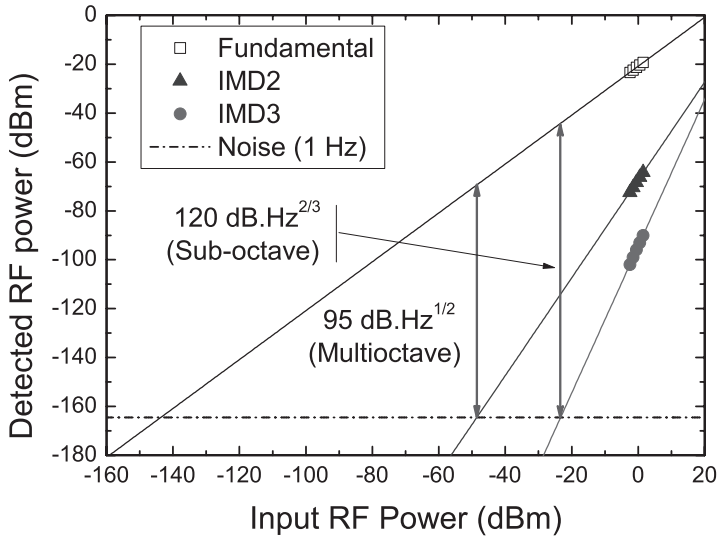


**Figure 5.7:** The measured SFDR at the tone center frequency of 2.5 GHz for the single arm APL with LD2. The multioctave SFDR is limited by the IMD2.

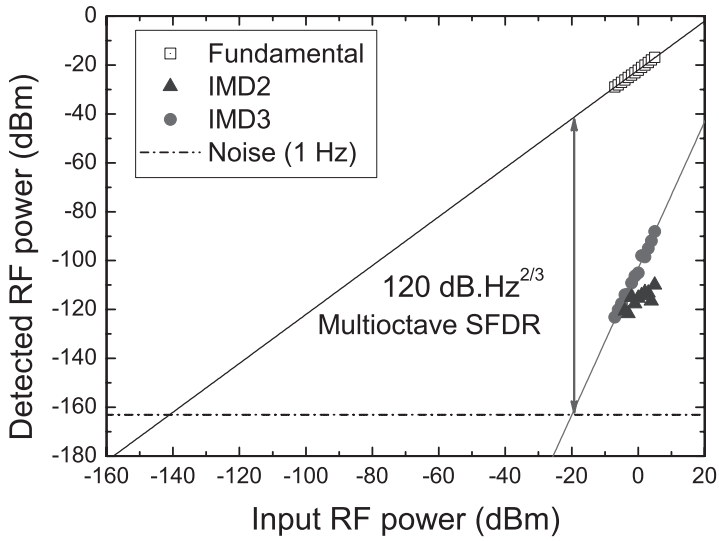


**Figure 5.8:** The measured SFDR at the tone center frequency of 2.5 GHz for the push-pull APL. The IMD2 is suppressed such that the limiting distortion is IMD3.

## 5.5 Frequency Range Extension

We have shown that in principle, the push-pull APL can provide high multioctave SFDR at the frequency of 2.50 GHz. In this section, we will extend the frequency range of the push-pull APL beyond 2.50 GHz [197].

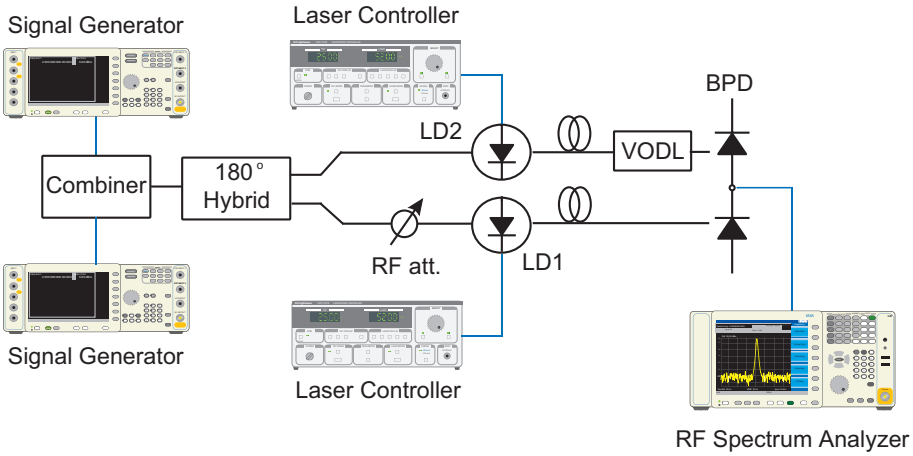


**Figure 5.9:** Schematic of the realized push-pull modulated APL. LD: laser diode, VODL: variable optical delay line, BPD: balanced photodetector.

In the previous measurements we have encountered instabilities of the IMD3 power of LD1. We suspected that source of the instabilities are the optical reflections [198] occurring along the optical path from the LD1 to the VOA, even though according to the datasheet the lasers are isolated by at least 25 dB. In order to minimize the reflections, we removed the VOA and replaced it with an RF attenuator, placed at the RF path from the hybrid coupler to the RF input of the laser mount hosting LD1. To reduce the optical reflections even further, we also applied an index matching fluid (Fluorinert from 3M) at the connector facets of the LD1 and one of the optical connectors of the BPD. Unfortunately, replacing the VOA with the RF attenuator will pose a limitation to the amplitude adjustments required to match the IMD2 powers of the two LDs. This is because the RF attenuator has a much coarser attenuation step (1 dB step) relative to the VOA which has an optical attenuation resolution of 0.01 dB. As the final adjustment in the measurement setup, we replaced the RF phase shifter with a variable optical delay line (VODL) which provide broadband delay instead of a frequency dependent phase-shift. The complete arrangement of this measurement setup is shown in Figure 5.9.

In the previous measurements, the bias currents selections were not optimized. Here, we repeat the two-tone measurements on the individual links in order to obtain the optimum operation points of the LDs. The tones are 10 MHz apart and their center frequency, $f_c$, is varied from 1 GHz to 4 GHz with a step of 100 MHz. The power per tone supplied to the LDs is -1.5 dBm, taking into account the 10.5 dB

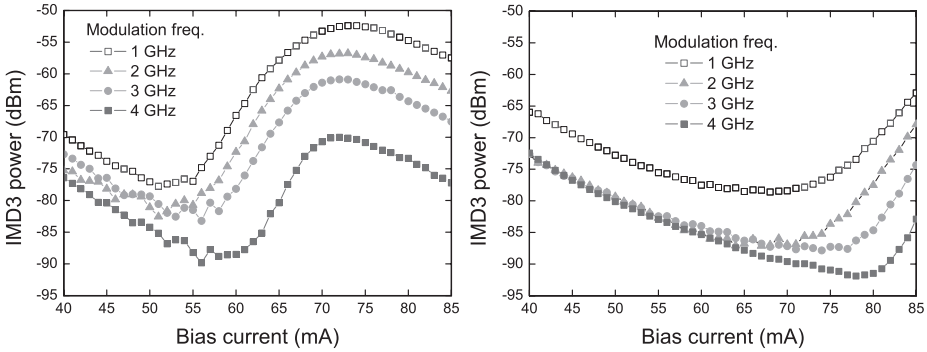


**Figure 5.10:** IMD3 power as a function of laser injection current for (a) LD1 and (b) LD2. The tone center frequency is used as a parameter. At the selected bias currents, the IMD3 powers are minimum for the frequency range of 1 GHz to 4 GHz.

insertion loss of the combiner and the hybrid coupler. The fundamental, IMD2 and the IMD3 powers are measured at the output of the BPD with an RF signal analyzer (Agilent MXA N9020A) at frequencies of $f_c + 5$ MHz , $2f_c$ and $f_c + 15$ MHz, respectively. The LDs bias currents are adjusted with a pair of laser diode controllers (ILX Lightwave LDC 3722 and LDC 3724). The injection current to each laser is varied from 40 mA to 85 mA and, for every bias point, the IMD3 power of the individual laser is measured. Furthermore, we have set the modulation frequency as the parameter. Our aim is to determine the bias currents of LD1 and LD2 that minimize the IMD3 power for the modulation frequency from 1 GHz to 4 GHz. We opted to use this criterion for the optimization because at the end, the SFDR of the push-pull APL will be determined by the $SFDR_3$ of the individual links as demonstrated in the previous section. This is because the IMD2 power can always be suppressed by choosing a proper attenuation of the VOA and the delay of the VODL. Thus, it is advantageous to choose the bias currents for optimum $SFDR_3$. The characterization results for LD1 and LD2 are shown in Figures 5.10(a) and 5.10(b), respectively. Based on these results, we selected the operating bias currents for LD1 and LD2 to be 55 mA and 73 mA, respectively.

Having selected the LDs bias currents, we optimize the system by adjusting the RF attenuator and the VODL with the objective of obtaining maximum IMD2 suppressions for a wide range of modulating frequencies. The optimum RF attenuation is found to be 4 dB and the maximum IMD2 suppression related to this attenuation is limited to 23 dB. Higher suppressions can be obtained by using an attenuator with a better step resolution.

Ideally, the way to correct the phase imbalances in the system is to observe - in real time - the IMD2 powers while adjusting the VODL to obtain maximum IMD2 suppressions. However, this type of measurement requires a synchronized frequency sweeping for modulation and detection at two different frequency ranges.

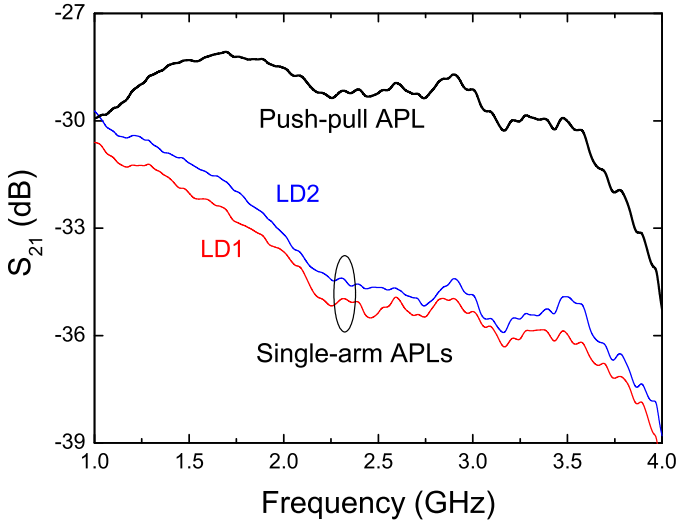


**Figure 5.11:** Signal enhancement in the push-pull APL measured with a network analyzer.

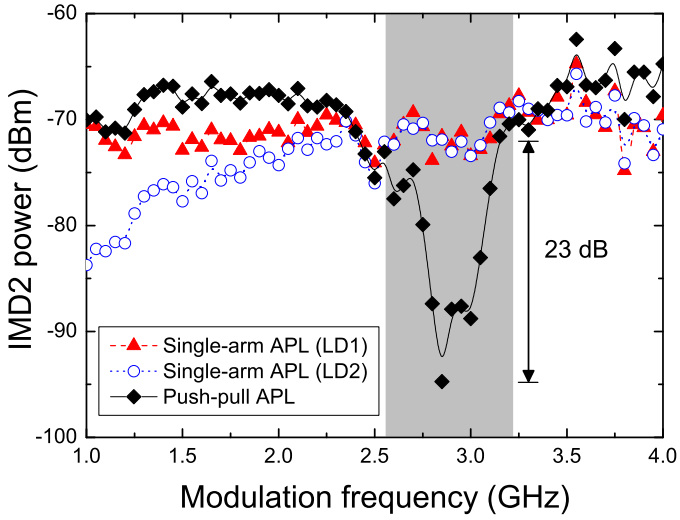


**Figure 5.12:** IMD2 suppression in the push-pull APL plotted against the center frequency of the two tones used in the measurements. Maximum suppression of 23 dB was achieved at the tone center frequency of 2.81 GHz.

For example, if the the modulation frequency is $f_c$, the detection should be done at $2\,f_c$. It should be possible to do this type of measurement with a dedicated setting in the network analyzer. However, due to the limitation in our measurement setup, this type of measurement was not performed. Instead, we optimize the system by means of adjusting the VODL while observing the fundamental signal power instead of the IMD2 power. This is done by measuring the $S_{21}$ parameter using the VNA. The optimum setting is thus determined by the widest range of the modulation frequency in which maximum signal enhancement relative to the case of single arm APL is achieved. This is illustrated in Figure 5.11. A maximum signal enhancement of 6 dB is obtained at a modulation frequency range of 2 GHz to 3.5 GHz.

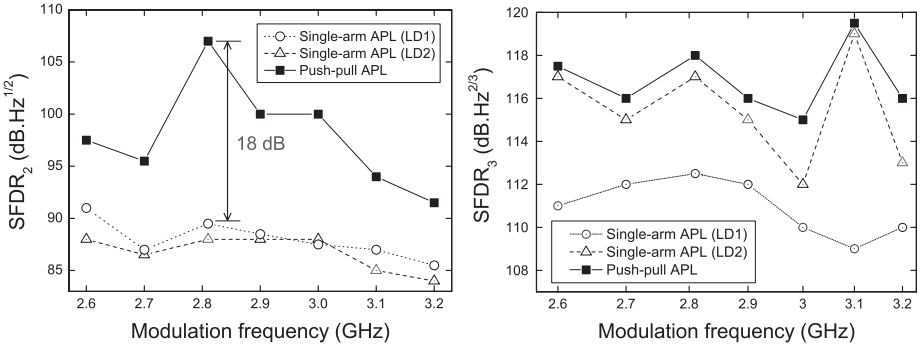


**Figure 5.13:** The measured $SFDR_2$ (a) and $SFDR_3$ (b) for the push-pull APL and the single-arm APLs as functions of the modulation frequencies.

With this arrangement, the IMD2 power in the push-pull configuration is measured using the signal analyzer, where the modulation frequency (i.e. the center frequency of the input RF tones) was swept automatically using LabVIEW. The result is shown in Figure 5.12. The suppression is achieved in the modulation frequency range of 2.5 GHz to 3.2 GHz, shown as a gray area in Figure 5.12. To avoid confusion, we re-iterate here that the IMD2 power itself was measured at twice the modulation frequency $(2f_c)$, but we choose to plot the results against the modulation frequency itself $(f_c)$. A maximum suppression of 23 dB is obtained at the frequency of 2.81 GHz. The overall suppression can be increased by using an attenuator with finer attenuation steps. The limited bandwidth of suppression is caused by two reasons. Firstly, using one attenuation value (in our case 4 dB) is not sufficient to match the IMD2 powers of LD1 and LD2 at the whole frequency band of 1 GHz to 4 GHz. This can be observed at the lower frequency region in Figure 5.12 where the difference in the IMD2 power of the LDs can be as much as 15 dB. Secondly, there is still a length mismatch between the upper arm and the lower arm of the APL which was not properly corrected by the VODL. As a result, for some modulation frequencies, the IMD2 components of the LDs add up instead of being cancelled. These limitations can be mitigated if a pair of LDs with matched IMD2 characteristics are used and if the length of the APL arms are properly matched.

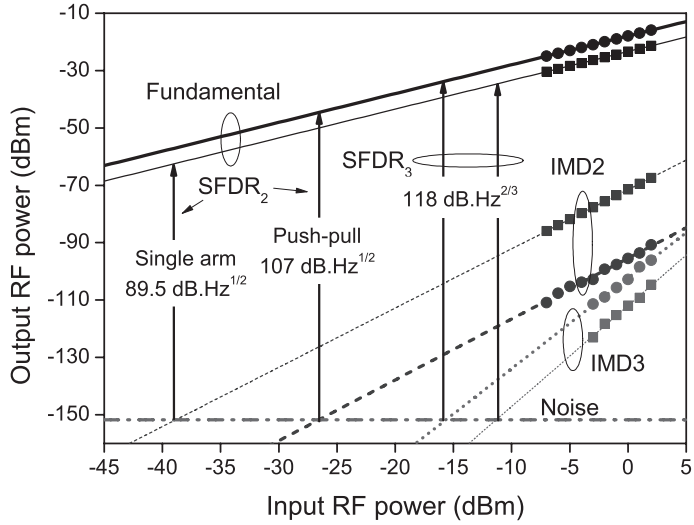


**Figure 5.14:** The measured SFDR for the push-pull APL and the single-arm APLs at the tone center frequency of 2.81 GHz.

In the frequency range where the IMD2 suppression occurs (2.6 to 3.2 GHz), the SFDRs of the push-pull and the single-arm APLs are characterized. As evident from Figure 5.13(a), the push-pull APL shows improved IMD2-SFDR, over a considerably wide frequency range, compared to the single-arm APLs. A maximum improvement of 18 dB is achieved at the modulation frequency of 2.81 GHz. As for the $SFDR_3$, the push-pull APL roughly has the dynamic range equal to the highest $SFDR_3$ of the two single-arm APLs. This is illustrated in Figure 5.13(b). At the frequency of 2.81 GHz, where the SFDR advantage is highest, the IMD2-SFDR and the IMD3-SFDR of the push-pull APL are 108 $dB.Hz^{1/2}$ and 118 $dB.Hz^{2/3}$, respectively. In contrast to the single arm APLs (IMD2-SFDR = 90 $dB.Hz^{1/2}$, IMD3-SFDR = 117 $dB.Hz^{2/3}$), the push-pull APL provides more comparable sub-octave and multioctave SFDR values. This is illustrated in Figure 5.14.

## 5.6 Summary

In this chapter the concept of a push-pull modulated APL using a pair of directly modulated laser diodes was introduced. This APL is different from the previously discussed balanced modulation and detection (BMD) APL in a sense that the LDs are not low biased. The biasing is carefully chosen in order to minimize the IMD3 powers, while the IMD2 powers are cancelled by carefully matching the power and the phase of the IMD2 contributions from the individual laser. With this architecture we have shown a suppression of second order distortion up to 40 dB and a signal power enhancement of 4.5 dB relative to the single arm APL. The multioctave SFDR of 120 $dB.Hz^{2/3}$ at 2.5 GHz modulating frequency to our knowledge is one

of the highest values ever reported for directly-modulated APL. We have extended the measurements in a frequency range from 1 GHz up to 4 GHz. At this frequency range a signal enhancement of 6 dB has been achieved. IMD2 suppression as much as 25 dB has been achieved within a bandwidth of 700 MHz. The bandwidth limitation stems from the different frequency dependences of the LDs IMD2 components as well as the path length difference in the APL arms. Performance improvements can be achieved if a pair of LDs with matched IMD2 characteristics and low IMD3 are used. This means that integrating the LDs in one wafer to match their characteristics might be advantageous. Moreover matching the path length of the APLs is also crucial to have a broadband IMD2 suppressions. If two different lasers are used instead, multiplexing two lasers with different wavelengths will simplify the link architecture since it will allow only a single fiber to be used.

# 6

# Optimization of Externally Modulated Links

## 6.1 Introduction

An externally modulated analog photonic link (APL) using a Mach-Zehnder modulator (MZM) is arguably the most popular and the most widely used APL nowadays. Numerous research that has been conducted over these years have resulted in steady improvements of the modulator characteristics. Nowadays, MZMs with a low insertion losses, low switching voltage [47, 49], chirpless operation, high power handling [45, 47] and ultrawide modulation bandwidth have been reported and some are already commercially available [199]. Earlier in this thesis (Chapter 3), we have reviewed some of the notable performance improvements reported for the MZM link. In this chapter, we will present the results on the characterization of various arrangements of an MZM link. We will compare the measurement results [†] with the simulation based on the standard performance metrics discussed in Chapter 2. These metrics will be briefly revisited in Section 6.2. The aim of this chapter is thus to show the expected challenges in optimizing such links performance and to highlight the important aspects in the link design. The rest of the chapter is organized as follows: in Section 6.3, the modulator characterizations is presented. This section will also include the performance characterization of a standard MZM. Section 6.4 will be devoted to the MZM link architecture using a high power laser. Optically amplified link will be the topic of Section 6.5. Finally the chapter closes with a summary.

[†]The work was carried out at the R&D department of The Netherlands Institute of Radio Astronomy (ASTRON)

## 6.2 Figures of Merit

The performance of an APL can be fully described by metrics such as link gain, noise figure, intercept points and spurious-free dynamic range (SFDR). These metrics can be expressed in terms of the link parameters which were introduced in Chapter 2. We summarize these parameters and their symbols used throughout this chapter in Table 6.1. We also list the values of these parameters used throughout the simulations.

**Table 6.1:** The parameters used in the simulation

| Parameter | Symbol | Value | Unit |
|---|---|---|---|
| Input optical power | $P_{\mathrm{i}}$ | – | W |
| MZM DC half-wave voltage | $V_{\pi,\mathrm{DC}}$ | 4.9 | V |
| MZM RF half-wave voltage | $V_{\pi,\mathrm{RF}}$ | 3.85 | V |
| MZM bias angle | $\phi_{\mathrm{B}}$ | – | – |
| MZM insertion loss | $L$ | 5 | dB |
| Average photocurrrent | $I_{\mathrm{av}}$ | – | A |
| Photodiode responsivity (A/W) | $r_{\mathrm{PD}}$ | 0.75 | A/W |
| Load resistance (Ω) | $R_{\mathrm{L}}$ | 50 | Ω |
| Boltzmann constant | $k$ | $1.38\times10^{-23}$ | J/K |
| Absolute temperature | $T$ | 290 | K |

Note that especially for the insertion loss, it is expressed in decibels while in the calculations the value in the linear scale should be used instead. The performance metrics can be summarized as follows:

- **Link Gain [Equation** (2.25)**]**

$$g_{\mathrm{MZM}} = \left(\frac{\pi R_{\mathrm{L}} r_{\mathrm{PD}} P_{\mathrm{i}} \sin\phi_{\mathrm{B}}}{4 L V_{\pi,\mathrm{RF}}}\right)^2 . \tag{6.1}$$

  Note that the link gain in Equation (6.1) is usually expressed in the decibels, $G_{\mathrm{MZM}}$, such that $G_{\mathrm{MZM}} = 10\log_{10}(g_{\mathrm{MZM}})$.

- **Noise Figure [Equations** (2.47) **&** (2.48) **]**

$$\begin{aligned}\mathrm{NF}_{\mathrm{MZM}} &= 10\log_{10}\left(\frac{p_{\mathrm{N}}}{g_{\mathrm{MZM}}\, k\, T}\right)\\ &= P_{\mathrm{N}}\ (\mathrm{dBm/Hz}) - G_{\mathrm{MZM}} + 174\ \mathrm{dBm/Hz}.\end{aligned} \tag{6.2}$$

  where $p_{\mathrm{N}}$ is the total noise power spectral density (PSD) in W/Hz and $P_{\mathrm{N}} = 10\log_{10}(p_{\mathrm{N}})$ is the noise PSD in dBm/Hz.

- **Second-order input intercept point (IIP2) [Equation** (2.79)**]**

$$\mathrm{IIP2}_{\mathrm{MZM}} = \frac{2}{R_{\mathrm{L}}}\left(\frac{V_{\pi,\mathrm{RF}}}{\pi}\tan\phi_{\mathrm{B}}\right)^2 \tag{6.3}$$

- **Third-order input intercept point (IIP3) [Equation** (2.80)]

$$\mathrm{IIP3_{MZM}} = \frac{4\left(V_{\pi,\mathrm{RF}}\right)^2}{\pi^2 R_\mathrm{L}} \tag{6.4}$$

  Both intercept points in Equation (6.3) and (6.4) are expressed in Watt.

- **Spurious-free dynamic range (SFDR$_n$) [Equation** (2.84)]

$$\mathrm{SFDR}_n = \frac{n-1}{n}\left(\mathrm{IIP}n\ \ (\mathrm{dBm}) - \mathrm{NF} + 174\ \mathrm{dBm/Hz}\right). \tag{6.5}$$

  For the SFDR calculation in Equation (6.5), the the $n^{\mathrm{th}}$ order input intercept point (IIP$n$) should be expressed in dBm. Moreover, we have completely dropped the subscript "MZM" for the IIP and the NF for the sake of generality.

## 6.3 MZM Characterization

### 6.3.1 Measurement Setup

The modulator used throughout the measurements presented here was an MZM F10 from Avanex. According to the datasheet, the modulator $V_{\pi,\mathrm{DC}}$,$V_{\pi,\mathrm{RF}}$ and $L$ are 5.5 V, 3.8 V and 5 dB, respectively and the 3-dB bandwidth is approximately 11 GHz. To verify these data, the modulator is characterized using a setup as shown in Figure 6.1.

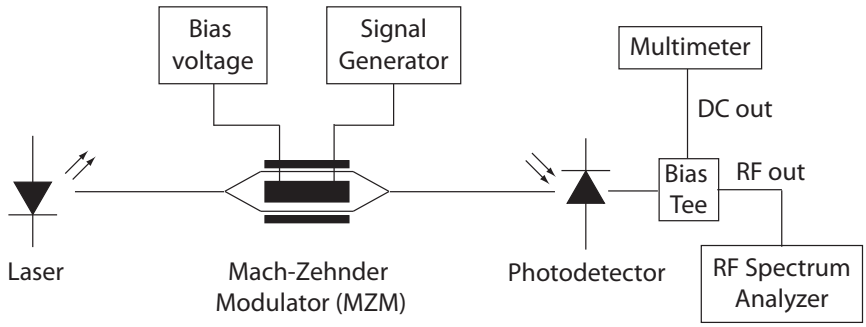


**Figure 6.1:** Schematic of the measurement setup

The laser used in this measurement was a DFB laser diode (LD) from Agere (D2525P26) with a wavelength of 1556.55 nm, a threshold current of 35 mA and a maximum optical output power of 10 mW at bias current of 110 mA. The LD is pigtailed with a polarization maintaining fiber (PMF). The laser was mounted on the laser diode mount (LDM-4984RF) and its temperature and injection current were controlled with a 4-channel laser diode controller (LDC-3900). The laser diode mount and controller are both from ILX-Lightwave. The MZM bias voltage

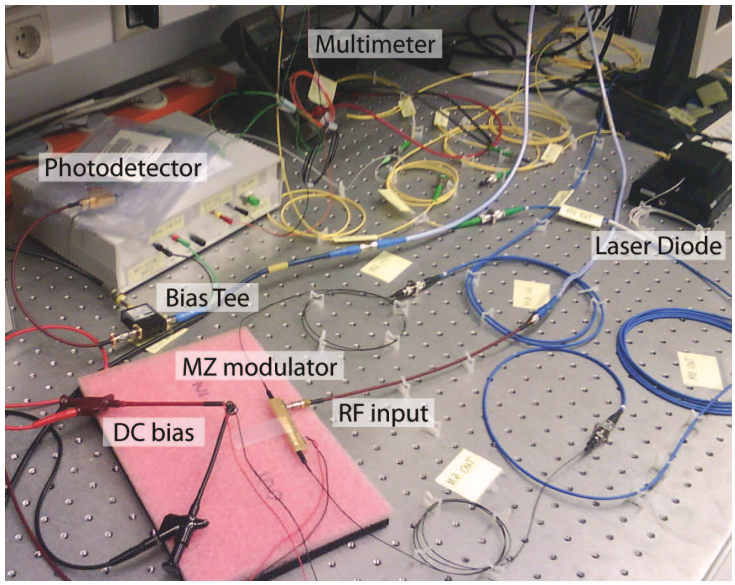


**Figure 6.2:** Photograph of the measurement setup.

was controlled with a voltage supply and the RF signal was supplied to the modulator using a microwave signal generator (SMR 30) from Rohde & Schwarz (frequency range of 10 MHz up to 30 GHz). The modulated optical power from the modulator was then detected using a photodetector (R2560A) from Emcore. According to the datasheet, the typical values of the detector responsivity and 3-dB bandwidth are 0.8 A/W and 13 GHz, respectively. The detector reverse bias is 10 V and the maximum average optical power that can be handled by the detector is 12 dBm. The output impedance of the photodetector is 50 Ω. The detector output was connected to a bias T (100 kHz up to 14 GHz from Ortel). The DC output of the bias T is connected to a multimeter, while the RF output was connected to an RF spectrum analyzer (frequency range of 9 kHz up to 13.6 GHz) from Rohde & Schwarz. The photograph of the measurement setup is shown in Figure 6.2.

### 6.3.2 MZM Bias Variation

The MZM characterization was done by means of varying the modulator bias voltage. In this measurement the laser bias current was set at 110 mA and the emitted optical power is 11 dBm. A single-tone RF signal with a frequency of 2 GHz and the power of 0 dBm was supplied from the signal generator to the RF input port of the MZM. The modulator bias voltage was varied from 0 to 6 V with a step of 0.5 V. Additionally, measurements at the bias voltage of 0.69 V and 5.54 V were also performed. For each modulator bias voltage, the fundamental signal, the second-order harmonic distortion (HD2) and the third-order harmonic distortion (HD3) powers were measured using the RF spectrum analyzer at the frequencies of 2 GHz,

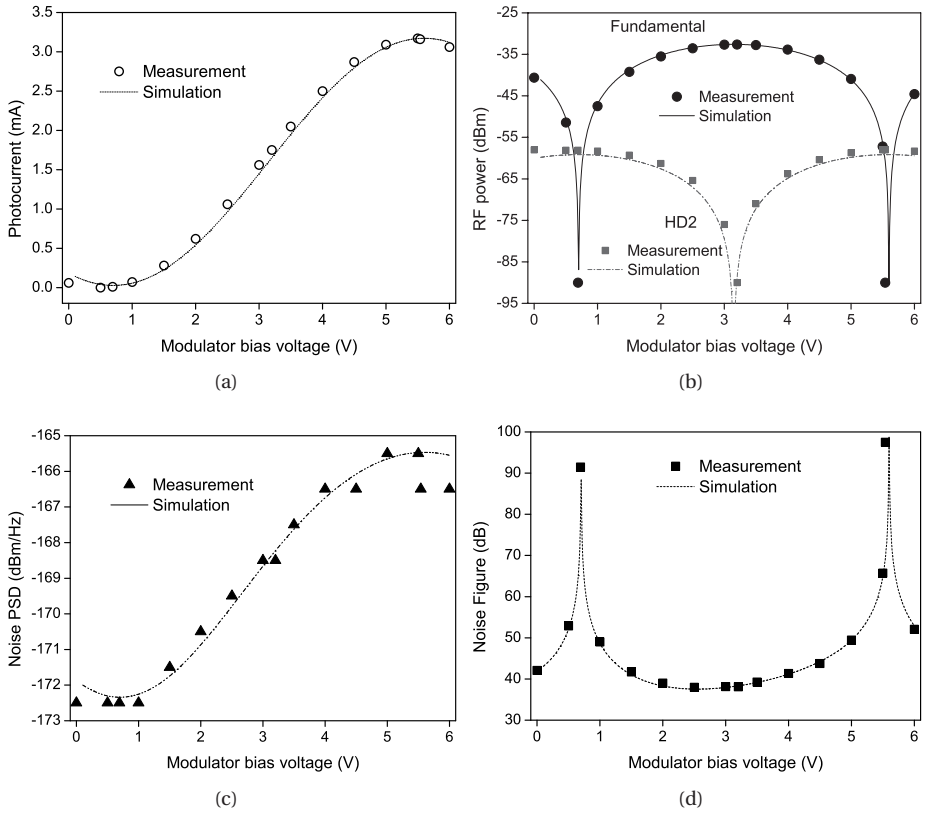


**Figure 6.3:** The characterization results of the MZM APL. (a) Average photocurrent, (b) Fundamental signal and HD2 powers, (c) Noise power spectral density, (d) Noise Figure.

4 GHz and 6 GHz, respectively. The average detected photocurrent was measured for every bias voltage using a multimeter connected to the DC output of the bias T. For the noise measurements, the RF signal was removed and an RF amplifier (from Miteq) with a gain of 36.5 dB was used to reduce the displayed analyzer noise level (DANL) of the RF spectrum analyzer. The noise was measured with a noise marker in a 30 kHz bandwidth and the result was displayed as a power spectral density in dBm/Hz unit.

The measurement results are compared with the simulation results, which are developed from the theory presented in Chapter 2. The aim is to fully determine the modulator characteristics from the measurement results. As an example, we can determine the values of $V_{\pi,\mathrm{DC}}$ and the modulator insertion loss ($L$) from the measured average photocurrent, depicted in Figure 6.3(a). The measured values are indicated by the circles. From Chapter 2, we know that this average photocurrent can be written as

$$I_{\mathrm{av,MZM}} = \frac{r_{\mathrm{PD}}\, P_{\mathrm{i}}}{2L}\left(1 - \cos\left(\frac{\pi V_{\mathrm{bias}}}{V_{\pi,\mathrm{DC}}}\right)\right). \tag{6.6}$$

Using the measured $P_{\mathrm{i}}$ value of 12.6 mW (11 dBm) and the responsivity of 0.75 A/W, the only unknown values in the equation above are $L$ and $V_{\pi,\mathrm{DC}}$. The plot of $I_{\mathrm{av,MZM}}$ in mA as a function of $V_{\mathrm{bias}}$ is the depicted as the dotted-line in Figure 6.3(a). The value of $L$ used in the simulation will determine the height of the curve, while the value of $V_{\pi,\mathrm{DC}}$ will determine the voltage difference where the maximum and the minimum current occurs. Thus, by properly selecting the simulation parameters, we can match the simulation results with the measurement results. From the average photocurrent measurements, we found that the values of $L$ and $V_{\pi,\mathrm{DC}}$ are 5 dB and 4.9 V, respectively. The insertion loss measurement agrees very well with the value listed in the modulator datasheet. As for the DC half-wave voltage, a relatively small difference was observed between the measured value and the value reported in the datasheet.

Having determined the modulator DC half-wave voltage and the insertion loss, we proceed with the determination of the RF half-wave voltage, $V_{\pi,\mathrm{RF}}$. This is done by matching the simulated and the measured values of the fundamental signal and the HD2 powers, as shown in Figure 6.3(b). These powers can be written as (see Chapter 2, Subsection 2.4.6),

$$p_{\mathrm{Fund,MZM}} = \frac{1}{32}\left(\frac{\pi V_{\mathrm{m}}}{V_{\pi,\mathrm{RF}}}\right)^2 \left(\frac{r_{\mathrm{PD}} P_{\mathrm{i}}}{L}\sin\phi_{\mathrm{B}}\right)^2 R_{\mathrm{L}}, \tag{6.7}$$

$$p_{\mathrm{HD2,MZM}} = \frac{1}{512}\left(\frac{\pi V_{\mathrm{m}}}{V_{\pi,\mathrm{RF}}}\right)^4 \left(\frac{r_{\mathrm{PD}} P_{\mathrm{i}}}{L}\cos\phi_{\mathrm{B}}\right)^2 R_{\mathrm{L}}, \tag{6.8}$$

where $V_{\mathrm{m}}$ is related to the input RF power, $p_{\mathrm{in}}$ via the relation

$$V_{\mathrm{m}} = \sqrt{2 p_{\mathrm{in}} R_{\mathrm{S}}}. \tag{6.9}$$

Here, $R_{\mathrm{s}}$ is the source resistance, which is taken to be 50Ω.

Since the input RF power is known, then $V_{\mathrm{m}}$ in Equations (6.7) and (6.8) is known as well. Using the previously determined parameters, the only unknown in these equations is $V_{\pi,\mathrm{RF}}$. It is important to mention here that we observed an additional 2.9 dB of RF loss in our measurement setup due to the losses in the RF cables and connectors and this effect has been taken into account for the determination of the RF half-wave voltage. The best match of simulation and measurement results is obtained if $V_{\pi,\mathrm{RF}}$ is equal to 3.8 V. Again this value agrees very well with the one listed in the component datasheet. Note that since the input RF power in this case is 0 dBm, the fundamental signal power is numerically equal to the link gain. Thus in this case, the $V_{\pi,\mathrm{RF}}$ value can also be deduced by matching the expression in Equation (6.1) with the measured signal power. Moreover, the quadrature bias point of the modulator can be easily identified from the measurements as the bias voltage that gives minimum HD2 power. In this case the value is approximately 3.15 V.

### 6.3.3 Noise Measurements

We proceed with the noise power spectral density (PSD) measurement, as shown in Figure 6.3(c). The measured values (after correction of the LNA gain) are shown as triangle markers while the simulation result is shown as a dashed line. The simulated noise PSD comprises the effects of thermal noise, shot noise and RIN. It can be written as

$$p_{\mathrm{N}} = p_{\mathrm{th}} + \frac{1}{4}\left(2q\, I_{\mathrm{av}}\, R_{\mathrm{L}} + 10^{\frac{\mathrm{RIN}}{10}}\, {I_{\mathrm{av}}}^2 R_{\mathrm{L}}\right), \tag{6.10}$$

where $p_{\mathrm{th}}$ is the thermal noise contribution and the first and the second terms in the parentheses are the shot noise and the RIN contributions, respectively. These quantities are expressed in W/Hz. Since we measured the average photocurrent, the unknown factors in the equation above are $p_{\mathrm{th}}$ and RIN. The thermal noise is dominant when the photocurrent is low whereas the RIN dominates when the photocurrent is high (see, for example, Figure 3.5 of Chapter 3). By carefully adjusting the values of these quantities, we can match the simulation result with the measured values. The best match is obtained when $p_{\mathrm{th}}$ and RIN, expressed in decibels, take the values of -172.5 dBm/Hz and -160 dB/Hz, respectively. The thermal noise value is slightly higher than the thermal noise contribution from a matched load which amounts to -174 dBm/Hz and this difference can be attributed to the noise contribution from the LNA (1.2 dB noise figure) used during the measurements. As for the RIN, the maximum value prescribed in the datasheet was -135 dB/Hz.

Furthermore, we calculated the noise figure (NF) of our APL using the expression in Equation (6.2). The results are shown in Figure 6.3(d). The square markers in the figure indicate the calculated NF using the measured data of $P_{\mathrm{N}}$ and $G$, while the dotted line indicates the simulation result, which is the expression in Equation (6.2) with the simulated values of $P_{\mathrm{N}}$ and $G$. As we can see that the measurement and the simulation results show a very good agreement.

### 6.3.4 SFDR Measurements

Finally, we characterized the system in terms of the SFDR. For this measurement, we choose to operate the modulator at the quadrature bias, i.e., $\phi_{\mathrm{B}} = \pi/2$. For our modulator this corresponds to $V_{\mathrm{bias}} = 3.15$ V. At this point, all even-order distortion terms vanish. Recall that the SFDR is defined as the ratio of two input powers, one being the power that gives a 0 dB SNR and the other being the input power where the intermodulation distortion (IMD) power is equal to the noise power (see Chapter 2 Section 2.5). The IMD terms are generated if a pair of modulating tones are used as the input signals. Due to the limitation in our measurements setup, we characterize the link nonlinearity using a single tone test instead of the two-tone test. This means that we can only generate harmonic distortions, which occur at frequencies which are integer multiples of the signal frequency. However, we can predict the powers of the IMD products that would have appeared if a two-tone test were performed instead. This prediction was based on the fact that the intermodulation products and the harmonic distortions come from the same nonlinearity

source, in this case in the MZM. The amplitudes relation of the IMD and the HD terms can be seen in Table 2.2 in Chapter 2. Providing that the input power of the individual tone in the two-tone test is equal to the tone power in the single tone test, the relation of IMD2 and IMD3 powers with respect to the HD2 and HD3 powers can be written as the following:

$$P_{\mathrm{IMD2}}\ (\mathrm{dBm}) = P_{\mathrm{HD2}}\ (\mathrm{dBm}) + 6\ \mathrm{dB}\,, \tag{6.11}$$

$$P_{\mathrm{IMD3}}\ (\mathrm{dBm}) = P_{\mathrm{HD3}}\ (\mathrm{dBm}) + 9.5\ \mathrm{dB}\,. \tag{6.12}$$

The equations above are very useful in predicting the SFDR of the system even though only a single tone test was performed. In practice, the condition when these relations hold depend strongly on the frequency response of the APL, particularly for the relation in Equation (6.12). For a single tone test with the tone frequency of $f_1$, the HD2 and HD3 terms will appear at frequencies $2f_1$ and $3f_1$, respectively. In a two-tone test with frequencies $f_1$ and $f_2$ where the tones are closely spaced $(f_1 \approx f_2)$, one of the IMD2 terms fall in the frequency of $f_1 + f_2$ while the one of the IMD3 terms appears at $2f_2 - f_1$. Thus, the frequency difference of the IMD2 product and the HD2 product is $|f_2 - f_1|$ while the difference of the HD3 and the IMD3 products is $4f_1 - 2f_2 \approx 2f_1$. Thus, the IMD2 and the HD2 terms are located in the same region while the HD3 and the IMD3 are located far more apart. This is illustrated in Figure 6.4.

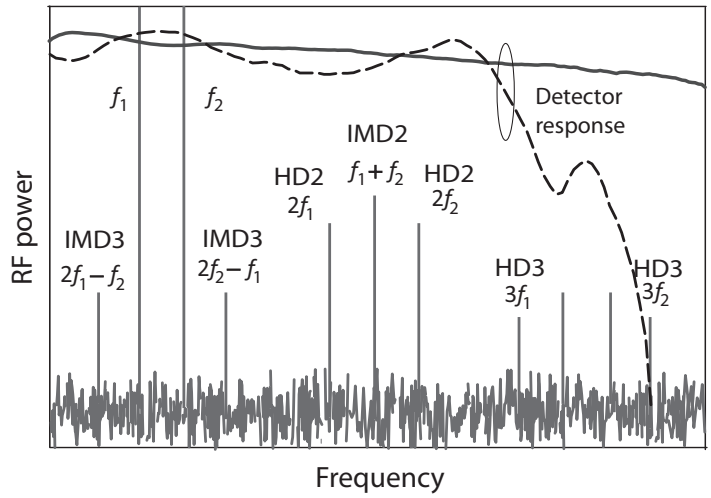


**Figure 6.4:** A two tone test spectrum superimposed with two photodetector responses. The solid line represents a wideband detector whereas the dashed-line represents a narrowband detector.

At the same figure, we superimpose two frequency responses, supposedly from a wideband (solid line) and a narrowband (dashed-line) photodetectors. For the

wideband detector, the frequency response is flat up to the high frequency of three times the tone frequency, whereas in the case of the narrowband detector, the frequency response decreases very sharply at high frequency. In both cases, the IMD2 and the HD2 components fall in the small region where the frequency responses still can be considered flat. this is not the case for HD3 and IMD3 components. Because they are separated relatively further, the HD3 components experience much lower frequency response relative to the IMD3 components, in the case of the narrowband detector. In this case, the relation in Equation (6.12) does not hold anymore. In contrast, the relation holds in the case of a wideband detector because the both the IMD3 and the HD3 components are still located in the flat portion of the response. In our measurements, we use a detector with a 3-dB bandwidth of 12 GHz. The modulating tone supplied to the system has the frequency of 2 GHz. The HD3 components appear at the frequency of 6 GHz, which is relatively small compared to the cut-off frequency of the detector. This will ensure that the relations in Equations (6.11) and (6.12) hold. In the rest of this chapter, we will use these relation in determining the IMD powers and subsequently the SFDR.

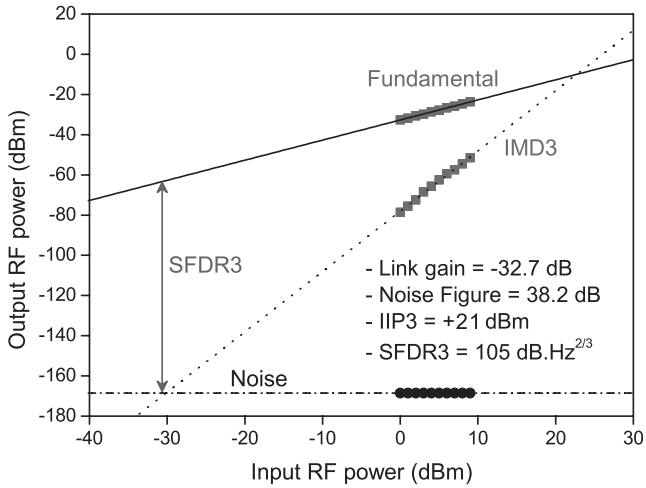


**Figure 6.5:** The SFDR measurement of the MZM APL described in this section.

For the SFDR measurements, the input optical power to the MZM was set at 11 dBm and the RF signal power was varied from 0 dBm to 9 dBm with a step of 1 dB. The fundamental signal and the HD3 powers at the photodetector output are measured with the spectrum analyzer. Because the MZM was biased at the quadrature, the HD2 power was very low and could not be measured. Using the measured HD3 power, the IMD3 power was calculated using Equation (6.12). The detected photocurrent in this case is 1.58 mA and the noise PSD amounts to -168.5 dBm/Hz. The measured fundamental signal, the IMD3 and the noise powers are then extrapolated to extract the information of the third-order input intercept point (IIP3) and the third-order SFDR ($SFDR_3$). The measured and the extrapolated values are

depicted in Figure 6.5. The IIP3 value obtained from the extrapolation is 21 dBm, while the $SFDR_3$ amounts to 105 $dB.Hz^{2/3}$. Furthermore, we can also determine the link gain and the noise figure values from these measurements which are -32.7 dB and 38.2 dB, respectively. These values are compared with the calculated values, derived from the data obtained from the previous measurements. Recall that the $V_{\pi,\mathrm{RF}}$ value derived from the measurements is 3.8 V. Using Equation (6.4), the calculated IIP3 is 20.8 dBm. Thus, there is a 0.2 dB difference between the measurement and the calculation, which can be attributed to the error in the distortion measurements.

We proceed with calculating the link gain from the measured average photocurrent. This can be done by inserting Equation (6.6) into Equation (6.1) and using the value $\phi_B = \pi/2$, yielding

$$g_{\mathrm{MZM,Q}} = \left(\frac{\pi R_L I_{\mathrm{av}}}{2 V_{\pi,\mathrm{RF}}}\right)^2, \tag{6.13}$$

where the additional subscript Q denotes quadrature biasing. Inserting the measured $I_{\mathrm{av}}$ value of 1.58 mA, the calculated link gain amounts to -29.8 dB. But recall that we have an additional 2.9 dB of RF loss in our setup. Thus, this portion should be extracted from the calculated link gain, yielding a link gain value of -32.7 dB. this is exactly the value obtained directly from the link gain measurement. Using this value and the noise PSD value, we calculate the NF using Equation (6.2) and the result is 32.8 dB. Finally, the $SFDR_3$ is calculated using Equation (6.5) resulting at the value of 104.4 $dB.Hz^{2/3}$. Thus the difference between the measured and the calculated $SFDR_2$ is 0.6 dB. The comparison between the measured and the calculated metrics for the link is summarized in Table 6.2.

**Table 6.2:** Comparison of Measurement and Simulation in the Standard APL

| Quantity | Measured | Calculated | Unit |
|---|---|---|---|
| Link Gain | −32.7 | −32.7 | dB |
| Noise Figure | 38.2 | 38.2 | dB |
| IIP3 | 21 | 20.8 | dBm |
| $SFDR_3$ | 105 | 104.4 | $dB.Hz^{2/3}$ |

## 6.4 APL with a High Power DFB Laser

In the previous section, we have shown the characterization results of the MZM used in the experiments. Moreover we have described the link performance in terms of the performance metrics. The link exhibits a very low link gain (-32 dB) and a very high noise figure (38 dB). These values are too high for practical applications [13]. Recall that the link performance can be improved by means of increasing the input optical power to the modulator (see Chapter 3). In this section, we will

present the measurement results on the APL using the same components described in the previous section apart from the laser source. We replace the laser with a high power laser diode with a maximum output optical power of 120 mW.

### 6.4.1 Laser Characterization

The laser used in the experiments is a high power DFB laser (AA1401-193200-080) from EM4, inc. The laser is packaged in a 14-pin butterfly package and pigtailed with a PM fiber. The emission wavelength of the laser is 1561.42 nm. The laser characterization started with the L-I curve determination. The measurement setup for this characterization is shown in Figure 6.6.

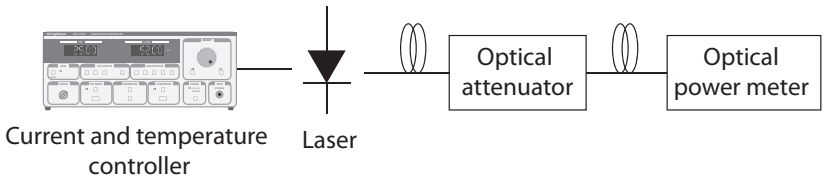


**Figure 6.6:** The measurement setup for L-I curve characterization.

The laser injection current was varied from 50 mA to 550 mA with a step of 50 mA. An optical attenuator (Agilent 8156A) was used to limit the optical power going to the optical power meter (HP 8153A) to avoid the saturation of this power meter. The measured insertion loss of the attenuator was approximately 3 dB. The resulting L-I curve is shown in Figure 6.7(a). At the injection current of 500 mA the laser emits an optical power of 112 mW.

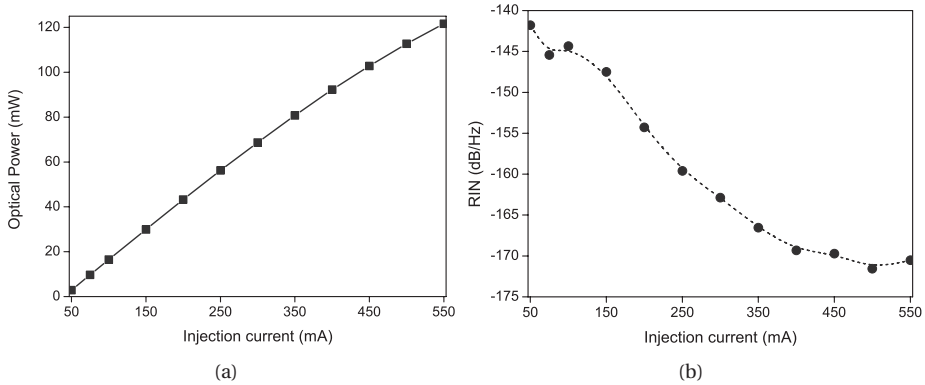


**Figure 6.7:** The measured LI curve (a) and RIN (b) of the high power laser used in the experiments, as functions of the injection current.

Next, the laser noise characteristic was investigated. The noise measurement setup is shown in Figure 6.8. As in the previous measurement, the injection current

was varied from 50 mA to 550 mA. The optical power is attenuated and the detected with a photodetector. The attenuation was set such that the maximum average photocurrent was 12.8 mA, at the laser bias of 550 mA. An LNA with a gain of 36.5 dB was used to reduce the DANL of the RF spectrum analyzer. The noise PSD was measured using a noise marker, placed at the frequency of 2 GHz.

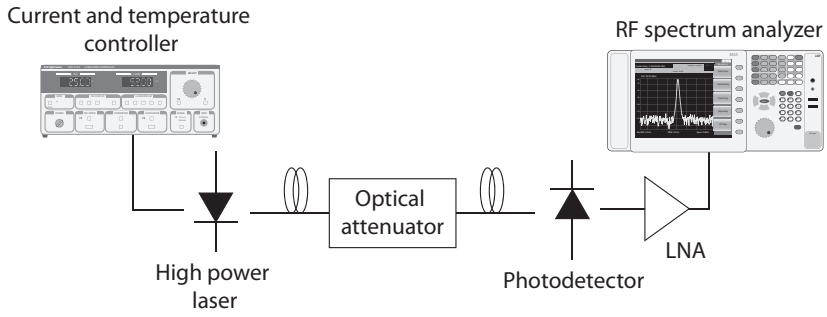


**Figure 6.8:** The measurement setup for laser RIN characterization.

The LNA gain was corrected from the measured noise PSD. Furthermore, the thermal noise and the shot noise contribution were subtracted from the corrected noise PSD (in W/Hz) yielding the laser RIN PSD (see Equation (6.10)). This procedure to extract the RIN from the measured noise PSD was described in detail in Chapter 4 Subsection 4.4.3. The resulting RIN, expressed in dB/Hz is shown in Figure 6.7(b). The lowest RIN is obtained at the laser injection current of 500 mA, which amounts to -171 dB/Hz. For this reason, we choose to use the bias current of 500 mA as the operating bias current of the APL.

### 6.4.2 APL Performance

We repeat the measurements presented in the previous section, with the measurement setup as shown in Figure 6.1, by varying the MZM bias voltage from 0 V to 3.5 V. The RF tone with a frequency of 2 GHz and power of 0 dBm was supplied to the MZM. The laser was biased at 500 mA resulting in an input optical power to the MZM of 112 mW or 20.5 dBm. The characterization results along with the simulation results are depicted in Figure 6.9 (a) to (f). From the measurements of the photocurrent, the link gain, the HD2 and the HD3 shown in Figure 6.9 (a) to (d), we verified the MZM characterization result presented in the previous section. Here, we obtained that the values of $V_{\pi,\mathrm{RF}}$, $L$ and $V_{\pi,\mathrm{DC}}$ are 3.8 V, 5 dB and 5.3 V, respectively. The RF half-wave voltage and the insertion loss values agree very well with the values obtained from the previous characterization. However, a slight difference is observed in the DC half-wave voltage value (4.9 V obtained in the previous experiment). This difference might be attributed to the bias drifting observed at both experiments that add to the uncertainty in the measured $V_{\pi,\mathrm{DC}}$. This bias drifting is a well-known phenomena and has been addressed in various publications [33, 165] as well as in this thesis, in Chapter 3.

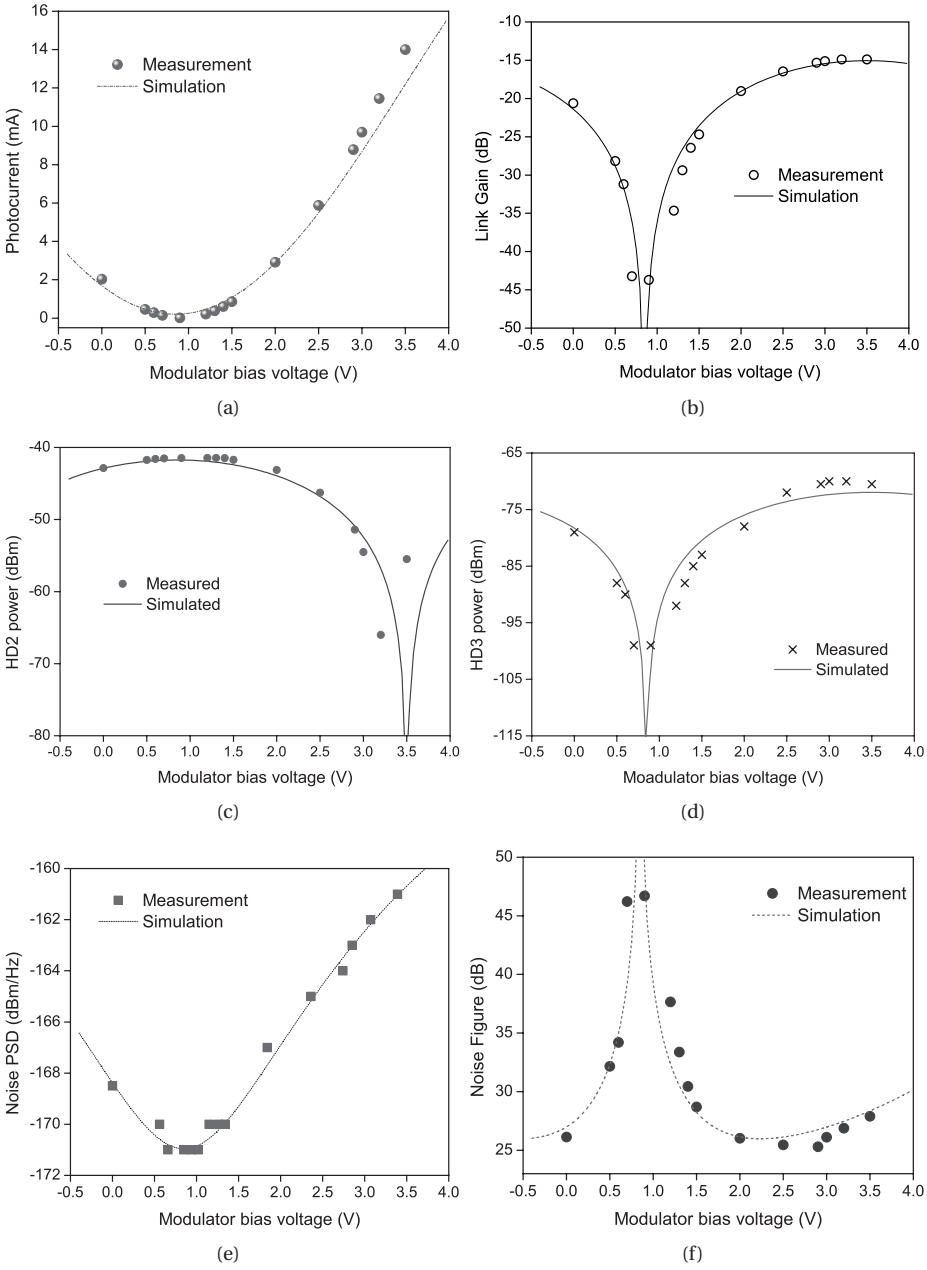


**Figure 6.9:** The measurement results of the MZM APL using the high power laser diode. (a) Average photocurrent, (b) Link gain, (c) HD2 power, (d) HD3 power, (e) Noise power spectral density, (f) Noise Figure.

In Figure 6.9 (e) and (f), the noise PSD and the noise figure as functions of the modulator bias are shown, respectively. From these data, we verified the thermal noise contribution to the total noise PSD was -171.1 dBm/Hz and the RIN of the laser of -171 dB/Hz. The thermal noise contribution measured previously was -172.5 dBm/Hz which is slightly different from the current measurement. A significant difference is observed in the RIN values of the laser used in the previous experiments, which has the RIN of-160 dB/Hz, with the high power laser used in this measurement. Since the high power laser also boosts the APL link gain, the noise figure of this link is vastly improved relative to the APL investigated earlier. The minimum noise figure in the previous case was in the neighborhood of 40 dB. Using the high power laser improves the noise figure to approximately 25 dB. We will discuss the improvements in the following subsection.

### 6.4.3 Quadrature Biasing: Noise Figure

Following the MZM characterization, we investigate the APL performance when the MZM is quadrature-biased. In this case the bias voltage that corresponds to the quadrature bias is 3.2 V. First of all, we investigate the noise figure behavior as a function of the received optical power. The setup for this measurement is shown in Figure 6.10.

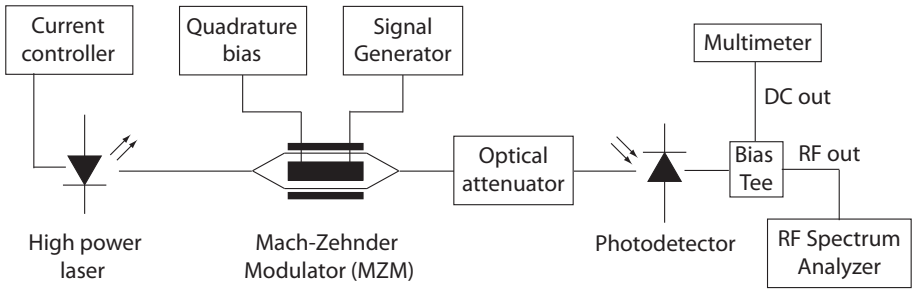


**Figure 6.10:** The measurement setup for noise figure characterization of the APL with the high power laser.

A variable optical attenuator (VOA) is used to adjust the received optical power in the detector. The attenuation was varied from 0 dB to 20 dB with a step of 1 dB. This measurement was performed for three different values of laser injection current, namely 100 mA, 200 mA and 500 mA. The reason to use different injection current values is to have different RIN levels, since from the previous investigation, we have shown that the laser RIN level varies significantly with the injection current variation. The modulating RF signal supplied to the modulator has the frequency of 2 GHz and 0 dBm power. For each injection current value and attenuation level the fundamental signal power and the noise PSD were measured at the detector output. The noise figure was then calculated using the expression in Equation (6.2).

The measurement results are shown in Figure 6.11. For low received optical power (from -15 dBm up to -2.5 dBm), the link noise figure improves as the received

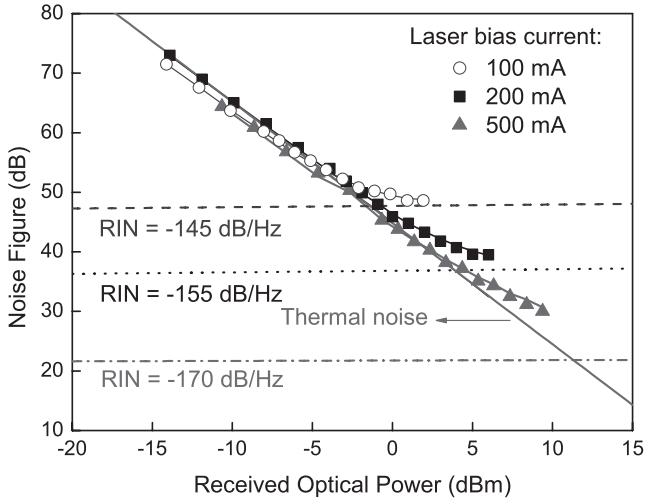


**Figure 6.11:** The noise figure for various values of the laser injection current plotted against the received optical power.

optical power increases. This is because in this region the link is limited by the thermal noise. The simulated NF taken into account only the thermal noise contribution is depicted and indicated in the figure. For the injection current of 100 mA, increasing the received optical power beyond 0 dBm will not improve the link NF. This due to the RIN that dominates at higher received power. As expected in a RIN dominated APL, NF saturation is observed. By properly adjusting the RIN value in the simulation, we can conclude that for an injection current of 100 mA, the laser RIN is approximately -145 dB/Hz. The NF contribution from this RIN is indicated as the horizontal line in the figure. If the injection current is increased to 200 mA, the NF saturation occurs at the received optical power of around 5 dBm. Hence, the laser yields lower RIN compared to the prior case. In this case, the RIN amounts to -155 dB/Hz. Note that the simulated RIN values at these two different injection current levels agree very well with the measured values shown in Figure 6.7(b), which are -144.3 dB/Hz and -154.2 dB/Hz for injection current of 100 mA and 200 mA, respectively. Finally, for an injection current of 500 mA, the NF keeps improving until the maximum received optical power of 10 dBm (or 0 dB attenuation in the measurement) was reached. According to the measured RIN at this current level (-171 dB/Hz), the NF would saturate at the value of around 21.5 dB.

### 6.4.4 Quadrature Biasing: SFDR

We proceed with the characterization of the APL SFDR. As mentioned earlier, due to the quadrature biasing, the even-order distortion vanishes leaving the third-order distortion as the primary source of APL nonlinearity. In the SFDR measurements, the laser is biased at 500 mA, yielding an optical power of 112 mW and minimum

RIN of -171 dB/Hz. The optical attenuator in the setup depicted in Figure 6.10 is removed to maximize the received optical power. The measured average photocurrent is 14.1 mA. The input RF power to the modulator was varied from -5 dBm up to 5 dBm with a step of 1 dB. For each input RF power the fundamental signal and the HD3 powers were measured and the IMD3 power was calculated using the relation in Equation (6.12). The measured noise PSD was -162 dBm/Hz. The measurement results are plotted in Figure 6.12.

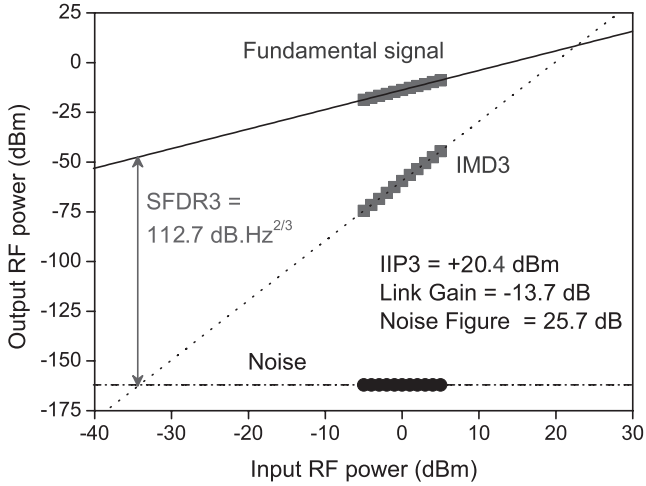


**Figure 6.12:** The measured SFDR for the quadrature biased link with the high power laser.

The link gain, NF, IIP3 and $SFDR_3$ values obtained from the measurements are -13.7 dB, 25.7 dB, 20.4 dBm and 112.7 dB.$Hz^{2/3}$, respectively. We can compare these values with the simulation results, using the expressions in Equations (6.13), (6.2), (6.4) and (6.5), respectively, for the link gain, NF, IIP3 and $SFDR_3$. Using the $I_{av}$ = 14.1 mA, $V_{\pi,RF}$ = 3.85 V and as the input parameters, the simulated link gain value is -10.8 dB. but taking into account the additional RF loss of 2.9 dB in the link, the corrected link gain is -13.7 dB, which agree very well with the measurements. The rest of the simulated metrics, compared with the measurements, are summarized in Table 6.3.

**Table 6.3:** Quadrature biased MZM with a high power laser diode

| Quantity | Measured | Calculated | Unit |
|---|---|---|---|
| Link Gain | −13.7 | −13.7 | dB |
| Noise Figure | 25.7 | 25.7 | dB |
| IIP3 | 20.4 | 20.8 | dBm |
| $SFDR_3$ | 112.7 | 112.8 | dB.$Hz^{2/3}$ |

Compared to the link investigated in the previous section, the APL with the high power laser has shown a significant performance improvements. The link gain is improved by 19 dB. This improvement is obtained due to the increase in the input optical power to the modulator. In the previous case, the input optical power is 11 dBm, while in this case it amounts to 20.5 dBm. Hence an increase of 9.5 dB of optical power has been achieved. Since the link gain is proportional to the square of this input power (see Equation (6.1)), the expected increase in the link gain is simply $2 \times 9.5 = 19$ dB, which is exactly the value obtained from the measurements. Besides the gain enhancement, NF reduction was also observed. The link NF has improved by 12.5 dB. This improvement is attributed to both the increase in the link gain and the reduction in the laser RIN. For example, supposed that the high power laser has the same RIN as the laser used in the previous experiments, i.e. RIN = -160 dB/Hz instead of -171 dB/Hz. Thus, the NF reduction will only come from the effect of the increase in the link gain and will be limited to approximately 8.2 dB.

Unlike the gain and the NF, theoretically the IIP3 value should not change with the increase of input optical power. The 0.6 dB difference between the two measurements is merely a measurement error. Since the IIP3 is unchanged, the increase of $SFDR_3$ in this case is simply 2/3 times the NF reduction. In this case $2/3 \times 12.5 = 8.3$ dB. The improvements obtained from the measurement is $112.7 - 105 = 7.7$ dB. The 0.6 dB difference is attributed to the measurement error. Nevertheless, we have shown the improvement in the link performance by means of using the high power laser diode.

### 6.4.5 Low Biasing: Noise Figure

We have shown that using a high power laser diode can improve the link performance. As discussed in Chapter 2, low biasing the modulator can reduce the noise figure of the APL. The NF reduction will lead to enhancement of $SFDR_3$ but comes at expense of elevated even-order distortion powers. Depending on the dominant noise source in the link, different NF improvement can be expected from low biasing. RIN limited links can benefit highly from low biasing while the advantage is very limited for shot noise limited links (see Chapter 3, Subsection 3.2.2). Here we will investigate the effect of low biasing on the link performance with the high power laser.

The simulated noise figure as function of the MZM bias voltage is shown in Figure 6.13. In this case the NF advantage obtained from low biasing is limited to slightly more that 1 dB. This is because the link is not RIN limited but shot noise limited instead. This can be seen by inspecting the ratio between the RIN PSD relative to the shot noise PSD at the quadrature bias. This quantity can be expressed as (RIN $I_{av}$) / $(2q)$, where $q$ is the electron charge. For RIN=-171 dB/Hz and $I_{av}$ = 14.1 mA, the ration of the RIN and the shot noise PSDs, express in decibels, amounts to -4.5 dB. Thus, we can conclude that the shot noise dominates over the RIN and the maximum advantage of low biasing is limited to 3 dB [141], as discussed in Chapter 3.

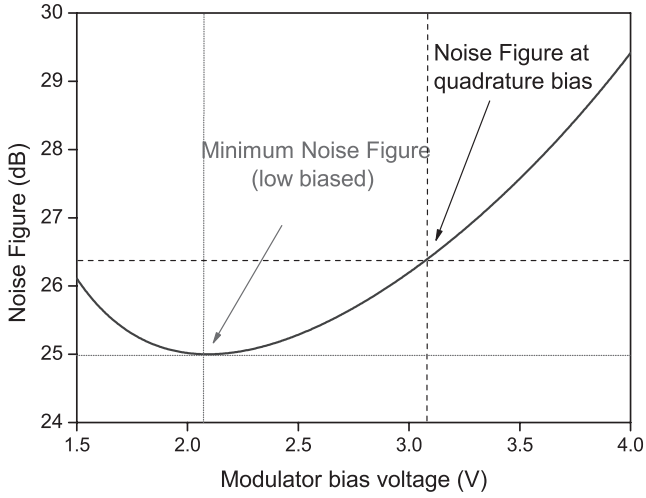


**Figure 6.13:** The simulated noise figure as function of the modulator bias voltage. The input optical power is set at 20.5 dBm and the RIN is -171 dB/Hz. Additional parameters: $V_{\pi,\mathrm{DC}} = 5.3$ V, $V_{\pi,\mathrm{RF}} = 3.85$ V and $L = 5$ dB

### 6.4.6 Low Biasing: SFDR

In this subsection we will measure the APL characteristics when the MZM is low biased. According the Figure 6.13, the minimum NF is obtained around bias voltage of 2.0 V. We choose this bias voltage as the operating point and perform the SFDR measurement by means of varying the RF input power to the MZM, from -5 dBm to 5 dBm with a step of 1 dB. Since the MZM is biased off-quadrature, the even-order distortion terms are not suppressed anymore. The fundamental signal, HD2 and HD3 powers are measured and the IMD2 and IMD3 powers are calculated from these harmonic distortions. The measured noise PSD was -166 dBm/Hz at the average photocurrent of 4.6 mA. The measurement results and the extrapolation of the output RF power components are shown in Figure 6.14.

As expected, the low biased APL has a second-order SFDR ($\mathrm{SFDR}_2$) which is much lower than $\mathrm{SFDR}_3$. This means that in contrast to the quadrature-biased link, the low biased link is only suitable for narrowband or sub-octave applications (see Chapter 2, Subsection 2.4.3 and Chapter 3, Subsection 3.2.2). Moreover, the noise figure reduction obtained with low biasing, relative to the quadrature biasing is limited to less than 1 dB. In order to verify the results obtained from the measurements, we use the measured average photocurrent (4.6 mA) and the modulator characteristics to calculate the the APL metrics. First of all, using Equation (6.6), we found that the modulator bias angle, $\phi_{\mathrm{B}}$ is equal to $49.1^{\mathrm{o}}$. If we use the definition $\phi_{\mathrm{B}} = \pi V_{\mathrm{bias}} / V_{\pi,\mathrm{DC}}$, we found that $V_{\mathrm{bias}} = 1.44$ V. Taking into account the minimum transmission point of our modulator is approximately at 0.71 V, the corrected bias voltage will be $1.44 + 0.71 = 2.15$ V, where compared to the setting point in our measurement which is 2.0 V.

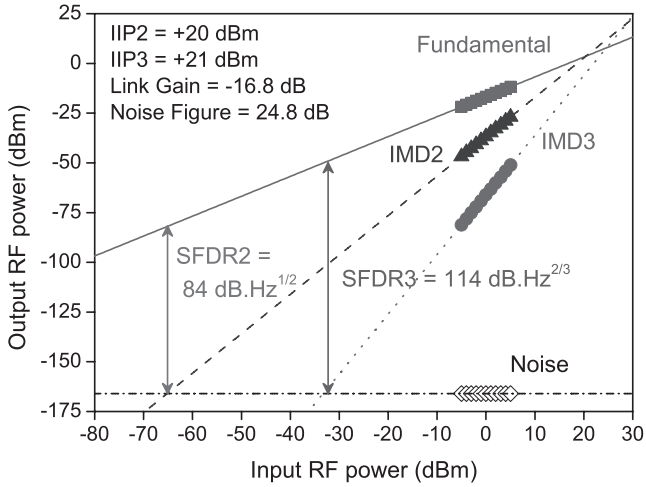


**Figure 6.14:** The measured SFDR for the low biased link with the high power laser.

Having verified the bias angle, we use the value of $\phi_B$ to calculate the link gain using Equation (6.1) (note that Equation (6.13) cannot be used anymore since the relation only holds for quadrature biasing). The calculated link gain is -16.6 dB (see Figure 6.9(b)). Using the information of this link gain and the measured noise PSD, the NF is calculated to be 25.6 dB (Figure 6.9(f)). Moreover, using Equation (6.3), the IIP2 is calculated to be 19 dBm, while the IIP3 value remains unchanged (20.8 dBm) since it is independent of the bias angle (see Chapter 2, Subsection 2.4.6). Finally, using the IIP values, the $SFDR_2$ and $SFDR_3$ were calculated, yielding the values of 84 dB.Hz$^{1/2}$ and 113.5 dB.Hz$^{2/3}$, respectively. The comparison between the measured and the simulated metrics of the low biased link is summarized in Table 6.4.

**Table 6.4:** Low biased MZM with a high power laser diode

| Quantity | Measured | Calculated | Unit |
|---|---|---|---|
| Link Gain | −16.8 | −16.6 | dB |
| Noise Figure | 24.8 | 24.6 | dB |
| IIP2 | 20 | 19 | dBm |
| IIP3 | 21 | 20.8 | dBm |
| $SFDR_2$ | 84 | 84.2 | dB.Hz$^{1/2}$ |
| $SFDR_3$ | 114 | 113.5 | dB.Hz$^{2/3}$ |

Comparing the values in the table above, we can see that most of the measured metrics agree very well with the calculation. A notable difference is obtained in the IIP3 results and subsequently the $SFDR_3$ values. Moreover, we have demonstrated that by means of low biasing, the link performance can be enhanced, but

the degree of enhancements depends strongly on the dominant noise source in the link. In our case, the laser RIN is already low such that the advantage of low biasing is negligible (Chapter 3, Subsection 3.2.2). However, we can compare the performance of the quadrature-biased and the low-biased link in terms of the average photocurrent. Note that comparable performance with the quadrature biased link can be achieved with the low biased link with merely one-third of the photocurrent (4.6 mA vs. 14.1 mA). Thus, if the system is limited by the maximum photocurrent of the detector and the bandwidth is not more that one octave, using such low bias scheme can be advantageous.

## 6.5 Optically Amplified APL

As we have learned from the previous section, increasing the optical power in the APL is attractive and useful to enhance the link performance. Beside using a high power laser, a common way to increase the optical power is to use an optical amplifier. Two types of amplifier widely used nowadays are the erbium doped fiber amplifier (EDFA) and the semiconductor optical amplifier (SOA). Choosing between one of them depends on the application and the system design constraints. In our measurements presented here, we use an EDFA to increase the received optical power. The measurement setup where the EDFA is incorporated is discussed in the following subsection.

### 6.5.1 Measurement Setup

The architecture of the optically amplified APL is shown in Figure 6.15. The laser used in the experiment is the 1550 nm DFB laser from Agere with maximum optical power of 11 dBm at 110 mA injection current. The modulator and the photodetector used in the setup were the ones described in the previous experiments. The EDFA was placed after the modulator and before the detector. In this way, we can avoid exceeding the prescribed maximum optical power to the modulator, which is 20 dBm. There are two variants of the setup considered here. First is the architecture where a variable optical attenuator (VOA) is placed between the MZM and the EDFA (Figure 6.15 (a)). We will refer this arrangement as the MZM-VOA-EDFA link. The second arrangement is shown in Figure 6.15 (b), where the positions of the EDFA and of the VOA in the link are interchanged. We will refer this arrangement as the MZM-EDFA-VOA link.

The VOA was used in the setup to for two different reasons. First, it is useful to investigate the behavior of the optically amplified link (i.e. gain, noise figure) for different modulated optical power levels. The VOA is in fact used to emulate an optical device or system that might contribute to a loss in the link. As an example of these systems are the optical delay elements of a beamforming network. The reason to differentiate the placements of the VOA is also related to this reason. One of the goals of the study presented here, beside the APL characterization is also to determine the optimum way to incorporate these loss-inducing systems or devices in the optically amplified APL.

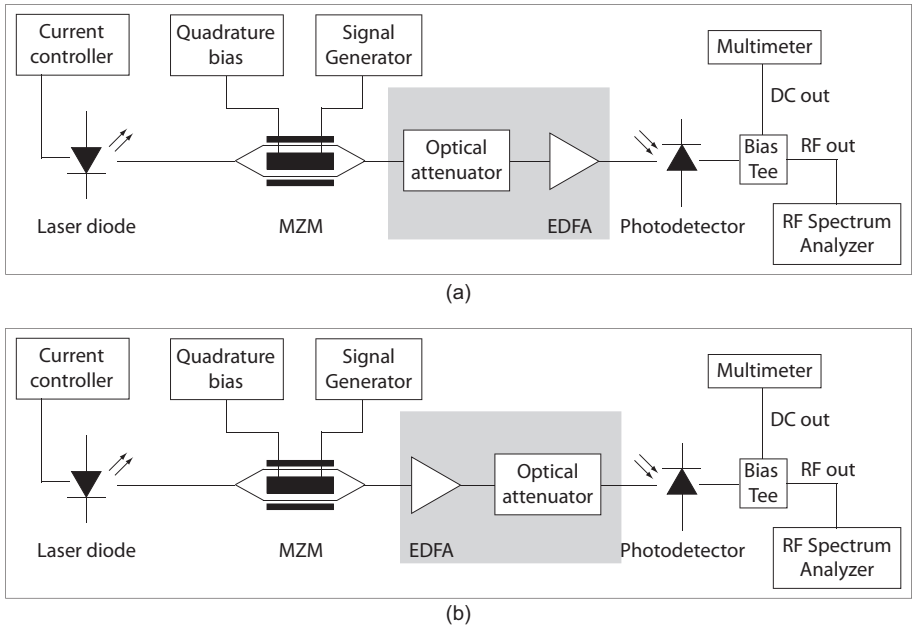


**Figure 6.15:** The two measurement setups used in the experiments. (a) APL with the VOA before the EDFA, and (b) APL with VOA after the EDFA.

Prior to the link characterizations, we characterize the EDFA. The results are discussed in the following subsection.

### 6.5.2 EDFA Characterization

The EDFA used in the measurement is the Keopsys KPS-BT-C-27-PB-FA, with a maximum output optical power of +27 dBm. The EDFA can be operated in two different modes. One is the so-called automatic current control (ACC) mode. In this mode, the current of the pump laser of the EDFA is fixed, i.e. specified by the user and the EDFA output optical power is proportional to the input optical power. The other mode is the so-called automatic power control (APC) mode. In this mode the output optical power is fixed regardless of the input optical power. The measured relation between the input optical power and the output optical power for both modes of operation are shown in Figure 6.16(a). For these measurements, the output optical power was fixed at 12.5 dBm for the APC mode, while for the ACC mode, the pump laser current was fixed at 0.44 A. The EDFA gain for both modes, defined as the ratio of the output optical power and the input, as functions of the input optical power are depicted in Figure 6.16(b). Note that for both cases, the EDFA gain decreases with the increase of input optical power. This is quite intuitive for the APC mode since the gain needed to amplify a high input optical power to reach a certain output optical power level is smaller relative to the gain required for

amplifying a lower power. As for the ACC mode, the gain decreases with the input power because it takes a higher energy to amplify a high optical power relative to the energy required to amplify a lower optical power. Since the pump laser current is fixed, only limited power of the pump can be transfered to the signal. For example, to amplify an optical signal with 0 dBm power with a 3 dB gain requires an additional power of 1 mW while to amplify a 20 dBm optical power by 3 dB requires an additional 100 mW of power.

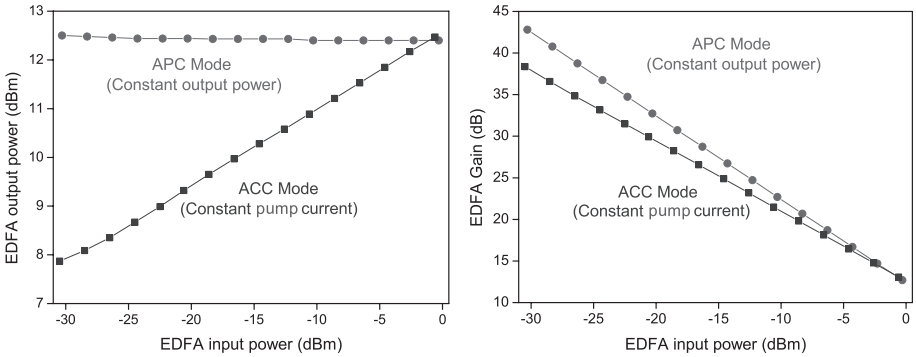


**Figure 6.16:** Characterization results of the EDFA operated in two different modes, automatic current control (ACC) and automatic power control (APC). (a) Output optical power vs. input optical power, and (b) Optical gain vs. input optical power.

### 6.5.3 MZM-EDFA-VOA Link Noise Figure

We start with characterization of the MZM-EDFA-VOA link. The modulator was biased at quadrature and the EDFA was operated in the APC mode. The average output optical power of the EDFA was set at 15.1 dBm . Since the insertion loss of the modulator amounts to 3 dB, the received optical power at 0 dB attenuation is 12.1 dBm, corresponding to an average photocurrent of 12 mA. The input RF power to the system was set at 0 dBm. Next, the attenuation was varied from 0 dB up to 20 dB with a step of 1 dB. The fundamental signal power, noise PSD and the average photocurrent were measured for each attenuation level. We plot the resulting link gain against the measured average photocurrent in Figure 6.17(a). In the same figure, the calculated link gain obtained by inserting the measured average photocurrent into the expression in Equation (6.13) is also shown. There is an excellent agreement obtained between the measured and the simulated values.

In Figure 6.17(b), the measured noise PSD is depicted as a function of the received optical power. These measured values are plotted together with the simulated values, taking into account various noise contributions, namely the thermal noise, shot noise and RIN. The best match between the simulation the mea-

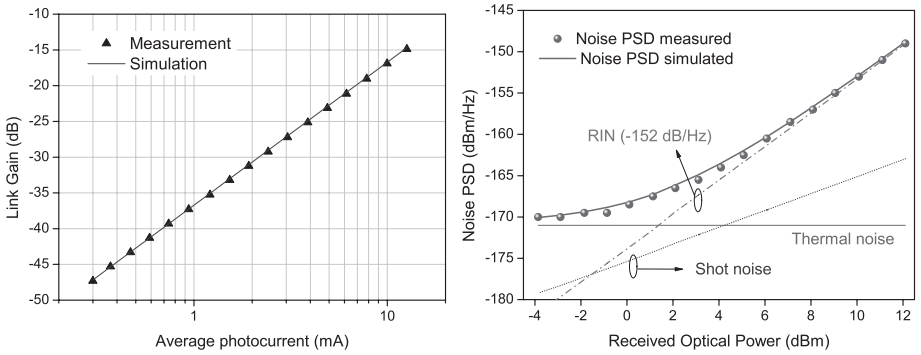


**Figure 6.17:** Characterization results of the MZM-EDFA-VOA link. (a) Link gain vs. average photocurrent photo, and (b) Noise PSD vs. received optical power.

sured values are obtained if the thermal noise PSD and RIN values are taken to be -171 dB/Hz and -152 dB/Hz, respectively. Note that in the previous section we have shown that the RIN from our laser used here amounts only to -160 dB/Hz. Thus it is clear that the RIN observed in our measurements comes not only from the laser but from the combination of the laser and the EDFA. We can conclude then that for the arrangement presented here, noise contribution from the EDFA can be regarded as and additional RIN to the one contributed from the laser [45, 161]. This additional RIN from the EDFA will increase the total link RIN by 8 dB. The noise PSD itself was dominated by the thermal noise at low received optical power and by the RIN at large received optical power.

Finally, we plot the link noise figure (NF) as a function of the received optical power in Figure 6.18. The calculated NF values due to the different noise contributions are depicted as well. Note that the thermal noise dominates up to the received power of 2 dBm. The NF improves when the received power is increased up to 4 dBm. Beyond this optical power, the link is RIN limited and the NF saturates at the values of approximately 40 dB. Supposed that the RIN is -160 dB/Hz instead of -152 dB/Hz, the APL will be thermal noise limited up to the received power of 4 dBm and the NF will saturates at a lower value of around 31 dB, at the received optical power beyond 12 dBm. Clearly adding the EDFA will deteriorate the link NF. We will come back to this conclusion later when we discuss the SFDR of the optically-amplified link.

### 6.5.4 MZM-VOA-EDFA Link Noise Figure

We have seen in the previous subsection that by putting the EDFA before the VOA (i.e. before the loss occurs), the EDFA noise can be regarded as additional RIN and the link NF will deteriorate when the RIN dominates. Here, we will investigate the

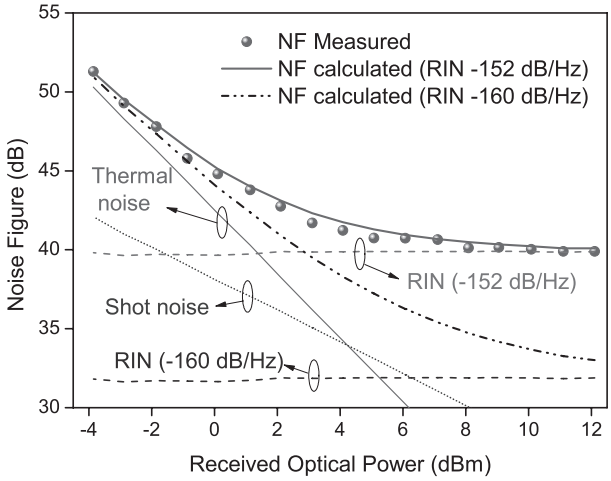


**Figure 6.18:** The link noise figure as a function of the received optical power for the MZM-EDFA-VOA amplified link.

link NF in the case where the EDFA is put after the loss occurs (MZM-EDFA-VOA configuration in Figure 6.15 (b)). One notable difference in the this arrangement compared to the previous one is that here the input power of the EDFA is varied in accordance with the attenuation variation while in the previous case it was kept constant and instead the output power was varied.

The measurements were performed for the ACC and the APC modes of the EDFA. For the ACC mode, the pump laser current was set at 0.44 A while for the APC mode the input optical power of the EDFA was specified at 12.5 dBm. The MZM was biased at the quadrature and the input optical power and RF power were kept the same as in the previous measurements. To vary the input optical power to the EDFA, the attenuation of the VOA was varied from 0 dB to 20 dB with a step of 2 dB. For each input power level, the EDFA gain can be obtained from the EDFA characterization results presented in Figure 6.16(b). The fundamental signal power, the average photocurrent and the noise PSD were then measured.

The measured link gain and the average photocurrent as functions of the input optical power are plotted in Figure 6.19. As expected, both the average photocurrent and the link gain of the APC mode are constant, except for a small deviation which occurs at a low input power. Keep in mind that the link gain and the photocurrent depend on the received optical power which, in this case, is the output optical power of the EDFA. Since in the APC mode the output EDFA power is kept constant, these two quantities will be constant as well. As for the ACC mode, both the link gain and the photocurrent increase with the input optical power. This is because in this mode the EDFA optical output power is proportional to the input power.

Next, we characterize the noise PSD and the noise figure of the link. For this in-

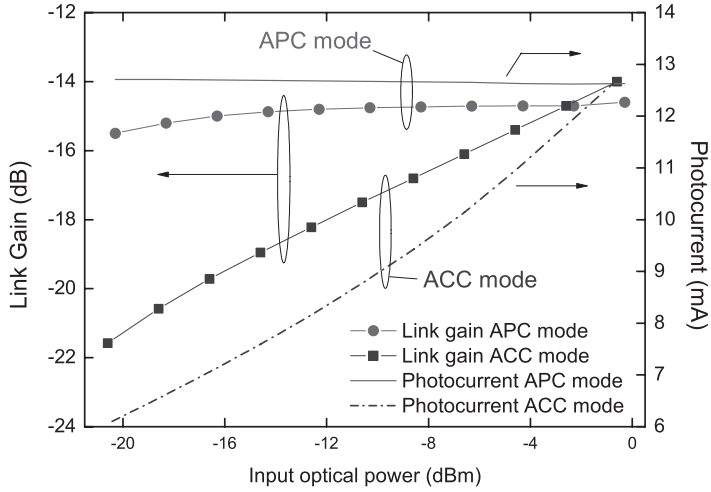


**Figure 6.19:** The measured link gain and photocurrent as functions of the input optical power to the EDFA for the APC and the ACC mode.

vestigation, we will limit ourselves only to the ACC mode. This is because the common noise sources like the shot noise and the laser RIN depend on the received optical power. Since in the APC mode the received optical power is constant, it is less insightful to investigate the noise performance in this mode. The measured noise PSD and the resulting link noise figure as functions of the received optical power are depicted in Figure 6.20(a) and 6.20(b), respectively. These measurement values are depicted together with the contributions of the laser RIN (-160 dB/Hz), the shot noise and the thermal noise (-171 dBm/Hz). Note that none of these sources can represent the behavior of the measured noise PSD, which decreases with the increase of the received optical power. Hence, immediately we can see that in contrast to the case where the EDFA is placed before the VOA, here the EDFA noise contribution cannot be regarded as the additional RIN to the laser RIN contribution. This is mainly because in this case the input optical power to the EDFA is varied, affecting the dynamic in the EDFA [147]. The noise source that can describe the measured noise behavior is the EDFA signal-spontaneous beat noise. The electrical power spectral density of this noise is given by [125, 200]

$$p_{\text{sig-sp,EDFA}} = \frac{1}{4}\left[4h\nu n_{\text{sp}} r_{\text{PD}} P_{\text{out,EDFA}} \left(g_{\text{EDFA}} - 1\right) R_{\text{L}}\right], \tag{6.14}$$

where $h = 6.63 \times 10^{-34}$ Js is the Planck constant, $\nu$ is the optical frequency, $n_{\text{sp}}$ is the spontaneous emission factor, $P_{\text{out,EDFA}}$ is the EDFA output optical power in Watt and $g_{\text{EDFA}}$ is the EDFA gain on linear scale. The factor 1/4 appears due to the resistive impedance matching imposed in the photodetector. For a constant EDFA gain, the sig-sp noise PSD in Equation (6.14) will increase with the EDFA output power, or the received optical power in this case. But note that in the situation described in Figure 6.20, both $P_{\text{out,EDFA}}$ and $g_{\text{EDFA}}$ are changing. In this

case, $P_{\text{out,EDFA}}$ is increasing while $g_{\text{EDFA}}$ is decreasing. The simulated $p_{\text{sig-sp,EDFA}}$ for $n_{\text{sp}} = 1$ [125, 201] and $\nu = 193$ THz is shown together with the measured noise in Figure 6.20(a). The calculated Sig-sp noise fits the behavior of the measured noise. Hence, we conclude that in the case where the input optical power and the gain of the EDFA is varied, the signal-spontaneous noise contribution of the EDFA dominates over the other noise sources. This observation agrees with the earlier reported results in [45, 125, 201]. Moreover, a comparison with the case of MZM-EDFA-VOA arrangement in the previous subsection shows that the MZM-VOA-EDFA architecture considered here shows a higher noise figure. For example, for a received optical power of 12.0 dBm, the previous arrangement yields a noise figure of approximately 40 dB, while here the noise figure is more than 44 dB.

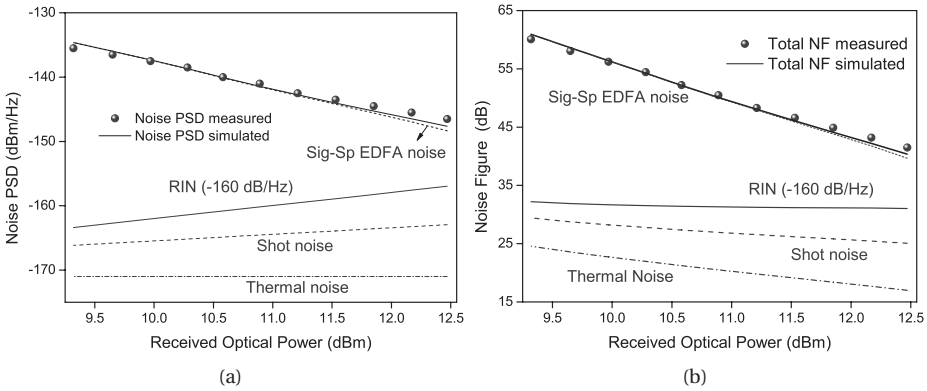


**Figure 6.20:** Noise characterization results of the MZM-VOA-EDFA link operated in the ACC mode. (a) Noise PSD vs. received optical power, and (b) Noise figure vs. received optical power. The link was dominated by the signal-spontaneous (Sig-sp) beat noise of the EDFA

A better comparison of the noise characteristics between these two architectures can be done if the received optical power is kept constant. In this case both the average photocurrent and link gain are also constant. For this purpose, the flow of the measurements was slightly adjusted. For both architectures, the EDFA was operated in the APC mode. For each attenuation level, the EDFA output power was adjusted such that the link gain is constant. Then the noise PSD was measured and the noise figure calculated. The results are shown in Figure 6.21. It is clear that as the attenuation increases the NF of the MZM-VOA-EDFA link deteriorates rapidly, while for the other link the NF remains constant. The NF behaviors of the two links can be predicted by the simulations, as shown as the solid and dash-dotted lines in the figure. For the MZM-EDFA-VOA case, the EDFA RIN (-152 dB/Hz) dominates while in the MZM-VOA-EDFA case, the signal-spontaneous beat noise is dominant.

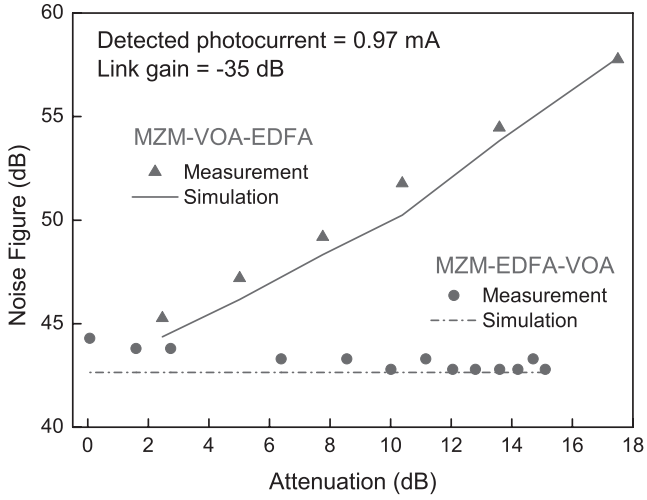


**Figure 6.21:** The measured noise figure comparison between the two link architectures in Figure 6.15 for a fixed photocurrent of 0.97 mA. The solid and the dash-dotted lines denote the simulations results.

### 6.5.5 Gain Enhancement with Low Biasing

We resume our investigation with the bias voltage variation of the optically amplified link. It was shown in Sisto et al. [147] and Urick et al. [67] that using an EDFA after a low-biased MZM will improve the link gain, relative to the quadrature-bias case. The improvements stem from the fact that the link gain scales with the optical gain of the EDFA, which depends on the input optical power to the amplifier. By low biasing then amplifying, a much higher optical gain can be achieved since the EDFA is less saturated, because in the low bias link, the average optical power is much lower compared to the quadrature-biased link.

To investigate this effect, we vary the modulator bias voltage and amplify the optical signals using the EDFA. The EDFA is operated in the APC mode and the output optical power is set at 12.5 dBm. The RF input power to the modulator is set at -10 dBm. We also performed measurements at input power level of 0 dBm, but for this input power the link gain improvement was less compared to the case when a lower RF power is used. The fundamental signal power and the noise PSD were then measured. The resulting link gain, noise PSD and link noise figure are shown in Figures 6.22(a), 6.22(b) and 6.22(c), respectively.

As expected, moving the bias away from the quadrature towards the lowest transmission point increases the link gain. In our measurements the optimum link gain of +5 dB has been obtained at the bias voltage of 0.6 V. There are several interesting aspects of this measured gain. First of all, the positive value indicates that we have obtained a nett RF gain in our link, whilst all the measured link gain values previously discussed here have the negative sign, indicating a nett RF loss. Surprisingly, this positive gain value has been shown with a moderate photocurrent of

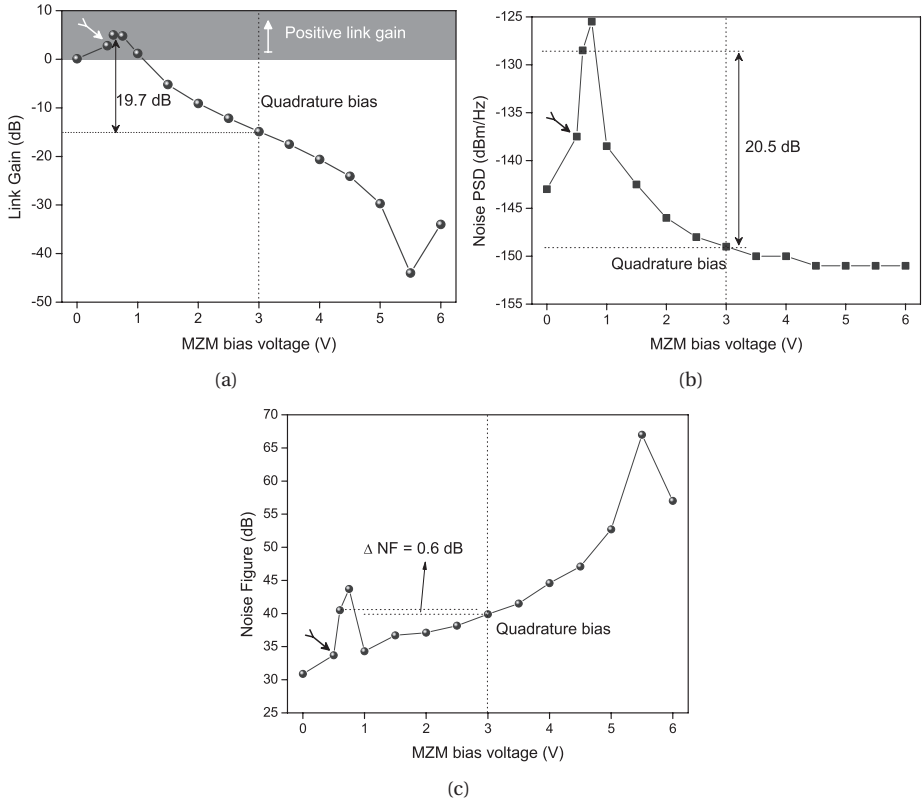


**Figure 6.22:** MZM bias variation in the optically amplified link. (a) Link gain, (b) Noise PSD and (c) Noise Figure. The arrows indicate the data used for the SFDR investigation in the next subsection.

12.6 mA. The quadrature biased link ($V_{\text{bias}}$ = 3 V) with the same photocurrent has the link gain of -14.9 dB. Thus, by optimizing the MZM bias we have shown a gain improvement of nearly 20 dB. Overall, a positive link gain was measured for bias voltages from 0 to 1 V.

Beside increasing the link gain, low biasing also increases the noise in the link. This is shown in Figure 6.22(b). At the bias voltage where the maximum link gain is achieved, the measured noise PSD amounts to -128 dBm/Hz, which is roughly 20 dB higher than the measured value at the quadrature, which is -149 dBm/Hz. Since the increase of noise power and the link gain is roughly equal, the noise figure at 0.6 V is equal to the noise figure at the quadrature bias which amounts to 39.9 dB. Thus, at the bias point where the link gain is maximum, there is no advantage of noise figure obtained. However, a closer look of of Figure 6.22(c) has hinted that the points just below the bias voltage that maximizes the gain yield lower NF relative to the quadrature biased. For example, at the bias voltage of 0.5 V (which

is indicated by the arrows in Figures 6.22(a),6.22(b) and 6.22(c)) the noise figure is 33.5 dB, which is 6.4 dB lower relative to the quadrature bias case. In the following subsection, we will compared the SFDR of the quadrature bias link and the link biased at this point.

### 6.5.6 SFDR Comparison

For the SFDR investigations, we varied the input power of the 2 GHz RF signal from -10 dBm to 3 dBm with a step of 1 dB. In addition to the fundamental signal and the noise powers, we measured the harmonic distortions in addition to the fundamental signals. The IMD2 and IMD3 powers needed to determine the SFDR are then calculated from these harmonic distortion powers using Equations (6.11) and (6.12). The quadrature biased link was biased at 3.0 V and the low biased link was biased at 0.5 V. The average photocurrent for both links was 12.7 mA.

For the quadrature biased link, the measured noise PSD was -149.5 dBm/Hz. The link gain, noise figure, IIP3 and $SFDR_3$ values obtained from the measurements are -15 dB, 39.5 dBm, 22 dBm and 104.5 $dB.Hz^{2/3}$, respectively. The measurement results are shown in Figure 6.23.

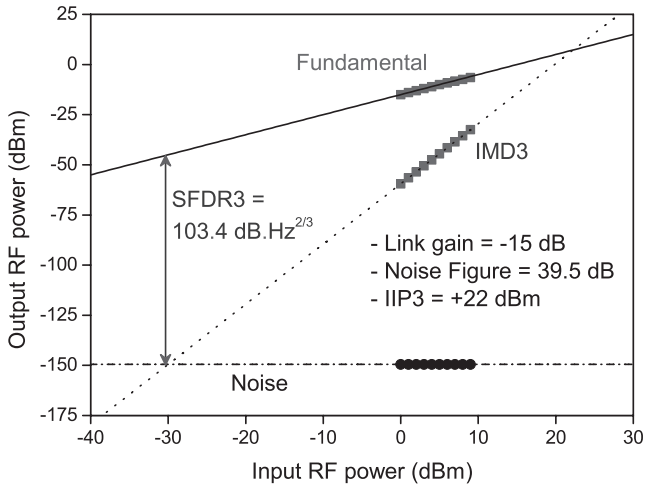


**Figure 6.23:** The measured SFDR for the quadrature biased link amplified with the EDFA.

As demonstrated earlier, the information of the measured noise PSD and average photocurrent are used to predict the gain, NF, IIP3 and the $SFDR_3$. The comparison between the values obtained from the measurements and the simulations are summarized in Table 6.5.

For the low bias link, the measured noise PSD was -137.5 dBm/Hz. The measured link gain and noise figure are +2.9 dB and 33.6 dB, respectively. Unlike the quadrature-biased link, this link is limited by the IMD2 rather than IMD3. The IIP2 and IIP3 values obtained from extrapolations of the measurement data are

**Table 6.5:** Quadrature biased MZM with EDFA

| Quantity | Measured | Calculated | Unit |
|---|---|---|---|
| Link Gain | −15 | −14.6 | dB |
| Noise Figure | 39.5 | 39.2 | dB |
| IIP3 | 22.0 | 20.8 | dBm |
| $SFDR_3$ | 104.5 | 103.8 | $dB.Hz^{2/3}$ |

7 dBm and 11.9 dBm, respectively. The measured $SFDR_2$ and $SFDR_3$ for this link are 73.5 $dB.Hz^{1/2}$ and 101.7 $dB.Hz^{2/3}$, respectively. The measurement results are shown in Figure 6.24.

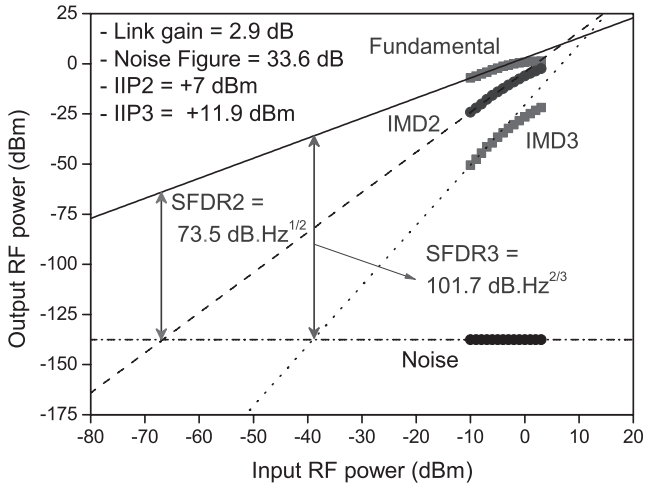


**Figure 6.24:** The measured SFDR for the low biased link amplified with the EDFA.

Although the low bias link shows improved gain and NF relative to the quadrature biased link, these improvements are obtained at the cost of decreased linearity. This is apparent from the reduced IIP3 values, from the expected value of 20.8 dB to 11.9 dB. This reduction primarily comes from the fact that the low bias link generates much more RF photocurrent compared to the quadrature biased link, in which the DC portion is dominant. The increase of this RF current might generate distortion due to the saturation of the photodetector. This saturation effects can be observed in the fundamental, the IMD2 and the IMD3 powers at high input RF power. Moreover, since the low bias link has a much lower $SFDR_2$ than $SFDR_3$ (see Table 6.6), this link is not suitable for broadband applications. But even though the link linearity is reduced, the low biased link is still attractive for applications where the linearity demand is not very high. One of those applications is the optoelectronic oscillator (OEO) [67].

**Table 6.6:** Low biased MZM link amplified with an EDFA

| Quantity | Measured | Simulated | Unit |
|---|---|---|---|
| Link Gain | +2.9 | – | dB |
| Noise Figure | 33.6 | – | dB |
| IIP2 | 7 | – | dBm |
| IIP3 | 11.9 | – | dBm |
| $SFDR_2$ | 73.5 | 73.7 | $dB.Hz^{1/2}$ |
| $SFDR_3$ | 101.7 | 101.5 | $dB.Hz^{2/3}$ |

## 6.6 Summary

In this chapter the measurement results on various MZM link architectures were presented. The so-called standard MZM link consists of a laser with a moderate output power, an MZM and a photodetector with a resistive matching . The performance of such a link is limited in terms of link gain and noise figure. A link gain of -33 dB and noise figure close to 40 dB have been achieved. The link $SFDR_3$ is in the order of 105 $dB.Hz^{2/3}$. If the laser is replaced with a higher power laser, with a ten-fold output power relative to the laser in the standard link, vast improvements in the link gain and noise figure are obtained. The gain, noise figure and $SFDR_3$ of this so-called high power laser MZM link are in the order of -14 dB, 26 dB and 114 $dB.Hz^{2/3}$, respectively. The 19 dB improvement in the link gain is due to the increase in input optical power. On the other hand, the noise figure and $SFDR_3$ improvements are obtained partly because of the increase in the optical power but also because the laser has shown a better RIN value of -170 dB/Hz, which is 10 dB better than the RIN of the laser in the standard link. This has demonstrated that using a higher input power to the MZM with a low noise laser is highly advantageous and desirable.

A further improvement can be achieved by moving the bias point of the modulator away from the quadrature bias towards the lowest transmission point. This low biasing technique reduces the noise figure which in turn increases the $SFDR_3$. But the improvements are obtained at the cost of a decreased link gain and increased even-order distortions. The latter will limit the link $SFDR_2$ and subsequently limit the usability of the link in multioctave (or broadband) systems. Low biasing the high power laser MZM link will reduce the noise figure by only 1 dB. This is because the link is shot noise limited and not RIN limited. It was shown in Chapter 3 that the advantage of the low bias technique is most prominent if the link is RIN limited. The maximum advantage for noise limited links is only 3 dB.

The final architecture considered is the optically amplified link. The optical amplifier used here is the EDFA. Two arrangements of the so-called EDFA MZM link have been considered. The different arrangements are used to determine the optimum placement of the EDFA relative to an optical device or a subsystem which is relatively lossy. The loss of the device was emulated with a variable optical at-

tenuator (VOA). In turns out that by placing the EDFA between the MZM and the VOA (MZM-EDFA-VOA link), the link shows better performance compared to the case where the EDFA is put after the VOA (MZM-VOA-EDFA link). In the earlier setup, the input power to the EDFA is fixed, hence the EDFA noise contribution can be regarded as an additional RIN in the system. In the latter, the optical power to the EDFA varies, affecting the EDFA dynamics. We have shown that in this case the dominant noise source is the EDFA signal-spontaneous beating.

In general, using the EDFA is attractive to increase the link gain but it will limit the link NF and $SFDR_3$. As a comparison, a link gain of approximately -14 dB can be achieved by both the high power laser link and the EDFA link. But for the earlier the noise figure is around 25 dB while the latter has a noise figure of nearly 40 dB. Additionally, the $SFDR_3$ of this EDFA link is 10 dB lower relative to the $SFDR_3$ of the high power laser link. Finally, an interesting behavior has been observed in the low biased EDFA link. A nett (positive) link gain as high as 5 dB has been observed in the measurements, which is a 20 dB improvement relative to the link gain at the quadrature bias. This significant improvement is because the EDFA is less saturated in the low bias case. Unfortunately, this high gain is obtained at the cost of decreased linearity due to increased even-order distortions and the photodetector saturation.

# 7 Conclusions and Outlook

## 7.1 Conclusions

This thesis has investigated the performance of an analog photonic link (APL). Key parameters to describe the link performance, namely the link gain, noise figure, intercept points and spurious-free dynamic range, have been introduced. Various existing methods to improve both directly and externally modulated links characteristics have been considered. These methods include low biasing the modulation device, employing a balanced detection architecture, and increasing the input optical power in the case of external modulation. Extensive measurements were conducted to characterize the performance of the APLs employing these enhancement techniques. The results were compared with the predicted behavior from simulations. Several conclusions can be drawn from these findings.

Several parameters, which are commonly defined for microwave components, have been used to describe the APL performance. These parameters are the link gain, noise figure, input and output intercept points and the spurious-free dynamic range (SFDR). In order to determine these parameters, several assumptions have been made. Both the modulation device and the photodetector are assumed to be resistively matched, leading to a 6 dB gain reduction relative to the unmatched case. In investigating the link nonlinearity, a static-weak nonlinearity assumption was used. This permits the Taylor expansion to be implemented in describing the nonlinear transfer function of the modulation devices. To describe the link noise, three dominant sources were considered: the laser relative intensity noise (RIN), shot noise and the thermal noise. Moreover, various definitions of the link dynamic range were introduced. A special emphasis was put on the SFDR, which is essentially the largest SNR that can be obtained by the link without any measurable dis-

tortion. Depending on the order of the limiting distortion terms of the SFDR, the link can be categorized into sub-octave and multioctave APLs. Multioctave bandwidth is desired for an APL in order to be applied in broadband systems.

For an externally-modulated link using a Mach-Zehnder modulator (MZM), increasing the input optical power to the modulator is very attractive for increasing the link performance. The most notable improvement is the link gain enhancement, which increases quadratically with the optical power. However, this high optical power will result in a high average photocurrent that might saturate or even damage the photodetector. Besides, this average current will directly contribute to APL noise because the shot noise and the RIN increase with the photocurrent. It has been shown that the low biasing scheme can be a solution to this limitation. Reducing the bias away from the quadrature towards the minimum transmission point will reduce the noise power faster than the the reduction of the link gain. This will result in an improvement of the APL noise figure. For a given modulator characteristic, an optimum bias operation which minimizes the link noise figure can be determined, taking into account the input optical power and the laser RIN level.

Although attractive from the noise figure point of view, low biasing increases second-order distortion, limiting the link to a sub-octave bandwidth. A Class-AB architecture using dual MZMs and a balanced detection scheme can be used to mitigate this problem. In this scheme, the MZMs are biased symmetrically from the lowest transmission point. The balanced detection will completely suppress even order distortions, provided perfect amplitude and RF modulation phase matchings. Beside the Class-AB scheme, an architecture using a dual-output MZM combined with a balanced detection scheme is also promising to provide very high link performance. Both the Class-AB link and the dual output MZM scheme benefit from the RIN cancellation at the balanced detector.

In order to verify these theoretical predictions, the realization and the characterization of an MZM APL were performed. Two ways of increasing the optical power to the modulator were considered: first, using a high power laser and second, using an erbium doped fiber amplifier (EDFA). Both methods proved to increase the link gain of the link. However, they differ in their noise and distortion contributions to the APL. The high power laser used in the experiments provide a considerable optical power of 100 mW with a very low RIN of -170 dB/Hz. An optimum noise figure of 25.7 dB was obtained with the quadrature biased link. Low biasing of this link improves the noise figure only by 1 dB. The small improvement is due to the fact that the APL is shot noise limited which limits the maximum noise figure advantage to only 3 dB.

In general, using the EDFA in the externally-modulated link is attractive to increase the link gain but it will limit the link noise figure and SFDR. This is due to the signal-spontaneous beating noise from the EDFA that dominates the total link noise. As a comparison, the link gain of around -14 dB can be achieved by both the high power laser link and the EDFA link. But for the earlier the noise figure is 25.7 dB while the latter has a noise figure of nearly 40 dB. The SFDR of this EDFA link is 10 dB lower relative to the high power laser link. An interesting behavior was

observed if a link containing an EDFA placed after a low biased MZM. Relative to the same arrangement where the MZM is biased at quadrature, the low bias link yields an impressive 20 dB improvement of link gain. For a detected photocurrent of less than 13 mA, a net (positive) link gain of 5 dB was achieved. This significant improvement is obtained because by means of low biasing, the small-signal gain of the EDFA can be fully accessed without saturating the amplifier. In contrast, quadrature biasing contributes to a large DC optical power that tends to compress the EDFA gain. Unfortunately, the high gain in the low biased link is obtained at the cost of decreased linearity. There are two reasons for this. Firstly, it is inherent that for the link biased away from the quadrature, elevation of the even-order distortion occurs. Secondly, due to the strong RF modulation in the optical power impinging on the photodetector, saturation of the photodetector response occurs. This will in turn reduce the input intercept points of the link and, subsequently, limiting the SFDR.

In contrast to external modulation, techniques to increase the performance of a directly modulated link are rather limited with most of them are directed towards device-level improvements. Unlike in the MZM link, low biasing in DML link is not advantageous to reduce the link noise due to RIN enhancement near threshold. This is also one of the reasons that the proposed balanced modulation and detection (BMD) scheme does not offer any performance improvement. The BMD scheme employs a pair of low biased diode lasers to create a pair of complementary half-wave rectified optical signals, which will be restored at the receiver using a balanced detection scheme. Ideally, the half-wave rectification will reduce the average photocurrent thereby reducing the noise and enhancing the link SNR. However, the experiments show that low biasing the laser will increase the RIN and the distortion in the link. Additionally, the laser bandwidth and response are also severely reduced by low biasing. This means that in contrast with the theoretical predictions, low biasing the laser diodes tends to degrade the APL performance.

Although low biasing tends to degrade the link performance, the premise of using a pair of laser diodes and a balanced detector is still promising for a performance enhancement. For this reason, the BMD architecture was slightly adjusted for a different purpose than the original idea of noise reduction. In the new arrangement, dubbed as the push-pull modulated APL, the lasers bias currents are optimized to obtain the lowest third order intermodulation (IMD3) powers. These lasers are modulated in a push-pull manner and, subsequently, the RF modulation amplitude and phase of each laser were adjusted using variable optical attenuator and delay line such that the second-order intermodulation distortion (IMD2) power at the output is minimized. With this arrangement, a high multioctave SFDR can be achieved. One of the highest broadband SFDR ever shown with a directly modulated laser link has been demonstrated at the frequency of 2.5 GHz using this arrangement. The SFDR value was 120 dB.Hz$^{2/3}$ and the IMD2 power suppression of 40 dB was obtained. The frequency extension of the measurements show a limited bandwidth of 700 MHz due to the difference in laser characteristics and a slight difference in the path lengths going to the balanced detector.

## 7.2 Outlook

In this section some directions for further research will be suggested. These include an extension of the link architectures that have been presented in this thesis as well as suggestions of promising new techniques that can be further explored in the future.

### 7.2.1 System Improvements

The measurements presented here are limited by the available components and measurement equipments. Since nowadays the trend in microwave photonics systems are moving toward high frequencies, it is interesting to demonstrate the performance enhancement techniques presented here at a higher frequency range, i.e. at microwave or millimeter-wave frequency range. Additionally the results presented here have been shown for back-to-back arrangements. It is important to show that these enhancement techniques also work for various link lengths. One aspects that might become a limiting factor for long link and high frequency is the chromatic dispersion effect in the optical fibers [65]. Moreover, in this work, the experiments were limited to tone modulations. The extension of this will be to use more advance modulation techniques and subsequently to rate the system performance in terms of bit error rate (BER) or error vector magnitude (EVM).

For the directly modulated APLs, it is attractive to incorporate vertical cavity surface emitting lasers (VCSELs) for further cost improvements. As briefly mentioned in Chapter 1, nowadays VCSELs have shown promising improvements in terms of performance. In the push-pull link arrangement, the use of lasers with similar characteristics will improve the performance. Thus, integrating the directly modulated lasers in one wafer to match their characteristics might become advantageous. Furthermore, improving the isolation can also be used to avoid the instabilities that were encountered during our measurements. Finally, to avoid the painstaking procedure of matching the length of the fibers, the architecture with a single optical fiber can be used. The system uses a wavelength multiplexer and a demultiplexer to combine and separate the antiphase signals carried by the two lasers [87]. The architecture is shown in Figure 7.1.

For the external modulation APLs, it is interesting to even improve the performance further by using even higher optical power, beyond the 100 mW that was shown here. This will dictate the use of a high power handling photodetector. Unfortunately, to our knowledge, the high power handling detectors reported in recent publications [47, 67] are not yet available commercially. It is also interesting to show the Class-AB arrangement with a high power laser and high power handling MZM and balanced detector, to obtain a very high quality link with very high gain, very low noise figure and a broadband high SFDR. Moreover, using electroabsorption modulators [196, 202–206] should definitely be considered to obtain further enhancements in links performance

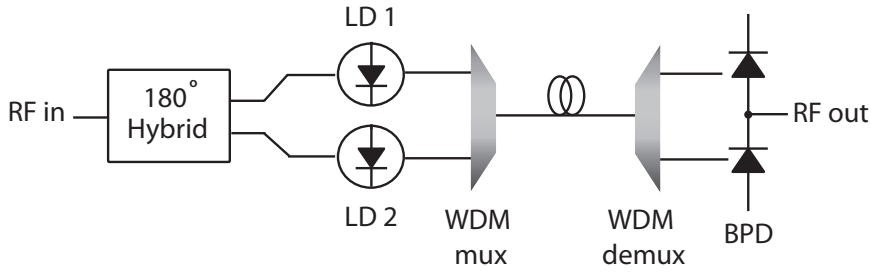


**Figure 7.1:** Single fiber architecture for the push/pull modulated APL. LD: laser diode, WDM: wavelength division multiplexing, BPD: balanced photodetector.

### 7.2.2 Frequency Modulation Scheme

The aim of proposing the BMD scheme in Chapter 4 was to obtain shot noise and RIN reduction by means of removing the unnecessary bias component in the optical signals. Complete removal of the bias will lead to optical signals that resemble complementary half-wave rectified versions of the modulating RF signal. This is the main characteristic of the so-called Class-B optical link. The term was derived from the Class-B electronic amplifier with similar characteristics. We have shown that using the the low biased laser diodes as transmitters cannot produce the desired Class-B characteristics due to the enhanced intensity noise and severe signal distortion close to threshold region. Various different approaches have been proposed to realize this desired characteristics. One promising way to achieve the desired characteristics is to use angle (phase or frequency) modulation techniques in conjunction with an optical frequency discriminator to yield intensity modulated signals. Optical filters are used as the the frequency discriminators, shaping the frequency or phase modulation into half-wave rectified intensity modulation signals. Up to now this scheme has been actively investigated by researchers at the University of Victoria in Canada led by T.E. Darcie [194, 195, 207–209]. We have started an investigation on a similar architecture using a chirp characteristic of a semiconductor laser diode as the frequency modulation source and a ring-resonator-based frequency discriminator [210].

# Bibliography


[1] K. Kao and G. Hockham, "Dielectric-fibre surface waveguides for optical frequencies," *Proc. Inst. Electr. Eng.*, vol. 133, no. 3, pp. 1151–1158, July 1966.

[2] S. Melle, R. Dodd, S. Grubb, C. Liou, V. Vusirikala, and D. Welch, "Bandwidth virtualization enables long-haul WDM transport of 40 Gb/s and 100 Gb/s services," *IEEE Commun. Mag.*, vol. 46, no. 2, pp. S22–S29, February 2008.

[3] G. Kramer and G. Pesavento, "Ethernet passive optical network (EPON): building a next-generation optical access network," *IEEE Commun. Mag.*, vol. 40, no. 2, pp. 66–73, Feb 2002.

[4] R. Williamson and R. Esman, "RF photonics," *J. Lightw. Technol.*, vol. 26, no. 9, pp. 1145–1153, May1, 2008.

[5] S. Personick, N. Rhodes, D. Hanson, and K. Chan, "Contrasting fiber-optic-component-design requirements in telecommunications, analog, and local data communications applications," *Proceedings of the IEEE*, vol. 68, no. 10, pp. 1254–1262, Oct. 1980.

[6] A. Seeds, "Microwave photonics," *IEEE Trans. Microw. Theory Tech.*, vol. 50, no. 3, pp. 877–887, Mar 2002.

[7] J. Capmany and D. Novak, "Microwave photonics combines two worlds," *Nat. Photonics*, vol. 1, no. 6, pp. 319–330, Jun 2007.

[8] D. Jäger, "Microwave photonics-from concepts to devices and applications," in *Microwave Photonics*, C. H. Lee, Ed. Boca Raton, Florida: CRC-Taylor and Francis, 2007, ch. 1, pp. 1–3.

[9] A. J. Seeds and K. J. Williams, "Microwave photonics," *J. Lightw. Technol.*, vol. 24, no. 12, pp. 4628–4641, Dec. 2006.

[10] ISI Web of Knowledge. [Online]. Available: http://www.isiknowledge.com

[11] C. Cox, E. Ackerman, R. Helkey, and G. Betts, "Techniques and performance of intensity-modulation direct-detection analog optical links," *IEEE Trans. Microw. Theory Tech.*, vol. 45, no. 8, pp. 1375–1383, Aug 1997.

[12] C. H. Cox and E. I. Ackerman, "Microwave photonics: Past, present and future," in *Proc. IEEE Int. Topical Meeting Microwave Photonics (MWP)*, Oct. 2008, pp. 9–11.

[13] C. Cox, E. Ackerman, G. Betts, and J. Prince, "Limits on the performance of RF-over-fiber links and their impact on device design," *IEEE Trans. Microw. Theory Tech.*, vol. 54, no. 2, pp. 906–920, Feb. 2006.

[14] E. Ackerman and C. Cox, "RF fiber-optic link performance," *IEEE Microw. Mag.*, vol. 2, no. 4, pp. 50–58, Dec 2001.

[15] S. Iezekiel, "Measurement of microwave behavior in optical links," *IEEE Microw. Mag.*, vol. 9, no. 3, pp. 100–120, June 2008.

[16] J. Yao, "Microwave photonics," *J. Lightw. Technol.*, vol. 27, no. 3, pp. 314–335, Feb.1, 2009.

[17] C. H. Cox, Analog Optical Links : Theory and Practice. Cambridge: Cambridge University Press, 2004.

[18] C. Lee, Microwave Photonics. Boca Raton, Florida: CRC- Taylor and Francis, 2007.

[19] H. Al-Raweshidy and S. Komaki, Radio over Fiber Technologies for Mobile Communications Networks. Boston: Artech House, 2002.

[20] (2008) IEEE topical meeting on microwave photonics (MWP). [Online]. Available: http://www.mwp2008.org/

[21] (2009) International Microwave Symposium (IMS). [Online]. Available: http://www.ims2009.org/

[22] (2009) European Conference and Exhibition on Optical Communication (ECOC). [Online]. Available: http://conference.vde.com/ecoc-2009/Pages/Home.aspx

[23] (2009) Optical Fiber Communication Conference and Exposition (OFCNFOEC). [Online]. Available: http://www.ofcnfoec.org/

[24] B. Mukherjee, "WDM optical communication networks: progress and challenges," *IEEE J. Sel. Areas Commun.*, vol. 18, no. 10, pp. 1810–1824, Oct 2000.

[25] Aircell plenum and plenum radiating cable products. [Online]. Available: http://www.trilogycoax.com/products_wireless_plenum.shtml

[26] M. Sauer, A. Kobyakov, and J. George, "Radio over fiber for picocellular network architectures," *J. Lightw. Technol.*, vol. 25, no. 11, pp. 3301–3320, Nov. 2007.

[27] A. Ng'oma, "Radio over fibre technology for broadband wireless communication systems," Ph.D. dissertation, Technische Universiteit Eindhoven, the Netherlands, 2005. [Online]. Available: http://alexandria.tue.nl/extra2/200512106.pdf

[28] S. Pappert, C. Sun, R. Orazi, and T. Weiner, "Photonic link technology for shipboard RF signal distributions," *Proceedings SPIE*, vol. 3463, pp. 123–134, 1998.

[29] R. Kalman, J. Fan, and L. Kazovsky, "Dynamic range of coherent analog fiber-optic links," *J. Lightw. Technol.*, vol. 12, no. 7, pp. 1263–1277, Jul 1994.

[30] B. Cai and A. Seeds, "Optical frequency modulation links: Theory and experiments," *IEEE Trans. Microw. Theory Tech.*, vol. 45, no. 4, pp. 505–511, Apr 1997.

[31] G. P. Agrawal, Fiber-Optic Communication Systems. New York: John Wiley & Sons, 1997.

[32] L. A. Coldren and S. W. Corzine, Diode Lasers and Photonic Integrated Circuits. New York: John Wiley & Sons, 1995.

[33] N. Dagli, "Wide-bandwidth lasers and modulators for RF photonics," *IEEE Trans. Microw. Theory Tech.*, vol. 47, no. 7, pp. 1151–1171, Jul 1999.

[34] T. Marozsak, A. Kovacs, E. Udvary, and T. Berceli, "Direct modulated lasers in radio over fiber applications," in *Proc. IEEE Int. Topical Meeting Microwave Photonics (MWP)*, Oct. 2002, pp. 129–132.

[35] X. Qian, P. Hartmann, J. Ingham, R. Penty, and I. White, "Directly-modulated photonic devices for microwave applications," in *Proc. IEEE MTT-S Int. Microwave Symp.*, 2005, pp. 4 pp.–.

[36] A. Larsson, C. Carlsson, J. Gustavsson, A. Haglund, P. Modh, and J. Bengtsson, "Direct high-frequency modulation of VCSELs and applications in fibre optic RF and microwave links," *New J. Phys.*, vol. 6, Nov 2004.

[37] P. Westbergh, E. Söderberg, J. Gustavsson, A. Larsson, Z. Zhang, J. Berggren, and M. Hammar, "Noise, distortion and dynamic range of single mode 1.3 $\mu$m InGaAs vertical cavity surface emitting lasers for radio-over-fibre links," *IET Optoelectronics*, vol. 2, no. 2, pp. 88–95, 2008.

[38] C. Carlsson, H. Martinsson, R. Schatz, J. Halonen, and A. Larsson, "Analog modulation properties of oxide confined VCSELs at microwave frequencies," *J. Lightw. Technol.*, vol. 20, no. 9, pp. 1740–1749, Sep 2002.

[39] C. Carlsson, A. Larsson, and A. Alping, "RF transmission over multimode fibers using VCSELs-comparing standard and high-bandwidth multimode fibers," *J. Lightw. Technol.*, vol. 22, no. 7, pp. 1694–1700, July 2004.

[40] Y. Inaba, H. Nakayama, M. Kito, M. Ishino, and K. Itoh, "High-power 1.55-$\mu$m mass-transport-grating DFB lasers for externally modulated systems," *IEEE J. Sel. Topics Quantum Electron.*, vol. 7, no. 2, pp. 152–158, Mar/Apr 2001.

[41] EM4, inc. AA1401 14-pin high power DFB laser. [Online]. Available: http://www.em4inc.com/product_transmission_lasers.htm

[42] G. Betts, J. Donnelly, J. Walpole, S. Groves, F. O'Donnell, L. Missaggia, J. Bailey, and A. Nagoleone, "Semiconductor laser sources for externally modulated microwave analog links," *IEEE Trans. Microw. Theory Tech.*, vol. 45, no. 8, pp. 1280–1287, Aug 1997.

[43] K. Williams, L. Nichols, and R. Esman, "Externally-modulated 3 GHz fibre optic link utilising high current and balanced detection," *Electron. Lett.*, vol. 33, no. 15, pp. 1327–1328, Jul 1997.

[44] ——, "Photodetector nonlinearity limitations on a high-dynamic range 3 GHz fiber optic link," *J. Lightw. Technol.*, vol. 16, no. 2, pp. 192–199, Feb 1998.

[45] V. Urick, M. Rogge, F. Bucholtz, and K. Williams, "The performance of analog photonic links employing highly compressed erbium-doped fiber amplifiers," *IEEE Trans. Microw. Theory Tech.*, vol. 54, no. 7, pp. 3141–3145, July 2006.

[46] H. Roussell, M. Regan, J. Prince, C. Cox, J. Chen, W. Burns, G. Betts, E. Ackerman, and J. Campbell, "Gain, noise figure and bandwidth-limited dynamic range of a low-biased external modulation link," in *Proc. IEEE Int. Topical Meeting Microwave Photonics (MWP)*, Oct. 2007, pp. 84–87.

[47] E. Ackerman, G. Betts, W. Burns, J. Campbell, C. Cox, N. Duan, J. Prince, M. Regan, and H. Roussell, "Signal-to-noise performance of two analog photonic links using different noise reduction techniques," in *Proc. IEEE MTT-S Int. Microwave Symp.*, 2007, pp. 51–54.

[48] Photonic Systems, inc. PSI-3600-LNLS light source. [Online]. Available: http://www.photonicsinc.com/light_sources.html

[49] J. McKinney, M. Godinez, V. Urick, S. Thaniyavarn, W. Charczenko, and K. Williams, "Sub-10-dB noise figure in a multiple-GHz analog optical link," *IEEE Photon. Technol. Lett.*, vol. 19, no. 7, pp. 465–467, April, 2007.

[50] Y. Shi, C. Zhang, H. Zhang, J. Bechtel, L. Dalton, B. Robinson, and W. Steier, "Low (sub-1-volt) halfwave voltage polymeric electro-optic modulators achieved by controlling chromophore shape," *Science*, vol. 288, no. 5463, pp. 119–122, Apr 2000.

[51] W. Steier *et al.*, "Polymer electro-optic devices for integrated optics," *Chem. Phys.*, vol. 245, no. 1-3, pp. 487–506, Jul 1999.

[52] W. M. J. Green, M. J. Rooks, L. Sekaric, and Y. A. Vlasov, "Ultra-compact, low RF power, 10 Gb/s silicon Mach-Zehnder modulator," *Opt. Express*, vol. 15, no. 25, pp. 17 106–17 113, Dec 2007.

[53] G. Li and P. Yu, "Optical intensity modulators for digital and analog applications," *J. Lightw. Technol.*, vol. 21, no. 9, pp. 2010–2030, Sept. 2003.

[54] M. Aoki, M. Suzuki, H. Sano, T. Kawano, T. Ido, T. Taniwatari, K. Uomi, and A. Takai, "InGaAs/InGaAsP MQW electroabsorption modulator integrated with a DFB laser fabricated by band-gap energy control selective area mocvd," *IEEE J. Quantum Electron.*, vol. 29, no. 6, pp. 2088–2096, Jun 1993.

[55] H. Kawanishi, Y. Yamauchi, N. Mineo, Y. Shibuya, H. Mural, K. Yamada, and H. Wada, "EAM-integrated DFB laser modules with more than 40-GHz bandwidth," *IEEE Photon. Technol. Lett.*, vol. 13, no. 9, pp. 954–956, Sep 2001.

[56] R. Welstand, S. Pappert, C. Sun, J. Zhu, Y. Liu, and P. Yu, "Dual-function electroabsorption waveguide modulator/detector for optoelectronic transceiver applications," *IEEE Photon. Technol. Lett.*, vol. 8, no. 11, pp. 1540–1542, Nov. 1996.

[57] Z. Bian, J. Christofferson, A. Shakouri, and P. Kozodoy, "High-power operation of electroabsorption modulators," *Appl. Phys. Lett.*, vol. 83, no. 17, pp. 3605–3607, Oct 2003.

[58] Y. Zhuang, W. Chang, and P. Yu, "Peripheral-coupled-waveguide MQW electroabsorption modulator for near transparency and high spurious free dynamic range RF fiber-optic link," *IEEE Photon. Technol. Lett.*, vol. 16, no. 9, pp. 2033–2035, Sept. 2004.

[59] C. Sun, S. Pappert, R. Welstand, J. Zhu, P. Yu, Y. Liu, and J. Chen, "High spurious free dynamic range fibre link using a semiconductor electroabsorption modulator," *Electron. Lett.*, vol. 31, no. 11, pp. 902–903, May 1995.

[60] Y. Kang, P. Mages, A. Clawson, A. Pauchard, S. Hummel, M. Bitter, Z. Pan, Y. Lo, and P. Yu, "Nonlinear distortions and excess noise behavior of fused InGaAs/Si avalanche photodiode," in *Proc. IEEE Int. Topical Meeting Microwave Photonics (MWP)*, Oct. 2002, pp. 153–156.

[61] J. Campbell, "Recent advances in telecommunications avalanche photodiodes," *J. Lightw. Technol.*, vol. 25, no. 1, pp. 109–121, Jan. 2007.

[62] D. Tulchinsky, X. Li, N. Li, S. Demiguel, J. Campbell, and K. Williams, "High-saturation current wide-bandwidth photodetectors," *IEEE J. Sel. Topics Quantum Electron.*, vol. 10, no. 4, pp. 702–708, July-Aug. 2004.

[63] K. Williams, D. Tulchinsky, and A. Hastings, "High-power and high-linearity photodiodes," in *Proc. IEEE LEOS Annual Meeting.*, Nov. 2008, pp. 290–291.

[64] A. Beling and J. C. Campbell, "InP-based high-speed photodetectors," *J. Lightw. Technol.*, vol. 27, no. 3, pp. 343–355, Feb.1, 2009.

[65] U. Gliese, S. Norskov, and T. Nielsen, "Chromatic dispersion in fiber-optic microwave and millimeter-wave links," *IEEE Trans. Microw. Theory Tech.*, vol. 44, no. 10, pp. 1716–1724, Oct 1996.

[66] P. Devgan, V. Urick, K. Williams, and J. Diehl, "Long-haul microwave analog link with shot-noise-limited performance above the stimulated Brillouin scattering threshold," in *Proc. IEEE Int. Topical Meeting Microwave Photonics (MWP)*, Oct. 2008, pp. 326–329.

[67] V. Urick, M. Rogge, F. Bucholtz, and K. Williams, "Wideband (0.045-6.25 GHz) 40 km analogue fibre-optic link with ultra-high (>40 dB) all-photonic gain," *Electron. Lett.*, vol. 42, no. 9, pp. 552–553, April 2006.

[68] H. J. Dutton, Understanding Optical Communications. New York: IBM corporation, 1998.

[69] T. Michaelis, "Laser diode evaluation for optical analog link," *IEEE Transactions on Cable Television*, vol. CATV-4, no. 1, pp. 30–42, Jan. 1979.

[70] E. Hara and T. Ozeki, "Optical video transmission by FDM analogue modulation," *IEEE Transactions on Cable Television*, vol. CATV-2, no. 1, pp. 18–34, Jan. 1977.

[71] H. Kim, R. Maciejko, and J. Conradi, "Effect of laser noise on analogue fibre optic systems," *Electron. Lett.*, vol. 16, no. 24, pp. 919–920, 1980.

[72] K.-I. Sato and K. Asatani, "Analogue baseband tv transmission experiments using semiconductor laser diodes," *Electron. Lett.*, vol. 15, no. 24, pp. 794–795, 22 1979.

[73] T. Darcie, "Subcarrier multiplexing for lightwave networks and video distribution systems," *IEEE J. Sel. Areas Commun.*, vol. 8, no. 7, pp. 1240–1248, Sep 1990.

[74] T. Darcie and G. Bodeep, "Lightwave subcarrier CATV transmission systems," *IEEE Trans. Microw. Theory Tech.*, vol. 38, no. 5, pp. 524–533, May 1990.

[75] A. Cooper, "'Fibre/radio' for the provision of cordless/mobile telephony services in the access network," *Electron. Lett.*, vol. 26, no. 24, pp. 2054–2056, Nov. 1990.

[76] J. Fan, C. Lu, and L. Kazovsky, "Dynamic range requirements for microcellular personal communication systems using analog fiber-optic links," *IEEE Trans. Microw. Theory Tech.*, vol. 45, no. 8, pp. 1390–1397, Aug 1997.

[77] H. Ogawa, D. Polifko, and S. Banba, "Millimeter-wave fiber optics systems for personal radio communication," *IEEE Trans. Microw. Theory Tech.*, vol. 40, no. 12, pp. 2285–2293, Dec 1992.

[78] A. Hirata, M. Harada, and T. Nagatsuma, "120-GHz wireless link using photonic techniques for generation, modulation, and emission of millimeter-wave signals," *J. Lightw. Technol.*, vol. 21, no. 10, pp. 2145–2153, Oct. 2003.

[79] G. Smith, D. Novak, and Z. Ahmed, "Overcoming chromatic-dispersion effects in fiber-wireless systems incorporating external modulators," *IEEE Trans. Microw. Theory Tech.*, vol. 45, no. 8, pp. 1410–1415, Aug 1997.

[80] D. Wake, A. Nkansah, N. Gomes, C. Lethien, C. Sion, and J. Vilcot, "Optically powered remote units for radio-over-fiber systems," *J. Lightw. Technol.*, vol. 26, no. 15, pp. 2484–2491, Aug, 2008.

[81] E. Jacobs, J. Rodgers, D. Evans, T. Weiner, and C. Lin, "Considerations for application of RF-over-fiber to navy systems," in *Proc. IEEE Avionics, Fiber-Optics, Photonics Technology Conf.*, Oct. 2007, pp. 3–4.

[82] E. Jacobs, R. Olsen, J. Rodgers, D. Evans, T. Weiner, and C. Lin, "RF-over-fiber and optical processing for navy applications," *Optical Fiber Commun. Conf. (OFC)*, pp. 1–3, March 2007.

[83] T. Merlet, S. Formont, D. Dolfi, S. Tonda-Goldstein, N. Vodjdani, G. Auvray, S. Blanc, C. Fourdin, Y. Canal, and J. Chazelas, "Photonics for RF signal processing in radar systems," in *Proc. IEEE Int. Topical Meeting Microwave Photonics (MWP)*, Oct. 2004, pp. 305–308.

[84] J. Roman, L. Nichols, K. Wiliams, R. Esman, G. Tavik, M. Livingston, and M. Parent, "Fiber-optic remoting of an ultrahigh dynamic range radar," *IEEE Trans. Microw. Theory Tech.*, vol. 46, no. 12, pp. 2317–2323, Dec 1998.

[85] K. Garenaux, T. Merlet, M. Alouini, J. Lopez, N. Vodjdani, R. Boula-Picard, C. Fourdin, and J. Chazelas, "Recent breakthroughs in RF photonics for radar systems," *IEEE Aerosp. Electron. Syst. Mag.*, vol. 22, no. 2, pp. 3–8, Feb. 2007.

[86] J. Prince, H. Roussell, E. Ackerman, R. Knowlton, and C. Cox, "Low-cost, high performance optoelectronic components for antenna remoting," *Opt. Quantum Electron.*, vol. 30, no. 11-12, pp. 1051–1063, Dec 1998.

[87] S. Pappert, C. Sun, R. Orazi, and T. Weiner, "Microwave fiber optic links for shipboard antenna applications," in *Proc. IEEE International Conference on Phased Array Systems and Technology*, Jan. 2000, pp. 345–348.

[88] M. Manka, "Microwave photonics for electronic warfare applications," in *Proc. IEEE Int. Topical Meeting Microwave Photonics (MWP)*, Oct. 2008, pp. 275–278.

[89] S. Pappert and B. Krantz, "RF photonics for radar front-ends," *IEEE Radar Conference*, pp. 965–970, April 2007.

[90] S. Montebugnoli, M. Boschi, F. Perini, P. Faccin, G. Brunori, and E. Pirazzini, "Large antenna array remoting using radio-over-fiber techniques for radio astronomical application," *Microw. Opt. Technol. Lett.*, vol. 46, no. 1, pp. 48–54, Jul 2005.

[91] P. Bolli, F. Perini, S. Montebugnoli, G. Pelosi, and S. Poppi, "Basic Element for Square Kilometer Array Training (BEST): Evaluation of the antenna noise temperature," *IEEE Antennas Propag. Mag.*, vol. 50, no. 2, pp. 58–65, APR 2008.

[92] R. Spencer, L. Hu, B. Smith, M. Bentley, I. Morison, B. Anderson, D. Moodie, M. Robertson, and D. Nesset, "The use of optical fibres in radio astronomy," *J. Mod. Opt.*, vol. 47, no. 11, pp. 2015–2020, Sep 2000.

[93] E. Ackerman, C. Cox, J. Dreher, M. Davis, and D. DeBoer, "Fiber-optic antenna remoting for radioastronomy applications," $27^{th}$ *URSI General Assembly*, p. 595, August 2002.

[94] P. Maat. (2009) Photonic phased array receiver systems for astronomy instrumentation. [Online]. Available: http://www.epixnet.org/workshop/

[95] L. D'Addario and W. Shillue. (2006) Applications of microwave photonics in radio astronomy and space communication. [Online]. Available: http://trs-new.jpl.nasa.gov/dspace/handle/2014/39938

[96] R. Beresford, "ASKAP photonic requirements," in *Proc. IEEE Int. Topical Meeting Microwave Photonics (MWP)*, Oct. 2008, pp. 62–65.

[97] W. Shillue, "Fiber distribution of local oscillator for Atacama Large Millimeter Array," *Optical Fiber Commun. Conf. (OFC)*, pp. 1–3, Feb. 2008.

[98] B. Shillue, S. AlBanna, and L. D'Addario, "Transmission of low phase noise, low phase drift millimeter-wavelength references by a stabilized fiber distribution system," in *Proc. IEEE Int. Topical Meeting Microwave Photonics (MWP)*, Oct. 2004, pp. 201–204.

[99] J. Payne and W. Shillue, "Photonic techniques for local oscillator generation and distribution in millimeter-wave radio astronomy," in *Proc. IEEE Int. Topical Meeting Microwave Photonics (MWP)*, Oct. 2002, pp. 9–12.

[100] W. Shieh, G. Lutes, S. Yao, L. Maleki, and J. Garnica, "Performance of a 12-Kilometer Photonic Link for X-Band Antenna Remoting in NASA's Deep Space Network," *Telecommunications and Mission Operations Progress Report*, vol. 138, pp. 1–8, Apr. 1999.

[101] The ATA website at SETI.org. [Online]. Available: http://www.seti.org/ata

[102] The ALMA website. [Online]. Available: http://www.almaobservatory.org

[103] The LOFAR website. [Online]. Available: http://www.lofar.org/

[104] The SKA website. [Online]. Available: http://www.skatelescope.org/

[105] S. Li, S. Pappert, R. Orazi, L. Koyama, and J. Feist, "An electro-optic probe for ship EMC applications," *IEEE Int. Symp. on Electromagnetic Compatibility*, pp. 81–86, Aug 1995.

[106] T. Sanford, R. Newell, G. Darmanin, B. O'Connor, and M. Nicholson, "A wide bandwidth, high dynamic range, analog fiber optic link for EMP and EMC testing," *Pulsed Power Conference, 1989. 7th*, pp. 372–375, 1989.

[107] R. Newell, T. Sanford, B. O'Connor, G. Darmanin, and M. Nicholson, "A wide bandwidth, high dynamic range, analogue fibre optic link for EMP and EMC testing," *IEE Colloquium on Analogue Optical Communications*, pp. 51/1–51/4, Dec 1989.

[108] J. Yuan, J. Wei, and G. Shen, "A direct modulated optical link for MRI RF receive coil interconnection," *J. Magn. Reson.*, vol. 189, no. 1, pp. 130–138, Nov 2007.

[109] ——, "A 4-channel coil array interconnection by analog direct modulation optical link for 1.5-T MRI," *IEEE Trans. Med. Imag.*, vol. 27, no. 10, pp. 1432–1438, Oct. 2008.

[110] U. Gliese, T. Nielsen, S. Norskov, and K. Stubkjaer, "Multifunctional fiber-optic microwave links based on remote heterodyne detection," *IEEE Trans. Microw. Theory Tech.*, vol. 46, no. 5, pp. 458–468, May 1998.

[111] J. Capmany, B. Ortega, and D. Pastor, "A tutorial on microwave photonic filters," *J. Lightw. Technol.*, vol. 24, no. 1, pp. 201–229, Jan. 2006.

[112] R. Minasian, "Photonic signal processing of microwave signals," *IEEE Trans. Microw. Theory Tech.*, vol. 54, no. 2, pp. 832–846, Feb. 2006.

[113] J. Capmany, B. Ortega, D. Pastor, and S. Sales, "Discrete-time optical processing of microwave signals," *J. Lightw. Technol.*, vol. 23, no. 2, pp. 702–723, Feb. 2005.

[114] H. Zmuda, R. Soref, P. Payson, S. Johns, and E. Toughlian, "Photonic beamformer for phased array antennas using a fiber grating prism," *IEEE Photon. Technol. Lett.*, vol. 9, no. 2, pp. 241–243, Feb. 1997.

[115] J. Lee, R. Loo, S. Livingston, V. Jones, J. Lewis, H.-W. Yen, G. Tangonan, and M. Wechsberg, "Photonic wideband array antennas," *IEEE Trans. Antennas Propag.*, vol. 43, no. 9, pp. 966–982, Sep 1995.

[116] M. Frankel and R. Esman, "True time-delay fiber-optic control of an ultrawideband array transmitter/receiver with multibeam capability," *IEEE Trans. Microw. Theory Tech.*, vol. 43, no. 9, pp. 2387–2394, Sep 1995.

[117] R. Minasian and K. Alameh, "Optical-fiber grating-based beamforming network for microwave phased arrays," *IEEE Trans. Microw. Theory Tech.*, vol. 45, no. 8, pp. 1513–1518, Aug 1997.

[118] J. Corral, J. Marti, S. Regidor, J. Foster, R. Laming, and M. Cole, "Continuously variable true time-delay optical feeder for phased-array antenna employing chirped fiber grating," *IEEE Trans. Microw. Theory Tech.*, vol. 45, no. 8, pp. 1531–1536, Aug 1997.

[119] J. Roman, M. Frankel, P. Matthews, and R. Esman, "Time-steered array with a chirped grating beamformer," *Electron. Lett.*, vol. 33, no. 8, pp. 652–653, Apr 1997.

[120] L. Zhuang, C. Roeloffzen, R. Heideman, A. Borreman, A. Meijerink, and W. van Etten, "Single-chip ring resonator-based 1 × 8 optical beam forming network in CMOS-compatible waveguide technology," *IEEE Photon. Technol. Lett.*, vol. 19, no. 15, pp. 1130–1132, Aug.1, 2007.

[121] W. van Etten, Introduction to Random Signals and Noise. Chisester, West Sussex: John Wiley & Sons, 2005.

[122] W. van Etten and J. van der Plaats, Fundamentals of Optical Fiber Communications. London: Prentice Hall, 1991.

[123] A. Yariv and P. Yeh, Photonics: Optical Electronics in Modern Communications, 6th ed. New York: Oxford University Press, 2007.

[124] T. Darcie and A. Moye, "Modulation-dependent limits to intensity-noise suppression in microwave-photonic links," *IEEE Photon. Technol. Lett.*, vol. 17, no. 10, pp. 2185–2187, Oct. 2005.

[125] X. Meng, "Designing high dynamic range microwave photonic links for radio applications," *Fiber Integrated Opt.*, vol. 23, no. 1, pp. 1–56, 2004.

[126] K. Williams, R. Esman, and M. Dagenais, "Nonlinearities in p-i-n microwave photodetectors," *J. Lightw. Technol.*, vol. 14, no. 1, pp. 84–96, Jan 1996.

[127] B. Kolner and D. Dolfi, "Intermodulation Distortion and Compression in an Integrated Electrooptic Modulator," *Appl. Optics*, vol. 26, no. 17, pp. 3676–3680, Sep 1987.

[128] J. C. Pedro and N. B. Carvalho, Intermodulation Distortion in Microwave and Wireless Circuits. Boston: Artech House, 2003.

[129] T. Darcie, R. Tucker, and G. Sullivan, "Intermodulation and harmonic distortion in InGaAsP lasers," *Electron. Lett.*, vol. 21, no. 16, pp. 665–666, 1985.

[130] K. Lau and A. Yariv, "Intermodulation Distortion in a Directly Modulated Semiconductor Injection-Laser," *Appl. Phys. Lett.*, vol. 45, no. 10, pp. 1034–1036, 1984.

[131] R. Meijerink, A. Meijerink, D. Marpaung, C. Roeloffzen, and W. van Etten, "Performance study of a ring resonator-based optical beam forming system for phased array receive antennas," in *Proc. IEEE SCVT Benelux*, Enschede, the Netherlands, Nov. 1–2, 2007, pp. 1–5.

[132] R. Alferness, "Waveguide electrooptic modulators," *IEEE Trans. Microw. Theory Tech.*, vol. 82, no. 8, pp. 1121–1137, Aug 1982.

[133] J. Schaffner and W. Bridges, "Intermodulation distortion in high dynamic range microwave fiber-optic links with linearized modulators," *J. Lightw. Technol.*, vol. 11, no. 1, pp. 3–6, Jan 1993.

[134] M. LaGasse, W. Charczenko, M. Hamilton, and S. Thaniyavarn, "Optical carrier filtering for high dynamic range fibre optic links," *Electron. Lett.*, vol. 30, no. 25, pp. 2157–2158, Dec 1994.

[135] R. Esman and K. Williams, "Wideband efficiency improvement of fiber optic systems by carrier subtraction," *IEEE Photon. Technol. Lett.*, vol. 7, no. 2, pp. 218–220, Feb 1995.

[136] $u^2t$ photonics. [Online]. Available: http://www.u2t.de

[137] K. Williams, D. Tulchinsky, and J. Campbell, "High-power photodiodes," in *Proc. IEEE Int. Topical Meeting Microwave Photonics (MWP)*, Oct. 2007, pp. 9–13.

[138] M. Islam, T. Jung, T. Itoh, M. Wu, A. Nespola, D. Sivco, and A. Cho, "High power and highly linear monolithically integrated distributed balanced photodetectors," *J. Lightw. Technol.*, vol. 20, no. 2, pp. 285–295, Feb 2002.

[139] E. Ackerman, S. Wanuga, D. Kasemset, A. Daryoush, and N. Samant, "Maximum dynamic range operation of a microwave external modulation fiber-optic link," *IEEE Trans. Microw. Theory Tech.*, vol. 41, no. 8, pp. 1299–1306, Aug 1993.

[140] M. Farwell, W. Chang, and D. Huber, "Increased linear dynamic range by low biasing the mach-zehnder modulator," *IEEE Photon. Technol. Lett.*, vol. 5, no. 7, pp. 779–782, Jul 1993.

[141] R. Helkey, "Relative intensity noise cancellation in bandpass external-modulation links," *IEEE Trans. Microw. Theory Tech.*, vol. 46, no. 12, pp. 2083–2091, Dec 1998.

[142] E. Ackerman and C. Cox, "Microwave photonic links with gain and low noise figure," in *Proc. IEEE LEOS Annual Meeting.*, Oct. 2007, pp. 38–39.

[143] J. Devenport and A. Karim, "Optimization of an externally modulated RF photonic link," *Fiber Integrated Opt.*, vol. 27, no. 1, pp. 7–14, Jan-Feb 2008.

[144] A. Karim and J. Devenport, "Noise figure reduction in externally modulated analog fiber-optic links," *IEEE Photon. Technol. Lett.*, vol. 19, no. 5, pp. 312–314, March1, 2007.

[145] ——, "Low noise figure microwave photonic link," *Microwave Symposium, 2007. IEEE/MTT-S International*, pp. 1519–1522, June 2007.

[146] X. Meng and A. Karim, "Microwave photonic link with carrier suppression for increased dynamic range," *Fiber Integrated Opt.*, vol. 25, no. 3, pp. 161–174, May-Jun 2006.

[147] M. M. Sisto, S. LaRochelle, and L. A. Rusch, "Gain optimization by modulator-bias control in radio-over-fiber links," *J. Lightw. Technol.*, vol. 24, no. 12, pp. 4974–4982, Dec. 2006.

[148] A. Lindsay, "An analysis of coherent carrier suppression techniques for photonic microwave links," *IEEE Trans. Microw. Theory Tech.*, vol. 47, no. 7, pp. 1194–1200, Jul 1999.

[149] W. Burns, G. Gopalakrishnan, and R. Moeller, "Multi-octave operation of low-biased modulators by balanced detection," *IEEE Photon. Technol. Lett.*, vol. 8, no. 1, pp. 130–132, Jan. 1996.

[150] M. Saiful h, T. Chau, S. Mathai, T. Itoh, M. Wu, D. Sivco, and A. Cho, "Distributed balanced photodetectors for broad-band noise suppression," *IEEE Trans. Microw. Theory Tech.*, vol. 47, no. 7, pp. 1282–1288, Jul 1999.

[151] G. Abbas, V. Chan, and T. Yee, "A dual-detector optical heterodyne receiver for local oscillator noise suppression," *J. Lightw. Technol.*, vol. 3, no. 5, pp. 1110–1122, Oct 1985.

[152] A. Madjar and O. Malz, "A balanced fiberoptic communication link featuring laser rin cancellation," in *Proc. IEEE MTT-S Int. Microwave Symp.*, 1992, pp. 563–566 vol.2.

[153] ——, "A Novel Architecture of a Balanced Fiber Optic Communication Link for Laser RIN Reduction," *Microw. Opt. Technol. Lett.*, vol. 6, no. 1, pp. 15–18, Jan 1993.

[154] E. Ackerman, S. Wanuga, J. MacDonald, and J. Prince, "Balanced receiver external modulation fiber-optic link architecture with reduced noise figure," in *Proc. IEEE MTT-S Int. Microwave Symp.*, 1993, pp. 723–726 vol.2.

[155] M. Islam, T. Chan, A. Nespola, S. Mathai, A. Rollinger, W. Deal, T. Itoh, M. Wu, D. Sivco, and A. Cho, "Distributed balanced photodetectors for high-performance RF photonic links," *IEEE Photon. Technol. Lett.*, vol. 11, no. 4, pp. 457–459, Apr 1999.

[156] K. Williams and R. Esman, "Optically amplified downconverting link with shot-noise-limited performance," *IEEE Photon. Technol. Lett.*, vol. 8, no. 1, pp. 148–150, Jan. 1996.

[157] L. Nichols, K. Williams, and R. Estman, "Optimizing the ultrawide-band photonic link," *IEEE Trans. Microw. Theory Tech.*, vol. 45, no. 8, pp. 1384–1389, Aug 1997.

[158] S. Datta, S. Agashe, and S. Forrest, "A high bandwidth analog heterodyne RF optical link with high dynamic range and low noise figure," *IEEE Photon. Technol. Lett.*, vol. 16, no. 7, pp. 1733–1735, July 2004.

[159] D. A. Marpaung, C. G. Roeloffzen, and W. van Etten, "A broadband high dynamic range analog photonic link using push-pull directly-modulated semiconductor lasers," in *Proc. IEEE MTT-S Int. Microwave Symp.*, 2008, pp. 507–510.

[160] Discovery Semiconductors, inc. [Online]. Available: http://www.chipsat.com

[161] T. Darcie, A. Moye, P. Driessen, J. Bull, H. Kato, and N. Jaeger, "Noise reduction in class-AB microwave-photonic links," in *Proc. IEEE Int. Topical Meeting Microwave Photonics (MWP)*, Oct. 2005, pp. 329–332.

[162] T. Darcie and P. Driessen, "Class-AB techniques for high-dynamic-range microwave-photonic links," *IEEE Photon. Technol. Lett.*, vol. 18, no. 8, pp. 929–931, April 2006.

[163] J. Bull, T. Darcie, J. Zhang, H. Kato, and N. Jaeger, "Broadband class-AB microwave-photonic link using polarization modulation," *IEEE Photon. Technol. Lett.*, vol. 18, no. 9, pp. 1073–1075, 1, 2006.

[164] C. Trask, "High efficiency broadband linear push-pull power amplifiers using linearity augmentation," in *Proc. IEEE Int. Symp. on Circuits and Systems (ISCAS)*, 2002, pp. II–432–II–435 vol.2.

[165] M. LaGasse and S. Thaniyavaru, "Bias-free high-dynamic-range phase-modulated fiber-optic link," *IEEE Photon. Technol. Lett.*, vol. 9, no. 5, pp. 681–683, May 1997.

[166] T. Darcie and A. Moye, "Modulation-dependent limits to intensity-noise suppression in microwave-photonic links," *IEEE Photon. Technol. Lett.*, vol. 17, no. 10, pp. 2185–2187, Oct. 2005.

[167] A. Hastings, V. Urick, C. Sunderman, J. Diehl, J. McKinney, D. Tulchinsky, P. Devgan, and K. Williams, "Suppression of even-order photodiode nonlinearities in multioctave photonic links," *J. Lightw. Technol.*, vol. 26, no. 15, pp. 2557–2562, Aug.1, 2008.

[168] G. Betts, "Linearized modulator for suboctave-bandpass optical analog links," *IEEE Trans. Microw. Theory Tech.*, vol. 42, no. 12, pp. 2642–2649, Dec 1994.

[169] L. Roselli, V. Borgioni, F. Zepparelli, F. Ambrosi, M. Comez, P. Faccin, and A. Casini, "Analog laser predistortion for multiservice radio-over-fiber systems," *J. Lightw. Technol.*, vol. 21, no. 5, pp. 1211–1223, May 2003.

[170] V. Urick, M. Rogge, P. Knapp, L. Swingen, and F. Bucholtz, "Wide-band predistortion linearization for externally modulated long-haul analog fiber-optic links," *IEEE Trans. Microw. Theory Tech.*, vol. 54, no. 4, pp. 1458–1463, June 2006.

[171] G. Wilson, T. Wood, M. Gans, J. Zyskind, J. Sulhoff, J. Johnson, T. Tanbun-Ek, and P. Morton, "Predistortion of electroabsorption modulators for analog CATV systems at 1.55 $\mu$m," *J. Lightw. Technol.*, vol. 15, no. 9, pp. 1654–1662, Sep 1997.

[172] G. Betts and F. O'Donnell, "Microwave analog optical links using suboctave linearized modulators," *IEEE Photon. Technol. Lett.*, vol. 8, no. 9, pp. 1273–1275, Sept. 1996.

[173] S. Korotky and R. de Ridder, "Dual parallel modulation schemes for low-distortion analog optical transmission," *IEEE J. Sel. Areas Commun.*, vol. 8, no. 7, pp. 1377–1381, Sep 1990.

[174] J. Brooks, G. Maurer, and R. Becker, "Implementation and evaluation of a dual parallel linearization system for am-scm video transmission," *J. Lightw. Technol.*, vol. 11, no. 1, pp. 34–41, Jan 1993.

[175] W. Burns, "Linearized optical modulator with fifth order correction," *J. Lightw. Technol.*, vol. 13, no. 8, pp. 1724–1727, Aug 1995.

[176] W. Bridges and J. Schaffner, "Distortion in linearized electrooptic modulators," *IEEE Trans. Microw. Theory Tech.*, vol. 43, no. 9, pp. 2184–2197, Sep 1995.

[177] U. Cummings and W. Bridges, "Bandwidth of linearized electrooptic modulators," *J. Lightw. Technol.*, vol. 16, no. 8, pp. 1482–1490, Aug 1998.

[178] T. Simpson, J. Liu, and A. Gavrielides, "Bandwidth enhancement and broadband noise reduction in injection-locked semiconductor lasers," *IEEE Photon. Technol. Lett.*, vol. 7, no. 7, pp. 709–711, Jul 1995.

[179] L. Chrostowski, X. Zhao, and C. Chang-Hasnain, "Microwave performance of optically injection-locked VCSELs," *IEEE Trans. Microw. Theory Tech.*, vol. 54, no. 2, pp. 788–796, Feb. 2006.

[180] X. Meng, T. Chau, D. Tong, and M. Wu, "Suppression of second harmonic distortion in directly modulated distributed feedback lasers by external light injection," *Electron. Lett.*, vol. 34, no. 21, pp. 2040–2041, Oct 1998.

[181] C. Cox, H. Roussell, R. Ram, and R. Helkey, "Broadband, directly modulated analog fiber link with positive intrinsic gain and reduced noise figure," in *Proc. IEEE Int. Topical Meeting Microwave Photonics (MWP)*, Oct. 1998, pp. 157–160.

[182] J. Getty, L. Johansson, E. Skogen, and L. Coldren, "1.55-$\mu$m bipolar cascade segmented ridge lasers," *IEEE J. Sel. Topics Quantum Electron.*, vol. 9, no. 5, pp. 1138–1145, Sept.-Oct. 2003.

[183] G. Keiser, Optical Fiber Communications. New York: McGraw-Hill, 1991.

[184] D. Marpaung, C. Roeloffzen, and W. van Etten, "A novel modulation scheme for noise reduction in analog fiber optic links," in *Proc. IEEE LEOS Benelux Symp.*, Enschede, the Netherlands, Dec. 1–2, 2005, pp. 113–116.

[185] ——, "Dynamic range enhancement in analog optical links with a balanced modulation and detection scheme," in *Proc. IEEE Int. Topical Meeting Microwave Photonics (MWP)*, Oct. 2006, pp. 1–4.

[186] ——, "Characterization of a balanced modulation and detection analog optical link," in *Proc. IEEE LEOS Benelux Symp.*, Brussels, Belgium, Dec. 17–18, 2007, pp. 255–258.

[187] S. B. Constant, Y. Le Guennec, G. Maury, M. Lourdiane, and B. Cabon, "Directly modulated laser diode in the nonlinear regime for low-cost digital frequency up-conversion," *Microw. Opt. Technol. Lett.*, vol. 50, no. 5, pp. 1214–1219, May 2008.

[188] S. Constant, Y. Le Guennec, G. Maury, N. Corrao, and B. Cabon, "Low-cost all-optical up-conversion of digital radio signals using a directly modulated 1550-nm emitting VCSEL," *IEEE Photon. Technol. Lett.*, vol. 20, no. 2, pp. 120–122, Jan.15, 2008.

[189] H. Ogawa and H. Kamitsuna, "Fiber optic microwave links using balanced laser harmonic generation, and balanced/image cancellation laser mixing," *IEEE Trans. Microw. Theory Tech.*, vol. 40, no. 12, pp. 2278–2284, Dec 1992.

[190] "Spectrum Analysis Basics. Application Note 150," Agilent Technologies, Inc, USA. [Online]. Available: http://cp.literature.agilent.com/litweb/pdf/5952-0292.pdf

[191] K. Petermann, Laser Diode Modulation and Noise. Dordrecht: Kluwer Academic Publishers, 1988.

[192] K. Sato, "Intensity noise of semiconductor laser diodes in fiber optic analog video transmission," *IEEE J. Quantum Electron.*, vol. 19, no. 9, pp. 1380–1391, Sep 1983.

[193] B. Wang, P.-Y. Chiang, M.-S. Kao, and W. Way, "Large-signal spurious-free dynamic range due to static and dynamic clipping in direct and external modulation systems," *J. Lightw. Technol.*, vol. 16, no. 10, pp. 1773–1785, Oct 1998.

[194] T. Darcie, J. Zhang, P. Driessen, and J.-J. Eun, "Class-B microwave-photonic link using optical frequency modulation and linear frequency discriminators," *J. Lightw. Technol.*, vol. 25, no. 1, pp. 157–164, Jan. 2007.

[195] P. Driessen, T. Darcie, and J. Zhang, "Analysis of a class-B microwave-photonic link using optical frequency modulation," *J. Lightw. Technol.*, vol. 26, no. 15, pp. 2740–2747, Aug.1, 2008.

[196] S. Mathai, F. Cappelluti, T. Jung, D. Novak, R. Waterhouse, D. Sivco, A. Cho, G. Ghione, and M. Wu, "Experimental demonstration of a balanced electroabsorption modulated microwave photonic link," *IEEE Trans. Microw. Theory Tech.*, vol. 49, no. 10, pp. 1956–1961, Oct 2001.

[197] D. Marpaung, C. Roeloffzen, and W. van Etten, "Enhancement of multioctave dynamic range in a push-pull modulated analog photonic link," in *Proc. IEEE LEOS Benelux Symp.*, Enschede, the Netherlands, Nov. 27–28, 2008, pp. 15–18.

[198] T. Marozsak, E. Udvary, A. Kovacs, and T. Berceli, "Effect of optical reflection on nonlinear characteristics of direct modulated lasers," in *Proc. IEEE Int. Topical Meeting Microwave Photonics (MWP)*, Oct. 2003, pp. 227–230.

[199] Photonic Systems, inc. PSI-3600-D1 modulator. [Online]. Available: http://www.photonicsinc.com/modulator.html

[200] P. C. Becker, N. A. Olsson, and J. R. Simpson, Erbium-Doped Fiber Amplifiers: Fundamentals and Technology. New York: Academic Press, 1999.

[201] M. Pettitt, "Use of optical amplifiers to increase distribution capacity of optical analogue video systems," *IEE Proceedings J Optoelectronics*, vol. 140, no. 6, pp. 404–410, Dec 1993.

[202] B. Masella and X. Zhang, "A novel single wavelength balanced system for radio over fiber links," *IEEE Photon. Technol. Lett.*, vol. 18, no. 1, pp. 301–303, 1, 2006.

[203] S. Sohn and S. Han, "Linear optical modulation in a serially cascaded electroabsorption modulator," *Microw. Opt. Technol. Lett.*, vol. 27, no. 6, pp. 447–450, Dec 2000.

[204] G. Lee and S. Han, "Linear dual electroabsorption modulator for analog optical transmission," *Microw. Opt. Technol. Lett.*, vol. 22, no. 6, pp. 369–373, Sep 1999.

[205] H. Jung, G. Lee, S. Han, and W. Choi, "Nonlinearity suppression of electroabsorption modulator through dual-parallel modulation," *Microw. Opt. Technol. Lett.*, vol. 29, no. 1, pp. 2–5, Apr 2001.

[206] S. Sohn and S. Han, "Simultaneous suppression of IMD2 and IMD3 in analog electroabsorption modulation," *Microw. Opt. Technol. Lett.*, vol. 29, no. 6, pp. 373–376, Jun 2001.

[207] J. Zhang and T. Darcie, "Low-biased microwave-photonic link using optical frequency or phase modulation and fiber-bragg-grating discriminator," in *Optical Fiber Commun. Conf. (OFC)*, Mar. 2006.

[208] ——, "Demonstration of a class-B microwave-photonic link using optical frequency modulation and complementary fiber-bragg-grating discriminators," in *Optical Fiber Commun. Conf. (OFC)*, 2006, postdeadline paper.

[209] T. Darcie and J. Zhang, "High-performance microwave-photonic links," in *Proc. IEEE Radio and Wireless Symposium*, Jan. 2008, pp. 125–128.

[210] R. Timens, D. A. Marpaung, C. Roeloffzen, and W. van Etten, "Design and simulation of an integrated optical ring resonator based frequency discriminator for analog optical links," in *Proc. IEEE LEOS Benelux Symp.*, Enschede, the Netherlands, Nov. 27–28, 2008, pp. 95–98.

# A

# Wide-sense Stationarity, Ergodicity and the Wiener-Khinchin Theorem

In this appendix, we briefly review the definitions of wide-sense stationarity and ergodicity of a stochastic process and the Wiener-Khinchin theorem used in the derivations of the noise power in Chapter 2.

## A.1 Wide-sense Stationarity

A stochastic process $X(t)$ is considered wide-sense stationary if it satisfies the conditions

$$\mathrm{E}[X(t)] = \mathrm{E}[X(t+\tau)] \quad \forall\, \tau \in \mathbb{R}, \tag{A.1}$$

and

$$\mathrm{E}[X(t)\,X(t+\tau)] = R_{XX}(\tau) \quad \forall\, \tau \in \mathbb{R}, \tag{A.2}$$

where the notation $\mathrm{E}[\cdot]$ denotes the expected value and $R_{XX}(\tau)$ is the autocorrelation function of $X(t)$. The first condition implies that the mean of $X(t)$ must be constant. The second condition implies that the autocorrelation function depends only on the time difference $\tau$ and not on the time instant $t$.

## A.2 Ergodicity

A wide-sense stationary stochastic process $X(t)$ is called ergodic if it satisfies two conditions

$$\mathrm{A}[X(t)] = \mathrm{E}[X(t)], \tag{A.3}$$

and

$$\mathrm{A}[X(t)\,X(t+\tau)] = R_{XX}(\tau) \quad \forall\, \tau \in \mathbb{R}, \tag{A.4}$$

where $\mathrm{A}[X(t)]$ is the time average given by

$$\mathrm{A}[X(t)] \triangleq \lim_{T\to\infty} \frac{1}{2T} \int_{-T}^{T} x(t)\,\mathrm{d}t. \tag{A.5}$$

Thus, an ergodic process has (non-random) time averages, $\mathrm{A}[X(t)]$ and $\mathrm{A}[X(t)\,X(t+\tau)]$, which are equal to the ensemble averages, $\mathrm{E}[X(t)]$ and $R_{XX}(\tau)$.

## A.3 Wiener-Khinchin Theorem

The Wiener-Khinchin theorem states that the power spectral density of a wide-sense stationary random process is the Fourier transform of the corresponding autocorrelation function. Thus we have a pair of relations:

$$S_{XX}(\omega) = \int_{-\infty}^{\infty} R_{XX}(\tau) \exp\left(-\mathrm{j}\omega\tau\right) \mathrm{d}\tau, \tag{A.6}$$

and

$$R_{XX}(\tau) = \frac{1}{2\pi} \int_{-\infty}^{\infty} S_{XX}(\omega) \exp\left(\mathrm{j}\omega\tau\right) \mathrm{d}\omega. \tag{A.7}$$

# B

# Spurious-Free Dynamic Range

In this appendix, the expressions of the spurious-free dynamic range (SFDR) in Equations (2.85) and (2.84) are derived. The $n^{\text{th}}$ order SFDR ($\text{SFDR}_n$) is defined as the signal-to-noise ratio (SNR) at the input power where the $n^{\text{th}}$ order intermodulation distortion power ($\text{IMD}_n$) is equal to the noise power spectral density ($P_{\text{N}}$). This is illustrated in Figure B.1. Recall that $\text{SFDR}_n$ can be defined as a range in either input or output powers.

Let us examine the Figure B.1 more closely. Suppose that $P_{\text{N}}$ is expressed in dBm/Hz and the $n^{\text{th}}$ order output intercept point of the system, expressed in dBm, is $\text{OIP}_n$. We can define two right triangles, namely A and B. The sides of triangle A are $\text{OIP}n - P_{\text{N}}$ and $x$, where the sides of triangle B are $\text{OIP}n - P_{\text{N}}$ and $x + \text{SFDR}_n$.

From triangle A we can determine the relation

$$x = \frac{(\text{OIP}n - P_{\text{N}})}{n}, \tag{B.1}$$

while from triangle B we have the relation

$$x + \text{SFDR}_n = (\text{OIP}n - P_{\text{N}}) . \tag{B.2}$$

Substituting Equation (B.1) into Equation (B.2) and re-arranging the terms will yield

$$\text{SFDR}_n = \frac{n-1}{n} (\text{OIP}n - P_{\text{N}}) . \tag{B.3}$$

If the link gain and the noise figure of the system, both expressed in decibels, are $G$ and NF, respectively, we can use Equation (2.48) in Chapter 2 to write the noise power spectral density as

$$P_{\text{N}} = G + \text{NF} - 174 \text{ (dBm/Hz)} . \tag{B.4}$$

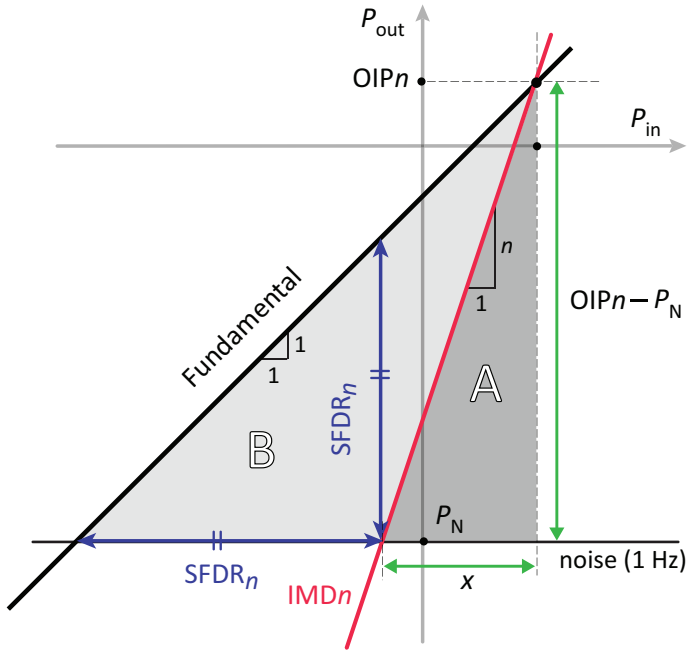


**Figure B.1:** SFDR Definition

Substituting Equation (B.4) into Equation (B.3) will give the desired expression as given in Equation (2.85) of Chapter 2

$$\mathrm{SFDR}_n = \frac{n-1}{n}\left(\mathrm{OIP}n - \mathrm{NF} - G + 174\ (\mathrm{dBm/Hz})\right). \tag{B.5}$$

Finally, substituting the relation OIP$n$ = IIP$n$ + $G$ into Equation (B.5) will give the relation in Equation (2.84) of Chapter 2

$$\mathrm{SFDR}_n = \frac{n-1}{n}\left(\mathrm{IIP}n - \mathrm{NF} + 174\ (\mathrm{dBm/Hz})\right). \tag{B.6}$$

# Acknowledgments

There are exactly 1640 days spanning the beginning (March 1st, 2005) and the end (August 27th, 2009) of the work presented in this thesis (Google it). For each and every day, I'm hugely indebted to a number of people. First, I'd like to thank my promoter Prof. Wim van Etten who has given me the opportunity to work on this project and for his guidance during the research. His "open door" policy has helped me a lot in the early struggle of this work. I thank my assistant promoter Dr. Chris Roeloffzen for the fruitful discussions and for his willingness to share his rich experiences in doing the experiments. I'm also very grateful for his support during the difficult times in the early stage of writing this thesis. I'm looking forward to continue our collaboration in the SANDRA project.

This work was carried out within the framework of the PACMAN project. I would like to acknowledge the funding from the Dutch Ministry of Economic Affair and I'd like thank all the project partners for the useful discussions during the project meetings. I especially acknowledge Peter Maat and Klaas Dijkstra for the fruitful discussions during my stay in ASTRON, Dwingeloo.

I would like to thank the other members of my graduation committee, Prof. Ton Mouthaan, Prof. Dieter Jäger, Prof. Jurriaan Schmitz, Prof. Alfred Driessen, Prof. Frank van Vliet and Dr. Peter Maat for agreeing to be in the committee and for reading the final draft of my thesis.

I've had four-and-a-half enjoyable years in the Telecommunication Engineering group, thanks to the current and the former members of the group. I would like to thank Eduard Bos, Rajeev Roy, Leimeng Zhuang (Brussels + sixty euros = bad idea), Laura "'Pronto"' Anitori, Anne Roc'h, Abdel Bekkaoui, Alex Blaj, Reza Khan, Riccardo Iannarelli, Roelof Timens, Elangovan Krishnan, Le An, Ramen Dutta, Frank Leferink, Joe Tauritz, Roland Meijerink, Mark Bentum, Jack van Galen and Martin Tijmes. Special thanks go to Arjan Meijerink for many many insightful discussions about microwave photonics as well as about "random" things, and to Annemiek Janssen and Lillian Hannink for taking care of the administrative matters but more importantly for their infallible kindness and their friendships. To Mauri, thanks for being one of my paranimfen and for voluntarily learning some "essential" Indonesia words from me. Practice them always and you'll earn your reward (on a second thought, perhaps it's wiser to keep them to yourself...).

I'm fortunate to share the friendship with Didit (who has traveled all the way from Barcelona to be one of my paranimfen, thanks DvW!) and Fiska, Arie (who has helped me a lot with the preparations of this thesis and the defense) and Meli, Danang and Mungki, Teduh and Emma, Zakia and Anne, Fausto (the professional

bowler) and Simona, Nur and Angela (thanks for the wonderful time in Rome and Palermo), "Bang" Boro and Grace, Anna Sembiring, Reza and Ocha, Wenny, Liam, Robert Taniman, Henri Uranus and the people from Calslaan 1: Mohammed, Robert, Desu and Jerry.

I've had some incredible supports from my family members in Indonesia during my (seemingly perpetual) struggle with laser noise and distortions. I thank my mother for her never ending support and love. *Tetap sehat ya ma. Tersenyumlah dan jangan menangis lagi.* I thank my brothers and sisters: bang Roelly, kak Butet, bang Ucok dan kak Itri, for their love and for carrying so much of the burdens so that I can manage to finish this task. I also thank my family in Tangerang: Amang, Inang, kak Helen, Grace, Echa and Bona for their support and for their love.

And finally I thank my lovely wife and my best friend Vince Evelina Sitorus, who has this knack of getting theses dedicated to her (effective index method, slow light or analog links, you never seem to mind). I just couldn't put into words how grateful I am to have you in my life. During so many rapid-hope-loss times that you've shown your love the most. I cannot promise, but hopefully this is the last time I dedicate a thesis to you. Shall we go to Canada ? :-D

*David Marpaung*

*Enschede, August 2009*

# About the Author

David Marpaung was born in Balikpapan, Indonesia, on March 19$^{th}$, 1979. He received his Bachelor of Science degree (cum laude) from the Physics department Institut Teknologi Bandung (ITB), Indonesia in March 2002 on a subject of the effective index method for rectangular optical waveguides under the supervision of Dr. Alexander Iskandar. In September of the same year he started his study at the Lightwave Devices Group (LDG) (now, Integrated Optical Microsystems (IOMS)) of the University of Twente, Enschede, the Netherlands. He received the Master of Science degree in November 2003 with the thesis title "Adiabatic Excitations of Slow Light Devices" under the supervision of Dr. Hugo Hoekstra. In March 2005, he started the PhD research in the Telecommunication Engineering group University of Twente on the topic of performance enhancement of analog photonic links, under the supervision of Prof. Wim van Etten. The work carried out in the project resulted in this thesis.

David Marpaung is now employed as a post-doctoral researcher in the Telecommunication Engineering group University of Twente, Enschede, working on a novel large-scale optical beamforming network in the framework of the SANDRA (Seamless Aeronautical Networking through integration of Data Links, Radios, and Antennas) project.